Universidade de Aveiro Departamento de Química
2015

Marta Luísa Salsas Batista

A Computational Study of Ionic Liquids Used In The Production of Fuels and Biofuels

Estudo Computacional de Líquidos Iónicos Usados na Produção de Combustíveis e Biocombustíveis

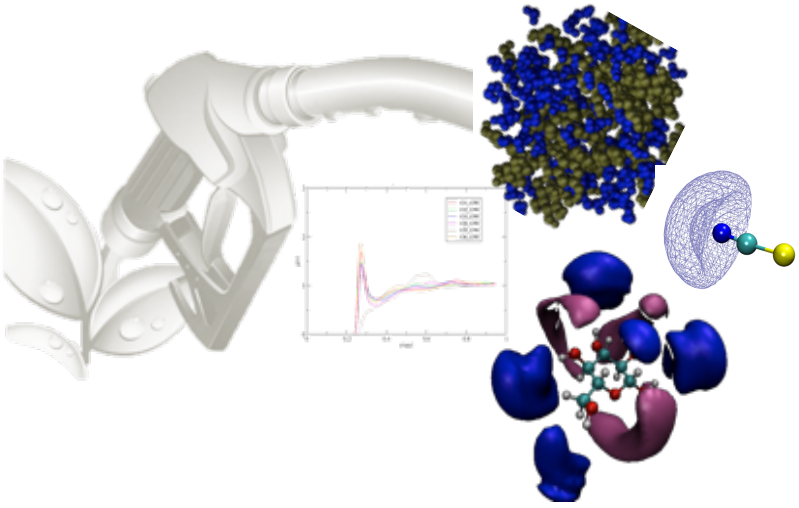

Universidade de Aveiro Departamento de Química
Ano 2015

Marta Luísa Salsas Batista

A Computational Study of Ionic Liquids Used In The Production of Fuels and Biofuels

Estudo Computacional de Líquidos Iónicos Usados na Produção de Combustíveis e Biocombustíveis

Tese apresentada à Universidade de Aveiro para cumprimento dos requisitos necessários à obtenção do grau de Doutor em Engenharia Química, realizada sob a orientação científica do Professor Doutor João Manuel da Costa e Araújo Pereira Coutinho, Professor Catedrático no Departamento de Química da Universidade de Aveiro, e do Doutor José Richard Baptista Gomes, Investigador Principal no Departamento de Química da Universidade de Aveiro

Apoio financeiro do POCTI no âmbito do III Quadro Comunitário de Apoio.

Apoio financeiro da FCT no âmbito do III Quadro Comunitário de Apoio. (SFRH/ BD / 74551 / 2010)

POPH PROGRAMA OPERACIONAL POTENCIAL HUMANO
QREN QUADRO DE REFERÊNCIA ESTRATÉGICO NACIONAL PORTUGAL 2007-2013
UNIÃO EUROPEIA Fundo Social Europeu
Governo da República Portuguesa

Dedico este trabalho à minha família.

o júri

presidente

Prof. Doutor Luís António Ferreira Martins Dias Carlos
Professor Catedrático da Universidade de Aveiro

Prof. Doutor João Manuel da Costa e Araújo Pereira Coutinho (orientador)
Professor Catedrático da Universidade de Aveiro

Prof. Doutor José Nuno Aguiar Canongia Lopes
Professor Associado da Universidade de Lisboa

Prof. Doutor Luís Manuel das Neves Belchior Faia dos Santos
Professor Associado da Universidade do Porto

Prof. Doutor João Paulo Cristóvão Almeida Prates Ramalho
Professor Associado da Universidade de Évora

Prof. Doutor Simão Pedro de Almeida Pinho
Professor Coordenador do Instituto Politécnico de Bragança

Doutor José Richard Baptista Gomes (co-orientador)
Investigador Principal da Universidade de Aveiro

Doutora Luciana Isabel Nabais Tomé
Estagiária de Pós Doutoramento da Universidade de Coimbra

agradecimentos

Não posso de deixar de começar por agradecer ao professor João Coutinho e ao Dr. José Richard Gomes, não só pela orientação e apoio ao longo destes quatro anos de doutoramento, mas também pelos seus ensinamentos e oportunidades que me proporcionaram. Ao professor Edward Maginn, devo um especial agradecimento, não só pela orientação mas pela recepção no seu grupo, motivação e apoio que precisava na altura em que eu estive na Universidade de Notre Dame. Finalmente, e não menos importante, quero também agradecer ao Professor Simão Pinho, com quem tive prazer em trabalhar.

"*Alone we can do so little, together we can do so much.*"

Hellen Keller

É com esta citação da famosa Hellen Keller que quero agradecer a todos os meus amigos/companheiros.
Aos meus colegas do Path, e do grupo liderado pelo Dr. Richard, aos meus amigos de toda vida, aos que conheci nesta longa caminhada. Felizmente, tenho um número significativo de pessoas a quem gostaria de dedicar um especial obrigado, mas é meu desejo poder continuar a dizê-lo pessoalmente, por muito tempo.

À minha família. *A eles e tudo por eles*. Pelo amor e apoio incondicional.
Ao meu companheiro de vida. Quero agradecer-lhe toda a paciência que teve comigo nos períodos menos bons, e ao seu apoio incondicional.

Obrigada, obrigada, obrigada!

palavras-chave

Líquidos iónicos, simulação de dinâmica molecular, combustíveis e biocombustíveis;

resumo

Nas últimas décadas a redução de emissões de gases poluentes resultantes da combustão de combustíveis fósseis tem sido uma preocupação mundial. Para tal, a redução de compostos à base de enxofre e a sua substituição por biocombustíveis (como o bioetanol, produzido em elevadas quantidades a partir de sacarose, amido ou compostos lenhocelulósicos) tem sido estudada e aplicada.

Visando este propósito, uma nova classe de solventes denominada de líquidos iónicos (LIs) têm sido estudada visando o desenvolvimento de novos processos de separação para a substituição dos solventes orgânicos atualmente utilizados. Os LIs podem ser constituídos por diferentes combinações de catiões e aniões, conferindo propriedades únicas a estes solventes. A capacidade de ajustar estas propriedades para um determinado fim ou aplicação é um dos aspetos mais relevantes dos LIs.

Dado o número elevado de combinações possíveis para os iões constituintes dos LIs, é necessário recorrer a abordagens preditivas que permitam avaliar, *a priori*, o potencial dos LIs para uma dada aplicação. Uma abordagem possível consiste em técnicas de simulação de dinâmica molecular, baseadas em mecânica estatística e nas leis de movimento de Netwon, que permitem a reprodução e caracterização de sistemas macroscópicos, pela previsão de propriedades e organização estrutural dos átomos nos sistemas em questão. No caso dos LIs, a aplicação da dinâmica molecular tem sido amplamente usada, com um desafio adicional dada a dinâmica (lenta) característica dos LIs, o que requer melhorias nos campos de força atualmente usados, como também um acrescido esforço computacional.

Esta tese aborda diferentes estudos realizados em sistemas representativos de linhas de produção dos combustíveis e biocombustíveis, onde são estudados os mecanismos de interação estabelecidos pelos LIs, através de simulações de dinâmica molecular. Desta forma, sistemas compostos por LIs e tiofeno, benzeno, água, etanol, e moléculas de glucose, serão caracterizados e avaliados. No caso das moléculas de glucose, será também estudado um campo de força recentemente publicado, de forma a avaliar a sua capacidade para reproduzir o comportamento dinâmico do sistema em solução aquosa.

Os resultados obtidos mostram que as interações estabelecidas pelos LIs estão relacionadas com as características individuais de cada LI. Em geral, a polaridade dos LIs estudados é determinante nas interações estabelecidas. Embora seja inquestionável as vantagens de usar simulação de dinâmica molecular nestes sistemas, é preciso reconhecer a necessidade de melhorias nos campos de força atuais, não só para uma correta descrição dos sistemas contendo LIs, mas também para os hidratos de carbono.

keywords Ionic liquids, molecular dynamics simulation, fossil fuels and biofuels.

abstract

For the past decades it has been a worldwide concern to reduce the emission of harmful gases released during the combustion of fossil fuels. This goal has been addressed through the reduction of sulfur-containing compounds, and the replacement of fossil fuels by biofuels, such as bioethanol, produced in large scale from biomass.

For this purpose, a new class of solvents, the Ionic Liquids (ILs), has been applied, aiming at developing new processes and replacing common organic solvents in the current processes. ILs can be composed by a large number of different combinations of cations and anions, which confer unique but desired properties to ILs. The ability of fine-tuning the properties of ILs to meet the requirements of a specific application range by mixing different cations and anions arises as the most relevant aspect for rendering ILs so attractive to researchers.

Nonetheless, due to the huge number of possible combinations between the ions it is required the use of cheap predictive approaches for anticipating how they will act in a given situation. Molecular dynamics (MD) simulation is a statistical mechanics computational approach, based on Newton's equations of motion, which can be used to study macroscopic systems at the atomic level, through the prediction of their properties, and other structural information. In the case of ILs, MD simulations have been extensively applied. The slow dynamics associated to ILs constitutes a challenge for their correct description that requires improvements and developments of existent force fields, as well as larger computational efforts (longer times of simulation).

The present document reports studies based on MD simulations devoted to disclose the mechanisms of interaction established by ILs in systems representative of fuel and biofuels streams, and at biomass pre-treatment process. Hence, MD simulations were used to evaluate different systems composed of ILs and thiophene, benzene, water, ethanol and also glucose molecules. For the latter molecules, it was carried out a study aiming to ascertain the performance of a recently proposed force field (GROMOS $56A_{CARBO}$) to reproduce the dynamic behavior of such molecules in aqueous solution.

The results here reported reveal that the interactions established by ILs are dependent on the individual characteristics of each IL. Generally, the polar character of ILs is deterministic in their propensity to interact with the other molecules. Although it is unquestionable the advantage of using MD simulations, it is necessary to recognize the need for improvements and developments of force fields, not only for a successful description of ILs, but also for other relevant compounds such as the carbohydrates.

Contents

List of Figures iii

List of Tables viii

Nomenclature ix

List of symbols x

Greek Letters x

Chemical formulas xi

ILs xi

Other compounds xii

Subscripts xiii

Superscripts xiii

1. *Introduction* 1

1.1. Scope and Objectives 2

1.2. Ionic Liquids 4

1.3. Fossil fuels improvement – desulfurization processes 6

1.4. Biofuels 8

1.4.1. Lignocellulosic materials and pre-treatment processes 9

References 16

2. *Computer approaches and Ionic Liquids' properties prediction* 20

2.1. Prediction of IL's properties through MD simulations 26

2.1.1. Density 29

2.1.2. Melting Point 33

2.1.3. Vapor pressure, boiling point and enthalpy of vaporization 35

2.1.4. Viscosity 39

2.1.5. Diffusion coefficient 42

2.1.6. Surface Tension 43

2.1.7. Structural characterization 46

Summary 49

References 51

3. *Developed Work* 58

3.1. *Evaluation of the Liquid-Liquid Equilibria of Ionic Liquids-based systems for Fuel Improvements* 60

Motivation 61

Methodology 64

Results and Discussion 68

Conclusions 89
References 90
3.2. ***Computational and Experimental Study of the Behavior of Cyano-Based Ionic Liquids in Aqueous Solutions*** 93
Motivation 94
Methodology 96
Results and Discussion 102
Conclusions 116
References 118
3.3. ***Complementary Study of Systems composed of Ethanol/Water with Cyano-based Ionic Liquids*** 123
Motivation 124
Methodology 127
Results and Discussion 130
Conclusions 147
References 148
3.4. ***Evaluation of the latest GROMOS Force Field for the Calculation of Structural, Volumetric and Dynamic Properties of Aqueous Glucose Systems*** 153
Motivation 155
Methodology 158
Results and Discussion 159
Conclusions 173
References 174
3.5. Ionic Liquids: Characterization and Assessment as Glucose Solvent 177
Motivation 178
Methodology 181
Results and Discussion 186
Conclusions 203
References 204
4. ***Conclusions and Future Work*** 210
5. ***Appendixes*** 213
Appendix A 214
Appendix B 236
Appendix C 249
Appendix D 256

Appendix E _____ **260**

List of Figures

Figure 1.1 - Primary energy use for fuel in the history of U.S.A from 1980 to 2040. Energy Information Administration (EIA), Monthly Energy Review, September 2013, DOE/EIA-0035 (2013/09).[2] _____ **2**

Figure 1.2.1 - Most common cations and anions found in literature composing ionic liquids (ILs). _____ **4**

Figure 1.4.1.1 - Structure of cellulose. _____ **10**

Figure 1.4.1.2 – Projection of the plane in cellulose I, showing the hydrogen bonding network and the numbering of the atoms. Each glucose residue forms two intramolecular hydrogen bond (O3-H—05´ and O6—H-02´) and one intermolecular bond (O6-H—O3). _____ **11**

Figure 1.4.1.3 – Mechanism of pretreating lignocellulosic materials[63]. _____ **12**

Figure 2.1 - Illustration of the different length and time scales that can be reached by most common computational approaches. _____ **21**

Figure 3.1.1 - Chemical structure of the aromatic compounds and of the cations and anions of the ILs studied in this work, and corresponding atom labelling. _____ **62**

Figure 3.1.2 - Liquid-liquid phase diagrams for [BMIM][NTf_2] (measured in this work), [BMIM][SCN][18] and [BMIM][CF_3SO_3][19] with thiophene. Dashed lines are guides to the eye. _____ **69**

Figure 3.1.3 - Excess molar volumes as a function of the mole fraction of the IL, in mixtures of [BMIM][SCN] with benzene, at different temperatures, namely, (◆) 298.15 K, (▲) 308.15 K, (■) 318.15 K and (●) 328.15 K. Solid lines represent the corresponding correlation of Redlich-Kister. The dotted line corresponds to the limit of miscibility, where at the left is the immiscibility region. _____ **75**

Figure 3.1.4 - Estimated excess molar volumes through Redlich-Kister's correlation as function of the mole fraction of the IL, at 298.15 K. _____ **75**

Figure 3.1.5 - Viscosity deviations as a function of the mole fraction of the IL, in mixtures of [BMIM][SCN] with thiophene, at different temperatures, namely, (◆) 298.15 K, (▲) 308.15 K, (■) 318.15 K and (●) 328.15 K. Solid lines represent the corresponding correlation of Redlich-Kister. The dotted line corresponds to the limit of miscibility, where at the left is the immiscibility region. _____ **76**

Figure 3.1.6 - Estimated viscosity deviations through Redlich-Kister's correlation as function of the mole fraction of the IL, at 298.15 K. _____ **76**

Figure 3.1.7 - ^{1}H NMR chemical shift deviations for [BMIM][SCN] in the mixture with thiophene. The dotted lines represent the hydrogen chemical shifts deviations for thiophene and full lines for the cation $[BMIM]^{+}$. 80

Figure 3.1.8 - ^{13}C NMR chemical shift deviations for [BMIM][SCN] in the mixture with thiophene. The dotted lines represent the carbon chemical shifts deviations for thiophene, full lines for the cation $[BMIM]^{+}$ and dashed lines for the anion $[SCN]^{-}$. 80

Figure 3.1.9 - ^{1}H NMR chemical shift deviations for [BMIM][NTf_2] in the mixture with thiophene. The dotted lines represent the hydrogen chemical shifts deviations for thiophene and full lines for the cation $[BMIM]^{+}$. 81

Figure 3.1.10 - ^{13}C NMR chemical shift deviations for [BMIM][NTf_2] in the mixture with thiophene. The dotted lines represent the carbon chemical shifts deviations for thiophene, full lines for the cation $[BMIM]^{+}$ and dashed lines for the anion $[NTf_2]^{-}$. 82

Figure 3.1.11 - Radial distribution functions of selected carbon atoms of a) $[BMIM]^{+}$ around the S atom of thiophene, b) thiophene atoms around the S atom of $[SCN]^{-}$, in the system [BMIM][SCN] + thiophene. 84

Figure 3.1.12 - Radial distribution functions of a) selected carbon atoms of $[BMIM]^{+}$ around the S atom of thiophene and b) thiophene atoms around the C1 atom of $[NTf_2]^{-}$, in the system [BMIM][NTf_2] + thiophene. 85

Figure 3.1.13 - Spatial distribution functions (SDF) for $[SCN]^{-}$ (a, b) and $[BMIM]^{+}$ (c) around thiophene from MD simulation of the [BMIM][SCN] + thiophene mixture. Yellow and blue regions represent SDF (isovalue = 25) for S and N atoms from the IL anion, respectively. Mauve, orange and brown regions represent SDF (isovalue = 32) for C10, C4 and C6 atoms of the IL cation, respectively. 85

Figure 3.1.14 - Spatial distribution functions (SDF) for $[NTf_2]^{-}$ (a, b) and $[BMIM]^{+}$ (c) around thiophene from MD simulation of the [BMIM][NTf_2] + thiophene mixture. White and red regions represent SDF (isovalues are 25 in a and 20 in b, respectively) for C and O atoms from the IL anion, respectively. Blue, orange and brown regions represent SDFs (isovalue = 32) for N2, C4 and C6 atoms of the IL cation, respectively. 86

Figure 3.1.15 - Atomic hits for SCN-constituting atoms at a) 2.5 Å, b) 3.0 Å and c) 3.5 Å around thiophene from MD simulation of the [BMIM][SCN] + thiophene mixture. Yellow, blue, cyan and white spheres stand for sulfur, nitrogen, carbon and hydrogen atoms, respectively. 88

Figure 3.2.1 - Chemical structures of the ions composing the studied ILs. 96

Figure 3.2.2 - Experimental and predicted water activity coefficients, at 298.2 K. Symbols are representing experimental data and full lines the COSMO-RS predictions (●,—)

[BMIM][DCA], (◆,—) [BMIM][SCN], (■,—) [BMIM][TCN] and (▲,—) [EMIM][TCB]. The dashed lines for [BMIM][TCN] and [EMIM][TCB] indicate the immiscibility region of these ILs in water. ____ 104

Figure 3.2.3 - Sigma profile for (—) water, (—) $[DCA]^-$, (—) $[SCN]^-$, (—) $[TCN]^-$, (—) $[TCB]^-$, (— —) $[BMIM]^+$ and (— ●) $[EMIM]^+$. ____ 105

Figure 3.2.4 - Contribution of specific interaction to the total excess enthalpy, at x_w = 0.5 and T = 298.15 K. The contribution of excess enthalpies from electrostatic/misfit is represented by the blue bars, hydrogen bonding through the red bars, van der Waals through the green bars, and total excess enthalpies of the mixtures by the purple bars. ____ 107

Figure 3.2.5. Radial distributions functions (RDFs) for mixtures of [BMIM][SCN] and water, at different mole fractions of IL and 298.15 K. RDFs for interaction of cation-water (H1-OW, —), anion-water (N-HW, —), cation-anion (H1-N, —) and solvent-solvent (OW-OW, —) are represented in each panel. ____ 109

Figure 3.2.6. Radial distributions functions (RDFs) for a) anion-water, b) cation-water, c) cation-anion and d) water-water interactions, at 80IL:20W and 298.15 K. RDFs for [BMIM][SCN] (—), [BMIM][DCA] (—), [BMIM][TCN] (—) and [EMIM][TCB] (—) are represented in each panel. ____ 110

Figure 3.2.7 - Spatial distribution functions (SDF) obtained by TRAVIS[72], for the mixture [BMIM][SCN] (above, left side), [BMIM][DCA] (above, right side), [BMIM][TCN] (down, left side) and [EMIM][TCB] (down, right side) and water, at 80IL:20W. Each anion is the center element, surrounded by oxygen atoms of water (blue surface). ____ 115

Figure 3.3.1 - Isobaric temperature-composition diagram of (a) [BMIM][SCN]+water, (b) [BMIM][DCA]+water, (c) [BMIM][TCN]+water, (d) [EMIM][TCB]+water. The solid lines represent COSMO-RS predictions. ____ 131

Figure 3.3.2 - Isobaric temperature-composition diagram of (a) [BMIM][SCN]+ethanol, (b) [BMIM][DCA]+ethanol, (c) [BMIM][TCN]+ethanol, (d) [EMIM][TCB]+ethanol. The solid lines represent COSMO-RS prediction. ____ 132

Figure 3.3.3 - Radial distributions functions (RDFs) for a) [BMIM][SCN], b) [BMIM][DCA], c) [BMIM][TCN] and d) [EMIM][TCB], at 0.20 (on the left side) and 0.40 (on the right side) mole fraction of IL and 298.15 K. In each picture is represented all types of interaction, namely RDFs for anion-ethanol (—), cation-ethanol (—), cation-anion (—) and ethanol-ethanol (—) interactions. ____ 142

Figure 3.3.4 - Spatial distribution functions (SDFs) obtained by TRAVIS[83], for the mixture [BMIM][SCN] (above, left side), [BMIM][DCA] (above, right side), [BMIM][TCN] (down,

left side) and [EMIM][TCB] (down, right side) and ethanol, at 0.20 mole fraction of IL. Each anion is the center element, surrounded by ethanol molecules (pink surface). _____146

Figure 3.4.1 - Atom labels used in this work for glucose. _____ 156

Figure 3.4.2 - Probability distribution of the hydroxymethyl group angle in glucose as a function of concentration._____ 159

Figure 3.4.3 - Comparison of experimental[36] and simulation density values at 303.15 K. __160

Figure 3.4.4. Comparison of experimental[36] and simulation viscosity values at 313.15 K. _ 163

Figure 3.4.5 - Radial distributions functions (RDFs) for glucose-water interactions, at six different glucose mole fraction and a temperature of 313.15 K. RDFs for interaction between O1-OW (—), O2-OW(—), O3-OW(—), O4-OW (—), O5-OW (—) and O6-OW (—) are represented in each figure. _____ 166

Figure 3.4.6 - Spatial distribution functions (SDFs) as a function of glucose concentration. A glucose molecule is the central element, surrounded by oxygen atoms of water (red surface)._____169

Figure 3.4.7 - The number of hydrogen bonds between glucose and water molecules (red, right axis) and water with water molecules (blue, left axis) as function of glucose concentration, at 313.15 K. _____170

Figure 3.4.8 - Comparison of experimental[36] (line series) and simulation density values estimated with scaled charges (dot series) and with the original charges (dotted-line series) at 313.15 K. _____172

Figure 3.4.9 - Comparison of experimental[36] (line series) and simulation viscosity values estimated with scaled charges (dotted series) and with the original charges (dotted-line series) at 313.15 K. _____172

Figure 3.5.1 – The solubility of glucose in water, [EMIM][SCN], [EMIM][DCA], [EMIM][TCN] and [EMIM][TCB], in a temperature range of (283.15 – 333.15) K. _____186

Figure 3.5.2 – Effect of different alkyl chain length of IL's cation on glucose solubility, in a temperature range of (283.15 – 333.15) K. _____187

Figure 3.5.3 – Comparison of experimental and computed density, for systems composed of glucose and [EMIM][SCN] and [EMIM][DCA], at 313.15 K. _____189

Figure 3.5.4 – Comparison of experimental and computed viscosity, for systems composed of glucose and [EMIM][SCN] and [EMIM][DCA], at 313.15 K. _____ 189

Figure 3.5.5 – Atom labels used in this study for glucose. _____191

Figure 3.5.6 - Radial distributions functions (RDFs) for glucose-water (above row), glucose-[EMIM][SCN] (middle row) and glucose-[EMIM][DCA] (bottom row) interactions, at six different glucose mole fraction and a temperature of 313.15 K. RDFs for interaction between

O_W/N-HO_{12}(—), O_W/N-HO_8(—), O_W/N-HO_6(—), O_W/N-HO_4(—), O_W/N-HO_2 (—) are represented in this figure. 193

Figure 3.5.7 - Spatial distributions functions (SDFs) for glucose-water and glucose-anion/cation interactions, at six different glucose mole fraction and a temperature of 313.15 K. The central molecule is glucose, surrounded by water molecules (red surfaces), cations of IL (mauve surfaces) and anions of IL (blue surface). Isovalues for atoms in water and ILs are 36 and 7 particle·nm^{-3}, respectively. 196

Figure 3.5.8 - Radial distributions functions (RDFs) and Spatial distribution functions for glucose-anion interactions for the anions of CN-based ILs, at infinite dilution and a temperature of 313.15 K. RDFs for interaction between [EMIM][SCN](—), [EMIM][DCA](—), [EMIM][TCN](—) and [EMIM][TCB](—) with glucose are represented in this figure. Additionally, at SDFs, the mauve surfaces represent the cations, and the blue surfaces the anions surrounding a glucose molecule. 199

Figure 3.5.9 - Radial distributions functions (RDFs) and Spatial distribution functions for glucose-anion interactions for the anions of CN-based ILs and [EMIM][Ac], at different glucose concentrations and a temperature of 313.15 K. RDFs for interaction between [EMIM][SCN](—), [EMIM][DCA](—), and [EMIM][Ac](—) with glucose are represented in this figure. Additionally, at SDFs, the blue surfaces represent the acetate anion surrounding a glucose molecule. 202

List of Tables

Table 2.1.1 - Detailed information concerning the MD simulations of studies reviewed in this section. 26

Table 2.1.1.1 - Estimated densities by means of MD simulations and experimental data, at different temperatures. 32

Table 2.1.2.1 - Comparison of estimated melting points obtained using different methodologies and MD simulations, $T_{m,sim}$, with available experimental, $T_{m,exp}$, data. 35

Table 2.1.3.1 - Calculated and Experimental Enthalpies of Vaporization, at T=298 K, for several ILs. 37

Table 2.1.4.1 - Estimated viscosities, at different temperatures, determined by means of MD simulations. 41

Table 2.1.5.1 - Estimated diffusion constants, at different temperatures, determined by means of MD simulations. 43

Table 2.1.2 - Accuracy of MD simulations for calculating structural and thermodynamic properties of ILs with respect to available experimental results. 50

Table 3.1.1 - Experimental density as function of temperature for pure ionic liquids, thiophene, benzene and for their mixtures, in different mole fractions and at atmospheric pressure. 69

Table 3.1.2 - Experimental viscosity data as function of temperature for pure ionic liquids, thiophene, and benzene, and also for their mixtures, in different mole fractions and at atmospheric pressure. 72

Table 3.1.3 - Coefficients for Redlich-Kister correlations for excess molar volume. 77

Table 3.1.4 - Coefficients for Redlich-Kister correlations for viscosity deviations. 77

Table 3.2.1 - Experimental water activities (a_w) and experimental and COSMO-RS water activity coefficients (γ_w) in the binary mixtures at T = 298.2 K. 102

Table 3.2.2 - Coordination number (Z) from the RDF peaks at distance below r_Z nm for anion-solvent, cation-solvent, cation-anion and solvent-solvent interaction, at each considered system and different IL mole fraction. 112

Table 3.3.1 - Experimental isobaric VLE data for the system [BMIM][SCN] (1) + water (2)[21] at (0.1, 0.07 and 0.05) MPa pressures. 134

Table 3.3.2 - Experimental isobaric VLE data for the system [BMIM][DCA] (1) + water (2) at (0.1, 0.07 and 0.05) MPa pressures. 134

Table 3.3.3 - Experimental isobaric VLE data for the system [BMIM][TCN] (1) + water (2) at (0.1, 0.07 and 0.05) MPa pressures. 135

Table 3.3.4 - Experimental isobaric VLE data for the system [BMIM][TCN] (1) + water (2) at (0.1, 0.07 and 0.05) MPa pressures. 136

Table 3.3.5 - Experimental isobaric VLE data for the system [BMIM][SCN] (1) + ethanol (2) at temperature *T*, liquid mole fraction *x*, at various system pressure 0.1, 0.07 and 0.05 MPa. 136

Table 3.3.6 - Experimental isobaric VLE data for the system [BMIM][DCA] (1) + ethanol (2) at temperature *T*, liquid mole fraction *x*, at various system pressure 0.1, 0.07 and 0.05 MPa. 137

Table 3.3.7 - Experimental isobaric VLE data for the system [BMIM][TCN] (1) + ethanol (2) at temperature *T*, liquid mole fraction *x*, at various system pressure 0.1, 0.07 and 0.05 MPa. 138

Table 3.3.8 - Experimental isobaric VLE data for the system [EMIM][TCB] (1) + ethanol (2) at temperature *T*, liquid mole fraction *x*, at various system pressure 0.1, 0.07 and 0.05 MPa. 139

Table 3.3.9 - Coordination number (Z) from the RDF peaks at distance below r_Z nm, for anion-ethanol, cation-ethanol, cation-anion and ethanol-ethanol interactions, at each system and different IL mole fraction, addressed in this study. 144

Table 3.4.1 - Experimental[36] and computational densities (ρ) for different glucose/water mixtures at 303.15 K. Values in parentheses denote the uncertainties (the standard deviation) estimated with the calculated results. AAD represents the absolute deviations of the simulated data from the experimental values. 161

Table 3.4.2 - Experimental[36] and calculated viscosities (η) at 313.15 K. Values in parentheses denote uncertainties estimated accordingly to equation 3.4.3. AAD represents the absolute deviations of the simulated data from the experimental values. 163

Table 3.4.3 - Computed self-diffusion coefficients at 313.15 K. Values in parentheses denote uncertainty (the standard deviation) associated with the calculated data. 164

Table 3.4.4 - Coordination number (CN) from the RDF peaks for glucose-water interactions, at each mixture considered. 167

Table 3.5.1 – Coordination numbers (Z) from the RDFs peaks for glucose-water (O_W-$HO_{glucose}$) and anion-glucose, at each mixture considered. 194

Table 3.5.2 – Number of hydrogen bonds established between glucose and water, [EMIM][SCN], [EMIM][DCA] and [EMIM][Ac], at two different glucose concentrations, at 313.15 K. 197

Table 3.5.3 – Numerical values for the enthalpies calculated by Gaussian code, at gas phase and at the temperature of 313.15 K. 198

List of Symbols

a_w	Activity (of water)
k_B	Boltzmann Constant
δ	Chemical Shift
$\Delta\delta$	Chemical Shift Deviation
Z	Coordination Number
A	Correlation/Fitting Parameter at equation 3.1.3 and 3.4.2/3
r_Z	Cutoffs
CN	Cyano
H	Enthalpy
ΔH^{vap}	Enthalpy of Vaporization
V^E	Excess Volume
G	Free Energy of Gibbs
R	Ideal Gas Constant
j_{xz}	Imposed Momentum Flux
L	Length of the simulation box
T_m	Melting Temperature/Point
x	Molar fraction
U	Molar Internal Energy
M	Molecular weight
P_{xx} , P_{xz}	Pressure Tensor (at different coordinates)
D	Self-diffusion/ Diffusion Coefficient
T	Temperature
t	Time
p_{total}	Total Exchanged Momentum
$\Delta\eta$	Viscosity Deviation, Viscosity Uncertainty - equation 3.4.3
V	Volume
DNS	3,5-dinitrosalycilic acid

Greek Letters

ρ	Density
α	Fitting Parameter at equation 3.4.2/3
τ	Fitting Parameter at equation 3.4.2/4
β	Solvatochromic Parameter
γ	Surface Tension, Activity Coefficient
η	Viscosity

Chemical Formulas

Ionic liquids

[EOHMIM][BF_4]	1-(2-hydroxyethyl)-3-methylimidazolium tetrafluoroborate
[OOHMIM][BF_4]	1-(8-hydroxyoctyl)-3-methylimidazolium tetrafluoroborate
[BMpyr][NTf_2]	1-butyl-1-methylpyrrolidinium bis(trifluoromethanesulfonyl)imide
[BMIM][Ac] / [BMIM][OAc] / [BMIM][C_1CO_2]	1-butyl-3-methylimidazolium acetate
[BMIM][NTf_2]	1-butyl-3-methylimidazolium bis(trifluoromethylsulfonyl)imide
[BMIM][Pf_2]	1-butyl-3-methylimidazolium bis[(perfluoroethyl)sulfonyl]imide
[BMIM][Br]	1-butyl-3-methylimidazolium bromide
[BMIM][Cl]	1-butyl-3-methylimidazolium chloride
[BMIM][DCA]	1-butyl-3-methylimidazolium dicyanamide
[BMIM][PF_6]	1-butyl-3-methylimidazolium hexafluorophosphate
[BMIM][I]	1-butyl-3-methylimidazolium iodide
[BMIM][CH_3SO_4]	1-butyl-3-methylimidazolium methane sulfate
[BMIM][C_1SO_3]	1-butyl-3-methylimidazolium methylsulfonate
[BMIM][NO_3]	1-butyl-3-methylimidazolium nitrate
[BMIM][BF_4]	1-butyl-3-methylimidazolium tetrafluoroborate
[BMIM][SCN]	1-butyl-3-methylimidazolium thiocyanate
[BMIM][TOS]	1-butyl-3-methylimidazolium tosylate
[BMIM][TCN]	1-butyl-3-methylimidazolium tricyanomethane
[BMIM][CF_3CO_2]	1-butyl-3-methylimidazolium trifluoroacetate
[BMIM][CF_3SO_3]	1-butyl-3-methylimidazolium trifluoromethanesulfonate
[pyr_{14}][NTf_2]	1-butyl-3-methylpyridinium bis(trifluoromethylsulfonyl)imide
[C_{10}MIM][NTf_2]	1-decyl-3-methylimidazolium bis(trifluoromethylsulfonyl)imide
[C_{12}MIM][NTf_2]	1-dodecyl-3-methylimidazolium bis(trifluoromethylsulfonyl)imide
[EMIM][Ac]	1-ethyl-3-methylimidazolium acetate
[EMIM][NTf_2]	1-ethyl-3-methylimidazolium bis(trifluoromethylsulfonyl)imide
[EMIM][Br]	1-ethyl-3-methylimidazolium bromide
[EMIM][Cl]	1-ethyl-3-methylimidazolium chloride
[EMIM][DCA]	1-ethyl-3-methylimidazolium dicyanamide
[EMIM][$C_2H_5SO_4$]	1-ethyl-3-methylimidazolium ethylsulfate
[EMIM][PF_6]	1-ethyl-3-methylimidazolium hexafluorophosphate
[EMIM][NO_3]	1-ethyl-3-methylimidazolium nitrate
[EMIM][TCB]	1-ethyl-3-methylimidazolium tetracyanoborate
[EMIM][BF_4]	1-ethyl-3-methylimidazolium tetrafluoroborate
[EMIM][SCN]	1-ethyl-3-methylimidazolium thiocyanate
[EMIM][TOS]	1-ethyl-3-methylimidazolium tosylate
[EMIM][TCN]	1-ethyl-3-methylimidazolium tricyanomethane
[EMIM][CF_3SO_3]	1-ethyl-3-methylimidazolium trifluoromethanesulfonate
[EMpy][$C_2H_5SO_4$]	1-ethyl-3-methylpyridinium ethylsulfate

[HMIM][NTf_2]	1-hexyl-3-methylimidazolium bis(trifluoromethylsulfonyl)imide
[HMIM][Cl]	1-hexyl-3-methylimidazolium chloride
[HMIM][PF_6]	1-hexyl-3-methylimidazolium hexafluorophosphate
[HMIM][I]	1-hexyl-3-methylimidazolium iodide
[BMpy][BF_4]	1-methyl-3-butylimidazolium tetrafluoroborate
[EMIM][$N(SO_2CF_3)_2$]	1-methyl-3-ethylimidazolium bis(trifluoromethane)sulfonamide
[patr][Br]	1-n-butyl-4-amino-1,2,4-trizolium bromide
[OMIM][NTf_2]	1-octyl-3-methylimidazolium bis(trifluoromethylsulfonyl)imide
[OMIM][PF_6]	1-octyl-3-methylimidazolium hexafluorophosphate
[OMIM][I]	1-octyl-3-methylimidazolium iodide
[OMIM][BF_4]	1-octyl-3-methylimidazolium tetrafluoroborate
[C_{14}MIM][NTf_2]	1-tetradecyl-3-methylimidazolium bis(trifluoromethylsulfonyl)imide
[$(OCH_3)_2C_1$im][$PF_3(C_2F_5)_3$]	1,3-dimethoxy-2-ethylimidazolium tris(pentafluoroethyl)trifluorophosphate
[DMIM][NTf_2]	1,3-dimethylimidazolium bis(trifluoromethanesulfonyl)imide
[DMIM][Cl]	1,3-dimethylimidazolium chloride
AP-N	acyclic pentamethylpropylguanidinium nitrate
AP-C	acyclic pentamethylpropylguanidinium perchlorate
CM-N	cyclic tetramethylguanidinium nitrate
[N_{4111}][NTf_2]	*N*-butyl-*N,N,N*-trimetylammonium bis(trifluoromethanesulfonyl)imide
[Bpy][BF_4]	n-butylimidazolium tetrafluoroborate
[Bpy][Cl]	*n*-butylpyridinium chloride
[K][$N(SO_2C_2F_5)_2$]	potassium *cis*-bis(perfluoro-*n*-butylsulfonyl)amide
[Na][$N(SO_2C_2F_5)_2$]	sodium *trans*-bis(perfluoro-n-butylsulfonyl)amide
[$P_{6\,6\,6\,14}$][OAc]	tetradecylphosphonium acetate
[$P_{10\,10\,10\,10}$][Br]	tetradecylphosphonium bromide
[$P_{6\,6\,6\,14}$][CF_3SO_3]	tetradecylphosphonium trifluoromethanesulfonate
[$P_{6\,6\,6\,14}$][NTf_2]	tetradecyltrihexylphosphonium bis(trifluoromethanesulfonyl)imide
[$N_{1\,1\,1\,1}$][DCA]	tetramethylammonium dicyanamide
[$PH(C_6H_5)_3$][$N(SO_2F)_2$]	triphenylphosphonium bis(fluorosulfonyl)amide

Other compounds

CO_2	Carbon Dioxide
CO	Carbon Monoxide
H_2	Hydrogen (gas)
H_2O_2	Hydrogen Peroxide
CH_4	Methane
NO_X	Nitrogen Oxide
N_2O	Nitrous Oxide
SO_2	Sulfur Dioxide
SO_X	Sulfur Oxide

Subscripts

exp	experimental
glucose	
i	specie
IL	Ionic Liquid
L	length of the simulation box
m	melting
max	
mix	mixture
pure	
ref	reference
sim	simulation
total	
w, water	water

Superscripts

cohesive	
E	excess
gas	gas phase
liq	liquid phase
vap	vaporization

1. Introduction

1.1. Scope and Objectives

Unlike the expectations of many, fossil fuels are today, and will remain for long, our main source of energy and transport fuel[1]. Nevertheless, the environmental impact of their continued usage is well known by the emission of pollutant gases released during their combustion with concomitant extremely severe climatic consequences. Emissions of NO_X (nitrogen oxides), SO_X (sulfur oxides), CO_2, N_2O and CH_4 are some of the most harmful gases responsible for acid rain and greenhouse effects, having also a significant negative impact on human health[1]. For this reason, there is a worldwide concern in reducing the high dependence on fossil fuels by replacing them for other alternatives, such as biofuels, as well as continuing to develop and improve technologies to reduce the emission of harmful gases from their combustion.

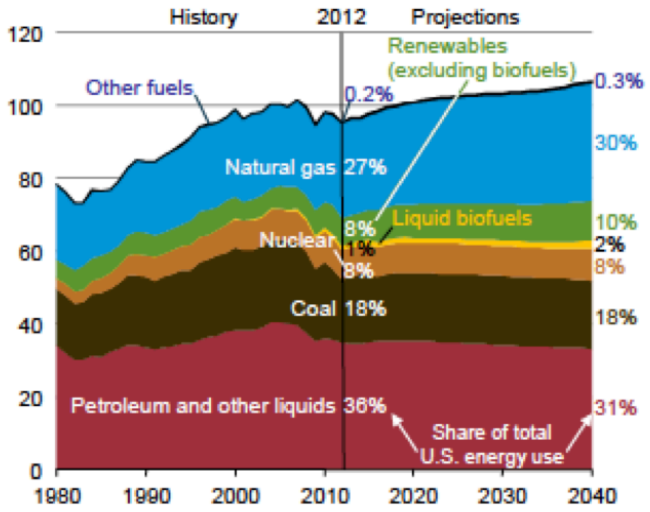

Figure 1.1 - Primary energy use in the U.S.A since 1980 and projections up to 2040. Energy Information Administration (EIA), Monthly Energy Review, September 2013, DOE/EIA-0035 (2013/09).[2]

Environmental regulations at different countries have imposed stringent rules, aiming at the reduction of SO_X emissions (responsible for acid rains and also for poisoning the catalytic activity implemented on motor engines), requiring refineries to produce fuels with ultra-low sulfur content of 10 ppm according to EU and US legislation[2,3]. At the same time, alternatives to the use of fossil fuels have gained an interesting place, with a prediction for concomitant increases in their usage and for important investments in the next decades (Figure 1.1). Within the possible alternatives, biofuels seem to be one of the most promising options, becoming the object of a significant number of studies

devoted to their production, such as bioethanol and biodiesel, through processes based on the consumption of biomass (renewable material). Albeit biofuels eliminate the emission of harmful gases, their production still requires a lot of attention, either from academia and industry, since they are not yet economic and sustainable alternatives.[4]

For the last decades, for both fuel improvement and biofuel production processes, a new class of solvents named ionic liquids (ILs)[5] has been studied and applied. These solvents are molten salts, that have attracted a lot of attention from academia and industry due to their unique properties, including a fine-tuning ability when combining different cations and anions, aimed for a specific application.[6] Considering the chemical industry, such as fuel and biofuel industries, the ILs have gained an interesting role acting as extractive solvents, by presenting attractive physicochemical properties which enable optimization of processes, as well as, reduction of operational costs.[7]

Predictive approaches, namely, methods based on equations of state (EoS), quantitative structure – property/activity relationships (QSPR/QSAR), and computer approaches (e.g. quantum density functional and wavefunction method, or classical molecular dynamics or Monte Carlo simulations) have been used to understand the behavior of ILs at different working conditions. Molecular dynamics (MD) simulation stands out by its ability to reproduce the dynamics of real systems, allowing to evaluate and estimate properties at the microscopic level.[8] Additionally, the reproduction of systems composed of ILs by means of MD simulation is a hot topic in scientific research. High viscosity and high ability to solubilize a wide range of compounds are some of the motivations for developments and improvements of computer and molecular approaches.[7]

Hereafter, this thesis is devoted to investigate the role and the mechanisms of ILs, acting as solvent, by means of MD simulations, in systems relevant for fuel and biofuel productions, and at biomass pre-treatment processes. With this aim simulations are performed for the characterization of binary systems composed of ILs and thiophene, benzene, ethanol or water (compounds of interest in fuel or biofuels streams), and also with glucose molecules (reproducing the existent interactions in pre-treatment processes of lignocellulosic materials for bioethanol production). After characterizing the systems, a general discussion is presented on how ILs interact with the various target compounds, including the mechanisms, type and strength of those interactions, aiming at an evaluation of their applicability in fuels and biofuels streams, as well as, for biomass pre-treatment processes.

Having defined the main objectives of this thesis, this chapter is going to briefly address the following issues: ILs and their main characteristics (Chapter 1.2), desulfurization processes and the role of ILs in this topic (Chapter 1.3), and biofuel production, emphasizing the second generation biofuels and processes of lignocellulosic material's pre-treatment (Chapter 1.4). In Chapter 2, it is

going to be presented and compared the available computational approaches, highlighting the molecular dynamics simulation and its usage in the prediction of ILs' properties. The Chapter 3 contains the description of the work performed, namely, the characterization of binary systems composed of ILs and thiophene or benzene, ILs and water or ethanol, and finally, glucose-based systems. The final chapter of this document will include a general discussion of the results obtained and will end with the conclusions.

1.2. Ionic Liquids (ILs)

In the early 20th century, a new generation of molten salts was discovered by Paul Walden[5]. These molten salts are known by different names, such as ionic melts, ionic fluids, or liquid electrolytes but the most common and better recognized designation is ionic liquids. [9] These compounds possess at least one asymmetric unit comprised of a large organic cation, *e.g.* derived from imidazolium, pyridinium, pyrrolidinium, ammonium or phosphonium, and an organic or inorganic anion, such as bis[(trifluoromethyl)sulfonyl]imide, trifluoromethylsulfonate, hexafluorophosphate, or tetrafluoroborate. Examples of the structures of common cations and anions are shown in Figure 1.2.1.[9,10]

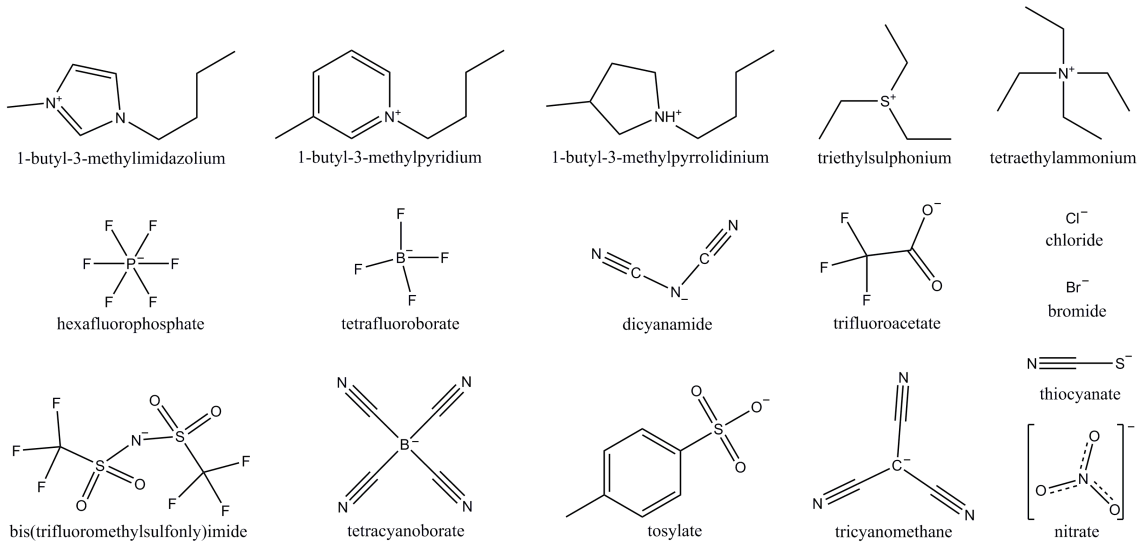

Figure 1.2.1 - Common cations and anions found in ionic liquids literature.

The structural asymmetry makes difficult their crystallization and minimizes the cation-anion interaction, which confers unique properties to ILs. They possess low melting point (<100 °C),

extremely low vapor pressure, high thermal and chemical stability, high ionic conductivity and good solvating capacity for organic and inorganic compounds and even biopolymers (cellulose). Furthermore, ILs are in general non-flammable and present a very broad liquidus temperature range. Moreover, it is possible to tune their properties by changing their constituting ions, within the large number of possible combinations of cations and anions, and by adding specific functional groups in order to achieve the desired physicochemical properties intended for a specific application. Given the possibility of fine-tuning the properties of ILs, their range of applicability is vast. Separation processing, chemical processing, biotechnology, electrochemistry are some of the possible application fields where ILs may act, for example, as solvents, lubricants, electrolytes or heat transfer fluids.[6,9] Although ILs appeared to be an alternative to replace common solvents, as for example the volatile organic compounds, VOCs, due to their "greener" character when compared with that of the latter, parameters such as toxicity and biodegradability have been lately a matter of concern.[11–13] Moreover, the viscosity of ILs is considered one of the main drawbacks for their application at industrial scale, with values reaching 100-1000 cP, *i.e.*, one hundred to one thousand times larger than the viscosity of water.[14] Polarity and ionization are other topics of interest and importance which are also discussed.[10]

The properties of ILs are greatly influenced by the structural specificities of their constituting cations and anions. The knowledge of the structure-property relationships of ILs is required for the selection or design of an IL for a specific application. Thus, information regarding some properties such as densities, viscosities, diffusivities, melting points or electric conductivities of as many ILs as possible is needed. However, the considerable number of potential cation/anion combinations makes this task daunting by an experimental approach alone. In an attempt to relate structure with property, group contribution methods and QSPR/QSAR (quantitative structure – property/activity relationships) approaches have been used to predict thermophysical properties, phase behaviors, toxicities, among others, of some ILs[15–18]. A review [19] on these types of methods for the estimation of thermophysical and transport properties of ionic liquids has been published. Also for the same purpose, quantum methods and statistical mechanics-based molecular approaches are gaining importance in this field since they have been helping to better understand, at the molecular level, the structure-property relationships and phase behavior of neat IL and IL in mixtures (with one or more compounds).[20–24] Inherent to the nature of each moiety is the nature of its self-organization, and its influence on their properties, especially on their performance as solvents, which is a theme of a growing relevance. Canongia-Lopes and co-workers[25–27] are among the pioneering researchers to show that the bulk liquid phase of ILs present a structure characterized by two main domains, a polar (high-charge density part composed by a hydrophilic head-group) and a non-polar (low-charge density part composed by a

hydrophobic tail) domains, at nanometer scale, which have been widely used to justify different behaviors (and properties) of ILs.[10] In a different study[28], it was possible to conclude that due to this unique structure, ILs present a "chameleonic behavior", a sort of amphiphilic character that allows their simultaneous interaction with two compounds of different polarities. The so-called chameleonic behavior is just an example of how ILs can be complex solvents and, thus, their characterization opened a new and interesting research field.

In this matter, in the past few years, several works including some extended studies or reviews[10,29,30] have been addressing the application of computational approaches to model neat ILs and also mixtures of ILs. Ab initio methods, Monte Carlo (MC) and molecular dynamics simulations employing atomistic or coarse-grained (CG) models, are computer approaches that are being widely used to investigate these systems at different time and length scales.[31–34] These different approaches are going to be briefly introduced in Chapter 2. Furthermore, focusing on MD simulations, an overview of methodologies applied to predict properties of neat ILs, namely, density, viscosity, diffusivity, melting point, vapor pressure and boiling point, enthalpy of vaporization and surface tension, will be presented.

1.3. Fossil fuels improvement – desulfurization processes

One way to reduce the emission of pollutant gases is to remove the sulfur-content from petroleum, through desulfurization processes. The most common desulfurization process applied on refineries is hydrodesulfurization (HDS). In this process, refined petroleum is submitted to high pressures (20 - 100 bar of H_2) and temperatures (300 - 400 ^{o}C) conventionally mediated with CoMo and NiMo-based catalysts.[1,35,36] Refined petroleum includes different aliphatic and aromatic sulfur-based compounds where some, like benzothiophene (BT), dibenzothiophene (DBT) and their derivatives, are resistant to HDS, due to steric hindrance. Therefore, in order to fulfill the increasing strictness of the environmental regulations, the HDS process demands more extreme operation conditions, being a disadvantage of its implementation.[35] Additionally, another problem associated with the HDS process is that some of non-sulfur aliphatic compounds, important for fuel performance, are also removed. Another drawback that can be associated with the process is that the presence of sulfur containing compounds, along with aromatic and nitrogen-based compounds, can poison the activities of the catalysts employed in the HDS process, which is also important to avoid.[1]

Several processes have been developed and improved to successfully replace HDS aiming at reducing the sulfur content, namely, desulfurization by adsorption, extraction, oxidation and biodesulfurization.[1,35,37–40]

Desulfurization by adsorption can be divided in physical and chemical adsorption, or more specifically, adsorptive and reactive desulfurization, respectively. As the name indicates, adsorptive desulfurization is based on the simple adsorption (van der Walls interactions) of sulfur compounds to adsorbents, usually zeolites[41,42], Ni-based adsorbents[43], CoMo/alumina[43] or even metal-organic frameworks (MOFs)[44,45]. As for reactive adsorption[46], an adsorbent such as Ni-ZnO has the ability to adsorb and convert sulfur compounds to sulfides and hydrocarbons. Sulfides are retained at the adsorbent and upon its regeneration SO_X species are released. Still, the adsorption capacity of these adsorbents can be limited, which also confines the applicability of these methods in fuel streams with high content of sulfur compounds.[1,35]

Desulfurization by oxidation is a two-step process.[1,35,47] The first step is the oxidation of sulfur compounds upon contact with an oxidant, usually hydrogen peroxide (H_2O_2), to form sulfoxides or sulfones. The latter compounds possess higher polarities than the sulfur ones present in petroleum, so they can be separated through liquid-liquid extraction using acetonitrile, dimethylformamide (DMF) or dimethyl sulfoxide (DMSO) as solvents, or alternatively by adsorption. Acetonitrile is the most commonly used solvent, owing to its low boiling point that allows its separation from the sulfones by simple distillation. Desulfurization by oxidation, however, is able to remove simultaneously olefins, requiring the management of a significant amount of the formed sulfone compounds.

Biodesulfurization is based on the use of microorganisms that selectively oxidize sulfur atoms, in the presence of water and oxygen under room temperature and pressure conditions.[1,35,48] However, only a few number of bacteria species can oxidize BT and just a single specie can deal with thiophene. In the case of DBT, it is not possible to achieve the intended sulfur content with biodesulfurization. Therefore, this methodology can only be applied as a complementary step of another process.

Desulfurization by extraction, also known as extractive desulfurization, is used as a complementary step to desulfurization by oxidation, or as a single process if low temperature and pressure conditions are considered.[1,35] This process is based on the high affinity and selectivity of a chosen solvent to interact with the sulfur compounds, which should be more soluble in the solvent than in the hydrocarbons present in the fuel. After solubilization, the solvent should be easily separated from the sulfur compounds by simple distillation, through the difference of the boiling temperatures. To attain an efficient process, the choice of the solvent must be adequate. Solvents such as methanol, ethylene glycol, acetonitrile, DMF, DMSO and sulfolane can be used or, to enhance the solubility, a mixture of solvents. Another alternative is the use of the ILs.[1,35–37,40]

ILs have some advantages over conventional solvents, namely their low vapor pressure enhancing the separation from sulfur compounds through distillation, their thermal and chemical stability, as well

as a liquidus profile in a wide range of temperatures. Composed of a bulky organic cation and an organic/inorganic anion, they can be chosen accordingly to their properties to fulfill a specific application, as mentioned previously in Chapter 1.1.[37] The selective sulfur removal is dependent on the size and structure of both cations and anions, as well as their affinity to different sulfur compounds, which is mainly made through π-π interactions, originally from their aromatic character. Regarding the cation's families, imidazolium, pyridinium-based ILs and Lewis and Brønsted acidic ILs have been studied, where it was recognized a significant efficiency of sulfur removal with the increase of the length of alkyl chains. The Lewis and Brønsted acidic ILs, have an enhanced extraction power due to their capacity to form sulfur-complexes. Concerning the anions, tetrafluoroborate, hexafluorophosphate, octyl sulfate, ethyl sulfate and dimethyl phosphate are usually studied.[1,35–37,40] Nevertheless, ILs of low viscosity that are composed of dicyanamide and thiocyanate anions, were also reported to have a good extraction performance, as well as, a significant selectivity under the presence of polyaromatic hydrocarbons also extracted from petroleum streams.[1,35] Additionally, it has been reported that ILs, along with hydrogen peroxide (H_2O_2) and other catalysts, can achieve sulfur removal efficiencies around 98.2 %, proving that a combination of catalytic oxidation with an ionic liquid can lead to sulfur compounds content, at ambient conditions and without H_2 consumption, in accordance with regulations.[35]

It is worth noting that, with the increase of petroleum exploration in the world, new sources of crude have been found, with significantly higher sulfur content, requiring an adjustment or a combination of different methods.[1]

1.4. Biofuels

In order to replace fossil fuels, the production of biofuels appeared as one of the most promising alternatives. Biofuels are classified as first, second and third generation. First generation biofuels are those produced from sugar, starch, vegetable oils or animal's fats, *i.e.*, mainly from food crops and oil seeds. Biofuels of second generation are produced from lignocellulosic materials, such as wood process wastes, agricultural and forest residues, vegetative grasses and bagasse. Third generation biofuels are produced from algae. The two latest generations are non-food feedstocks, avoiding problems related to economic and social impacts. Nevertheless, for a sustainable replacement of fossil fuels, the production of biofuels should be an economic and sustainable option, with an availability of the feedstock as high as possible, and simultaneously be able to produce power and chemicals, which

may require high investments not only for the process, but also for storage and delivery of biofuels to its final destination.[4,49]

Hereafter, it will be emphasized the second generation biofuels production, addressing the processes of converting biomass in biofuel, and also the lignocellulosic material's pre-treatment processes.

For the conversion of biomass into biofuels, two routes are adopted, namely the thermochemical and biochemical conversion. Thermochemical conversion processes include liquefaction, pyrolysis and gasification.[4] Generally, the latter processes are based on a chemical change suffered by the lignocelllulosic material when heat is applied, in the absence or presence of oxygen. Changing the temperature, pressure, heating rate or time of gas residence, different final products can be obtained, from chemicals to hydrocarbons, bioethanol, biodiesel and heat. From gasification is also produced fuel gases and syngas (gas rich in H_2, CO and CO_2) that can be further used in the synthesis of long-chain hydrocarbons for producing high cetane number fuels (Fischer-Tropsch process).[4,49–52]

As for biochemical conversion processes, these are performed at low temperatures and low reaction rates, where enzymatic hydrolysis of hemicellulose and cellulose (wood's constituents) are carried, followed by the fermentation of their small molecules that will give origin to biofuel.[4,53,54] The definition of biochemical conversion process is commonly associated with bioethanol production, using lignocellulosic biomass. Nevertheless, the structural organization of lignocellulosic biomass compounds (cellulose, hemicellulose and lignin) is complex, which causes difficulties in the assessment of enzymes or acids to cellulose and hemicellulose and, consequently, hinders the process of fermentation to obtain bioethanol.[55,56] To overcome this, pre-treatment processes (chemical, physical or biological) are required. The resulting sugars are then fermented and the ethanol produced is used as fuel, chemical or product.[4]

1.4.1. Lignocellulosic materials and pre-treatment processes

Carbohydrates are an amazing and diversified class of biomolecules, characterized by a vast heterogeneity of compounds differing on their stereochemistry and functionalization. These compounds are essential to many biological functions and are also applied in a wide range of industrial processes such as food, textile, pulp and paper, biofuels, and personal care/cosmetic industries.[55,57,58]

Wood is a renewable source of carbohydrates usually composed of 35-50% of cellulose, 35% of hemicelluloses, 5 - 30% of lignin and extractives. Cellulose is the most

abundant compound, characterized for being a homopolysaccharide composed of *β*-D-glucopyranose units, which are linked together through (1-4)-glycosidic bonds (see Figure 1.4.1.1) in a linear direction and also by intra and intermolecular hydrogen bonds.[56,59]

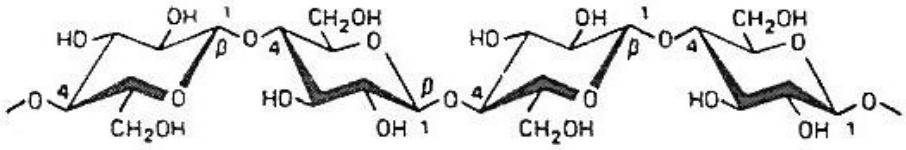

Figure 1.4.1.1 - Structure of cellulose.[59]

Cellulose molecules aggregate to microfibrils with highly ordered regions (crystalline) and less ordered regions (amorphous). Bundles of microfibrils compose fibrils, which comprise cellulose fibers. The crystalline region of cellulose can present different polymorphs, beginning with the native cellulose, cellulose I (Figure 1.4.1.2), characterized by cellulose microfibrils oriented in the same direction (parallel chains) and establishing van der Waals interactions between layers. The establishment of three characteristic hydrogen bonds between molecules is observed (two intramolecular hydrogen bonds and one intermolecular hydrogen bond), responsible for the ordered structure and for the lack of interactions with water and most of organic solvents. When cellulose is dissolved and then regenerated, the order of cellulose microfibrils is altered and additional hydrogen bonds are established between layers, which are now antiparallel chains. In this form, cellulose is usually named cellulose II.[59] Other two polymorphs can be obtained by heating or chemical treatment, namely cellulose III and IV.[59]

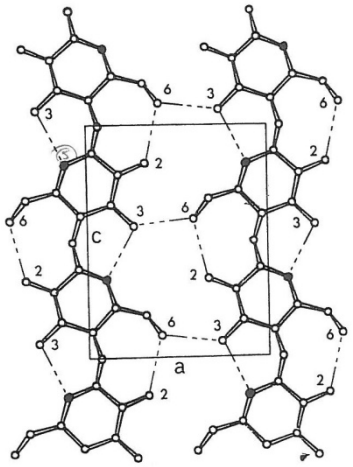

Figure 1.4.1.2 – Projection of the plane in cellulose I, showing the hydrogen bonding network and the numbering of the atoms. Each glucose residue forms two intramolecular hydrogen bond (O3-H—05´ and O6—H-02´) and one intermolecular bond (O6-H—O3).[59]

Contrary to cellulose, hemicellulose is a heteropolysaccharide that can be composed of D-xylose, D-mannose, D-glucose or D-galactose monosaccharides connected linearly and/or with branches. According to its structure, hemicellulose is characterized by being an amorphous polymer, accessible to enzymatic attack, which enables hydrolysis and further conversion of its simple sugars. Hemicellulose and cellulose are embedded by another compound, lignin. Lignin is a complex, amorphous polymer composed of aromatic alcohols units, namely, coniferyl, sinapyl and p-coumaryl alcohols. The composition on wood of each of these compounds can vary, depending on the source of the wood.[56,59]

Aiming at separating cellulose, hemicellulose and lignin, mainly to obtain their monosaccharides for the production of biofuels, different solvents were studied and applied. Regarding cellulose dissolution, solvents such as carbon disulfide, LiCl-based solvents[60], dimethylsulfoxide (DMSO)/paraformaldehyde[61] and also N-methylmorpholine-N-oxide (NNMO)[62] have been used. However, these solvents are volatile, toxic, expensive and difficult to recover.[56]

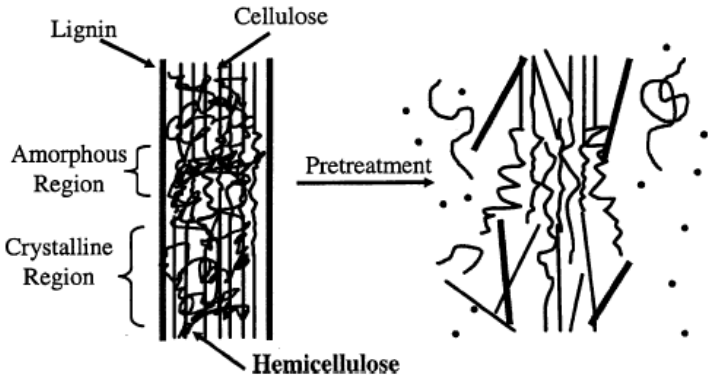

Figure 1.4.1.3 – Mechanism of pretreating lignocellulosic materials[63].

Alternatively, and as mentioned previously, pre-treatment processes can be applied to biomass, being divided in biochemical, physical, biological and physicochemical pre-treatments.[4,56,64,65] As Figure 1.4.1.3 illustrates, the aim of pre-treatment processes is to open the structure, breaking lignin and disrupting the crystalline structure of cellulose, promoting the accessibility of enzymes responsible for the hydrolysis of cellulose into its monosaccharides. These processes impose structural changes to the initial lignocellulosic biomass, but there are several factors that should be addressed. One factor to take into account is the composition of the biomass (in each of its three main constituents) which affects, accordingly, the choice of the most adequate pre-treatment process.[64,65] Additionally, the process chosen should not degrade hemicellulose or cellulose, should not produce toxic compounds nor solid-waste residues, it must operate at reduced cost (either in heat and power demands), as well as with small enzyme dosages and short reaction times. Moreover, it should be possible to recover lignin, enhance fermentation process and finally, obtain high yields of sugars' conversion.[64]

Biological pre-treatments employ microorganisms that will mainly attack hemicellulose and lignin, being a reduced cost procedure, with low energy consumption and mild operation conditions. However, the sugar conversion yield is usually low.[64,65]

Physical pre-treatments such as, extrusion and mechanical procedures can also be applied. These are based on the reduction of the particle size through milling or submitting the biomass to heat, mixing and shearing (extrusion process), which also disrupt the crystalline structure, and destroy fibers of biomass, enabling the enzymatic attack. Nonetheless, these processes require high power consumption.[64,65]

The physicochemical pre-treatments include SO_2-steam explosion, CO_2 explosion, liquid hot water, ammonia fibber explosion (AFEX), wet oxidation, among others.[64,65] The *steam explosion* is a hydrothermal process where biomass is under a pressurized steam for a specific period of time, and then depressurised. This procedure allows high yields of sugar content, causing lignin transformation and hemicellulose degradation, requiring lower capital investment, as well as, less hazardous operation conditions and chemicals. Nevertheless, the degradation of hemicelluloses and the formation of toxic compounds that are inhibitors of hydrolysis and fermentation processes are the main disadvantages.[64–66] The *CO_2 explosion* process[64,65,67], similar to the steam explosion process, places the biomass into pressure, but here the CO_2 is a supercritical fluid, since the gas is compressed at a temperature above the critical point being able to penetrate the lignocellulose biomass and to disrupt its structure, promoting enzymatic attacks. However, to improve the efficiency of the process, high pressures are required. The *liquid hot water* process operates at high temperature and pressure, without the use of catalysts or chemicals. With this procedure, the lignocellulosic biomass suffers structural alterations with low degradation of compounds, as well as, formation of small amount of hydrolysis and/or fermentation inhibitors. However, high volumes of water and significant power consumption are required.[64–66] Regarding the *AFEX* process, biomass is placed for a specific period of time to a pressurized environment, followed by the release of that pressure, similar to other explosion methods. Here, the biomass is treated with liquid anhydrous ammonia, at low temperatures and high pressures, causing the physical disruption of fibbers and partial decrystallization of cellulose. Hence, the yield of the enzymatic hydrolysis is high and the amount of inhibitors formed is small. Some disadvantages are associated with this process, *i.e.*, high costs for the recovery of ammonia and low conversion yields when biomass presents high content of lignin.[64,65,68] Finally, the *wet oxidation* process uses oxygen or air as catalysts being, essentially, an oxidative process that operates at low temperatures and with short times of reaction. This process is efficient in the removal of lignin, it has low formation of inhibitors and does not require high demands of energy. Nevertheless, the cost of catalyst and oxygen are its main drawbacks.[64,69]

Biochemical pre-treatments includes alkali and acid pre-treatments, ozonolysis, organosolv and ionic liquids.[64] The *alkali pre-treatment* is based on the use of sodium, potassium, calcium or ammonium hydroxides, at room temperatures with reaction times ranging from seconds to several days. Common to other processes, it enhances the accessibility to cellulose for enzymatic attacks, but formation of inhibitors occurs.[64,70] The *acid pre-*

treatment can be divided in concentrated and diluted acid, at lower or high temperatures, with specific reaction periods of time. Formation of inhibitors to hydrolysis and fermentation are also produced, and it must be considered the possibility of corrosion the equipments, consequently requiring higher operation costs.[64] In the *ozonolysis* process, biomass is in contact with ozone, at room temperature and pressure, with the ability to successfully remove lignin and enhance further hydrolysis without formation of inhibitors. The main drawback is the amount of ozone required for this process, which is not sustainable.[64,65] The *organosolv* pre-treatment employs common organic solvents, such as methanol, ethanol, acetone, ethylene glycol and tetrahydrofurfuryl alcohol. Using this process, lignin can be fully recovered without degradation, and cellulose enzymatic attack is promoted. Nonetheless, these solvents can also act as inhibitors to hydrolysis or fermentation, and thus, they must be removed from the reaction medium, imposing higher operation costs.[64,65,71] Finally, pre-treatment with ionic liquids can also be applied.[55,56,64]

As mentioned previously, ionic liquids have excellent properties that are desired for different industrial applications, being the pre-treatment of lignocellulosic biomass a good example. These solvents have the ability to solubilize simultaneously lignin and the other constituents, mainly through the establishment of hydrogen bonds, being able to disrupt the crystalline structure of cellulose without degradation of the other compounds. This process operates at mild conditions, and due to their low vapor pressure the solvents are easily recovered and it has been proved that they can be reused around seven times maintaining their initial properties.[56,64] Usually, imidazolium, pyridinium and triethylammonium based ILs, with short length chain, are the cations with better performance to dissolve cellulose. Regarding the anions, those with high polarity, such as the chloride or acetate anions, are good solvents for cellulose; nonetheless, the anions dicyanamide and thiocyanate, which present low polarity, are also able to successfully dissolve cellulose's monosaccharide.[56] Additionally, knowing that the route of interaction occurs via the establishment of hydrogen bonds, the functionalization of ILs with the increment of hydroxyl groups on the cations would, in principle, enhance the interactions with cellulose. Nevertheless, the cation will compete with cellulose for the anions, with a concomitant decrease in the solubility of cellulose in ILs. On the whole, the right combination between cations and anions is the key for a successful pre-treatment of lignocellulosic biomass. Afterwards, the IL (and cellulose) can be easily recovered with the addition of water or ethanol, acting as anti-solvents in the medium.[55,56]

In this chapter, it was introduced the topic ionic liquids and their advantageous role in specific applications, such as in the field of fuels and biofuels, acting as solvents. In the following chapters, it will be addressed and discussed the advantage of using molecular dynamics simulation for the reproduction of systems composed of ILs, as well as, for the capacity of ILs to act as extracting solvents, for their further implementation at industry.

References

(1) Pawelec, B.; Navarro, R. M.; Campos-Martin, J. M.; Fierro, J. L. G. *Catal. Sci. Technol.*, **2011**, *1*, 23.

(2) http://www.epa.gov/otaq/fuels/gasolinefuels/index.htm.

(3) http://www.dieselnet.com/standards/eu/fuel.php.

(4) Fatih Demirbas, M. *Appl. Energy*, **2009**, *86*, S151–S161.

(5) Walden, P. *Bull. l'Académie Impériale des Sci. St.-pétersbg.*, **1914**, *8*, 405–422.

(6) Plechkova, N. V; Seddon, K. R. *Chem. Soc. Rev.*, **2008**, *37*, 123–150.

(7) Pereiro, A. B.; Araújo, J. M. M.; Esperança, J. M. S. S.; Marrucho, I. M.; Rebelo, L. P. N. *J. Chem. Thermodyn.*, **2012**, *46*, 2–28.

(8) Allen, M. P.; Tildesley, D. J. *Computer Simulation of Liquids*; Oxford University Press, 1987.

(9) Kokorin, A. Ionic Liquids: Theory, Properties, New Approaches, 2011.

(10) Kirchner, B. *Topics in Current Chemistry*; Meijere, V. B. A. De; Kessler, K. N. H. H.; Ley, J. L. S. V; Schreiber, M. O. S.; Vogel, B. M. T. P.; Wong, F. V. H., Eds.; Springer: Germany, 2009.

(11) Thi, P. T. P.; Cho, C. W.; Yun, Y. S. *Water Res.*, **2010**, *44*, 352–372.

(12) Bubalo, M. C.; Radošević, K.; Redovniković, I. R.; Halambek, J.; Srček, V. G. *Ecotoxicol. Environ. Saf.*, **2014**, *99*, 1–12.

(13) Coleman, D.; Gathergood, N. *Chem. Soc. Rev.*, **2010**, *39*, 600–637.

(14) Aparicio, S.; Atilhan, M.; Karadas, F. *Ind. Eng. Chem. Res.*, **2010**, *49*, 9580–9595.

(15) Gardas, R. L.; Coutinho, J. A. P. *AIChE J.*, **2009**, *55*, 1274–1290.

(16) Bini, R.; Malvaldi, M.; Pitner, W. R.; Chiappe, C. *J. Phys. Org. Chem.*, **2008**, *21*, 622–629.

(17) Carvalho, P. J.; Coutinho, J. A. P. *J. Phys. Chem. Lett.*, **2010**, *1*, 774–780.

(18) Freire, M. G.; Neves, C.; Ventura, S. P. M.; Pratas, M. J.; Marrucho, I. M.; Oliveira, J.; Coutinho, J. A. P.; Fernandes, A. M. *Fluid Phase Equilib.*, **2010**, *294*, 234–240.

(19) Coutinho, J. A. P.; Carvalho, P. J.; Oliveira, N. M. C. *RSC Adv.*, **2012**, *2*, 7322–7346.

(20) Torrecilla, J. S.; Palomar, J.; Lemus, J.; Rodriguez, F. *Green Chem.*, **2010**, *12*, 123–134.

(21) Freire, M. G.; Carvalho, P. J.; Santos, L. M. N. B. F.; Gomes, L. R.; Marrucho, I. M.; Coutinho, J. A. P. *J. Chem. Thermodyn.*, **2010**, *42*, 213–219.

(22) Canongia Lopes, J. N.; Pádua, A. A. H. *J. Phys. Chem. B*, **2004**, *108*, 16893–16898.

(23) Lopes, J. N. C.; Deschamps, J.; Padua, A. A. H. *J. Phys. Chem. B*, **2004**, *108*, 2038–2047.

(24) Maginn, E. J. *J. Phys. Condens. Matter*, **2009**, *21*, 373101–373118.

(25) Canongia Lopes, J. N.; Costa Gomes, M. F.; Pádua, A. A. H. *J. Phys. Chem. B*, **2006**, *110*, 16816–16818.

(26) Canongia Lopes, J. N. A.; Padua, A. A. H. *J. Phys. Chem. B*, **2006**, *110*, 3330–3335.

(27) Shimizu, K.; Costa Gomes, M. F.; Pádua, A. A. H.; Rebelo, L. P. N.; Canongia Lopes, J. N. *J. Mol. Struct. THEOCHEM*, **2010**, *946*, 70–76.

(28) Batista, M. L. S.; Neves, C. M. S. S.; Carvalho, P. J.; Gani, R.; Coutinho, J. A. P. *J. Phys. Chem. B*, **2011**, *115*, 12879–12888.

(29) Hunt, P. A. *Mol. Simul.*, **2006**, *32*, 1–10.

(30) Bhargava, B. L.; Yasaka, Y.; Klein, M. L. *Chem. Commun.*, **2011**, *47*, 6228–6241.

(31) Bessac, F.; Maseras, F. *J. Comput. Chem.*, **2008**, *29*, 892–899.

(32) Canongia Lopes, J. N.; Deschamps, J.; Pádua, A. A. H. *J. Phys. Chem. B*, **2004**, *108*, 2038–2047.

(33) Wang, Y.; Feng, S.; Voth, G. A. *J. Chem. Theory Comput.*, **2009**, *5*, 1091–1098.

(34) Wittich, B.; Deiters, U. K. *J. Phys. Chem. B*, **2010**, *114*, 8954–8960.

(35) Kulkarni, P. S.; Afonso, C. A. M. *Green Chem.*, **2010**, *12*, 1139–1149.

(36) Kowsari, E. *Ionic Liquids - New Aspects for the Future*; Kadokawa, J., Ed.; InTech, 2013.

(37) Francisco, M.; Arce, A.; Soto, A. *Fluid Phase Equilib.*, **2010**, *294*, 39–48.

(38) Hansmeier, A. R.; Meindersma, G. W.; de Haan, A. B. *Green Chem.*, **2011**, *13*, 1907–1913.

(39) Kedra-Krolik, K.; Mutelet, F.; Moise, J.-C.; Jaubert, J.-N. *Energy & Fuels*, **2011**, *25*, 1559–1565.

(40) Królikowski, M.; Walczak, K.; Domańska, U. *J. Chem. Thermodyn.*, **2013**, *65*, 168–173.

(41) Yang, R. T.; Hernández-Maldonado, A. Jy.; H., F. *Sci. 7/4/2003*, **5629**, *301*, 79–81. 3p. 1 Diagram.

(42) Hernández-Maldonado, A. J.; Yang, R. T. *Catal. Rev.*, **2004**, *46*, 111–150.

(43) Kim, J. H.; Ma, X.; Zhou, A.; Song, C. *Catal. Today*, **2006**, *111*, 74–83.

(44) Blanco-Brieva, G.; Campos-Martin, J. M.; Al-Zahrani, S. M.; Fierro, J. L. G. *Fuel*, **2011**, *90*, 190–197.

(45) Cychosz, K. A.; Wong-Foy, A. G.; Matzger, A. J. *J. Am. Chem. Soc.*, **2008**, *130*, 6938–6939.

(46) Slater, P.; Johnson, B.; Kidd, D. *NPRA Annu. Meet. Pap.*, **2002**, 9.

(47) Ito, E.; van Veen, J. A. R. *Catal. Today*, **2006**, *116*, 446–460.

(48) Soleimani, M.; Bassi, A.; Margaritis, A. *Biotechnol. Adv.*, **2007**, *25*, 570–596.

(49) Salvi, B. L.; Subramanian, K. A.; Panwar, N. L. *Renew. Sustain. Energy Rev.*, **2013**, *25*, 404–419.

(50) Demirbas, A. *Energy Sources, Part A Recover. Util. Environ. Eff.*, **2007**, *30*, 38–44.

(51) Balat, M. *Energy Sources, Part A Recover. Util. Environ. Eff.*, **2008**, *30*, 649–659.

(52) Balat, M. *Energy Sources, Part A Recover. Util. Environ. Eff.*, **2008**, *30*, 636–648.

(53) Demirbas, A. *Energy Sources, Part B Econ. Planning, Policy*, **2008**, *3*, 177–185.

(54) Demirbas, A. *Energy Sources*, **2005**, *27*, 327–337.

(55) Zakrzewska, M. E.; Bogel-Lukasik, E.; Bogel-Lukasik, R. *Energy & Fuels*, **2010**, *24*, 737–745.

(56) Mäki-Arvela, P.; Anugwom, I.; Virtanen, P.; Sjoholm, R.; Mikkola, J. P. *Ind. Crops Prod.*, **2010**, *32*, 175–201.

(57) Robyt, J. *Essentials of Carbohydrate Chemistry*; Springer VerlaG: New York, 1998.

(58) Walter, R. *Polysaccharide Aassociation Structures in Food*; Marcel Dekker Inc: New York, 1998.

(59) Sjöström, E. Wood Chemistry: Fundamentals and Applications, Second Edition, 1993.

(60) Tamai, N.; Tatsumi, D.; Matsumoto, T. *Biomacromolecules*, **2004**, *5*, 422–432.

(61) Masson, J. F.; Manley, R. S. *Macromolecules*, **1991**, *24*, 6670–6679.

(62) Heinze, T.; Liebert, T. *Prog. Polym. Sci.*, **2001**, *26*, 1689–1762.

(63) Mosier, N.; Wyman, C.; Dale, B.; Elander, R.; Lee, Y. Y.; Holtzapple, M.; Ladisch, M. *Bioresour. Technol.*, **2005**, *96*, 673–686.

(64) Alvira, P.; Tomás-Pejó, E.; Ballesteros, M.; Negro, M. J. *Bioresour. Technol.*, **2010**, *101*, 4851–4861.

(65) Sun, Y.; Cheng, J. *Bioresour. Technol.*, **2002**, *83*, 1–11.

(66) Mosier, N.; Wyman, C.; Dale, B.; Elander, R.; Lee, Y. Y.; Holtzapple, M.; Ladisch, M. *Bioresour. Technol.*, **2005**, *96*, 673–686.

(67) Zheng, Y. Z.; Lin, H. M.; Tsao, G. T. *Biotechnol. Prog.*, **1998**, *14*, 890–896.

(68) Teymouri, F.; Laureano-Perez, L.; Alizadeh, H.; Dale, B. E. *Bioresour. Technol.*, **2005**, *96*, 2014–2018.

(69) Martín, C.; Thomsen, M. H.; Hauggaard-Nielsen, H.; Belindathomsen, A. *Bioresour. Technol.*, **2008**, *99*, 8777–8782.

(70) Kumar, R.; Wyman, C. E. *Biotechnol. Prog.*, **2009**, *25*, 302–314.

(71) Zhao, X.; Cheng, K.; Liu, D. *Appl. Microbiol. Biotechnol.*, **2009**, *82*, 815–827.

2. Computational Approaches and Their Usage in the Calculation of Structural and Physical Properties of Ionic Liquids and Ionic Liquids' properties prediction

Adapted from:

Marta L. S. Batista, João A. P. Coutinho, José R. B. Gomes

Prediction of Ionic Liquids Properties through Molecular Dynamics Simulation

Curr. Phys. Chem, 151-172, 4, 2014

(Submitted in 2012)

There are three main categories of computer approaches able to model and characterize ILs, namely quantum chemical, atomistic, and mesoscale methods.[1] These categories may be distinguished by their capacities to handle different length and time scales, as schematically represented in Figure 2.1.

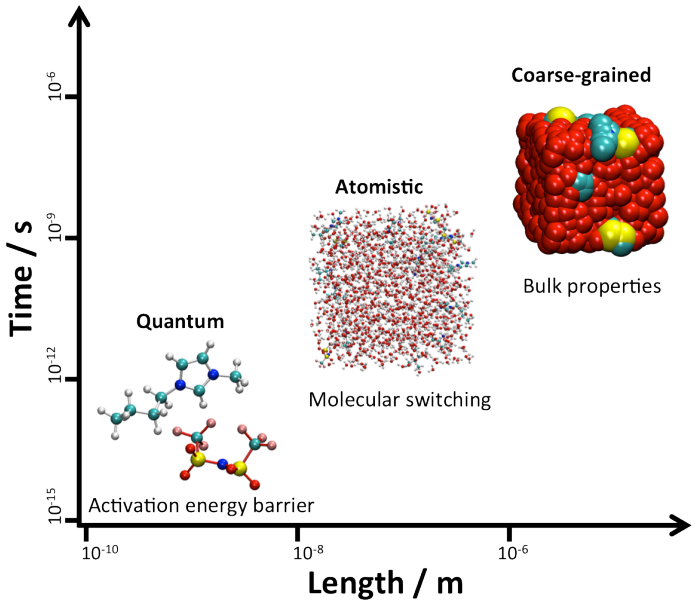

Figure 2.1 - Illustration of the different length and time scales that can be reached by most common computational approaches.

The first category comprising the quantum chemical (QC) methods is at the electronic scale and considers the fundamental particles constituting the atoms, *i.e.*, electrons and nuclei which in the field of ILs translates into the accurate characterization of a single IL molecule (ion pair) or, less accurately, of a small cluster of ILs ions. The electronic structure methods are characterized by requiring large computational efforts due to their full electronic details, which limits their application only to systems composed of a restricted number of atoms (few tens or few hundreds) and when combined with finite temperature dynamics (ab initio molecular dynamics, AIMD[2]), to very short time scales. The electronic structure methods can be divided in methods that formulate the many-electron problem in terms of a many-body wavefunction[1] (Hartree-Fock, HF, approach or the much more accurate – but demanding further computational resources – post-HF methods) or in terms of the electron density[3] (density functional theory, DFT). When high accuracy is required, higher level ab initio approaches (post-HF methods, such as, N-order Moller-Plesset[4,5], coupled-cluster[6], configuration interaction[7] approaches)

are used. Nevertheless, these high level methods require large computational efforts limiting their application to rather small systems (a few tents of atoms) and are usually employed to refine energies (single-point calculations).[8,9] The DFT approaches require less computational resources than post-HF methods without compromising too much the accuracy of the calculations and they are able to deal, chemically speaking, with more interesting molecular systems.[8,9] Finally, composite methods such as the popular Gaussian-N or Complete Basis Set, CBS, approaches[10] combine the results of several calculations performed at different levels of theory for correction of the deficiencies, *e.g*. incomplete electron correlation or basis set limited size, in the energy of a system optimized with a standard computational approach.

The second category, the atomistic simulations, considers methods at the microscopic level where the constituting particles in the preceding class are now replaced by atoms (all atom (AA) approach) or groups of atoms (united atom (UA) approach) that interact through a force field (FF) or intermolecular potential energy, obeying to statistical mechanics.

Since electrons are not being considered in these approaches, the study of chemical reactions (bond making and bond breaking) is not possible. Nevertheless, these approaches are quite appealing since they enable the description of a larger number of constituting atoms than that is possible with QC methods, as well as, to simulate longer times of simulation (nanosecond time scale). This kind of simulation usually makes use of periodic boundary conditions (replicas of the central simulation box surrounding it on all sides). This category includes, the widely used Monte Carlo (MC) and molecular dynamics (MD) simulation approaches. The MC simulation approach is characterized by being a pure stochastic technique, composed by simple algorithms[11], typically performed on a fixed number of molecules, *N*, placed on a fixed volume, *V*, and maintained at a constant absolute temperature *T*, *i.e*., the canonical ensemble (NVT). An initial configuration (positions, orientation angles, among others, for the constituting particles) is required and then an atom (or group of atoms) chosen randomly is moved or rotated by a random amount to another and new configuration. All random configurations are then compiled in a sequence from which equilibrium properties are calculated by average. [9,12,13] In the field of ILs, MC simulations have been applied to determine thermodynamic (molar volume, cohesive energy density, isothermal compressibility, cubic expansion coefficient, Henry's law constant, partial molar enthalpy of absorption and solubility in water and CO_2) and structural properties.[8,14–16]

MD simulation is employed in the study of the natural motion of molecules under the effects of their own intermolecular forces. In the most natural formulation, the simulations are performed for an isolated system (the sum of the molecular kinetic and potential energies yields the total energy, *E*, which is conserved, *i.e.*, it corresponds to an adiabatic process with no heat exchange) on a fixed

number of particles, *N*, and in a fixed volume, *V*, *i.e.*, the microcanonical (NVE) ensemble. Algorithms included in this methodology are more complex and more information is obtained, than those obtained through MC simulations, reproducing motions of individual molecules through the determination of velocities, positions and orientations over time by numerically solving the Newton's equations of motion rather than using a random generator as in Monte Carlo. The forces between the particles and the potential energy of the system are defined by a set of mathematical functions (force field, FF) with parameters derived from experimental or computational (ab initio) work. The storage of both velocities and positions (large trajectories of systems composed by many particles) in MD requires large amounts of computer memory/disk. From averaging the trajectories, equilibrium and non-equilibrium properties are obtained. In this matter, the MD methods can be divided in two groups, one applied to study systems at equilibrium (equilibrium MD, EMD) and another group to study systems away from equilibrium (non-equilibrium MD, NEMD). The latter, is recognized to be an excellent alternative to EMD for computing transport properties.[9,12,13]

MC can be more advantageous than MD simulations for discontinuous phenomena, *i.e.*, for systems where molecules interact through discontinuous forces (*i.e.*, perturbation/changes that a system can suffer such a slow phase transition, micelle formation or polymer folding) though Liu and co-workers[17] showed that MD can also be used for that purpose. Nevertheless, MD simulations stand out due to their ability to describe dynamical behavior and transport properties, *e.g.*, diffusive, convective and other motion phenomena at molecular level.[9,12,13]

It is important to add that MD simulations can also be formulated for ensembles other than the microcanonical one, but it is imperative to make sure that the correct dynamic trajectories are preserved. For that, thermostats and barostats can be attached to the system for controlling temperature and pressure, respectively. For controlling the temperature, the simplest method is to the rescale velocities at periodic intervals such that a desired temperature is maintained. However, this does not obey Maxwell-Boltzmann distribution (the equilibrium distribution of velocities) and improvements have been made, such as the Andersen[18] and the Nosé-Hoover[19] thermostats. For controlling the pressure, the same limitation is observed, and an extension of Nosé-Hoover thermostat[20] can be used as barostat by using volume fluctuations. Other barostats such as the Berendsen[21] or Parrinello-Rahman[22,23] also exist and can be applied (again the main difference is that the latter can, in theory, give a true NPT ensemble). The influence of employing different barostats and thermostats in the trajectories, however, is not relevant when the purpose is to obtain static and thermodynamic properties, as long as they are able to produce the correct canonical ensemble distribution (NVT), or the correct isothermal-isobaric ensemble (NPT).[9]

Standard MD simulations, as well as, MC simulations are performed with fixed charges (this is a topic that has been strongly discussed in the past years)[8,24–28], affecting directly the quality and accuracy of the results coming from the calculations. Variations in charge distribution can be taken into account with the so-called polarizable force fields, which are more accurate but demanding more computational resources. Thus, the choice of the force field for a specific simulation on a specific system is very important: standard CHARMM (Chemistry at HARvard Molecular Mechanics)[29], OPLS-UA (Optimized Potential for Liquid Simulation – United Atoms)[30], OPLS-AA (Optimized Potential for Liquid Simulation – All Atoms)[31] and AMBER (Assisted Model Building and Energy Refinement)[32] are some of the existing FFs commonly used for ILs. However, the force fields were originally optimized to reproduce the properties of liquids or to handle biomolecular systems and, hence, their parameters have to be adjusted for ILs. Moreover, the question of transferability of parameters from one force field to another is a very important issue.[33]

The speed of computers can also be limiting, especially when the simulation time is one of the main requirements to reproduce accurately the properties of the systems of interest (*e.g.* transport properties). In all atom (or even united atom) MD simulations, due to these time limitations, very large systems and slow phenomena are beyond the length and time scales permitted. Still, in the field of ILs, MD presents enormous advantages over other computationally more expensive approaches (ab initio methods) providing reliable structural, thermodynamic and transport properties.[8]

The third and last category involves mesoscale methods, such as the coarse-grained (CG) approach. This approach considers particles that are used to represent molecules, segments of molecules or even clusters of molecules. Additionally, the CG approach can also perform the discretization of phase space and representation of the system in terms of groups/sections, rather than the description of every atom in the system. In other words, the representation of molecules or groups of small molecules is now made by a small number of large particles, reducing the degrees of freedom and the number of pair interactions and hence, the computational efforts required for the simulation of a specific system.[9,34] Thus, with this approach, it is possible to increase the number of particles that can be simulated and/or to increase the time scale of the simulations. This can be very convenient in the study of large molecules such as polymers (proteins, carbohydrates) or ILs with long side chains (butyl, heptyl or decyl), increasing the time scale and the number of particles that can be simulated, or even in the simulation of slow phenomena.[8,9,34,35] Nonetheless, the price that has to be paid is that the local information is lost. In fact, the contribution of atom vibrations is removed, as well as the internal degrees of freedom, which promotes a simulation to occur rather faster than the real one, losing the true dynamics of the system in study. Due to these limitations, multiscale modelling is usually useful, in the

sense that the information obtained from CG simulations may be used *a posteriori* in MC or MD simulations (combination of information obtained from different level scales).[9,34] Recently, Chen and co-workers[36] reviewed different coarse-grained models and highlighted differences, applications and limitations of these computational methodologies.

2.1. Prediction of ILs' properties through MD simulations

In the forthcoming sub-chapters, it will be reported MD simulation studies for neat ILs, aiming at their characterization by the estimation of some common properties. Some computational details concerning the MD simulation studies reviewed here are compiled in Table 2.1.1.

Table 2.1.1 - Detailed information concerning the MD simulations in the studies reviewed in this section.

Author(s)	IL	pair[a]	charges, value[b,c]	potential[c]	Ref.
Alavi and co-workers	[patr][Br]	144	NPA, ±1 e	AMBER & OPLS-AA & GAFF	37
Alavi and Thompson	[EMIM][PF_6]	192	CHelpG , ±1 *e*	AMBER & OPLS-AA	38
Aparicio and co-workers	[EMIM][TOS]	250	ESP, ±1*e*	OPLS-AA	39
Bhargava and Balasubramanian	[BMIM][PF_6]	256	CHelpG , ±0.80 *e*	AMBER & OPLS-AA	24
Borodin	[EMIM][NTf_2]	125-180		polarizable	40
	[BMIM][NTf_2]				
	[HMIM][NTf_2]				
	[BMIM][PF_6]				
	[BMIM][BF_4]				
	[BMIM][CF_3SO_3]				
	[N_{4111}][NTf_2]				
	[pyr_{14}][NTf_2]				
Brandés and co-workers	[Bpy][BF_4]	125	ESP, ±1 *e*	OPLS-AA	41
	[BMpy][BF_4]				
Canongia Lopes and co-workers	[DMIM][Cl]	192	CHelpG , ±1 *e*	AMBER & OPLS-AA	42
	[EMIM][Cl]	144			
	[EMIM][NO_3]	96			
	[EMIM][PF_6]	192			
Canongia Lopes and Pádua	[Bpy][Cl]	144	CHelpG , ±1 *e*	OPLS-AA	43
	[$P_{10\,10\,10\,10}$][Br]	16			
	[$N_{1\,1\,1\,1}$][DCA]	96			
Chaban	[DMIM][NTf_2]	128	uniform scaling charges	AMBER & OPLS-AA	44
Ghatee and co-workers	[BMIM][I]	512	CHelpG, scaled charges	OPLS-AA	45
	[HMIM][I]				
	[OMIM][I]				

Heggen and co-workers	[BMIM][PF_6]	512	CHelpG , ±0.80 *e*	AMBER & OPLS-AA	[46]
Jayaraman and Maginn	[BMIM][Cl]	144	CHelpG , ±1 *e*	OPLS-AA CHARMM	[47]
Kelkar and co-workers	[EMIM][NTf_2]	200	CHelpG , ±1 *e*	CHARMM	[48]
	[BMIM][NTf_2]				
	[HMIM][NTf_2]				
	[OMIM][NTf_2]				
Klähn and co-workers	AP-N[d]	500	CHelpG , ±1 *e*	Molecular Mechanics (MM)	[49]
	AP-C[e]				
	CM-N[f]				
Koddermann and co-workers	[EMIM][NTf_2]	173	CHelpG , ±1 *e*	AMBER & OPLS-AA	[50]
	[BMIM][NTf_2]				
	[HMIM][NTf_2]				
	[OMIM][NTf_2]				
Liu and co-workers	[BMIM][Pf_2]	200	RESP , ±0.80 *e*	GAFF	[51]
	[BMpyr][NTf_2]				
	[N_{4111}][NTf_2]				
Margulis and co-workers	[BMIM][PF_6]	256	ESP, ±1 *e*	OPLS-AA	[52]
Pensado and co-workers	[EMIM][BF_4]	1024	CHelpG , ±1 *e*	AMBER & OPLS-AA	[53]
	[EOHMIM][BF_4]	700			
	[OMIM][BF_4]	700			
	[OOHMIM][BF_4]	800			
Prado and co-workers	[BMIM][BF_4]	125	CHelpG , ±1 *e*	OPLS-AA	[54]
Santos and co-workers	[EMIM][NTf_2]	400	CHelpG , ±1 *e*	AMBER/OPLS	[55]
	[BMIM][NTf_2]				
	[HMIM][NTf_2]				
	[OMIM][NTf_2]				
Shimizu and co-workers	[EMIM][NTf_2]	150	CHelpG , ±1 *e*	AMBER/OPLS - AA	[56]
	[BMIM][NTf_2]				
	[HMIM][NTf_2]				
	[OMIM][NTf_2]				
	[C_{10}MIM][NTf_2]				
	[C_{12}MIM][NTf_2]				
	[C_{14}MIM][NTf_2]				
	[BMIM][PF_6]				
	[HMIM][PF_6]				
	[OMIM][PF_6]				
	[$P_{6\,6\,6\,14}$][NTf_2]				

	$[P_{6\,6\,6\,14}][CF_3SO_3]$				
	$[P_{6\,6\,6\,14}][OAc]$				
	[BMIM][CF_3SO_3]				
	[BMIM][CH_3SO_4]				
	[BMIM][BF_4]				
	[BMIM][OAc]				
Shimizu and co-workers	$[PH(C_6H_5)_3][N(SO_2F)_2]$	144	CHelpG , ±1 *e*	OPLS-AA	57
	$[Na][N(SO_2C_2F_5)_2]$	96			
	$[K][N(SO_2C_2F_5)_2]$	128			
	$[(OCH_3)_2C_1im][PF_3(C_2F_5)_3]$	144			
Van-Oanh and co-workers	[EMIM][NTf_2]	50 and 150	CHelpG , ±1 *e*	C: CHARMM & A: OPLS-AA	58
Yan and co-workers	[BMIM][NO_3]	400	RESP, ±1 e	non-polarizable	59
				polarizable	
Zhang and Maginn	[BMIM][Cl]	108	CHelpG , ±1 *e*	C: CHARMM ; A: OPLS	60
Zhang and Maginn	[BMIM][PF_6]	250	gpFC, ±1 e	CHARMM	61
			gpSC, ±0.80 e		
			AIMD-c, ±0.80 e		
			AIMD-1, ±0.85 e		
			AIMD-b, ±0.80 *e*		
	[EMIM][PF_6]	400	gpFC, ±1 e		
			gpSC, ±0.80 *e*		
			AIMD-c, ±0.80 *e*		
			AIMD-1, ±0.85 *e*		
			AIMD-b, ±0.76 *e*		
Zhao and co-workers	[BMIM][PF_6]	768	CHelpG , ±0.80 *e*	OPLS-AA	62
Zhong and co-workers	[C_{10}MIM][NTf_2]	150	RESP , ±0.80 *e*	GAFF	63
	[EMIM][NTf_2]				
	[HMIM][NTf_2]				
	[OMIM][NTf_2]				
	[BMIM][CF_3CO_2]				
	[BMIM][CH_3CO_2]				
	[BMIM][PF_6]				
	[BMIM][NTf_2]				

[a]Number of anion+cation pairs in the simulation box;

[b]ESP/RESP and CHelpG are charges based on the fitting of the electrostatic potential on a grid of points according to the schemes of Merz-Singh-Kollman[64–66] or of Bayly and co-workers[67], respectively. NPA and Blöchl stand for charges derived from a natural population analysis of the natural bond orbitals approach of the atoms in a molecular system[68] or for charges calculated using the Blöchl method[69]. The labels gpFC and gpSC are used to denote full and scaled RESP charges for the isolated ions in the gas-phase calculated with Gaussian-type orbitals, AIMD-c is used for ESP charges calculated for the

crystalline system using a plane-wave approach while AIMD-l and AIMD-b stand for charges calculated after liquid phase simulations employing a plane-wave approach and the ESP or the Blöchl schemes, respectively. Note: 1 *e* = 1.602176487 x 10^{-19} C.

[c]C and A stand for cation and for anion, respectively;

[d]acyclic pentamethylpropylguanidinium nitrate;

[e]acyclic pentamethylpropylguanidinium perchlorate;

[f]cyclic tetramethylguanidinium nitrate;

2.1.1. Density

This is one of the most important properties of fluids that is easily measured experimentally and is fundamental for the prediction of thermophysical properties required for process design purposes or for solution theories of liquids. For ambient pressure and temperature conditions, density of common ILs range from 900 to 1500 kg·m^{-3} [70]. Available data for ILs density, in literature, is impressive and it is well reproduced by MD simulations.[71–73] In Maginn´s review[71] on the application of atomistic simulations to the prediction of thermodynamic and transport properties of ILs, computed and experimental densities were found to differ at most by 1 % to 5 %, depending on the applied force field and on its parameterization. Density is essentially a mean-field property that is insensitive to specific interactions and energies; yet, it is one of the properties that is widely used to validate force fields due to the two factors introduced above, *i.e.*, simplicity of calculation and availability of very accurate experimental values[74].

Densities of several different ILs were studied by means of MD simulations. Margulis and co-workers[52] conducted MD simulations considering the OPLS-AA (optimized potentials for liquid simulations developed by Jorgensen and co-workers[31] combined with an all atoms approach and total charges on the ions equal to unity) force field for at least 200 ps in the NPT ensemble, *i.e.*, constant pressure (1 atm, Nosé Hoover thermostat) and constant temperature (303 K, Anderson-Hoover barostat), for 1-butyl-3-methylimidazolium hexafluorophosphate ([BMIM][PF_6]), obtaining a density with the value of 1310.0 kg·m^{-3}; Zhong and co-workers have considered a different FF and different total charges on the ions (±0.8 *e*) being able to reach a density value for the same IL that matches the experimental result, *i.e.*, 1370.0 kg·m^{-3} (Table 2.1.1.1). Prado and co-workers[54] using the OPLS-AA force field and charges equal to unit performed simulations for at least 5 ns and reached a density value of 1178.0 kg·m^{-3} for 1-

butyl-3-methylimidazolium tetrafluoroborate, [BMIM][BF_4], also very close to the experimental result (Table 2.1.1.1). In these MD simulations, it was found that the density is converged for quite short simulation times. Densities of a series of different ILs, 1-alkyl-3-methylimidazolium bis(trifluoromethylsulfonyl)imide ([C_nMIM][NTf_2]) and 1-butyl-3-methylimidazolium cation ([BMIM]$^+$) with different anions, such as, trifluoroacetate ([CF_3CO_2]$^-$), acetate ([CH_3CO_2]$^-$) or hexafluorophosphate([PF_6]$^-$), were obtained at different temperatures through NPT MD simulations and considering the general AMBER force field, GAFF[75], by Zhong and co-workers[63]. The deviation of the results from experimental data (cited in the article[63]) is less than 1 %. In that work, a linear behavior of the density with the temperature was observed for all studied ILs. Furthermore, as expected, the densities of different alkyl chain lengths of imidazolium based-ILs with the anion [NTf_2]$^-$, decreased with the increase of temperature. Similarly, Liu and co-workers[51] published a complete study, estimating density for [NTf_2]$^-$-based ILs, obtaining a linear and a decreasing dependence with the increase of the temperature. The comparison of their results with published experimental data showed that densities are overestimated. For two other families of ILs, namely, pyridinium-based ILs and iodide-based ILs studied by Bandrés and co-workers[41] (with a maximum deviation of 14 % from experimental data) and by Ghatee and co-workers[45] (with a maximum deviation of 0.8 % from experimental data), respectively, a similar trend with the temperature was observed. Shimizu and co-workers[56], reported densities for imidazolium-based ILs and for some phosphonium-based ILs, with deviations not exceeding 4.5 %.

Densities of 1-ethyl-3-methylimidazolium hexafluorophosphate, [EMIM][PF_6], and 1-*N*-butyl-3-methylimidazolium hexafluorophosphate, [BMIM][PF_6], were obtained at 173 K by Zhang and Maginn[61], through NVT and NPT MD simulations considering the GAFF force field. These authors evaluated the influence of five different strategies for the calculation of atomic charges, which were incorporated in GAFF FF, on the prediction of static, dynamic and thermodynamic properties of [BMIM][PF_6] and [EMIM][PF_6] ILs by MD simulations. They tested the influence of atomic charges derived from periodic DFT/plane-wave calculations, for the crystalline and liquid phases, or from quantum chemistry calculations for the isolated ions. In the case of the periodic crystalline phase, the total charges calculated with the ESP scheme[64] were +0.80 *e* on the cation and -0.80 *e* on the two anions considered. The ESP charges were calculated by fitting the electrostatic potential of a molecule on a uniform distribution of points in the vicinity of the molecule. In the case of liquid phase, the calculation of the atomic charges was based on 50 different configurations taken from an AIMD simulation with 8 IL pairs per

unit cell and considering two different schemes, *i.e.*, the Blöchl[69] and the ESP[65–67,69] schemes. The Blöchl method decouples the density of a molecule calculated with a periodic plane-wave approach from its periodic images, *i.e.*, by subtracting the electrostatic interaction between periodic images of the densities of the isolated molecules. The interaction energy between separated densities is expressed in electrostatic multipole moments reproducing the original density and are used to fit the partial charges. The total charges in the cation and in the anion calculated with the ESP scheme were ±0.85 *e* for both ILs while those calculated with the Blöchl scheme were ±0.80 *e* for [BMIM][PF6] and ± 0.76 *e* for [EMIM][PF6] (Table 2.1.1). Finally, Zhang and Maginn also considered full atomic charges derived from quantum chemistry calculation of isolated ions in vacuum (total charge ±1.0 *e* for each ion), and charges derived from uniform scaling by a factor of 0.8 of the charges of the isolated ions in vacuum. As can be seen in Table 2.1.1.1, the densities calculated with the five different sets of charges resulted in similar density values presenting a maximum deviation of 6 % from available experimental data. Thus, it seems that the value of the total charge in the ions of ILs and the strategy used for the calculation of the atomic charges have a small effect on the calculation of this property.

Due to the fact that density is a validation parameter for ascertaining the quality of force fields, almost all the MD computational studies in this field present density data, which is compared with experimental results or with other published computational data. Nonetheless, with all reviewed studies, density presents itself as a property insensitive to specific interactions and energies, as well as, independent of the use of polarizable or non-polarizable FFs (see Table 2.1.1.1).[33] A similar conclusion was reached by Yan and co-workers[59], who, in an evaluation of the main differences in the application of polarizable and non-polarizable force fields in the estimation of properties of 1-ethyl-3-methylimidazolium nitrate, [EMIM][NO_3], obtained the values of 1177 $kg \cdot m^{-3}$ and 1174 $kg \cdot m^{-3}$ from simulations employing polarizable and non-polarizable force fields, respectively. These findings are in agreement with the results due to Zhang and Maginn[61] where total charges in the ions of two ILs ranging from ±0.76 *e* to ±1.0 *e* yielded practically the same densities and have showed that this property is, in fact, quite insensitive to the values of the charges considered in the simulations.

Table 2.1.1.1 - Estimated densities by means of MD simulations and experimental data, at different temperatures.

Author(s)[a]	IL	T / K	ρ_{sim} / kg·m^{-3}	ρ_{exp} / kg·m^{-3}
Ghatee and co-workers	[BMIM][I]	323	1414.0	1418.0
	[HMIM][I]		1313.0	1318.0
	[OMIM][I]		1248.0	1240.0
Liu and co-workers	[BMIM][NTf_2]	298	1446.0	1437.0[68]
	[BMIM][Pf_2]		1523.0	1517.7
	[BMpyr][NTf_2]		1439.0	1406.1
	[N_{4111}][NTf_2]		1493.0	1398.4
Margulis and co-workers	[BMIM][PF_6]	298	1310.0	1370.0[76]
Prado and co-workers	[BMIM][BF_4]	298	1178.0	1170.0
Shimizu and co-workers	[EMIM][NTf_2]	298	1580.0	1515.0
	[BMIM][NTf_2]		1150.0	1436.0
	[HMIM][NTf_2]		1430.0	1371.0
	[OMIM][NTf_2]		1360.0	1319.0
	[C_{10}MIM][NTf_2]		1310.0	1278.0
	[C_{12}MIM][NTf_2]		1270.0	1245.0
	[C_{14}MIM][NTf_2]		1240.0	1201.0
	[BMIM][PF_6]		1330.0	1364.0
	[HMIM][PF_6]		1250.0	1292.0
	[OMIM][PF_6]		1210.0	1234.0
	[$P_{6\,6\,6\,14}$][NTf_2]		1070.0	1065.0
	[$P_{6\,6\,6\,14}$][CF_3SO_3]		1000.0	982.0
	[$P_{6\,6\,6\,14}$][OAc]		910.0	891.0
	[BMIM][CF_3SO_3]		1340.0	1299.0
	[BMIM][CH_3SO_4]		1190.0	1211.0
	[BMIM][BF_4]		1160.0	1199.0
	[BMIM][OAc]		1080.0	1053.0
Zhang and Maginn	[BMIM][PF_6]	173	1484.0[b]	1560.0
			1461.0[c]	
			1475.0[d]	
			1479.0[e]	
			1471.0[f]	
	[EMIM][PF_6]		1615.0[b]	1656.0
			1578.0[c]	
			1593.0[d]	

			1599.0[e]	
			1577.0[f]	
Zhong and co-workers	[BMIM][PF_6]	298	1370.0	1370.0[76]
	[BMIM][NTf_2]		1445.0	1437.0[68]
	[C_{10}MIM][NTf_2]		1578.0	1570.0[77]
	[EMIM][NTf_2]		1531.0	1519.2
	[HMIM][NTf_2]		1375.0	1371.0[78]
	[OMIM][NTf_2]		1324.0	1325.0[68]
	[BMIM][CF_3CO_2]		1212.0	1210.0[79]
	[BMIM][CH_3CO_2]		1055.0	1019.2[80]

[a]Corresponding references and details of each study are compiled at Table 2.1.1.

[b]gpFC; [c]gpSC; [d]AIMD-c; [e]AIMD-1; [f]AIMD-b charges defined in footnotes of Table 2.1.1.

2.1.2. Melting point

As mentioned previously, a large and asymmetric cation together with an (in)organic anion confers to the IL a specific structure that prevents its crystallization, and thus decreases its melting point. This is one of the main differences between common molten salts and ILs, which also make ILs attractive to be used as replacements of common solvents, and thus, applied in a vast range of applications.

From experimental data[81,82] it is known that melting points of ILs decrease with changes in the symmetry between cation and anion, in the flexibility of the chains of the anions and in the charge dispersion. However, an increase in the length of the alkyl chains of the cations (with concomitant increase in the dispersive interactions) will increase the melting point.[72,83]

For the estimation of melting points, through atomistic methods, two approaches can be distinguished, the "direct" and the free-energy based methods. In the direct approaches it is included the solid-liquid interface[84] methods, the hysteresis method[85] (the most common) and the void method[84,85]. In an attempt to reproduce experimental measurements, Alavi and Thompson[37,38] used the solid-liquid interface method considering constant temperature and pressure MD simulations, to estimate melting points for 1-ethyl-3-methylimidazolium hexafluorophosphate ([EMIM][PF_6]) and for 1-n-butyl-4-amino-1,2,4-trizolium bromide([patr][Br]). These simulations were made for the crystal phase at increasing

temperature until a melting transition, identified by an abrupt change in density, was observed. However, these melting transitions may occur at higher temperatures than the true melting point, and hence, cannot be detected in the time scales accessible by MD. To overcome this, the void induced melting method systematically introduces voids in the crystal, removing atoms or ion pairs from the lattice. At void densities between 6 % and 10 %, the apparent melting points level off and this value is taken as the true melting point. Above 10 %, the crystal becomes mechanically unstable and results may be unreliable.

Melting point can be thermodynamically defined as the temperature at which the free energy of the liquid becomes equal to that of the solid, and this is the basis for the second group, the free-energy based methods. From the first free-energy based method[86–88], Jayaraman and Maginn[47] developed a new one, an extension of pseudo-supercritical path (PSPC) sampling procedure, to estimate melting points without the knowledge of fluid and solid reference state absolute free energies (Equation 2.1.2.1).

$$\frac{G}{RT} - \left(\frac{G}{RT}\right)_{ref} = \int_{T_{ref}}^{T} -\frac{H}{RT^2} \cdot dt \qquad (2.1.2.1)$$

This procedure is detailed in the literature[47], taking the 1-*n*-butyl-3-methylimidazolium chloride IL ([BMIM][Cl]) as a case study for which melting points were estimated for two crystal polymorphs. The calculated results are in good agreement with the experimental ones taken from Holbrey and co-workers[81]. Recently, Zhang and Maginn[60] published an extended study on different methods that can be used to calculate melting points. By considering potential parameters derived from the CHARMM force field, they have estimated the melting point for the [BMIM][Cl] IL through three different methods, *e.g.*, interface, voids and pseudo-supercritical path (PSCP) methods (Table 2.1.2.1). The former method, as mentioned before should present a transition in density (or volume), and in this specific IL it was only possible to detect a sharp increase in the density in a range between 450 K and 500 K. In the case of the second method, three transitions steps were observed, not being possible to determine the melting point. Regarding the PSCP method, this have yielded the best result, *i.e.*, it was possible to calculate the melting point for a temperature of 320 K, and therefore it seems to be a reliable approach for the determination of melting point of complex molecules, such as ILs.

The same authors in a subsequent work estimated melting points for [EMIM][PF_6] and [BMIM][PF_6], through NVT and NPT MD simulations considering GAFF force field and different methodologies to estimate the atomic charges (see previous section and Table 2.1.1).[61] Taking these two ILs, the best agreement between computed and experimental melting points is obtained with the charges calculated from the periodic crystalline phase plane-wave calculations, *i.e.*, AIMD-c charges. These results show that, contrary to what was found for the density, the strategy followed to compute the atomic point charges has an important influence in the quality of the calculated melting points.

Table 2.1.2.1 - Comparison of estimated melting points obtained using different methodologies and MD simulations, $T_{m,sim}$, with available experimental, $T_{m,exp}$, data.

Author(s)[a]	IL	Method	$T_{m,sim}$ / K	$T_{m,exp}$ / K
Zhang and co-workers	[BMIM][Cl]	Interface	450~500	342[89]
		Voids	not possible to identify	
		PSCP	320	
Zhang and Maginn	[BMIM][PF_6]	PSCP	292 [b]	284[90]
			245 [c]	
			284 [d]	
			260 [e]	
			308 [f]	
	[EMIM][PF_6]	PSCP	382 [b]	338[91]
			297 [c]	
			330 [d]	
			332 [e]	
			289 [f]	

[a]Corresponding references and details of each study are compiled at Table 2.1.1.

[b]gpFC; [c]gpSC; [d]AIMD-c; [e]AIMD-1; [f]AIMD-b charges.

2.1.3. Vapor pressure, boiling point and enthalpy of vaporization

The volatility of ILs had been initially considered to be negligible.[92] ILs were regarded as having no measurable vapor pressure and not able to be distilled. However, Earle and co-workers[93] showed that ILs could be distilled under specific temperature and pressure conditions. Later, Rebelo[94] and Paulechka[95] and their co-workers have fully explored the

volatility of ILs by demonstrating the potential of vaporizing certain ILs at reduced pressure. These findings paved the way for the measurement of vapor pressures for ionic liquids, mainly by Knudsen effusion methods.[94,96] The experimental measurement of the vapor pressure and the enthalpy of vaporization was found to be extremely difficult due to the very low vapor pressures and to the competition between vaporization and thermal decomposition (preventing the measurement of critical properties) or to the presence of impurities.[63,72,83] In a recent review by Esperança and co-workers[92], the nature of the vapor phase was discussed and the approaches used to predict and measure boiling points, vapor pressures and enthalpies of vaporization of ILs were analyzed. This particular study, highlights the difficulties in the measurement of these properties, and that the accuracy of those data is essential for theoretical and practical purposes.

In simulation, enthalpy of vaporization (ΔH^{vap}) is calculated from the difference between the molar internal energy of the gas/vapor (U^{vap}) and of the liquid (U^{liq}) phases (Equation 2.1.3.1).

$$\Delta H^{vap} = RT - \left(U^{liq} - U^{vap}\right) \quad (2.1.3.1)$$

$$\Delta H^{vap} = U^{cohesive} + RT \quad (2.1.3.2)$$

The gas phase is reproduced through a simulation of an isolated ion pair of ILs at the same temperature as the liquid phase.[97,98] Though the review of Esperança and co-workers[92] does the survey of MD simulations in the prediction of the enthalpies of vaporization of ILs, it can be highlighted some computational works. Santos and co-workers[55], estimated enthalpies of vaporization of 1-alkyl-3-methylimidazolium bis(trifluoromethylsulfonyl)imide ($[C_nMIM][NTf_2]$) according to Equation 2.1.3.1, based on the force field developed by Canongia-Lopes, Deschamps and Pádua[42]. The same ILs were studied by Kelkar and Maginn[48], but considering a force field developed accordingly to CHARMM parameters. The values calculated by the latter authors are compared in Table 2.1.3.1 with those obtained by Shimizu and co-workers[56] and by Köddermann and co-workers[50] from the estimation of the cohesive energy ($U^{cohesive}$) in accordance to Equation 2.1.3.2. As it can be seen in Table 2.1.3.1, different force field parameters and/or different strategies to calculate the enthalpy of vaporization lead to enthalpic differences that can be of several tens of $kJ \cdot mol^{-1}$, being the values calculated by Köddermann and co-workers systematically smaller than the experimental results and than those calculated by other research groups. In fact, the computational results from these four

independent studies differ significantly from the experimental results. Several different authors performed computational studies for this family of ILs, also calculating enthalpies of vaporization. Results obtained with different sets of computational parameters, are closer to the values of Köddermann and co-workers than to those from the other authors listed above. Borodin[40], and more recently Zhong and co-workers[63], estimated enthalpies of vaporization for the same family of ILs, presenting underestimated and overestimated values, respectively, when compared to results obtained by previously mentioned authors.

As it can be seen from the values collected in Table 2.1.3.1, a large discrepancy of values exists for the same IL, *e.g.* [EMIM][NTf_2] or [BMIM][NTf_2], which is a result of different computational strategies, *i.e.*, by the different parameters from force fields and different values of the total charges in the cation and in the anion for the same ILs. The latter argument is supported by the large difference in the enthalpies of vaporization of [EMIM][PF_6] and [BMIM][PF_6] calculated with total charges close to unity or close to ±0.8 *e* reported by Zhang and Maginn[61]. Nevertheless, values obtained by Koddermann, Borodin and Zhong and their co-workers are similar, but only for a few cases, the calculated results are in close agreement with the experimental data reported until now. Unfortunately, in addition to problems related with the choice of the best simulation strategy, difficulties in the experimental measurement of enthalpies of vaporization lead to the existence of inaccurate experimental data, and results obtained by simulation cannot be fully validated (differences can be up to 50 $kJ \cdot mol^{-1}$).

In literature, it is also possible to find values for the enthalpy of vaporization for pyridinium-based ILs calculated by Bandrés and co-workers[41], with maximum deviation of ~ 11 % from experimental results, and for guanidinium-based ILs calculated by Khähn and co-workers[49], with maximum deviation of ~13 % from the experimental ones.

As a final conclusion from the analysis of the enthalpies of vaporization available for some families of ILs, it is clear both from the computational and from the experimental studies that an increase of the alkyl chain length of the cations leads to an increase of ΔH^{vap} (Table 2.1.3.1).

Table 2.1.3.1 - Calculated and Experimental Enthalpies of Vaporization, at *T*=298 K, for several ILs.

Author(s)[a]	IL	ΔH^{vap}_{sim} / $kJ \cdot mol^{-1}$	ΔH^{vap}_{exp} / $kJ \cdot mol^{-1}$
Brandés and co-workers	[Bpy][BF_4]	190.6	167.0[99]
	[BMpy][BF_4]	180.5	162.1[100]
Borodin	[BMIM][PF_6]	150.6	157.0[101]
	[BMIM][CF_3SO_3]	142.7	

	[BMIM][BF_4]	140.8	
	[EMIM][NTf_2]	127.7	134.0-141.0[55,92,99]
	[BMIM][NTf_2]	133.7	134.0-155.0[55,90,92]
	[HMIM][NTf_2]	141.9	139.0[99], 173.0[55]
Kelkar and co-workers	[EMIM][NTf_2]	146.0	134.0-141.0[55,92,99]
	[BMIM][NTf_2]	151.0	134.0-155.0[55,92,99]
	[HMIM][NTf_2]	157.0	139.0[99], 173.0[55]
	[OMIM][NTf_2]	162.0	149.0[99], 192.0[55]
Klähn and co-workers	AP-N	174.5	201.4
	AP-C	189.2	192.4
	CM-N	200.8	218.4
Koddermann and co-workers	[EMIM][NTf_2]	130.6	134.0-141.0[55,92,99]
	[BMIM][NTf_2]	135.1	134.0-155.0[55,92,99]
	[HMIM][NTf_2]	143.8	139.0[99], 173.0[55]
	[OMIM][NTf_2]	153.8	149.0[99], 192.0[55]
Santos and co-workers	[EMIM][NTf_2]	159.0	134.0-141.0[55,92,99]
	[BMIM][NTf_2]	174.0	134.0-155.0[55,92,99]
	[HMIM][NTf_2]	184.0	139.0[99],173.0[55]
	[OMIM][NTf_2]	201.0	149.0[99], 192.0[55]
Shimizu and co-workers	[EMIM][NTf_2]	173.5	134.0-141.0[55,92,99]
	[BMIM][NTf_2]	180.5	134.0-155.0[55,92,99]
	[HMIM][NTf_2]	185.5	139.0[99], 173.0[55]
	[OMIM][NTf_2]	189.5	149.0[99], 192.0[55]
	[C_{10}MIM][NTf_2]	199.5	
	[C_{12}MIM][NTf_2]	207.5	
	[C_{14}MIM][NTf_2]	217.5	
	[BMIM][PF_6]	186.5	157.0[101]
	[HMIM][PF_6]	194.5	
	[OMIM][PF_6]	202.5	169.0[99]
	[$P_{6\,6\,6\,14}$][NTf_2]	269.5	
	[$P_{6\,6\,6\,14}$][CF_3SO_3]	258.5	
	[$P_{6\,6\,6\,14}$][OAc]	282.5	
	[BMIM][CF_3SO_3]	181.5	
	[BMIM][CH_3SO_4]	201.5	
	[BMIM m][BF_4]	182.5	
	[BMIM][OAc]	281.5	
Zhang and Maginn	[BMIM][PF_6]	188.2 [b]	157.0[101]
		145.1 [c]	
		143.0 [d]	
		144.6 [e]	

		142.6 [f]	
	[EMIM][PF_6]	191.8 [b]	160.0[101]
		144.8 [c]	
		138.7 [d]	
		144.6 [e]	
		128.5 [f]	
Zhong and co-workers	[EMIM][NTf_2]	142.2	134.0-141.0[55,92,99]
	[BMIM][NTf_2]	138.1	134.0-155.0[55,92,99]
	[HMIM][NTf_2]	148.5	139.0[99], 173.0[55]
	[OMIM][NTf_2]	156.8	149.0[99], 192.0[55]

[a]Corresponding references and details of each study are compiled at Table 2.1.1.

[b]gpFC; [b]gpSC; [d]AIMD-c; [e]AIMD-1; [f]AIMD-b charges.

2.1.4. Viscosity

Viscosity, η, is a key transport property for industrial purposes, required for the design of process units. Its influence is evident on, for example, the behavior of ILs as lubricants and on mass and heat transfer processes. ILs present values of viscosity significantly higher than those for water or for organic solvents, *e.g.* at T = 298.15 K, η(water) = 0.89 mPa·s and η(methanol) = 0.54 mPa·s, while η([BMIM][SCN]) = 64.81 mPa·s and η([BMIM][DCA]) = 31.80 mPa·s. Large viscosities may be considered as disadvantageous for the use of ILs, in processes involving pumping and mixing, and processes that involve heat and mass transfer[8,72], while they may be considered quite appealing when applied as lubricants. Changes in temperature, pressure and also in the cation or in the anion that compose the IL will influence directly its viscosity. The presence of water was also found to have an important influence on the viscosity of ILs and hence, on their performance.[72] Though there is still limited available experimental data in literature, MD simulations have been performed. Hess[102], and more recently Tenney and Maginn[103], have discussed new strategies based on classical MD simulations for the calculation of viscosity. Essentially, viscosities can be estimated by EMD simulations, using a Green-Kubo integral (Equation 2.1.4.1) or Einstein relation (Equation 2.1.4.2) to relate fluctuations of off-diagonal elements of pressure tensor to viscosity, at specific limit conditions, such as in Equation 2.1.4.3. This obliges many simulation steps, *i.e.*, very long simulation runs and concomitant storage of large trajectory files, to achieve good statistics.

$$\eta = \frac{V}{k_B T} \int_0^\infty \langle P_{xz}(0) \cdot P_{xz}(t) \rangle \cdot dt \tag{2.1.4.1}$$

$$\eta = \lim_{t \to \infty} \frac{V}{2tk_B T} \langle \int_0^t P_{xz}(t') \cdot dt' \rangle \tag{2.1.4.2}$$

$$\eta = \frac{V}{10k_B T} \int_0^\infty \langle P_{ij}^{OS}(0) \cdot P_{ij}^{OS}(t) \rangle \cdot dt$$
$$P_{ij}^{OS} = \frac{P_{ij} + P_{ji}}{2} - \delta_{ij} \left(\frac{1}{3} \sum_k P_{kk} \right) \tag{2.1.4.3}$$

In Equations 2.1.4.1 – 2.1.4.3, V is the volume of the system, k_B is the Boltzmann constant, T is the temperature, t is the time and P is the pressure tensor. In the case of NEMD simulations, the response of the system to an external perturbation (shear strain) is used to calculate viscosity through Navier-Stokes equations. The most widely used nonequilibrium approach for viscosity calculations at a given shear rate, is the SLLOD algorithm[104], which imposes a shear strain on the system and measures the resulting steady state stress (Equation 2.1.4.4).[102,103]

$$\eta(\dot{\gamma}) = -\frac{P_{ij}}{\dot{\gamma}} \tag{2.1.4.4}$$

Nonetheless, Maginn and co-workers[71,105] discussed the use and application of reverse nonequilibrium MD (RNEMD) to estimate the viscosity of ILs. The RNEMD method imposes the hard-to-measure heat flux and computes the resulting easy-to-measure shear rate or velocity profile, promoting the convergence of the viscosity calculation (Equation 2.1.4.5), where j is the imposed momentum flux, p_{total} is the total exchanged momentum and L defines the length of the simulation box along an axis.

$$j_{xz}(P_x) = \frac{p_{total}}{2tL_x L_y}$$
$$\eta(\dot{\gamma}) = -\frac{j_{xz}}{\dot{\gamma}} \tag{2.1.4.5}$$

The authors were able to conclude that though RNEMD successfully predicts viscosities for several ILs, (agreeing well with the SLLOD and EMD results, at low shear), only under very specific conditions should it be preferably considered, presenting underestimated viscosities at high shear when compared with those calculated with the SLLOD algorithm.

Yan[59], Borodin[40], Van Oanh[58], Zhong[63] and Liu[51] and their co-workers, are among those who used EMD to calculate the viscosity of imidazolium-based ILs. Ghatee and co-workers[45], determined viscosities for some iodide-based ILs (with maximum deviation of 37 %). Other authors, *e.g.*, Zhao[62] or Van Oanh[58] and their co-workers, used NEMD approaches for calculating viscosities of 1-butyl-3-methylimidazolium hexafluorophosphate ([BMIM][PF_6]), 1-methyl-3-ethylimidazolium bis(trifluoromethane)sulfonamide ([EMIM][$N(SO_2CF_3)_2$]) and 1-ethyl-3-methylimidazolium bis(trifluoromethanesulfonyl)imide ([EMIM][NTf_2]). Some of these data are compiled in Table 2.1.4.1. From the results therein reported, the trend that stands out is that, in general, results from EMD and NEMD simulations were found to overestimate the experimental viscosity data and that as the cation alkyl chain length increases, viscosity values also increase. Liu and co-workers[51] have demonstrated also the dependence of viscosity with temperature. As expected, with the increase of temperature the values of the viscosity decrease. Finally, adding the systematic overestimation of viscosity values to the great computational efforts required for their calculation clearly suggests that improvements of the methods to compute viscosity of ILs are still required.

It was mentioned before that NEMD should be preferably used for the estimation of transport properties, but from the analysis of the studies described above, it is perceived that acceptable results can be also obtained by using EMD formalism. In fact, as it can be seen in Table 2.1.4.1, the viscosities calculated by Van-Oanh and co-workers[58] for [EMIM][NTf_2] IL with the EMD formalism or with the NEMD approach differ by only 0.13 mPa·s at T = 500 K.

Table 2.1.4.1 - Estimated viscosities, at different temperatures, determined by means of MD simulations.

	Author(s)	IL	T / K	η_{sim} / mPa·s	η_{exp} / mPa·s
EMD	Borodin	[BMIM][CF_3SO_3]	298	90.0[b]	84.2[106]
		[N_{4111}][NTf_2]		93.0[b]	99.0[107]
		[pyr_{14}][NTf_2]		78.0[b]	75.7[107]
		[EMIM][NTf_2]		31.2[b]	32.2[108]
	Ghatee and co-workers	[BMIM][I]	298	26.7[c]	29.0

		[HMIM][I]		28.2[c]	40.3
		[OMIM][I]		35.3[c]	55.7
	Liu and co-workers	[BMIM][NTf_2]	298	28.0[c]	5.1
	Van-Oanh and co-workers	[EMIM][NTf_2]	500	3.5[c]	
	Yan and co-workers	[EMIM][NO_3]	400	4.7[b]	4.2
				6.8[c]	
	Zhao and co-workers	[BMIM][PF_6]	300	127.0[c]	
	Zhong and co-workers	[EMIM][NTf_2]	353	8.3[c]	7.7[107]
		[BMIM][NTf_2]		12.6[c]	9.2[50]
		[HMIM][NTf_2]		15.5[c]	10.8[107]
		[OMIM][NTf_2]		18.5[c]	12.7[107]
NEMD	Van-Oanh and co-workers	[EMIM][NTf_2]	500	3.6[c]	
RNEMD	Zhao and co-workers	[BMIM][PF_6]	298	139.6[c]	228.8[106]

[a] Corresponding references and details of each study are compiled at Table 2.1.1.

[b] Polarizable force field

[c] Non-polarizable force field

2.1.5. Diffusion coefficient

Diffusion coefficient (*D*) is a transport property, which is important in applications involving mass transfer. This is another property that can also be used to validate force fields, similar to what is done with density but, in opposition to this, available experimental values of diffusion coefficients for ILs are scarce in the literature. The diffusion coefficient may be described by the Stokes-Einstein equation, Equation 2.1.5.1, considering mean square displacements at very large times, and showing a great dependence on the viscosity. Similarly to viscosity, long MD simulations are required to obtain accurate values of *D* due to the slow dynamics that is characteristic of ILs.

$$D_i = \frac{1}{6}\lim_{t\to\infty}\frac{d}{dt}\langle[\vec{r_i}(t) - \vec{r_i}(0)]^2\rangle \qquad (2.1.5.1)$$

Margulis[52], Aparicio[39], Borodin[40], Zhong[63], Liu[51] and their co-workers calculated, using MD simulations, the diffusion coefficients for different imidazolium-based ILs, while Klähn and co-workers[49] calculated for guanidinium-based ILs. Their results are shown in Table

2.1.5.1 and it is demonstrated that the diffusion coefficients for both the cation and anion decrease with the increase of alkyl chain length. The temperature dependence of diffusion coefficients was predicted by Liu and co-workers[51], for the following ILs: 1-butyl-3-methylimidazolium bis[(perfluoroethyl)sulfonyl]imide ([BMIM][PF_2]), 1-butyl-3-methylimidazolium bis(trifluoromethanesulfonyl)imide ([BMIM][NTf_2]), 1-butyl-1-methylpyrrolidinium bis(trifluoromethanesulfonyl)imide, ([BMpyr][NTf_2]), and *N*-butyl-*N,N,N*-trimetylammonium bis(trifluoromethanesulfonyl)imide, ([N_{4111}][NTf_2]), and was found to be well described by the Arrhenius temperature dependence, *i.e.,* there is a linear dependence of log *D* with the inverse of temperature (1/*T*).

All mentioned simulations produced values that underestimate the experimental results, which were found to be approximately one third of the latter ones. Deviations between experimental and simulation results have been suggested to be caused by some inaccuracies of force fields. Importantly, it is possible to conclude from the results in Table 2.1.5.1 that the simulations conducted by Borodin[40] with a polarizable force field, yield values that are closer to the experimental ones[72,83], than those calculated with a non-polarizable force-field. This suggests that polarizable force fields are essential for the calculation of diffusion coefficients for ILs. Unfortunately, as mentioned above, clear conclusions are not possible since the calibration of the computational procedures suffers from the lack of reliable experimental data for this property.

Table 2.1.5.1 - Estimated diffusion constants, at different temperatures, determined by means of MD simulations.

Author(s)[a]	IL	*T* / K	D^+_{sim} / $m^2 \cdot s^{-1}$	D^-_{sim} / $m^2 \cdot s^{-1}$	D^+_{exp} / $m^2 \cdot s^{-1}$	D^-_{exp} / $m^2 \cdot s^{-1}$
Aparicio and co-workers	[EMIM][TOS]	318	5.82×10^{-11}	2.69×10^{-11}		
Borodin	[BMIM][BF_4]	298	0.101×10^{-10}	0.105×10^{-10}	0.145×10^{-10} [106]	0.134×10^{-10} [106]
	[pyr_{14}][NTf_2]		0.119×10^{-10}	0.104×10^{-10}	0.177×10^{-10}	0.142×10^{-10}
	[BMIM][PF_6]		0.032×10^{-10}	0.028×10^{-10}	0.069×10^{-10} [106]	0.052×10^{-10} [106]
	[EMIM][NTf_2]		0.516×10^{-10}	0.347×10^{-10}	0.495×10^{-10} [109]	0.309×10^{-10} [109]
	[BMIM][NTf_2]		0.289×10^{-10}	0.196×10^{-10}	0.275×10^{-10} [106]	0.218×10^{-10} [106]
	[HMIM][NTf_2]		0.149×10^{-10}	0.144×10^{-10}	0.168×10^{-10}	0.153×10^{-10} [108]
Margulis and co-workers	[BMIM][PF_6]	298	1.420×10^{-11}	1.280×10^{-11}	6.700×10^{-11} [109]	5.700×10^{-11} [107]
Klähn and co-workers	AP-N	298	1.300×10^{-12}	2.000×10^{-12}	2.900×10^{-12}	2.900×10^{-12}
	AP-C		0.500×10^{-12}	0.500×10^{-12}	3.600×10^{-12}	4.300×10^{-12}

	CM-N		$0.300x10^{-12}$	$0.300x10^{-12}$	$1.300x10^{-12}$	$1.600x10^{-12}$
Zhong and co-workers	[BMIM][PF_6]	353	$4.700x10^{-11}$	$3.200x10^{-11}$	$6.700x10^{-11}$ [109]	$5.700x10^{-11}$ [107]
	[EMIM][NTf_2]		$18.500x10^{-11}$	$10.200x10^{-11}$	$22.000x10^{-11}$ [109]	$14.000x10^{-11}$ [107]
	[BMIM][NTf_2]		$10.900x10^{-11}$	$7.800x10^{-11}$	$15.000x10^{-11}$ [109]	$13.000x10^{-11}$ [107]
	[HMIM][NTf_2]		$6.900x10^{-11}$	$6.200x10^{-11}$	$12.000x10^{-11}$ [109]	$11.000x10^{-11}$ [107]
	[OMIM][NTf_2]		$4.000x10^{-11}$	$4.000x10^{-11}$	$9.000x10^{-11}$ [109]	$8.800x10^{-11}$ [107]

[a]Corresponding references and details of each study are compiled at Table 2.1.1.

2.1.6. Surface tension

This is an important property that measures the cohesive forces between liquid molecules present at a surface between the coexisting liquid and gas phases, and also allows one to explore different types of segregation/orientation that occur at an ionic/molecular level, very important in the evaluation of complex molecules, such as ILs.[110] It is, then, a property related with the mass transfer efficiency for gas-liquid / liquid-liquid extraction processes and multiphase homogeneous catalysis, and has scarcely been studied. Similar to what is observed for viscosity, the presence of water can affect the surface tension, especially in the case of hydrophobic ILs as shown recently by Freire and co-workers[111].

Bhargava and Balasubramanian[112] estimated the surface tension for [BMIM][PF_6] through MD simulations by using the formula of diagonal components of the pressure tensor P_{ii}, as demonstrated in Equation 2.1.6.1 where L_z is the length of the simulation box in the z direction.

$$\gamma = -\frac{L_z}{4}\left(P_{xx} + P_{yy} - 2(P_{zz})\right) \quad (2.1.6.1)$$

In their work, it was considered a refined force field with charges on the cation and on the anion of ±0.8 *e* based on the AMBER/OPLS type potential parameters for the intramolecular interactions by Canongia-Lopes and co-workers[42] (see Table 2.1.1). The authors obtained a value for the surface tension of 47 $mN{\cdot}m^{-1}$ which is in good agreement with the experimental result of 42.3 $mN{\cdot}m^{-1}$. Canongia Lopes and co-workers[42], considered charges on the cation and on the anion of ±1.0 *e*, and using the same equation they obtained a much higher value (γ =74 $mN{\cdot}m^{-1}$) than that calculated by Bhargava and Balasubramanian.

Following the same methodology, Heggen and co-workers[46] studied the impact on the calculated surface tension values for [BMIM][PF_6] of running the MD simulations with

different simulation packages (YASP[113] or GROMACS[114]), and considering different treatments for the electrostatics (particle-mesh Ewald, PME, or reaction field, RF). They found that the calculation of surface tension values with bond constraints lead to different results when YASP/RF or GROMACS/RF were considered. For instance, at T=300K, the surface tensions calculated by these codes are 37.3 and 49.0 $mN \cdot m^{-1}$, respectively, while the experimental result is 43.5 $mN \cdot m^{-1}$. The results obtained with YASP/RF underestimated systematically the experimental values by about 20 % in all range of temperatures studied, decreasing as the temperature increase. However, with GROMACS/RF, the calculated results overestimate the experimental ones in the order of 13 %. Releasing bond constraints, the YASP/RF was able to give a value closer to the experimental result (44.7 $mN \cdot m^{-1}$, *i.e.*, a slight overestimation) while GROMACS/RF, with constraints, and GROMACS/RF, without constraints, give practically the same result (49.0 *vs* 49.3 $mN \cdot m^{-1}$, respectively). A much better value was calculated with GROMACS, γ = 46.4 $mN \cdot m^{-1}$, but using PME. The latter result is almost identical to that calculated by Bhargava and Balasubramanian (see above).

González-Melchor and co-workers[115] computed the surface tension for some ILs by running MD simulations with the aim of studying the size effects of the ions in the surface tension. Interestingly, it was found that the surface tensions of the ILs, considered in that work, decreased with the increase of cation to anion asymmetry. Later, Pensado and co-workers[53] performed MD simulations, based again on the AMBER/OPLS-AA force field, for interpreting the effect of the length of the alkyl side chain and the presence of a polar hydroxyl group at the end of the side chain on the surface tension, of the following ionic liquids: 1-ethyl-3-methylimidazolium tetrafluoroborate ([EMIM][BF_4]), 1-(2-hydroxyethyl)-3-methylimidazolium tetrafluoroborate ([EOHMim][BF_4]), 1-octyl-3-methylimidazolium tetrafluoroborate ([OMIM][BF_4]) and 1-(8-hydroxyoctyl)-3-methylimidazolium tetrafluoroborate ([OOHMIM][BF_4]). The calculated values for these ILs were, respectively, 39.9 $mN \cdot m^{-1}$ (against 44 $mN \cdot m^{-1}$ from experimental work), 55.5 $mN \cdot m^{-1}$ (against 56.9 $mN \cdot m^{-1}$ from experimental work), 35.6 $mN \cdot m^{-1}$ and 27.2 $mN \cdot m^{-1}$ (against 24.7 $mN \cdot m^{-1}$ from experimental work). The maximum deviation with respect to the experimental data was only of 10 %. They concluded also from their results that the increase of the length lowered the values calculated for the surface tension but the introduction of the polar hydroxyl group was found to have an opposite effect (surface tension values increased), which was related with the increase of the electrostatic and repulsion-dispersion contributions.

2.1.7. Structural characterization

MD simulations can be used to successfully predict properties other than transport and thermodynamic ones. The structural information of ILs can also be obtained by theoretical means and a common way to do this is through the estimation of the radial distribution functions (RDFs or *g(r)*), which gives information concerning the structural organization of a system. More specifically, this function gives the probability of finding a particle at the distance *r* from another particle (considered as the reference particle) and it is commonly used to aid the interpretation of the experimental results, and for this reason is found in most every study where simulation and experimental means complement each other.

$$g(r) = \frac{n(r)}{4\pi\rho r^2 dr} \tag{2.1.7.1}$$

Bhargava and Balasubramanian[112], calculated RDFs for anion-anion and cation-anion interactions in the 1-butyl-3-methylimidazolium hexafluorophosphate ([BMIM][PF_6]) ionic liquid. The idea was to understand the local structural effects in the IL and also check the quality of their refined potential, which was done by comparison with the structural information in the liquid obtained from ab initio molecular dynamics (AIMD) simulation. Due to the consideration of different force field parameters in the calculations, the positioning and the magnitude of the RDF peaks differed visibly from those calculated with the original force field introduced by Canongia-Lopes and co-workers[42]. For the same [BMIM][PF_6] IL, Margulis and co-workers[52] also calculated RDFs between the cation and anions and RDFs were computed, as well for 1-ethyl-3-methylimidazolium hexafluorophosphate ([EMIM][PF_6])[38], 1-ethyl-3-methylimidazolium tetrafluoroborate ([EMIM][BF_4])[54], and 1,3-dimethylimidazolium bis(trifluoromethanesulfonyl)imide ([DMIM][NTf_2])[116]. In these studies, it was possible to identify interactions established (hydrogen bonds) between the hydrogen atoms from the imidazolium cation and the fluorine atoms from the anions that compose the ILs. Though these interactions are established by different hydrogen atoms in the imidazolium cation with the anion's atoms, the acidic hydrogen in the ring revealed a higher propensity to interact with the halogen atoms from both anions. Simultaneously, it was found higher probability of interaction between the acidic carbon of the imidazolium cation and the boron and phosphorous atoms

from the anions. In the study of Alavi and co-workers[37], the same kind of interactions was observed for the anion Br^-, from 1-n-butyl-4-amino-1,2,4-triazolium bromide IL.

It is worthwhile mentioning the work developed by Canongia Lopes and co-workers[117] , who, through the estimation of RDFs, demonstrated the complex microscopic structure of ILs that is characterized by the existence of different domains/regions, with different polarities, which has been considered as reference for many studies since then. The RDFs, additionally, can have a 3D representation, through the spatial distribution functions (SDFs). The SDFs are a three dimensional visualization of regions of high probability of atoms/particles surrounding a reference one, allowing a better understanding of the structural atom organization.[59,61,118,119]

Furthermore, and complementing the information giving by radial and spatial distributions functions, the quantification of the total number of atoms/particles on the surroundings of a reference one, can be obtained through the integration of RDFs, usually named as the coordination number[120,121].

Molecular dynamics simulation, also allows to evaluate the crystal structure of ILs. The crystal structure is defined, accordingly, by dimensions (a, b, c) and director angles (α, β, γ) of the unit cell, which have been tentatively predicted by means of MD simulations. Canongia Lopes and co-workers[42] attempted to predict the crystal structure of several ILs, $[C_{10}MIM][Cl]$, [EMIM][Cl], $[EMIM][NO_3]$ and $[EMIM][PF_6]$, based on the dimensions and occupancy of the unit cells of each crystalline structure taken from the Cambridge Structural Database (CSD), and considering classical simulations with their developed force field based on AMBER/OPLS-AA force fields parameters. The results obtained agreed well with the experimental ones, and the highest deviation around 3.5 %, was observed for the value of the β vector. In following works[43,57], the prediction of the crystal structure was attempted for *n*-butylpyridinium chloride ([Bpy][Cl]), tetradecylphosphonium bromide ($[P_{10,10,10,10}][Br]$), tetramethylammonium dicyanamide ($[N_{1,1,1,1}][DCA]$), triphenylphosphonium bis(fluorosulfonyl)amide ($[PH(C_6H_5)_3][N(SO_2F)_2]$), sodium *trans*-bis(perfluoro-n-butylsulfonyl)amide ($[Na][N(SO_2C_2F_5)_2]$) , potassium *trans*-bis(perfluoro-*n*-butylsulfonyl)amide and potassium *cis*-bis(perfluoro-*n*-butylsulfonyl)amide ($[K][N(SO_2C_2F_5)_2]$) and, finally, for 1,3-dimethoxy-2-ethylimidazolium tris(pentafluoroethyl)trifluorophosphate ($[(OMe)_2MIM][PF_3(C_2F_5)_3]$). Using the methodology applied in previous work[42], it was possible to obtain results in good agreement with the experimental ones (obtained through X-ray experiments), for cell vector lengths and cell vector angles, with deviations ranging from 2 % to 4 %. The prediction of the crystal structure was

considered as a good test to develop and to validate the force fields applied for the different ILs. Jayaraman and Maginn[47], predicted the crystal structure of [BMIM][Cl] with two different potentials, namely, that developed by Canongia Lopes and co-workers[42], based on OPLS parameters, and that developed by Cadena and Maginn[122] based on CHARMM force field. The results calculated from the two force fields were found to reproduce well the experimental ones with a maximum deviation of 1 %. Nevertheless, when the two possible polymorphs of this IL were studied, only the second one was able to reproduce both structures in a stable form. Later, Zhang and Maginn[61] reported not only densities, enthalpies of vaporization and melting points of [EMIM][PF_6] and [BMIM][PF_6] but also the prediction of their crystal structure. The simulations were performed at T = 173 K through NVT and NPT ensembles, considering GAFF force field and five different sets of atomic charges. From obtained results, it was found that the lattice parameters are not affected by the differences in ILs' atomic charges, with a maximum deviation of 4 % in the case of [BMIM][PF_6] and a maximum deviation of 2.5 % in the case of [EMIM][PF_6]).

Borodin[40] in his extensive study regarding the prediction of thermodynamic, transport and structural properties of ILs, was also able to obtain very good results for the crustal structure of the ILs studied with deviations not more than 2.5 % from the results obtained through X-ray measurements. This author have applied a many-body polarizable force field and performed the NPT ensemble to model the [EMIM][NTf_2], [pyr_{13}][NTf_2], [pyr_{14}][NTf_2] and [EMIM][CF_3SO_3] ILs, with initial dimensions and occupancy of the unit cells of each crystalline structure taken from the CSD.

Summary

Most of the works reported in this chapter considered non-polarizable force fields. These force fields, in general, produced underestimated diffusion coefficients, overestimated viscosities values and present, however, quite good agreement between calculated and experimental results for the densities and surface tensions of ILs (Table 2.1.2). The usage of polarizable force fields, in some cases, leads to results that are closer to the experimental ones (see Tables 2.1.4.1 and 2.1.5.1) which is probably related with the fact that the charges on the ILs' ions vary with the nature of the charged units (species/compounds), with the number and the nature of the surrounding units, and with the fact that the total charges of ILs' ions seem to be often different from unit, which was considered only in some of the computational studies reported here. Thus, the point charges seem to have a very important role in the quality of the thermodynamic properties calculated with MD simulations. Most of non-polarizable force fields used in the studies reviewed in this study considered several different strategies for calculating the atomic charges used for each IL constituting cation or anion. The methods based on the fitting of the electrostatic potential in the vicinity of a molecule (ESP), or restrained electrostatic potential (RESP), and the method ESP but using a grid base (CHelpG) are the ones most common applied methods (being the latter the most considered in the studies reported in this work). Nevertheless, is has been also applied the Blöchl method[69,123,124], which derives the partial charges under bulk conditions, by fitting the system expressed in multipole moments. In this way, the method allows the charge distribution of an IL in the liquid phase assigning the partial charges and showing its great capacity to obtained reduced charges in dense systems (liquid phase) and in periodic boundary conditions[33,124]. Chaban and co-workers[44], on other hand, determined a charge scaling factor that matches experimental properties of ILs. It was also shown that its application in non-polarizable force field will improve its quality and the prediction of ILs' properties. In a recent work, Zhang and Maginn[61], derived atomic charges using several different strategies and compared the calculated results for several properties with experimental data, being able to conclude that the consideration of charges resulting from a fitting of the charges in a crystal phase yielded quite good static and dynamic properties, and therefore consisting in a simple and reliable methodology.

Despite all the efforts made in the field of MD simulations, it is possible to realize (especially in the case of viscosity) that a lot of improvements need to be made. Along with technology improvements, it is important to highlight that a straight line between experimental and theoretical procedures must exist. Experimentally, caution is needed in the purification of ILs in order to minimize

impurities that affect the determination of their properties. The latter, constitutes a problem for the simulations since, without available accurate experimental data, it is quite difficult to calibrate computational strategies (*e.g.* force fields) for the calculation of properties of ILs.

Table 2.1.2 - Accuracy of MD simulations for calculating structural and thermodynamic properties of ILs with respect to available experimental results.

Calculated Property	Comparison to Experimental Results
Density	Very Good
Melting Point	Good
Enthalpy of Vaporization	? [a]
Viscosity	Overestimated
Diffusion Coefficients	Underestimated
Surface Tension	Overestimated/Underestimated
Structural Data	Very Good Complement of Information Retrieved from Experimental Work

[a]Hard to be defined due to several different experimental results determined by different authors for the same IL.

References

(1) Cramer, C. J. Essentials of Computational Chemistry - Theories and Models, 2004.

(2) Marx, D.; Hutter, J. *Ab Initio Molecular Dynamics: Basic Theory and Advanced Method*; Cambrigde University Press, 2009.

(3) Parr, R.; Yang, W. *Density-Functional Theory of Atoms and Molecules*; Oxford University Press: New York, 1989.

(4) Møller, C.; Plesset, M. S. *Phys. Rev.*, **1934**, *46*, 618–622.

(5) Krishnan, R.; Pople, J. A. *Int. J. Quantum Chem.*, **1978**, *14*, 91–100.

(6) Purvis, G. D. *J. Chem. Phys.*, **1982**, *76*, 1910–1918.

(7) Maurice, D.; Head-Gordon, M. *Mol. Phys.*, **1999**, *96*, 1533–1541.

(8) Kirchner, B. *Topics in Current Chemistry*; Meijere, V. B. A. De; Kessler, K. N. H. H.; Ley, J. L. S. V; Schreiber, M. O. S.; Vogel, B. M. T. P.; Wong, F. V. H., Eds.; Springer: Germany, 2009.

(9) Gubbins, K. E.; Moore, J. D. *Ind. Eng. Chem. Res.*, **2010**, *49*, 3026–3046.

(10) Jensen, F. *Introduction to Computational Chemistry*; John Wiley and Sons Ltd: Chichester, West Sussex, England, 2007.

(11) Metropolis, N.; Rosenbluth, A. W.; Rosenbluth, M. N.; Teller, A. H.; Teller, E. *J. Chem. Phys.*, **1953**, *21*, 1087–1092.

(12) Kroese, D. P.; Taimre, T.; Botev, Z. I. Handbook of Monte Carlo Methods, 2011.

(13) Haile, J. M. Molecular Dynamics Simulation: Elementary Methods, 1992.

(14) Shah, J. K.; Brennecke, J. F.; Maginn, E. J. *Green Chem.*, **2002**, *4*, 112–118.

(15) Bresme, F.; Alejandre, J. *J. Chem. Phys.*, **2003**, *118*, 4134–4139.

(16) Shi, W.; Maginn, E. J. *J. Phys. Chem. B*, **2008**, *112*, 2045–2055.

(17) Liu, J.; Bowman, T. L.; Elliott, J. R. *Ind. Eng. Chem. Res.*, **1994**, *33*, 957–964.

(18) Andersen, H. C. *J. Chem. Phys.*, **1980**, *72*, 2384–2393.

(19) Nose, S. *J. Chem. Phys.*, **1984**, *81*, 511–519.

(20) Hoover, W. G. *Phys. Rev. A*, **1985**, *31*, 1695–1697.

(21) Berendsen, H. J. C.; Postma, J. P. M.; Vangunsteren, W. F.; Dinola, A.; Haak, J. R. *J. Chem. Phys.*, **1984**, *81*, 3684–3690.

(22) Parrinello, M.; Rahman, A. *J. Appl. Phys.*, **1981**, *52*, 7182–7190.

(23) Parrinello, M.; Rahman, A.; Vashishta, P. *Phys. Rev. Lett.*, **1983**, *50*, 1073–1076.

(24) Bhargava, B. L.; Balasubramanian, S. *J. Chem. Phys.*, **2007**, *127*, 114510–114516.

(25) Buhl, M.; Chaumont, A.; Schurhammer, R.; Wipff, G. *J. Phys. Chem. B*, **2005**, *109*, 18591–18599.

(26) Kossmann, S.; Thar, J.; Kirchner, B.; Hunt, P. A.; Welton, T. *J. Chem. Phys.*, **2006**, *124*, 174506–174518.

(27) Schmidt, J.; Krekeler, C.; Dommert, F.; Zhao, Y.; Berger, R.; Delle Site, L.; Holm, C. *J. Phys. Chem. B*, **2010**, *114*, 6150–6155.

(28) Schroeder, C.; Steinhauser, O. *J. Chem. Phys.*, **2008**, *128*, 224503–224510.

(29) Brooks, B. R.; Brooks, C. L.; Mackerell, A. D.; Nilsson, L.; Petrella, R. J.; Roux, B.; Won, Y.; Archontis, G.; Bartels, C.; Boresch, S.; Caflisch, A.; Caves, L.; Cui, Q.; Dinner, A. R.; Feig, M.; Fischer, S.; Gao, J.; Hodoscek, M.; Im, W.; Kuczera, K.; Lazaridis, T.; Ma, J.; Ovchinnikov, V.; Paci, E.; Pastor, R. W.; Post, C. B.; Pu, J. Z.; Schaefer, M.; Tidor, B.; Venable, R. M.; Woodcock, H. L.; Wu, X.; Yang, W.; York, D. M.; Karplus, M. *J. Comput. Chem.*, **2009**, *30*, 1545–1614.

(30) Jorgensen, W. L.; Tirado-Rives, J. *J. Am. Chem. Soc.*, **1988**, *110*, 1657–1666.

(31) Jorgensen, W. L.; Maxwell, D. S.; Tirado-Rives, J. *J. Am. Chem. Soc.*, **1996**, *118*, 11225–11236.

(32) Cornell, W. D.; Cieplak, P.; Bayly, C. I.; Gould, I. R.; Merz, K. M.; Ferguson, D. M.; Spellmeyer, D. C.; Fox, T.; Caldwell, J. W.; Kollman, P. A. *J. Am. Chem. Soc.*, **1995**, *117*, 5179–5197.

(33) Dommert, F.; Wendler, K.; Berger, R.; Delle Site, L.; Holm, C. *Chemphyschem*, **2012**, *13*, 1625–1637.

(34) McCarty, J.; Lyubimov, I. Y.; Guenza, M. G. *J. Phys. Chem. B*, **2009**, *113*, 11876–11886.

(35) Velinova, M.; Sengupta, D.; Tadjer, A. V; Marrink, S.-J. *Langmuir*, **2011**, *27*, 14071–14077.

(36) Chen, Y.; Zimmerman, J.; Krivtsov, A.; McDowell, D. L. *Int. J. Eng. Sci.*, **2011**, *49*, 1337–1349.

(37) Alavi, S.; Thompson, D. L. *J. Phys. Chem. B*, **2005**, *109*, 18127–18134.

(38) Alavi, S.; Thompson, D. L. *J. Chem. Phys.*, **2005**, *122*, 154704–154715.

(39) Aparicio, S.; Alcalde, R.; Garcia, B.; Leal, J. M. *J. Phys. Chem. B*, **2009**, *113*, 5593–5606.

(40) Borodin, O. *J. Phys. Chem. B*, **2009**, *113*, 11463–11478.

(41) Bandrés, I.; Alcalde, R.; Lafuente, C.; Atilhan, M.; Aparicio, S. *J. Phys. Chem. B*, **2011**, *115*, 12499–12513.

(42) Canongia Lopes, J. N.; Deschamps, J.; Pádua, A. A. H. *J. Phys. Chem. B*, **2004**, *108*, 2038–2047.

(43) Canongia Lopes, J. N.; Padua, A. A. H. *J. Phys. Chem. B*, **2006**, *110*, 19586–19592.

(44) Chaban, V. V; Voroshylova, I. V; Kalugin, O. N. *Phys. Chem. Chem. Phys.*, **2011**, *13*, 7910–7920.

(45) Ghatee, M. H.; Zolghadr, A. R.; Moosavi, F.; Ansari, Y. *J. Chem. Phys.*, **2012**, *136*, 124706–124720.

(46) Heggen, B.; Zhao, W.; Leroy, F.; Dammers, A. J.; Mueller-Plathe, F. *J. Phys. Chem. B*, **2010**, *114*, 6954–6961.

(47) Jayaraman, S.; Maginn, E. J. *J. Chem. Phys.*, **2007**, *127*, 214504–214518.

(48) Kelkar, M. S.; Maginn, E. J. *J. Phys. Chem. B*, **2007**, *111*, 9424–9427.

(49) Klähn, M.; Seduraman, A.; Wu, P. *J. Phys. Chem. B*, **2008**, *112*, 13849–13861.

(50) Koddermann, T.; Paschek, D.; Ludwig, R. *Chemphyschem*, **2007**, *8*, 2464–2470.

(51) Liu, H.; Maginn, E.; Visser, A. E.; Bridges, N. J.; Fox, E. B. *Ind. Eng. Chem. Res.*, **2012**, *51*, 7242–7254.

(52) Margulis, C. J.; Stern, H. A.; Berne, B. J. *J. Phys. Chem. B*, **2002**, *106*, 12017–12021.

(53) Pensado, A. S.; Gomes, M. F. C.; Canongia Lopes, J. N.; Malfreyt, P.; Padua, A. A. H. *Phys. Chem. Chem. Phys.*, **2011**, *13*, 13518–13526.

(54) Prado, C. E. R.; Freitas, L. C. G. *J. Mol. Struct.*, **2007**, *847*, 93–100.

(55) Santos, L. M. N. B. F.; Lopes, J. N. C.; Coutinho, J. A. P.; Esperanca, J. M. S. S.; Gomes, L. R.; Marrucho, I. M.; Rebelo, L. P. N. *J. Am. Chem. Soc.*, **2007**, *129*, 284–285.

(56) Shimizu, K.; Tariq, M.; Costa Gomes, M. F.; Rebelo, L. P. N.; Canongia Lopes, J. N. *J. Phys. Chem. B*, **2010**, *114*, 5831–5834.

(57) Shimizu, K.; Almantariotis, D.; Costa Gomes, M. F.; Pádua, A. A. H.; Canongia Lopes, J. N. *J. Phys. Chem. B*, **2010**, *114*, 3592–3600.

(58) Van-Oanh, N.-T.; Houriez, C.; Rousseau, B. *Phys. Chem. Chem. Phys.*, **2010**, *12*, 930–936.

(59) Yan, T. Y.; Burnham, C. J.; Del Popolo, M. G.; Voth, G. A. *J. Phys. Chem. B*, **2004**, *108*, 11877–11881.

(60) Zhang, Y.; Maginn, E. J. *J. Chem. Phys.*, **2012**, *136*, 144116–144128.

(61) Zhang, Y.; Maginn, E. J. *J. Phys. Chem. B*, **2012**, *116*, 10036–10048.

(62) Zhao, W.; Leroy, F.; Balasubramanian, S.; Mueller-Plathe, F. *J. Phys. Chem. B*, **2008**, *112*, 8129–8133.

(63) Zhong, X.; Liu, Z.; Cao, D. *J. Phys. Chem. B*, **2011**, *115*, 10027–10040.

(64) Singh, U. C.; Kollman, P. A. *J. Comput. Chem.*, **1984**, *5*, 129–145.

(65) Besler, B. H.; Merz, K. M.; Kollman, P. A. *J. Comput. Chem.*, **1990**, *11*, 431–439.

(66) Breneman, C. M.; Wiberg, K. B. *J. Comput. Chem.*, **1990**, *11*, 361–373.

(67) Bayly, C. I.; Cieplak, P.; Cornell, W.; Kollman, P. A. *J. Phys. Chem.*, **1993**, *97*, 10269–10280.

(68) Jacquemin, J.; Husson, P.; Mayer, V.; Cibulka, I. *J. Chem. Eng. Data*, **2007**, *52*, 2204–2211.

(69) Blöchl, P. E. *J. Chem. Phys.*, **1995**, *103*, 7422–7428.

(70) Ionic Liquids Database - (IL Thermo). NIST Standard Reference Database #47. , 2006.

(71) Maginn, E. J. *Acc. Chem. Res.*, **2007**, *40*, 1200–1207.

(72) Aparicio, S.; Atilhan, M.; Karadas, F. *Ind. Eng. Chem. Res.*, **2010**, *49*, 9580–9595.

(73) Paduszyński, K.; Domańska, U. *Ind. Eng. Chem. Res.*, **2011**, *51*, 591–604.

(74) Maginn, E. J. *J. Phys. Condens. Matter*, **2009**, *21*, 373101–373118.

(75) Wang, J.; Wolf, R. M.; Caldwell, J. W.; Kollman, P. A.; Case, D. A. *J. Comput. Chem.*, **2004**, *25*, 1157–1174.

(76) Suarez, P. A. Z.; Einloft, S.; Dullius, J. E. L.; de Souza, R. F.; Dupont, J. *J. Chim. Phys. Physico-Chimie Biol.*, **1998**, *95*, 1626–1639.

(77) Krummen, M.; Wasserscheid, P.; Gmehling, J. *J. Chem. Eng. Data*, **2002**, *47*, 1411–1417.

(78) Kandil, M. E.; Marsh, K. N.; Goodwin, A. R. H. *J. Chem. Eng. Data*, **2007**, *52*, 2382–2387.

(79) Soriano, A. N.; Doma Jr, B. T.; Li, M.-H. *J. Chem. Thermodyn.*, **2009**, *41*, 301–307.

(80) Shiflett, M. B.; Kasprzak, D. J.; Junk, C. P.; Yokozeki, A. *J. Chem. Thermodyn.*, **2008**, *40*, 25–31.

(81) Holbrey, J. D.; Reichert, W. M.; Nieuwenhuyzen, M.; Johnston, S.; Seddon, K. R.; Rogers, R. D. *Chem. Commun.*, **2003**, 1636–1637.

(82) Holbrey, J. D.; Seddon, K. R. *J. Chem. Soc. Trans.*, **1999**, 2133–2139.

(83) Weingaertner, H. *Angew. Chemie-International Ed.*, **2008**, *47*, 654–670.

(84) Yoo, S.; Zeng, X. C.; Xantheas, S. S. *J. Chem. Phys.*, **2009**, *130*, 221102–221104.

(85) Luo, S.-N.; Strachan, A.; Swift, D. C. *J. Chem. Phys.*, **2004**, *120*, 11640–11649.

(86) Frenkel, D.; Ladd, A. J. C. *J. Chem. Phys.*, **1984**, *81*, 3188–3193.

(87) Grochola, G. *J. Chem. Phys.*, **2004**, *120*, 2122–2126.

(88) Hoover, W. G.; Ree, F. H. *J. Chem. Phys.*, **1967**, *47*, 4873–4878.

(89) Domańska, U.; Mazurowska, L. *Fluid Phase Equilib.*, **2004**, *221*, 73–82.

(90) Dibrov, S. M.; Kochi, J. K. *Acta Crystallogr. C.*, **2006**, *62*, 19–21.

(91) Reichert, W. M.; Holbrey, J. D.; Swatloski, R. P.; Gutowski, K. E.; Visser, A. E.; Nieuwenhuyzen, M.; Seddon, K. R.; Rogers, R. D. *Cryst. Growth Des.*, **2007**, *7*, 1106–1114.

(92) Esperanca, J.; Lopes, J. N. C.; Tariq, M.; Santos, L.; Magee, J. W.; Rebelo, L. P. N. *J. Chem. Eng. Data*, **2010**, *55*, 3–12.

(93) Earle, M. J.; Esperanca, J. M.; Gilea, M. A.; Lopes, J. N.; Rebelo, L. P.; Magee, J. W.; Seddon, K. R.; Widegren, J. A. *Nature*, **2006**, *439*, 831–834.

(94) Rebelo, L. P. N.; Lopes, J. N. C.; Esperanca, J.; Filipe, E. *J. Phys. Chem. B*, **2005**, *109*, 6040–6043.

(95) Paulechka, Y. U.; Zaitsau, D. H.; Kabo, G. J.; Strechan, A. A. *Thermochim. Acta*, **2005**, *439*, 158–160.

(96) Rocha, M. A. A.; Bastos, M.; Coutinho, J. A. P.; Santos, L. M. N. B. F. *J. Chem. Thermodyn.*, **2012**, *53*, 140–143.

(97) Liu, Z. P.; Huang, S. P.; Wang, W. C. *J. Phys. Chem. B*, **2004**, *108*, 12978–12989.

(98) Liu, Z. P.; Wu, X. P.; Wang, W. C. *Phys. Chem. Chem. Phys.*, **2006**, *8*, 1096–1104.

(99) Deyko, A.; Lovelock, K. R. J.; Corfield, J.-A.; Taylor, A. W.; Gooden, P. N.; Villar-Garcia, I. J.; Licence, P.; Jones, R. G.; Krasovskiy, V. G.; Chernikova, E. A.; Kustov, L. M. *Phys. Chem. Chem. Phys.*, **2009**, *11*, 8544–8555.

(100) Emel'yanenko, V. N.; Verevkin, S. P.; Heintz, A. *Thermochim. Acta*, **2011**, *514*, 28–31.

(101) Deyko, A.; Hessey, S. G.; Licence, P.; Chernikova, E. A.; Krasovskiy, V. G.; Kustov, L. M.; Jones, R. G. *Phys. Chem. Chem. Phys.*, **2012**, *14*, 3181–3193.

(102) Hess, B. *J. Chem. Phys.*, **2002**, *116*, 209–217.

(103) Tenney, C. M.; Maginn, E. J. *J. Chem. Phys.*, **2010**, *132*, 014103–014111.

(104) Evans, D. J.; Morriss, G. P. Statistical Mechanics of Nonequilibrium Liquids, 1990.

(105) Kelkar, M. S.; Maginn, E. J. *J. Phys. Chem. B*, **2007**, *111*, 4867–4876.

(106) Tokuda, H.; Hayamizu, K.; Ishii, K.; Abu Bin Hasan Susan, M.; Watanabe, M. *J. Phys. Chem. B*, **2004**, *108*, 16593–16600.

(107) Tokuda, H.; Tsuzuki, S.; Susan, M.; Hayamizu, K.; Watanabe, M. *J. Phys. Chem. B*, **2006**, *110*, 19593–19600.

(108) Tokuda, H.; Hayamizu, K.; Ishii, K.; Susan, M.; Watanabe, M. *J. Phys. Chem. B*, **2005**, *109*, 6103–6110.

(109) Tokuda, H.; Ishii, K.; Susan, M. A. B. H.; Tsuzuki, S.; Hayamizu, K.; Watanabe, M. *J. Phys. Chem. B*, **2006**, *110*, 2833–2839.

(110) Tariq, M.; Freire, M. G.; Saramago, B.; Coutinho, J. A. P.; Canongia Lopes, J. N.; Rebelo, L. P. N. *Chem. Soc. Rev.*, **2012**, *41*, 829–868.

(111) Freire, M. G.; Carvalho, P. J.; Gardas, R. L.; Marrucho, I. M.; Santos, L.; Coutinho, J. A. P. *J. Phys. Chem. B*, **2008**, *112*, 1604–1610.

(112) Bhargava, B. L.; Balasubramanian, S. *J. Chem. Phys.*, **2007**, *127*, 114510–114516.

(113) Tarmyshov, K.; Muller-Plathe, F. **2005**, *45*, 1943–1952.

(114) Lindahl, E.; Hess, B.; van der Spoel, D. **2001**, *7*, 306–317.

(115) Gonzalez-Melchor, M.; Bresme, F.; Alejandre, J. *J. Chem. Phys.*, **2005**, *122*, 104710–104718.

(116) Chaban, V. *Phys. Chem. Chem. Phys.*, **2011**, *13*, 16055–16062.

(117) Canongia Lopes, J. N.; Costa Gomes, M. F.; Pádua, A. A. H. *J. Phys. Chem. B*, **2006**, *110*, 16816–16818.

(118) Thar, J.; Brehm, M.; Seitsonen, A. P.; Kirchner, B. *J. Phys. Chem. B*, **2009**, *113*, 15129–15132.

(119) Paredes, X.; Fernández, J.; Pádua, A. A. H.; Malfreyt, P.; Malberg, F.; Kirchner, B.; Pensado, A. S. *J. Phys. Chem. B*, **2012**, *116*, 14159–14170.

(120) Tome, L. I. N.; Jorge, M.; Gomes, J. R. B.; Coutinho, J. A. P. *J. Phys. Chem. B*, **2012**, *116*, 1831–1842.

(121) Tomé, L. I. N.; Pinho, S. P.; Jorge, M.; Gomes, J. R. B.; Coutinho, J. A. P. *J. Phys. Chem. B*, **2013**, *117*, 6116–6128.

(122) Cadena, C.; Maginn, E. J. *J. Phys. Chem. B*, **2006**, *110*, 18026–18039.

(123) Schmidt, J.; Krekeler, C.; Dommert, F.; Zhao, Y. Y.; Berger, R.; Delle Site, L.; Holm, C. *J. Phys. Chem. B*, **2010**, *114*, 6150–6155.

(124) Dommert, F.; Schmidt, J.; Krekeler, C.; Zhao, Y. Y.; Berger, R.; Delle Site, L.; Holm, C. *J. Mol. Liq.*, **2010**, *152*, 2–8.

3. Developed work

In this chapter there will be described studies performed with the aim of characterizing binary mixtures relevant for the production of fuels and biofuels, namely, ILs and thiophene/benzene, ILs and water/ethanol, and glucose with ILs/water. The aim was the evaluation of the role and the magnitude of the interactions established by the ILs with the other solvents in the mentioned mixtures and, simultaneously, the assessment of the ability of ILs to act as extracting solvents.

The approach here adopted is primarily based on the use of MD simulations for the assessment of the quality of the force fields and also for a more comprehensive understanding of the behavior of the systems under study, of the resulting data on the properties measured and calculated, and finally on phase equilibria of these mixtures. Accordingly, for benchmarking the calculations, experimental measurements of different properties were performed, which are going to be detailed in the following chapters along with the results of the MD simulations.

3.1. Evaluation of the Liquid-Liquid Equilibria of Ionic Liquid-Based Systems for Fuel Improvement

Adapted from:

Marta L. S. Batista, Luciana I. N. Tomé, Catarina M. S. S. Neves, Eugénio M. Rocha, José R. B. Gomes, João A. P. Coutinho

The Origin of the LCST on the Liquid–Liquid Equilibrium of Thiophene with Ionic Liquids

J. Phys. Chem. B, 5985-5992, 116, 2012

Marta L. S. Batista, Luciana I. N. Tomé, Catarina M. S. S. Neves, José R. B. Gomes, João A. P. Coutinho

Characterization of Systems of Thiophene and Benzene with Ionic Liquids

J. Mol. Liquids, 26-31, 192, 2014

My direct contribution:
I declare that I have carried out the experimental measurements of density and viscosity, the theoretical modeling in order to obtain excess volumes and viscosity deviations and the molecular dynamics simulations (with the estimation of density, enthalpy of vaporization and radial distribution functions for the systems under study). For these studies I had the supervision of my advisors, Prof. Dr. João A. P. Coutinho and Dr. José R. B. Gomes, and the contribution of Dr. Catarina Neves, Dr. Luciana Tomé and Dr. Eugénio Rocha.

Motivation

As mentioned previously, in the petroleum industry strict regulatory restrictions require the reduction of the level of sulfur-based compounds and aliphatic-aromatic compounds content in fuels, aiming at the minimization of their environmental impact.[1,2] Several aspects involving the desulfurization processes have been addressed in a previous chapter (Chapter 1.3). Nonetheless, the separation of aromatic from aliphatic hydrocarbons is also a challenging task because these compounds have similar boiling points, which lead to the formation of different types of azeotropes that cannot be overcome by conventional distillation processes.[1]

Extractive distillation, azeotropic distillation and liquid-liquid extraction have been used for the removal of those compounds, being the latest the most applied technique.[3] Several extractive solvents have been tested for the extraction of toluene, benzene, ethylbenzene or xylene from their mixtures with, for instance, hexane, heptane and octane. However, the selection of the solvent to be applied in the extraction process is a crucial step, affecting the efficiency of the separation. Until recently, conventional organic compounds, such as sulfolane, were typically used as extraction solvents, but environmental issues and additional operation costs associated to their regeneration have led to the search for adequate alternatives.[1]

Presenting unique properties, ILs have been identified as advantageous substitutes for conventional solvents in separation processes, as well as in oxidative and extractive desulfurization processes. These advantages are essentially related to their higher density when compared to common organic solvents, low solubility in aliphatic hydrocarbons and high capacity to dissolve aromatic compounds (and consequently high selectivity in the separation of aromatics from aliphatic compounds).[3–6]

In order to properly design novel separation processes and to choose the most suitable IL to perform the extraction, the knowledge of the thermophysical properties of ILs, including density and viscosity, as well as, the Liquid-Liquid Equilibrium (LLE) phase diagrams of their binary and ternary mixtures, is required.[7,8]

Studies devoted to the separation of aromatic from aliphatic compounds using ILs composed by different combinations of cations and anions have been extensively reported and reviewed by Ferreira *et al.*[5,6]. These reviews provide a complete compilation of LLE data for binary and ternary systems involving ILs, aromatic and aliphatic hydrocarbons. Moreover, several studies on the application of ILs for the removal of sulfur compounds have also been reported in the literature and a large number of ILs including imidazolium[9–12], pyridinium[13–15], Lewis and Brønsted acid and oxidative ILs[16,17] have been tested as extractive solvents. Anions such as bis[(trifluoromethyl)sulfonyl]imide, hexafluorophosphate,

tetrafluoroborate, ethylsulfate, acetate and thiocyanate have been considered, with the latest showing higher selectivity. [2,18–20] While measuring the binary[7,18,19,21,22] and ternary[1,2,23,24] phase diagrams of systems composed of sulfur compounds and ILs, different LLE behaviors were observed, showing a dependence with the anion of the IL. In most cases, these systems present the common upper critical solution temperature (UCST) with their mutual miscibilities increasing with temperature, for example, 1-butyl-3-methylimidazolium bis[(trifluoromethyl)sulfonyl]imide, [BMIM][NTf_2], with thiophene, but some systems display a lower critical solution temperature (LCST), for instance, 1-butyl-3-methylimidazolium thiocyanate, [BMIM][SCN], with thiophene and benzene.

Aiming at the characterization of the systems under consideration, the densities and viscosities of the binary systems of [BMIM][SCN] and [BMIM][NTf_2] with thiophene, and of [BMIM][SCN], [BMIM][CF_3SO_3] and [EMIM][NTf_2] with benzene, were measured at atmospheric pressure and in the temperature range 298.15 K to 328.15 K. Attained measured data were further used to calculate excess molar volumes and viscosity deviations, which were correlated by the Redlich-Kister polynomial expansion, with a purpose of supplying additional information regarding the type and strength of the interactions established by ILs.

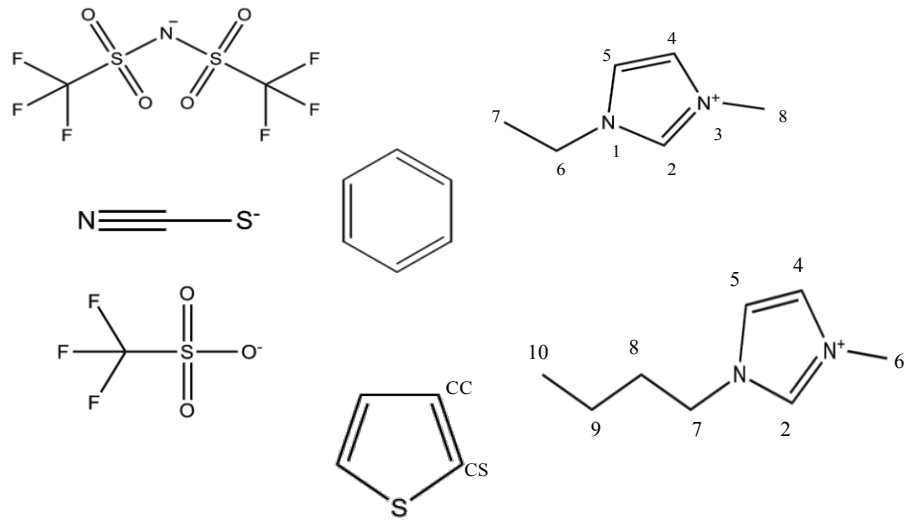

Figure 3.1.1 - Chemical structures of the aromatic compounds and of the cations and anions of the ILs studied in this work, and corresponding atom labelling.

Furthermore, a special attention was devoted to the systems composed of thiophene and two ILs, namely, [BMIM][SCN] and [BMIM][NTf_2]. A phase diagram of the binary system composed of [BMIM][NTf_2] and thiophene was measured, after verifying its absence in the literature. Aiming at inferring the differences in the interactions between these two ILs and thiophene presenting UCST and

LCST behavior, respectively, ^{1}H and ^{13}C NMR spectroscopy experiments were performed, from which chemical shift deviations ($\Delta\delta$) were then analysed. Moreover, MD simulations were performed for the two systems and RDFs were used to investigate the interactions between the constituting species. Analysing the atomic local organization, a comprehensive picture of the molecular interactions was drawn, explaining the formation of the two types of phase diagrams (UCST and LCST).

Methodology

Experimental Section

Materials

Thiophene was supplied by Acros with a purity of 99.5 wt% and benzene by Merck with a purity of 99.7 wt%. The ILs used in this work were supplied by IoLiTec and comprise 1-butyl-3-methylimidazolium bis(trifluoromethylsulfonyl)imide, [BMIM][NTf_2], mass fraction purity > 99 %, 1-butyl-3-methylimidazolium thiocyanate, [BMIM][SCN], mass fraction purity > 98 %, 1-butyl-3-methylimidazolium triflate, [BMIM][CF_3SO_3], mass fraction purity > 99 %, and 1-ethyl-3-methylimidazolium bis(trifluoromethylsulfonyl)imide, [EMIM][NTf_2], mass fraction purity > 99 %. Their purities were further confirmed by ^{1}H, ^{13}C and ^{19}F (whenever applicable) NMR. In order to reduce the amount of volatile impurities, all samples were dried for at least 48 h under vacuum (10^{-3} Pa) at room temperature before use. After the drying procedure, the water content in the samples range from 208 to 324 ppm, measured by Karl–Fischer titration. The molecular structures of the compounds studied in this work are presented in Figure 3.1.1.

Experimental Procedure

Mixtures of thiophene with [BMIM][SCN] and [BMIM][NTf_2], as well as mixtures of benzene with [BMIM][SCN], [BMIM][CF_3SO_3] and [EMIM][NTf_2] were prepared gravimetrically with an uncertainty of $\pm 10^{-5}$ g. In order to homogenize the mixtures, they were constantly stirred for at least 24 h at room temperature.

Liquid-liquid equilibrium

The phase diagram for the binary system of thiophene and [BMIM][NTf_2] was measured by turbidimetry. The onset of the liquid-liquid immiscibility (cloud point temperature) was determined by visual observation of the phase demixing (turbidity followed by phase separation). Mixtures were introduced in Pyrex-glass capillaries with a stirrer, and the concentration range studied, $0.15 < x_{IL} < 0.17$, was restricted by experimental limitations (the visual method was not applicable at mole fractions of the IL out of this range, since the experimental setup is limited either for low or high temperatures) and was established on the basis of titrations carried out prior to the experiments. The sealed capillaries were placed in a thermostated bath and were kept under continuous stirring during the whole experiment.

Solutions presenting two phases at ambient temperature were heated into the homogeneous region and then slowly cooled until visual detection of phase demixing. The cooling rate was about 10 ºC for each 30 minutes. The temperature at which the first sign of turbidity appeared upon cooling was taken as the temperature of the liquid-liquid phase transition. For monophasic solutions at room temperature, the heating process was suppressed. The temperature was controlled with a calibrated U1252A, Handheld Digital Multimeter 4.5-digit associated to a calibrated Pt100 temperature sensor immersed in the thermostating liquid. This equipment has an uncertainty of ±0.01 K. Three consistent measurements were carried out for each solution.

Density and viscosity

Density and viscosity measurements were performed at atmospheric pressure and in the temperature range (283.15 to 333.15) K, using an automated SVM 3000 Anton Paar rotational Stabinger viscometer-densimeter. The SVM 3000 Anton Paar rotational Stabinger viscometer-densimeter uses Peltier elements for fast and efficient thermostatization.

The viscosimeter is based on a tube filled with the sample in which floats a hollow measuring rotor. Due to its low density, the rotor is centred in the heavier liquid by buoyancy forces. Consequently, a measuring gap is formed between the rotor and the tube. The rotor is forced to rotate by shear stresses in the liquid and is guided axially by a built-in magnet, which interacts with a soft iron ring. The rotating magnetic field delivers the speed signal and deduces eddy currents in the surrounding copper casing. These eddy currents are proportional to the speed of the rotor and exert a retarding torque on the rotor. Two different torques influence the speed of the measuring rotor, and at the equilibrium, the two torques are equal and the viscosity can be traced back to a single speed measurement.

The obtained uncertainty in temperature is within ±0.02 K. The relative uncertainty for the dynamic viscosity is ±0.35 % and the absolute uncertainty for density is ±0.5 $kg.m^{-3}$.

NMR measurements

For the NMR analysis, it was used a stem coaxial capillary tube with acetone-*d6* that was inserted into 5 mm NMR tubes with the different mixtures composed of IL and thiophene. The ^{1}H and ^{13}C spectra were recorded using a Bruker Avance 300 spectrometer operating at 300.13 MHz and 75.47 MHz, respectively.

Thermodynamic models - Mixture Properties

The excess thermodynamic properties are employed to describe the deviation in behavior of a mixture from the ideality, giving important information concerning the nature of the molecular interactions present in binary systems. The excess molar volumes, V^E, were estimated from the measured densities according to the following equation,

$$V^E = \sum x_i M_i \left(\frac{1}{\rho_{mix}} - \frac{1}{\rho_i}\right) \tag{3.1.1}$$

where x_i, M_i, and ρ_i are, respectively, the molar fraction, molar mass, and density for each component of the binary system, and ρ_{mix} is the density of the mixture.

Similarly, viscosity deviations were estimated from measured viscosities according to the following equation,

$$\Delta ln(\eta) = ln(\eta_{mix}) - \sum x_i ln(\eta_i) \tag{3.1.2}$$

where x_i and η_i are, respectively, the molar fraction and viscosity for each component that composes the binary system, and η_{mix} is the viscosity of the mixture.

The excess volumes and viscosity deviations were correlated at each temperature with a Redlich-Kister polynomial expansion as shown in the following equation,

$$Q = x_{aromatic}\, x_{IL} \sum_{j=0}^{m} A_j (x_{aromatic} - x_{IL})^j \tag{3.1.3}$$

where Q represents either the excess molar volume V^E, or the viscosity deviations $\Delta\eta$, $x_{aromatic}$ corresponds to the molar fraction of benzene or thiophene, x_{IL} is the molar fraction for all ILs studied, A_j are the correlation parameters, and m is the degree of the polynomial expansion. For our systems, a second-order polynomial was found to be adequate level for V^E, and a first-order polynomial for $\Delta\eta$.

Computational details

The interactions between ILs and thiophene were investigated by molecular dynamics (MD) simulations using the GROMACS 4.5.4 computer code[27]. The simulations were carried out in the constant temperature and constant pressure (NPT) ensemble. Constant temperature (298.15 K) was maintained by using the Nosé-Hoover[28,29] thermostat while the pressure (1 bar) was maintained by using the Parrinelo-Rahman[30] barostat. All systems (each one considering 80 pairs of IL ions and 40 molecules of thiophene) were prepared by randomly placing all species in the simulation boxes. In each of these simulations, the equations of motion were integrated with the Verlet-Leapfrog[31] algorithm and a time step of 2 fs. A 10 000 step energy minimization was performed and the systems were equilibrated (at least 150 000 steps). Furthermore, quite long simulations were carried out, with 25 000 000 steps for [BMIM][SCN] with thiophene and 50 000 000 steps for [BMIM][NTf_2] with thiophene (50 ns). The intermolecular interaction energy between pairs of neighboring atoms was calculated using a Lennard-Jones potential to describe dispersion/repulsion forces and the point-charge Coulomb potential was used for electrostatic interactions. Long-range electrostatic interactions were accounted for using the particle-mesh Ewald[32] method with a cutoff of 1.0 nm for the real-space part of the interactions. A cutoff radius of 1.2 nm was used for the Lennard-Jones potential, and long-range dispersion interactions were added to both energy and pressure. Rigid constraints were enforced on all bonds lengths.

The all-atom force field for [BMIM][NTf_2] considered the parameters from the works of Cadena and Maginn[33] and of Canongia Lopes and Pádua[34] for the cation and for the anion, respectively, as in the work of Tomé *et al.*[35]. The charges for the cation and the anion were recalculated with the CHelpG scheme[36] using an optimized geometry for the BMIM-NTf_2 dimer in the gas-phase[35]. The calculations considered the B3LYP/6-311+G(d) approach as included in the Gaussian 03 code[37], *i.e.*, using the same computational strategy employed by Morrow and Maginn[38] for the [BMIM][PF_6] ionic liquid. The total CHelpG charges on the cation and anion are +0.797 *e* and -0.797 *e*, respectively. The estimation of partial charges for an IL from calculations of an ion pair in vacuum can be a problematic issue as addressed and discussed in other works.[39,40] Nevertheless, it has been demonstrated that models with total charges on each ion in the range ±0.7 to 0.8 yield a better description of both structural and (most noticeably) dynamic properties of ionic liquids.[40–42] Furthermore, we have also performed calculations considering a pair of ions surrounded by other IL ions and no significant differences were found in the results obtained. The full set of atomic charges is supplied in Appendix A (Tables A.1 to A.3).

The calculated density and enthalpy of vaporization for [BMIM][NTf_2] are 1486 $kg \cdot m^{-3}$ and 131.74 $kJ \cdot mol^{-1}$, respectively, which compare well with the range of experimental results, *i.e.*, [1429;

1437.4] $kg \cdot m^{-3}$ (taken from Huddleston *et al.*[43] and measured in this work, at Table 3.1.1) and 134-155 $kJ \cdot mol^{-1}$ [44], respectively. In the case of [BMIM][SCN], we have used the all-atom force field from the work of Cadena and Maginn[33] for the cation and we have adapted standard GROMOS potential parameters for the anion (additional details given in Tables A.4 to A.7 in Appendix A). The CHelpG total charges on the cation and anion are +0.791 *e* and -0.791 *e*, respectively. These values were also calculated using a B3LYP/6-311+G(d) optimized geometry (minimum energy from several initial configurations) for the BMIM-SCN dimer in the gas-phase. It was quite encouraging to see that the charges above are close to those computed for the central cation/anion pair in clusters containing several [BMIM][SCN] pairs; for instance, the mean values calculated for the central dimer in different clusters containing 13 BMIM-SCN pairs are +0.804 ± 0.020 *e* and -0.804 ± 0.020 *e* for the cation and the anion, respectively. The calculated density and enthalpy of vaporization for [BMIM][SCN] are 1082 $kg \cdot m^{-3}$ and 123.0 $kJ \cdot mol^{-1}$, respectively. Very encouraging, these results, compare well with the range of experimental results for density and enthalpy of vaporization, *i.e.*, [1070; 1069.8] $kg \cdot m^{-3}$ (taken form Domanska and Laskowska[45] and measured in this work) and 114.5 - 148 $kJ \cdot mol^{-1}$ [46], respectively. The spatial distribution functions (SDF), which can be briefly described as 3D representations of the probability of finding a particle at a certain position, were calculated using a bin width of 0.05 nm.

Results and Discussion

Liquid-liquid equilibrium (LLE)

Figure 3.1.2 shows the liquid-liquid phase diagram measured in this work for the binary system of thiophene and [BMIM][NTf_2] (the experimental numerical results are supplied at Appendix A, Table A.8), along with the liquid-liquid phase diagrams of mixtures of [BMIM][SCN], and [BMIM][CF_3SO_3] with thiophene, taken from literature[18,19]. Two distinct types of phase behavior are observed, with ([BMIM][NTf_2]+thiophene) presenting the UCST-type of liquid-liquid phase diagram and the two other systems displaying the LCST behavior.

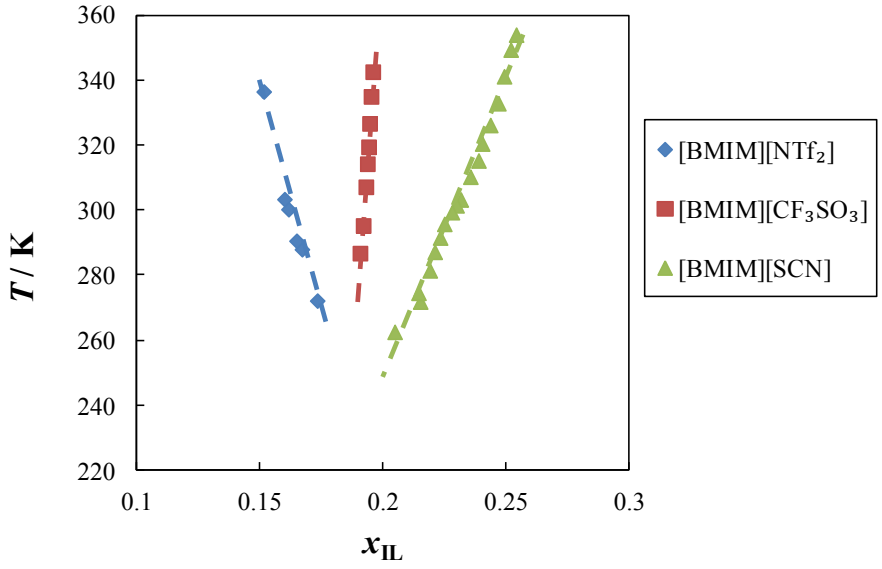

Figure 3.1.2 - Liquid-liquid phase diagrams for [BMIM][NTf_2] (measured in this work), [BMIM][SCN][18] and [BMIM][CF_3SO_3][19] with thiophene. Dashed lines are guides to the eye.

Densities and viscosities (ρ, η)

The experimental data for the density, ρ, and viscosity, η, obtained in this work are compiled in Tables 3.1.1 and 3.1.2. For all studied systems, the density presents a linear dependence with temperature, whereas the viscosity presents the expected exponential dependence, in the entire range of compositions. The values of both properties decrease with the increase of temperature and aromatic compound concentration, with the pure IL presenting the highest values for these properties (Appendix A – Figures A.1, A.2 and A.4). The exception is the system of thiophene with [BMIM][SCN], for which the density decreases with the increasing of the concentration of the IL. In the latter case, densities of the mixtures are higher than that of the pure IL (Figure A.3 in Appendix A).

Table 3.1.1 - Experimental density as function of temperature for pure ionic liquids, thiophene, benzene and for their mixtures, in different mole fractions and at atmospheric pressure.

[BMIM][SCN] + Thiophene

	T / K			
x_{IL}	298.15	308.15	318.15	328.15
	ρ / g·cm^{-3} [a]			
1.000	1.070	1.064	1.058	1.052
0.897	1.073	1.067	1.061	1.055
0.857	1.075	1.068	1.062	1.056
0.754	1.077	1.070	1.064	1.058
0.390	1.082	1.075	1.068	1.061
0.299	1.084	1.076	1.069	1.061
0.000	1.059	1.047	1.034	1.022

[BMIM][NTf_2] + Thiophene

	T / K			
x_{IL}	298.15	308.15	318.15	328.15
	ρ / g·cm^{-3}			
1.000	1.437	1.428	1.418	1.409
0.911	1.429	1.420	1.410	1.401
0.724	1.406	1.396	1.386	1.376
0.664	1.397	1.387	1.377	1.368
0.439	1.369	1.359	1.349	1.339
0.230	1.308	1.298	1.287	1.277
0.000	1.059	1.047	1.034	1.022

[BMIM][SCN] + Benzene

	T / K			
x_{IL}	298.15	308.15	318.15	328.15
	ρ / g·cm^{-3}			
1.0000	1.072	1.066	1.060	1.054
0.7666	1.053	1.046	1.040	1.034
0.7420	1.050	1.044	1.038	1.031
0.6081	1.036	1.029	1.023	1.017
0.4906	1.019	1.012	1.005	0.999
0.0000	0.874	0.863	0.852	0.841

[BMIM][CF_3SO_3] + Benzene

	T / K			
x_{IL}	298.15	308.15	318.15	328.15
	ρ / g·cm^{-3}			
1.000	1.300	1.292	1.284	1.276
0.878	1.280	1.272	1.264	1.256
0.696	1.246	1.237	1.229	1.221

0.647	1.232	1.224	1.216	1.208
0.427	1.169	1.160	1.152	1.143
0.000	0.874	0.863	0.852	0.841

[EMIM][NTf$_2$] + Benzene

	T / K			
x_{IL}	298.15	308.15	318.15	328.15
	ρ / g·cm^{-3}			
1.000	1.519	1.509	1.499	1.489
0.865	1.490	1.480	1.469	1.460
0.661	1.431	1.421	1.411	1.401
0.529	1.381	1.371	1.360	1.350
0.508	1.373	1.363	1.352	1.342
0.000	0.874	0.863	0.852	0.841

[a] Standard uncertainties u are $u(T) = 0.02$ K, $u(p) = 10$ kPa, and the combined expanded uncertainty U_c is $U_c(\rho) = 0.5$ kg·m^{-3}, with an expanded uncertainty at the 0.95 confidence level (k ~ 2).

Table 3.1.2 - Experimental viscosity data as function of temperature for pure ionic liquids, thiophene, and benzene, and also for their mixtures, in different mole fractions and at atmospheric pressure.

[BMIM][SCN] + Thiophene				
	T / K			
x_{IL}	298.15	308.15	318.15	328.15
	η / mPa·s[a)]			
1.000	57.396	37.358	25.801	18.697
0.897	47.236	31.408	22.072	16.222
0.857	42.880	28.748	20.364	15.071
0.754	31.952	22.025	15.962	12.024
0.390	13.355	9.937	7.672	6.103
0.299	9.926	7.566	5.959	4.834
0.000	0.655	0.585	0.525	0.470
[BMIM][NTf_2] + Thiophene				
	T / K			
x_{IL}	298.15	308.15	318.15	328.15
	η / mPa·s			
1.000	51.320	34.434	24.353	17.981
0.911	42.625	29.035	20.805	15.528
0.724	26.615	18.817	13.903	10.658
0.664	23.223	16.584	12.367	9.545
0.439	14.725	10.949	8.449	6.721
0.230	6.861	5.347	4.288	3.525
0.000	0.655	0.585	0.525	0.470
[BMIM][SCN] + Benzene				
	T / K			
x_{IL}	298.15	308.15	318.15	328.15
	η / mPa·s			
1.0000	62.810	40.562	27.836	20.086
0.7666	32.980	22.508	16.197	12.192
0.7420	30.691	21.072	15.231	11.518
0.6081	20.092	14.292	10.641	8.250
0.4906	12.511	9.269	7.157	5.650
0.0000	0.605	0.527	0.466	0.363
[BMIM][CF_3SO_3] + Benzene				
	T / K			
x_{IL}	298.15	308.15	318.15	328.15
	η / mPa·s			
1.000	87.964	56.429	38.308	27.254

0.878	64.295	42.193	29.228	21.168
0.696	37.168	25.406	18.233	13.621
0.647	32.799	22.579	16.331	12.299
0.533	19.811	14.218	10.644	8.200
0.427	12.622	9.370	7.215	5.715
0.000	0.605	0.527	0.466	0.363

[EMIM][NTf$_2$] + Benzene

	T / K			
x_{IL}	298.15	308.15	318.15	328.15
	η / mPa·s			
1.000	33.001	23.663	17.693	13.679
0.865	25.188	18.438	14.017	10.930
0.661	15.638	11.755	9.107	7.258
0.529	11.405	8.654	6.803	5.503
0.508	10.402	7.979	6.314	5.159
0.000	0.605	0.527	0.466	0.363

a) standard uncertainties u are $u(T)$ = 0.02 K, $u(p)$ = 10 kPa, and the combined expanded uncertainty U_c is $U_c(\rho)$ = 0.35 %, with an expanded uncertainty at the 0.95 confidence level (k ~ 2).

Excess molar volumes (V^E) and viscosity deviations ($\Delta\eta$)

The estimated excess molar volumes, V^E, and viscosity deviations, $\Delta\ln(\eta)$, of the binary systems composed by the ILs and benzene or ILs and thiophene are depicted in Figures 3.1.3 to 3.1.6. The corresponding data are provided in Appendix A (Tables A.9 and A.10). The Redlich-Kister coefficients obtained in the estimation of V^E and $\Delta\ln(\eta)$ are compiled in Tables 3.1.3 and 3.1.4. In general, the Redlich-Kister polynomial expansion correlates successfully the data of V^E and $\Delta\ln(\eta)$, providing a good description of the solution behavior of all the binary systems studied.

Negative excess molar volumes are observed for all considered mixtures, in the entire range of composition. The same temperature dependence – a decrease of V^E with the increase of temperature – is also observed for all systems, as shown in Figure 3.1.3 for mixtures of [BMIM][SCN] with benzene. The negative values of V^E are indicative of favorable interactions between both aromatic compounds and the ILs. Differences in the magnitude of V^E values can be related to several effects, such as the size and structure of the species and the type/strength of the interactions present in the mixture. The first factor influences the effective packing of

the solute/solvent molecules, hindering or promoting specific and oriented interactions, while the type or strength of the interactions depends on the nature of the compounds. Both benzene and thiophene possess an aromatic ring with delocalized π-electrons being, thus, able to establish π - π interactions with the imidazolium cation of the IL. However, the lone electron pairs on the sulfur atom of thiophene confer a higher polarity to this molecule, and consequently, interactions with the IL ions are more likely to take place.

The benzene-containing systems present negative values of V^E in the entire range of compositions, and they are very similar to each other, having the maximum V^E values ranging from -2.35 to -2.85 $cm^3 \cdot mol^{-1}$, for [BMIM][SCN] and [BMIM][CF_3SO_3], respectively. Consistently, larger negative V^E values are observed for the thiophene-containing systems. The [BMIM][NTf_2]+thiophene mixtures present negative values of V^E which are larger than the values obtained for [BMIM][SCN]. That system also shows a different concentration dependency when compared to all the other systems studied, with a minimum at lower concentrations. Its V^E values are also less dependent with temperature. The different behavior of this system suggests that a different type of interactions dominates it, which is in agreement with the observed differences in the phase diagram behavior.

As illustrated in Figure 3.1.5 for the [BMIM][SCN]+thiophene mixtures, the values obtained for the $\Delta\ln(\eta)$ are positive and decrease with temperature for all the systems studied, in the entire range of compositions. As shown in Figure 3.1.6, two different behaviors are observed for the viscosity deviations. Smaller values of $\Delta\ln(\eta)$ are found for the benzene-containing mixtures, while the thiophene systems present larger values of $\Delta\ln(\eta)$. This pattern can be related to the polarity of the aromatic compound, which is higher in the case of thiophene, suggesting stronger interactions with the ILs. Slightly lower viscosity deviations are observed for the $[SCN]^-$-containing systems, suggesting that the dominant effect is the possibility to establish more points of contact, which is more probable to occur in the cases of [EMIM][NTf_2], [BMIM][NTf_2] and [BMIM][CF_3SO_3], than in the case of [BMIM][SCN].

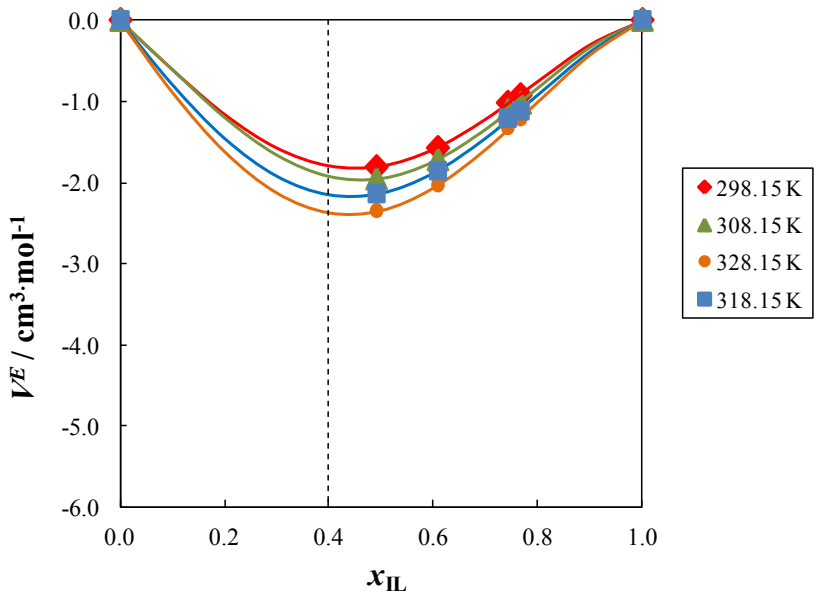

Figure 3.1.3 - Excess molar volumes as a function of the mole fraction of the IL, in mixtures of [BMIM][SCN] with benzene, at different temperatures, namely, (◆) 298.15 K, (▲) 308.15 K, (■) 318.15 K and (●) 328.15 K. Solid lines represent the corresponding correlation of Redlich-Kister. The dotted line corresponds to the limit of miscibility, where at the left is the immiscibility region.

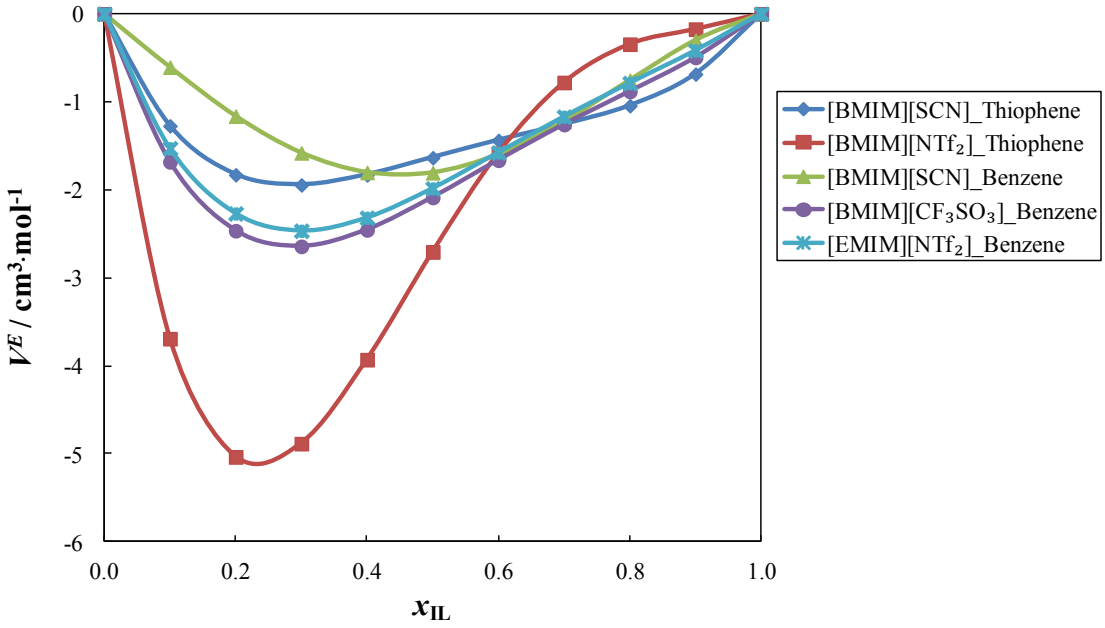

Figure 3.1.4 - Estimated excess molar volumes through Redlich-Kister's correlation as function of the mole fraction of the IL, at 298.15 K.

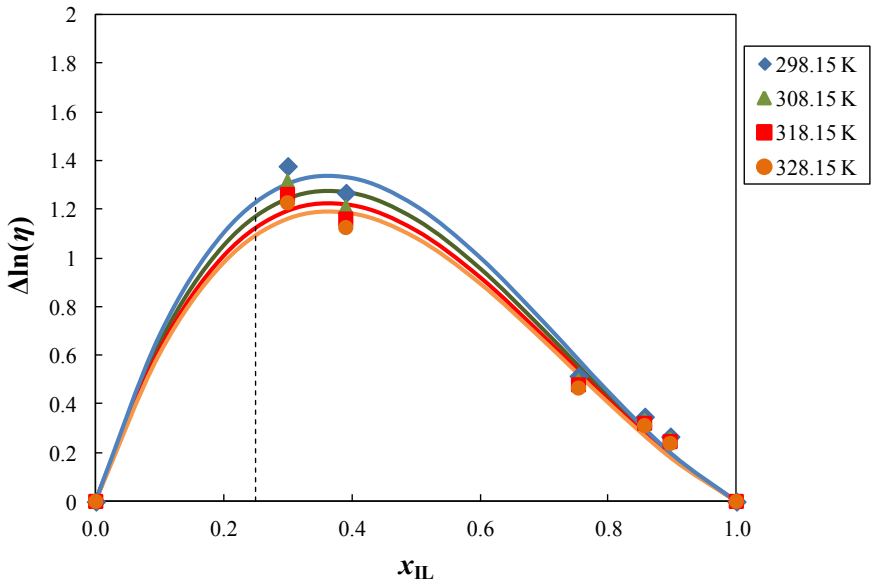

Figure 3.1.5 - Viscosity deviations as a function of the mole fraction of the IL, in mixtures of [BMIM][SCN] with thiophene, at different temperatures, namely, (◆) 298.15 K, (▲) 308.15 K, (■) 318.15 K and (●) 328.15 K. Solid lines represent the corresponding correlation of Redlich-Kister. The dotted line corresponds to the limit of miscibility, where at the left is the immiscibility region.

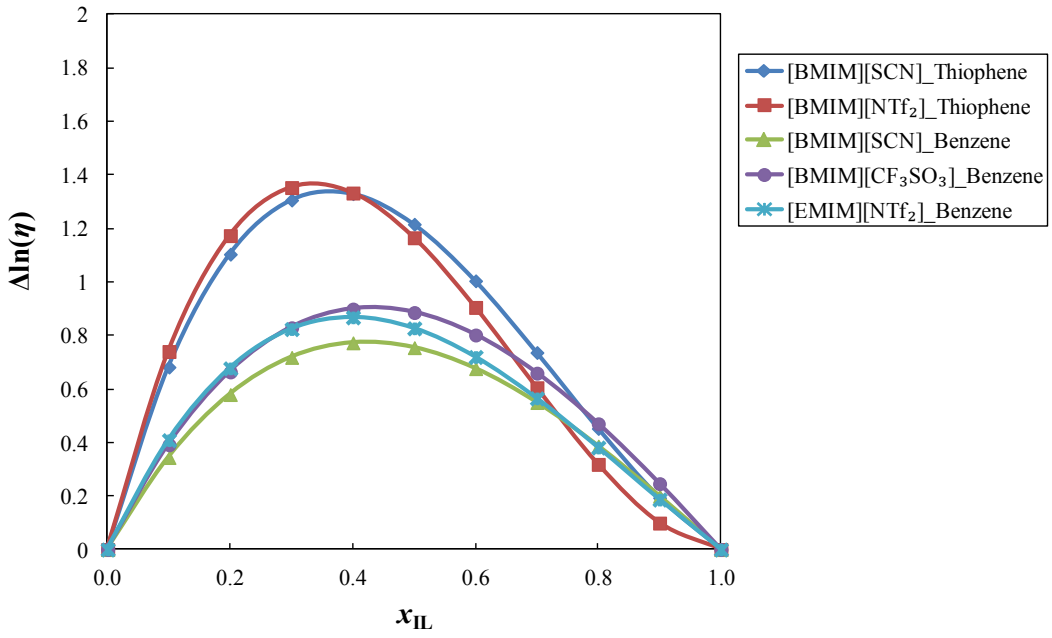

Figure 3.1.6 - Estimated viscosity deviations through Redlich-Kister's correlation as function of the mole fraction of the IL, at 298.15 K.

Table 3.1.3 - Coefficients for Redlich-Kister correlations for excess molar volume.

[BMIM][SCN] + Thiophene				
	T / K			
RK coeff	298.15	308.15	318.15	328.15
A_o	-6.541	-7.155	-7.814	-8.660
A_1	-4.087	-4.815	-5.515	-6.269
A_2	-6.778	-7.327	-7.872	-8.309
[BMIM][NTf_2] + Thiophene				
	T / K			
RK coeff	298.15	308.15	318.15	328.15
A_o	-10.825	-11.213	-11.704	-12.321
A_1	-24.428	-25.217	-25.910	-26.835
A_2	-16.642	-17.145	-17.670	-18.293
[BMIM][SCN] + Benzene				
	T / K			
RK coeff	298.15	308.15	318.15	328.15
A_o	-7.225	-7.794	-8.528	-9.358
A_1	-2.122	-1.887	-2.789	-3.175
A_2	3.414	4.073	3.117	3.303
[BMIM][CF_3SO_3] + Benzene				
	T / K			
RK coeff	298.15	308.15	318.15	328.15
A_o	-8.349	-8.851	-9.498	-10.119
A_1	-8.242	-8.515	-8.990	-9.463
A_2	-5.867	-5.692	-5.870	-6.146
[EMIM][NTf_2] + Benzene				
	T / K			
RK coeff	298.15	308.15	318.15	328.15
A_o	-7.937	-8.412	-8.936	-9.459
A_1	-7.716	-8.003	-7.921	-8.242
A_2	-4.485	-4.626	-4.079	-4.645

Table 3.1.4 - Coefficients for Redlich-Kister correlations for viscosity deviations.

[BMIM][SCN] + Thiophene				
	T / K			
RK coeff	298.15	308.15	318.15	328.15

A_o	4.862	4.639	4.458	4.331
A_1	3.391	3.219	3.078	2.990

[BMIM][NTf_2] + Thiophene

	T / K			
RK coeff	298.15	308.15	318.15	328.15
A_o	4.660	4.424	4.234	4.100
A_1	4.452	4.217	4.025	3.896

[BMIM][SCN] + Benzene

	T / K			
RK coeff	298.15	308.15	318.15	328.15
A_o	3.017	2.948	2.894	3.095
A_1	1.004	1.041	1.080	1.202

[BMIM][CF_3SO_3] + Benzene

	T / K			
RK coeff	298.15	308.15	318.15	328.15
A_o	3.542	3.411	3.301	3.480
A_1	1.010	1.053	1.080	1.285

[EMIM][NTf_2] + Benzene

	T / K			
RK coeff	298.15	308.15	318.15	328.15
A_o	3.306	3.175	2.957	3.253
A_1	1.541	1.420	1.731	1.542

Chemical shift deviations (Δδ)

^{1}H and ^{13}C NMR spectroscopies are widely used to identify the structure of compounds through differentiation of the atomic neighborhood of protons and carbons, but they may also be powerful techniques to identify favorable of non-favorable interactions among different compounds.[47,48] Each type of proton or carbon in a different structural/chemical environment has a characteristic chemical shift (δ_i), represented by a peak in the NMR spectrum. The peaks are shifted to higher or lower chemical shifts when compared to those in a reference compound depending on the type of interactions that a given carbon and/or proton suffer in a mixture. Herewith, we are interested in the differences between chemical shifts with respect to pure IL for the same atom in a compound inserted in different chemical environments, usually

designated by chemical shift deviation ($\Delta\delta$), which is defined by the following equation,

$$\Delta\delta = \delta_{mix} - \delta_{IL} \quad (3.1.4)$$

where, δ_{mix} is the ^{1}H /^{13}C chemical shift of the IL in mixtures with thiophene, and δ_{IL} is related to the chemical shift of the pure IL. In general, positive $\Delta\delta$ identify favorable interactions involving those nuclei, while negative $\Delta\delta$ values identify atoms with a lower propensity to interact. Finally, protons or carbons with $\Delta\delta$ values close to zero are not involved in significant and additional interactions.

Figures 3.1.7 and 3.1.8 represent the ^{1}H and ^{13}C chemical shift deviations ($\Delta\delta$) for mixtures composed of [BMIM][SCN] and thiophene, whereas Figures 3.1.9 and 3.1.10 depict the ^{1}H and ^{13}C chemical shift deviations ($\Delta\delta$) for mixtures of [BMIM][NTf_2] and thiophene. Detailed information regarding the individual chemical shifts is presented in Tables A.11 to A.18 in Appendix A.

For the two evaluated mixtures, the chemical shift deviations of thiophene's atoms present positive values, suggesting favorable interactions with both ILs. Additionally, in the two mixtures, the protons of the cation (which is the same for the considered ILs) present negative deviations indicating that they are not actively interacting with thiophene. Moreover, these less favorable interactions observed at the ^{1}H NMR seem more evident in the mixture containing [BMIM][NTf_2]. Therefore, there is clear evidence that the favorable interactions of thiophene occur with the anions of the IL. This is confirmed by the ^{13}C chemical shift deviations presented in Figures 3.1.8 and 3.1.10. In the former figure, it is possible to observe higher positive chemical shift deviations for the aromatic thiophene carbons along with the $[SCN]^-$ carbon, while the carbon atoms of the cation present negative chemical shift deviations. Note that, with the exception of the carbon atom of the anion, the other carbon atoms present increasing values of the chemical shift deviations with the content of IL. Figure 3.1.10 shows that, contrary to what was observed for the [BMIM][SCN], not only the carbon atoms of the anion $[NTf_2]^-$ but also some carbon atoms of the cation $[BMIM]^+$ present positive chemical shift deviations, suggesting that both ions of the IL are participating in the interaction with thiophene. Therefore, the comparison of the two considered systems suggest that the interaction of [BMIM][SCN] and thiophene is a specific interaction established by the anion, presenting higher and positive values of chemical shift deviation than the other IL that, although interacting through its ions seems to present less propensity to interact (accordingly to

the chemical shift deviation values).

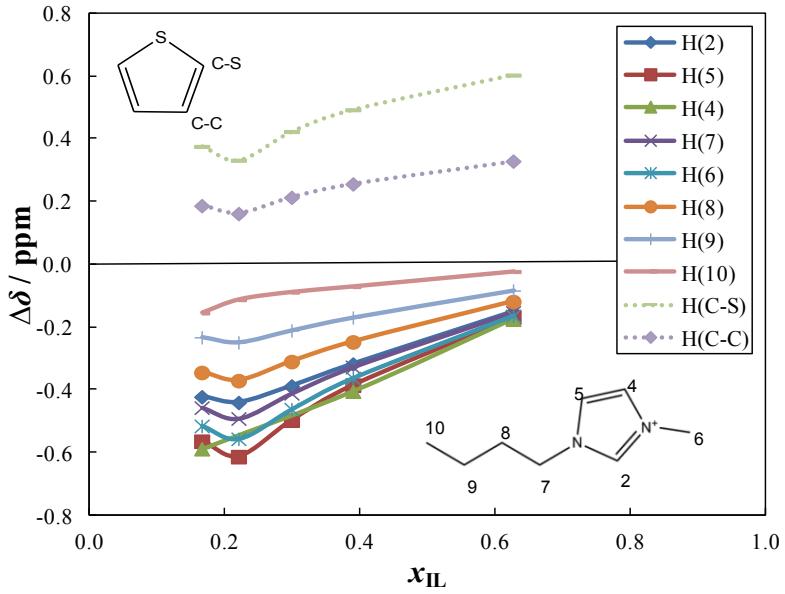

Figure 3.1.7 - ^{1}H NMR chemical shift deviations for [BMIM][SCN] in the mixture with thiophene. The dotted lines represent the hydrogen chemical shifts deviations for thiophene and full lines for the cation [BMIM]$^{+}$.

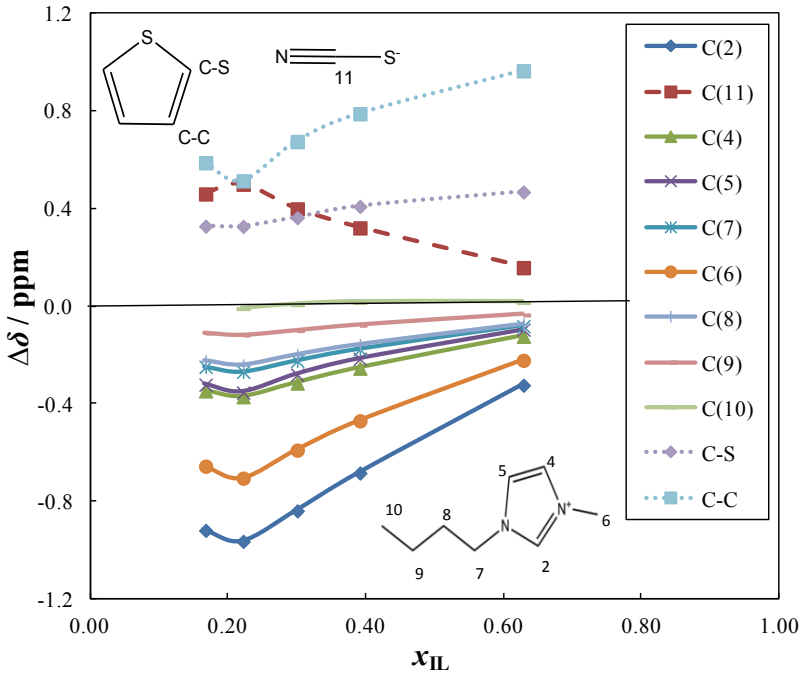

Figure 3.1.8 - ^{13}C NMR chemical shift deviations for [BMIM][SCN] in the mixture with thiophene. The dotted lines represent the carbon chemical shifts deviations for thiophene, full lines for the cation [BMIM]$^{+}$ and dashed lines for the anion [SCN]$^{-}$.

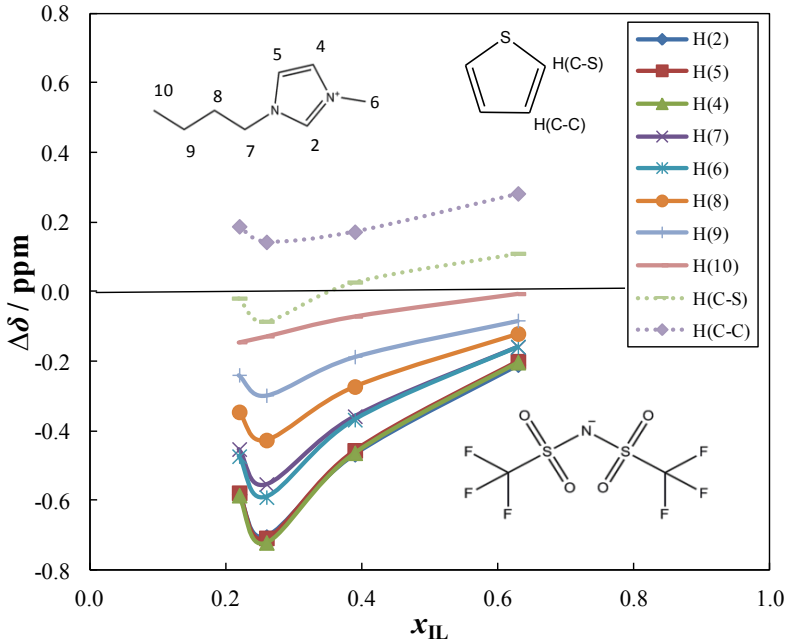

Figure 3.1.9 - ^{1}H NMR chemical shift deviations for [BMIM][NTf$_2$] in the mixture with thiophene. The dotted lines represent the hydrogen chemical shifts deviations for thiophene and full lines for the cation [BMIM]$^{+}$.

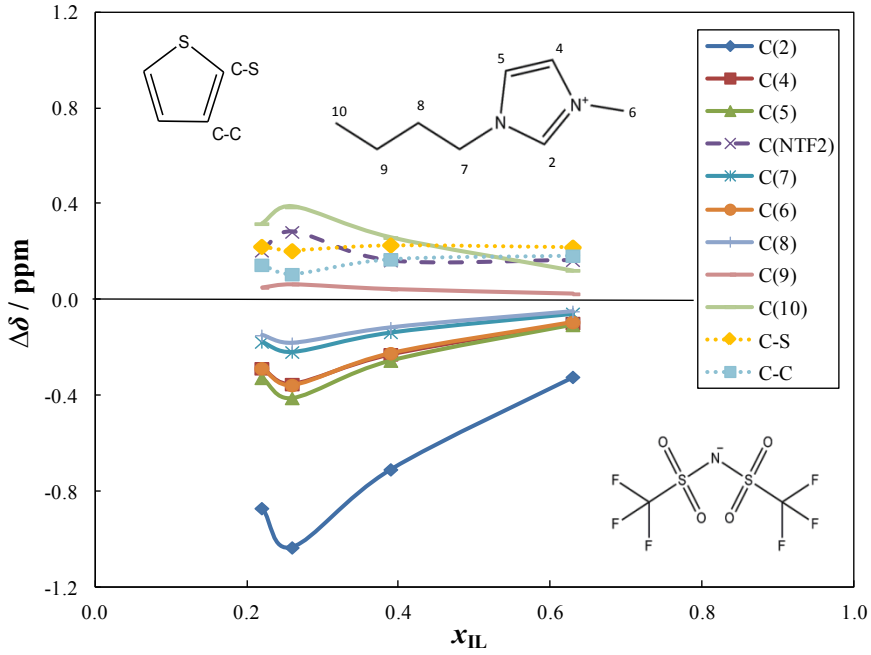

Figure 3.1.10 - ^{13}C NMR chemical shift deviations for [BMIM][NTf$_2$] in the mixture with thiophene. The dotted lines represent the carbon chemical shifts deviations for thiophene, full lines for the cation [BMIM]$^+$ and dashed lines for the anion [NTf$_2$]$^-$.

Molecular dynamics simulations

In this type of computer approach, involving a large number of atoms, the radial distribution function, *g(r)* or RDF, can be employed to describe the structural organization of a system. The calculated radial distribution functions are depicted in Figures 3.1.11 and 3.1.12, and A.5 to A.8 at Appendix A, while collected values of their peak maxima are compiled in Tables A.19 to A.32 (Appendix A).

Cation-thiophene interactions

For the cation [BMIM]$^+$ and thiophene RDFs, depicted in Figures 3.1.11.a and 3.1.12.a (and Table A.19 and A.20) for both considered systems, it is possible to observe a high intensity peak for the atom C10 (for atom numbering please refer to Figure 3.1.1), the carbon at the alkyl chain extremity, especially when considering the atom of sulfur of thiophene (Figure 3.1.11.a). However, the atoms at the ring of the imidazolium cation (except the C2), as well as,

the carbon C6 from the methyl group, show also significant probabilities to interact with thiophene. Since both ILs are composed by the same cation, it is not surprising to observe that in the case of [BMIM][NTf_2], Figure 3.1.12.a, the radial distribution functions are similar to those calculated for [BMIM][SCN], *i.e.*, the interactions involve the same atoms. However, in the case of [BMIM][NTf_2], the intensities of the S-C(cation) peaks are higher than those observed with [BMIM][SCN], suggesting that in the case of the former IL, interactions establish by $[BMIM]^+$ and thiophene are more likely to occur.

RDFs showing interactions established by the cation $[BMIM]^+$ with the carbon atoms of thiophene, at the two considered systems are depicted at Figures A.5 and A.6, Appendix A. Corresponding collected values for their peak maxima are compiled at Tables A.23 to A.26.

Anion-thiophene interactions

The RDFs calculated for the interactions involving the $[SCN]^-$ and $[NTf_2]^-$ anions and thiophene are displayed in Figures 3.1.11.b and 3.1.12.b (Tables A.21 and A.22), respectively. Figure 3.1.11.b shows that the sulfur atom of thiocyanate has higher probability to surround the carbon atoms of thiophene (the CS and CC carbons) than to surround the sulfur atom, with peak intensity maxima of 1.26 for CS and 1.08 / 1.11 double peak corresponding to CC atoms. Additionally, it is demonstrated that for the C and N atoms of $[SCN]^-$ there is no visible peak intensity maxima (Figure A.7, and Tables A.27 to A.28 in Appendix A) suggesting that S atoms are pointing towards the thiophene carbon atoms while the former atoms are rotating in a conical shape oriented outwards the thiophene ring. For systems composed of [BMIM][NTf_2] and thiophene, the RDFs for atoms of $[NTf_2]^-$ and thiophene show peaks that occur at large distances, with *g(r)* values being close to or lower than unity (Figures 3.1.12.b, A.8 and Tables A.29 to A.32, in Appendix A). Nevertheless, in the case of the carbon from the anion (note that the anion $[NTf_2]^-$ is here considered to possess a centre of symmetry at the central nitrogen atom), in Figure 3.1.12.b, there is significant interaction between this atom and thiophene constituting atoms, which is represented by a double peak (with very similar RDFs shapes for the three different atomic species of thiophene). In summary, the RDFs show a more specific orientation of the anion $[SCN]^-$ around the thiophene moiety, with a preferable orientation towards to CS and CC atoms of thiophene suggesting more favorable interactions with the latter atoms than with the sulfur atom of thiophene. These specific orientations are not evident in the case of the $[NTf_2]^-$ anion for which similar RDFs were obtained for all the interactions with thiophene.

MD simulations corroborated the results obtained experimentally, since it was possible to identify a specific interaction between $[SCN]^-$ and thiophene through a well-defined spatial orientation, which is thus responsible for the LCST behavior. For the system composed of [BMIM][NTf_2] and thiophene the common UCST behavior is observed, which is a typical behavior of systems with weaker or less favorable interactions.

The results here reported confirm the suggestion of Revelli *et al.*[20] that a specific interaction is present in the binary system [BMIM][SCN]+thiophene; nevertheless, the molecular picture gathered from this work is completely different from that initially proposed. They suggested that four thiophene molecules in a pseudo tetrahedron spatial orientation were surrounding the $[SCN]^-$ anion with its sulfur atom pointing towards the anion. This suggestion is not compatible with the results here reported. In fact, both NMR and MD observations presented and discussed above show that the anion $[SCN]^-$ preferentially surrounds the CS and CC carbons of thiophene, as shown in Figures 3.1.13 to 3.1.15. As it can be seen from the spatial distribution functions (SDFs), there is clear preference for $[SCN]^-$ constituting atoms to be located closer to CC and CS atoms than to S atom of thiophene (Figure 3.1.13), while in the case of the $[NTf_2]^-$ species any signs of preferential orientation are unseen (Figure 3.1.14). The same figures show that the location of the cation, which is the same in the two ILs considered in this work, is similar.

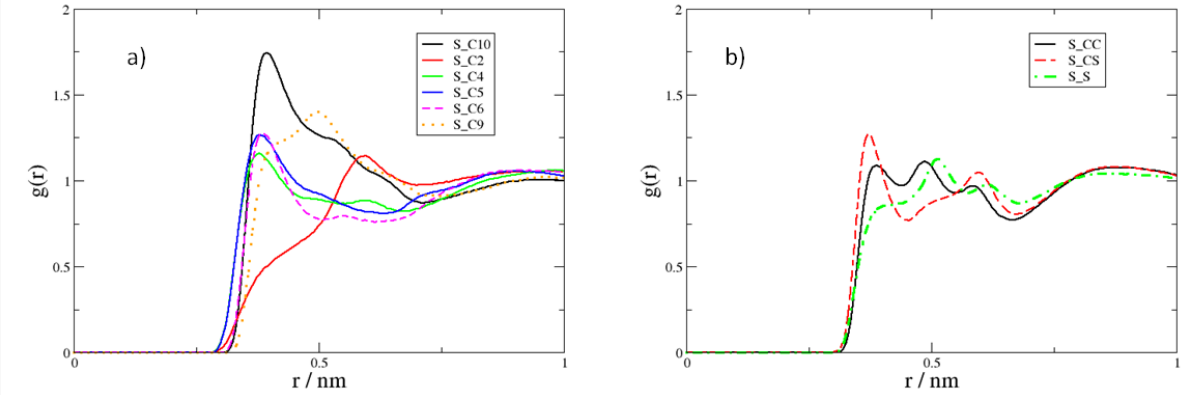

Figure 3.1.11 - Radial distribution functions of selected carbon atoms of a) $[BMIM]^+$ around the S atom of thiophene, b) thiophene atoms around the S atom of $[SCN]^-$, in the system [BMIM][SCN]+thiophene.

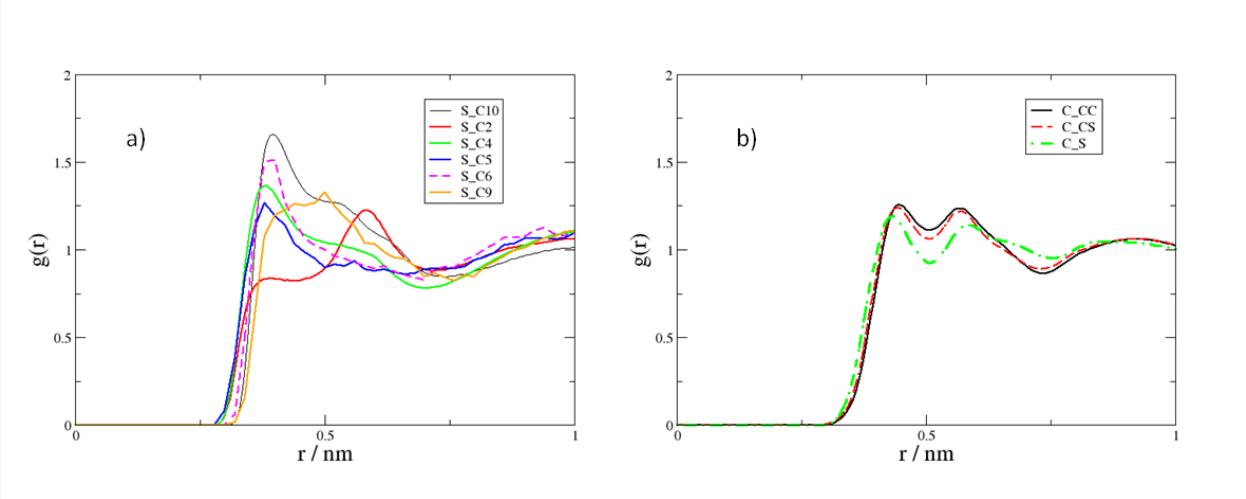

Figure 3.1.12 - Radial distribution functions of a) selected carbon atoms of $[BMIM]^+$ around the S atom of thiophene and b) thiophene atoms around the C1 atom of $[NTf_2]^-$, in the system $[BMIM][NTf_2]$+thiophene.

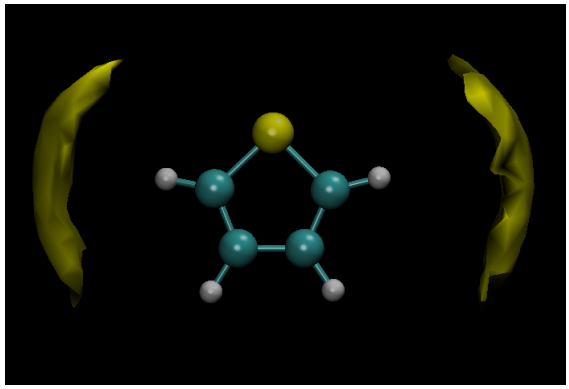

(a)

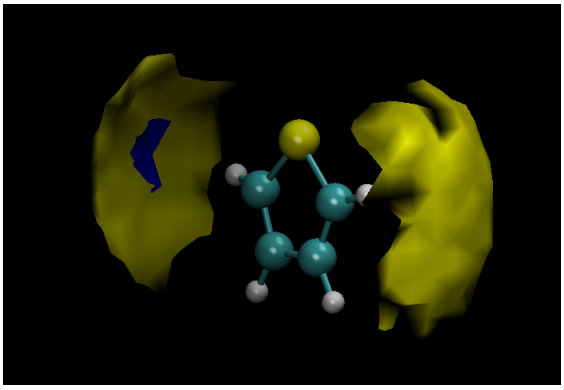

(b)

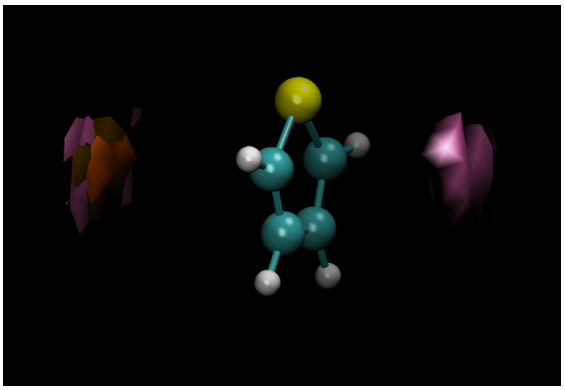

(c)

Figure 3.1.13 - Spatial distribution functions (SDF) for $[SCN]^-$ (a, b) and $[BMIM]^+$ (c) around thiophene from MD simulation of the [BMIM][SCN]+thiophene mixture. Yellow and blue regions represent SDF (isovalue = 25 particle·nm^{-3}) for S and N atoms from the IL anion, respectively. Mauve, orange and brown regions represent SDF (isovalue = 32 particle·nm^{-3}) for C10, C4 and C6 atoms of the IL cation, respectively.

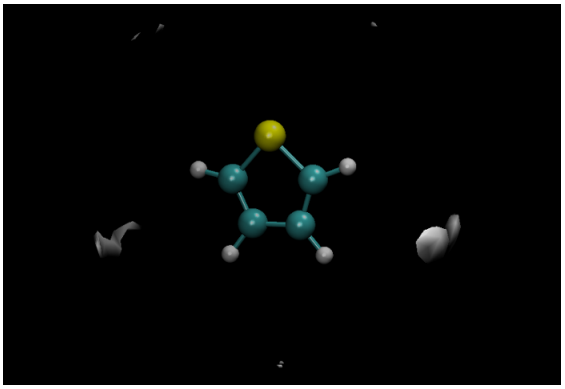

(a)

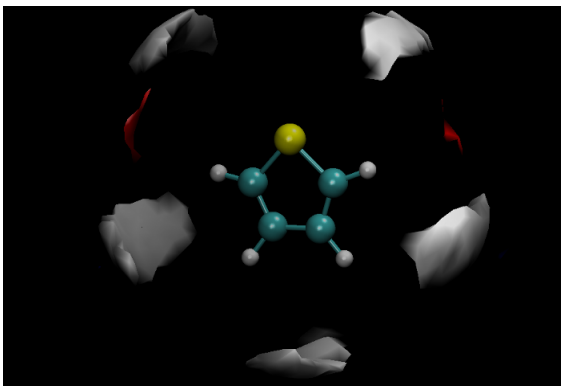

(b)

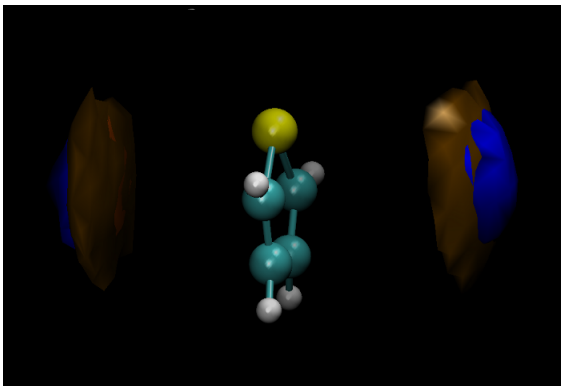

(c)

Figure 3.1.14 - Spatial distribution functions (SDF) for $[NTf_2]^-$ (a, b) and $[BMIM]^+$ (c) around thiophene from MD simulation of the [BMIM][NTf_2]+thiophene mixture. White and red regions represent SDF (isovalues are 25 particle·nm^{-3} in a and 20 particle·nm^{-3} in b, respectively) for C and O atoms from the IL anion, respectively. Blue, orange and brown regions represent SDFs (isovalue = 32 particle·nm^{-3}) for N2, C4 and C6 atoms of the IL cation, respectively.

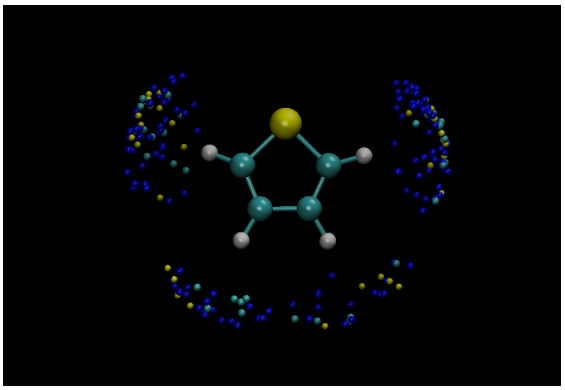

(a)

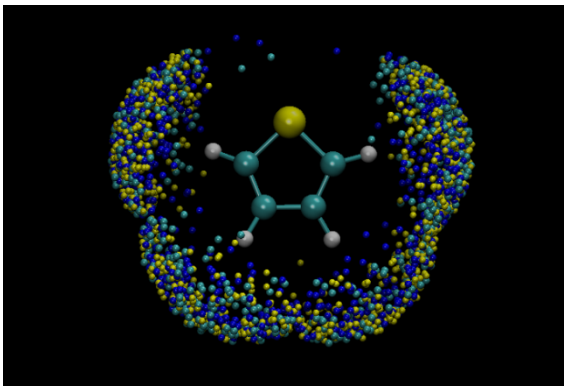

(b)

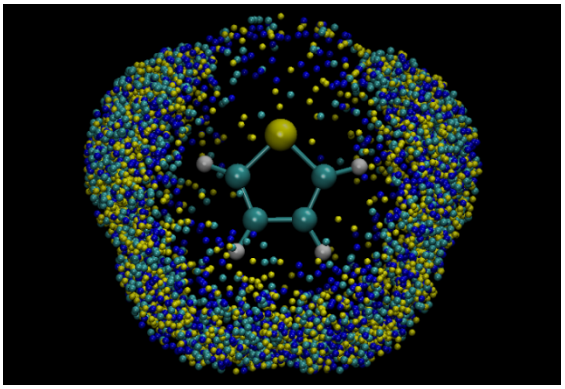

(c)

Figure 3.1.15 - Atomic hits for SCN-constituting atoms at a) 2.5 Å, b) 3.0 Å and c) 3.5 Å around thiophene from MD simulation of the [BMIM][SCN]+thiophene mixture. Yellow, blue, cyan and white spheres stand for sulfur, nitrogen, carbon and hydrogen atoms, respectively.

Conclusions

In this work, experimental density and viscosity data were measured and are reported for systems of benzene with [BMIM][SCN], [BMIM][CF_3SO_3] and [EMIM][NTf_2], and for systems of thiophene with [BMIM][SCN] and [BMIM][NTf_2]. The obtained experimental densities and viscosities were further applied to calculate the excess molar volumes and the viscosity deviations of the systems in consideration. These data were successfully correlated with the Redlich-Kister polynomial expansion, providing a good description of the solution behavior. Additionally, aiming at providing a better understanding of different liquid-liquid equilibrium behaviors, systems of [BMIM][SCN] and [BMIM][NTf_2] with thiophene were investigated by measuring ^{1}H and ^{13}C NMR spectra for further estimation of the chemical shift deviations and also through MD simulations for understanding the molecular basis of the phenomena observed. For the binary system of thiophene with [BMIM][NTf_2] the liquid-liquid equilibrium phase diagram was also determined and is here reported.

The results obtained show a decrease of the density and of the viscosity with temperature and with the increase of benzene or thiophene content in the mixture, with the pure ILs presenting the highest values. A distinct behavior is found for the system of thiophene with [BMIM][SCN], for which the density decreases with the increase of x_{IL}. All the mixtures studied show negative values of V^E and positive $\Delta\ln(\eta)$, in all range of compositions. Factors such as the size, structure and nature of the compounds present in the mixtures, and the consequent type and strength of the interactions established were considered to explain the behavior of the solutions. A different behavior is observed for the [BMIM][NTf_2]+thiophene mixtures, with larger values of V^E and with a different concentration dependency than for all the other systems studied that correlates well with the observed differences in the phase diagram behavior.

Furthermore, from the chemical shift deviations results, high positive chemical shift deviations for the carbon atom from the anion $[SCN]^-$ obtained for the [BMIM][SCN] systems, suggested the presence of a specific interaction between the IL's anion and thiophene. The MD simulations further supported this view. For [BMIM][SCN] it was possible to identify a specific spatial orientation of the sulfur atom of the anion with the thiophene's protons, which is suggested to be responsible for the LCST behavior. The interactions of thiophene with other ILs, here represented by the [BMIM][NTf_2], are of a different nature, being of a dispersive type between the cation alkyl chains and the thiophene, leading to the more common UCST type of liquid-liquid phase diagram.

References

(1) Arce, A.; Earle, M. J.; Rodriguez, H.; Seddon, K. R.; Soto, A. *Green Chem.*, **2008**, *10*, 1294–1300.

(2) Kedra-Krolik, K.; Fabrice, M.; Jaubert, J.-N. *Ind. Eng. Chem. Res.*, **2011**, *50*, 2296–2306.

(3) Meindersma, G. W.; Hansmeier, A. R.; de Haan, A. B. *Ind. Eng. Chem. Res.*, **2010**, *49*, 7530–7540.

(4) Meindersma, G. W.; Podt, A.; Klaren, M. B.; De Haan, A. B. *Chem. Eng. Commun.*, **2006**, *193*, 1384–1396.

(5) Ferreira, A. R.; Freire, M. G.; Ribeiro, J. C.; Lopes, F. M.; Crespo, J. G.; Coutinho, J. A. P. *Ind. Eng. Chem. Res.*, **2012**, *51*, 3483–3507.

(6) Ferreira, A. R.; Freire, M. G.; Ribeiro, J. C.; Lopes, F. M.; Crespo, J. G.; Coutinho, J. A. P. *Ind. Eng. Chem. Res.*, **2011**, *50*, 5279–5294.

(7) Domanska, U.; Zawadzki, M.; Tshibangu, M. M.; Ramjugernath, D.; Letcher, T. M. *J. Chem. Thermodyn.*, **2010**, *42*, 1180–1186.

(8) Krolikowska, M.; Karpinska, M.; Zawadzki, M. *J. Phys. Chem. B*, **2012**, *116*, 4292–4299.

(9) Alonso, L.; Arce, A.; Francisco, M.; Rodriguez, O.; Soto, A. *AIChE J.*, **2007**, *53*, 3108–3115.

(10) Mochizuki, Y.; Sugawara, K. *Energy & Fuels*, **2008**, *22*, 3303–3307.

(11) Nie, Y.; Li, C.; Sun, A.; Meng, H.; Wang, Z. *Energy & Fuels*, **2006**, *20*, 2083–2087.

(12) Królikowski, M.; Walczak, K.; Domańska, U. *J. Chem. Thermodyn.*, **2013**, *65*, 168–173.

(13) Gao, H.; Luo, M.; Xing, J.; Wu, Y.; Li, Y.; Li, W.; Liu, Q.; Liu, H. *Ind. Eng. Chem. Res.*, **2008**, *47*, 8384–8388.

(14) Holbrey, J. D.; Lopez-Martin, I.; Rothenberg, G.; Seddon, K. R.; Silvero, G.; Zheng, X. *Green Chem.*, **2008**, *10*, 87–92.

(15) Domańska, U.; Walczak, K.; Zawadzki, M. *J. Chem. Thermodyn.*, **2014**, *69*, 27–35.

(16) Bosmann, A.; Datsevich, L.; Jess, A.; Lauter, A.; Schmitz, C.; Wasserscheid, P. *Chem. Commun.*, **2001**, 2494–2495.

(17) Ko, N. H.; Lee, J. S.; Huh, E. S.; Lee, H.; Jung, K. D.; Kim, H. S.; Cheong, M. *Energy & Fuels*, **2008**, *22*, 1687–1690.

(18) Domańska, U.; Krolikowski, M.; Slesinska, K. *J. Chem. Thermodyn.*, **2009**, *41*, 1303–1311.

(19) Marciniak, A.; Karczemna, E. *Fluid Phase Equilib.*, **2011**, *307*, 160–165.

(20) Revelli, A. L.; Mutelet, F.; Jaubert, J. N. *J. Phys. Chem. B*, **2010**, *114*, 4600–4608.

(21) Domanska, U.; Krolikowski, M. *J. Chem. Thermodyn.*, **2010**, *42*, 355–362.

(22) Lachwa, J.; Szydlowski, J.; Makowska, A.; Seddon, K. R.; Esperanca, J.; Guedes, H. J. R.; Rebelo, L. P. N. *Green Chem.*, **2006**, *8*, 262–267.

(23) Francisco, M.; Arce, A.; Soto, A. *Fluid Phase Equilib.*, **2010**, *294*, 39–48.

(24) Kedra-Krolik, K.; Mutelet, F.; Moise, J.-C.; Jaubert, J.-N. *Energy & Fuels*, **2011**, *25*, 1559–1565.

(25) Neves, C.; Batista, M. L. S.; Claudio, A. F. M.; Santos, L.; Marrucho, I. M.; Freire, M. G.; Coutinho, J. A. P. *J. Chem. Eng. Data*, **2010**, *55*, 5065–5073.

(26) Neves, C. M. S. S.; Carvalho, P. J.; Freire, M. G.; Coutinho, J. A. P. *J. Chem. Thermodyn.*, **2011**, *43*, 948–957.

(27) Hess, B.; Kutzner, C.; van der Spoel, D.; Lindahl, E. *J. Chem. Theory Comput.*, **2008**, *4*, 435–447.

(28) Hoover, W. G. *Phys. Rev. A*, **1985**, *31*, 1695–1697.

(29) Nose, S. *Mol. Phys.*, **1984**, *52*, 255–268.

(30) Parrinello, M.; Rahman, A. *J. Appl. Phys.*, **1981**, *52*, 7182–7190.

(31) Hockney, R. W.; Goel, S. P.; Eastwood, J. W. *J. Comput. Phys.*, **1974**, *14*, 148–158.

(32) Essmann, U.; Perera, L.; Berkowitz, M. L.; Darden, T.; Lee, H.; Pedersen, L. G. *J. Chem. Phys.*, **1995**, *103*, 8577–8593.

(33) Cadena, C.; Maginn, E. J. *J. Phys. Chem. B*, **2006**, *110*, 18026–18039.

(34) Canongia Lopes, J. N.; Pádua, A. A. H. *J. Phys. Chem. B*, **2004**, *108*, 16893–16898.

(35) Tome, L. I. N.; Jorge, M.; Gomes, J. R. B.; Coutinho, J. A. P. *J. Phys. Chem. B*, **2012**, *116*, 1831–1842.

(36) Breneman, C. M.; Wiberg, K. B. *J. Comput. Chem.*, **1990**, *11*, 361–373.

(37) A Frisch, M. J.; A Trucks, G. W.; A Schlegel, H. B.; A Scuseria, G. E.; A Robb, M. A.; A Cheeseman, J. R.; A Montgomery Jr, J. A.; A Vreven, T.; A Kudin, K. N.; A Burant, J. C.; A

Millam, J. M.; A Iyengar, S. S.; A Tomasi, J.; A Barone, V.; A Mennucci, B.; A Cossi, M.; A Scalmani, G.; A Rega, N.; A Petersson, G. A.; A Nakatsuji, H.; A Hada, M.; A Ehara, M.; A Toyota, K.; A Fukuda, R.; A Hasegawa, J.; A Ishida, M.; A Nakajima, T.; A Honda, Y.; A Kitao, O.; A Nakai, H.; A Klene, M.; A Li, X.; A Knox, J. E.; A Hratchian, H. P.; A Cross, J. B.; A Bakken, V.; A Adamo, C.; A Jaramillo, J.; A Gomperts, R.; A Stratmann, R. E.; A Yazyev, O.; A Austin, A. J.; A Cammi, R.; A Pomelli, C.; A Ochterski, J. W.; A Ayala, P. Y.; A Morokuma, K.; A Voth, G. A.; A Salvador, P.; A Dannenberg, J. J.; A Zakrzewski, V. G.; A Dapprich, S.; A Daniels, A. D.; A Strain, M. C.; A Farkas, O.; A Malick, D. K.; A Rabuck, A. D.; A Raghavachari, K.; A Foresman, J. B.; A Ortiz, J. V; A Cui, Q.; A Baboul, A. G.; A Clifford, S.; A Cioslowski, J.; A Stefanov, B. B.; A Liu, G.; A Liashenko, A.; A Piskorz, P.; A Komaromi, I.; A Martin, R. L.; A Fox, D. J.; A Keith, T.; A Al-Laham, M. A.; A Peng, C. Y.; A Nanayakkara, A.; A Challacombe, M.; A Gill, P. M. W.; A Johnson, B.; A Chen, W.; A Wong, M. W.; A Gonzalez, C.; A Pople, J. A. *Gaussian 03, revision D.02*; Wallingford, 2004.

(38) Morrow, T. I.; Maginn, E. J. *J. Phys. Chem. B*, **2002**, *106*, 12807–12813.

(39) Logothetit, G.-E.; Ramos, J.; Economou, I. G. *J. Phys. Chem. B*, **2009**, *113*, 7211–7224.

(40) Zhong, X.; Liu, Z.; Cao, D. *J. Phys. Chem. B*, **2011**, *115*, 10027–10040.

(41) Youngs, T. G. A.; Hardacre, C. *Chem phys chem*, **2008**, *9*, 1548–1558.

(42) Wendler, K.; Zahn, S.; Dommert, F.; Berger, R.; Holm, C.; Kirchner, B.; Delle Site, L. *J. Chem. Theory Comput.*, **2011**, *7*, 3040–3044.

(43) Huddleston, J. G.; Visser, A. E.; Reichert, W. M.; Willauer, H. D.; Broker, G. A.; Rogers, R. D. *Green Chem.*, **2001**, *3*, 156–164.

(44) Esperanca, J.; Lopes, J. N. C.; Tariq, M.; Santos, L.; Magee, J. W.; Rebelo, L. P. N. *J. Chem. Eng. Data*, **2010**, *55*, 3–12.

(45) Domanska, U.; Laskowska, M. *J. Chem. Eng. Data*, **2009**, *54*, 2113–2119.

(46) Marciniak, A. *Int. J. Mol. Sci.*, **2010**, *11*, 1973–1990.

(47) Freire, M. G.; Neves, C. M. S. S.; Silva, A. M. S.; Santos, L. M. N. B. F.; Marrucho, I. M.; Rebelo, L. P. N.; Shah, J. K.; Maginn, E. J.; Coutinho, J. A. P. *J. Phys. Chem. B*, **2010**, *114*, 2004–2014.

(48) Freire, M. G.; Carvalho, P. J.; Silva, A. M. S.; Santos, L. M. N. B. F.; Rebelo, L. P. N.; Marrucho, I. M.; Coutinho, J. A. P. *J. Phys. Chem. B*, **2009**, *113*, 202–211.

3.2. Computational and Experimental Study of the Behavior of Cyano-Based Ionic Liquids in Aqueous Solutions

Adapted from:

Marta L. S. Batista, Kiki A. Kurnia, Simão P. Pinho, José R. B. Gomes, João A. P. Coutinho

Computational and Experimental Study of the Behavior of Cyano-Based Ionic Liquids

J. Phys. Chem. B, 2015, 119 (4), 1567-1578

My direct contribution:

I declare that I have carried out the experimental measurements of water activity in the facilities of Instituto Politécnico de Bragança, under supervision of Prof. Dr. Simão P. Pinho. Also, I have carried out estimation of water activity coefficient and the molecular dynamics simulations, with the estimation of density, radial and spatial distribution functions, solvent accessible solvent area and coordination numbers. For this study I had the supervision of my advisors, Prof. Dr. João A. P. Coutinho and Dr. José R. B. Gomes, and the contribution of Prof. Dr. Simão P. Pinho and Dr. Kiki Kurnia (that had calculated the activity coefficients with COSMO-RS).

Motivation

At Chapter 1.2, it was discussed what are ionic liquids and their properties which enable them to act as selective solvents for compounds of interest. Additionally, it was also mentioned that the presence of water on ILs modifies their properties, such as viscosity[1,2] (lowering) or surface tension[3] (increasing) but in fact, water can also change their structure and, above a given concentration, is capable of disrupting the ionic interaction between the cation and the anion.[4] The knowledge of the ILs' properties in aqueous solution is very important for their design and use in specific applications namely, absorption refrigeration, extractive distillation or liquid-liquid extraction.[5,6] Furthermore, the mechanism of interaction between ILs and water is based on the establishment of hydrogen bonds (H-bonds), which is related mainly with the nature of the anions, that affects not only their physical and chemical properties (as already mentioned), but also their solvation potential, *e.g.*, the dissolution of carbohydrates.[7]

In the literature, it is possible to find several experimental works based on infra-red[8,9] (IR) and nuclear magnetic resonance[10,11] (NMR) spectroscopic techniques, or liquid-liquid equilibria[12,13] (LLE), vapor-liquid equilibria[14,15] (VLE), solid-liquid equilibria[16] (SLE), and activity coefficients[17] measurements that aimed at a characterization of water-IL systems. Moreover, theoretical approaches such as COnductor like Screening MOdel for Real Solvents (COSMO-RS)[5,18,19] or classical molecular dynamics (MD)[20–22] simulations have also been employed to complement the experimental studies and were found to provide important insights regarding the interactions involved in those systems. In addition, several review articles[4,23–25] reporting studies on binary systems composed of water and ILs by means of MD simulations were also published. Different factors governing the IL-water interactions, such as the nature of the cation, anion or combination of both, the cation's alkyl chain length, formation of aggregates and the dichotomy ion pairs *vs.* isolated ions, were addressed in those studies. It is generally accepted that the anion predominantly establishes interactions with water and hence, the chemical nature of the anion assumes a pivotal role in the solvation of ILs.[8,25–27]

Formation of water and/or IL aggregates is observed, and the composition at which it occurs is related with the nature/strength of the IL-water interactions. It is important to highlight that ILs have an unique structure, with microscopic domains (as mentioned on Chapter 1.2), responsible for their high capability to dissolve a variety of compounds.[28] These domains are divided into two regions with polar and nonpolar character, with the latter being essentially formed by the cation's alkyl chains. In aqueous solution, these chains tend to aggregate into hydrophobic clusters, inducing similarly the formation of small clusters of water that, eventually, can become a homogeneous network, disrupting the cation-

anion interactions. However, it should be noted that MD simulations are dependent on the accuracy of the applied force field, *e.g.*, the bonded and non-bonded parameters or on the applied atomic charges (Chapter 2). From the latter arises the question of the applicability of polarizable force fields which is currently a hot topic of discussion.[29] Therefore, it is important to develop force fields that can reproduce properties of ILs or mixtures containing ILs. In this regard, comparing the predicted physical properties, for example, density and viscosity, against experimental data, generally it can be assessed the quality of the new developed force field. While densities of ILs are easily reproduced with short time computer simulations, longer times are required to obtain accurate viscosities due to their low dynamics/high viscosity (Chapter 2). Therefore, as will be shown later, the reliability of the force field used in this work is compared with the experimental density data.

Within the huge number of possible combinations between cations and anions, the cyano (CN) - based ILs are interesting for industrial purposes because they present lower melting points and viscosities than most of ILs.[30] They have been studied and characterized for specific applications, mainly for electrolytes and dye-sensitized solar cells,[31,32] but also as extracting solvent for alcohols from fermentation broth,[33] for aromatic - aliphatic separation,[34] as well as for the extraction of added-value compounds from biomass, such as phenolic compounds,[35] carbohydrates[36,37] and sugar alcohols[38]. Recently, Neves *et al.*[30] published density and viscosity data for the pure imidazolium-based IL with CN-based anions, addressing the effect of the increase of the CN-groups on these properties.

In the present Chapter, binary systems composed of water and the ILs based on the 1-butyl-3-methylimidazolim cation ($[BMIM]^+$) combined with the anion thiocyanate ($[SCN]^-$), dicyanamide ($[DCA]^-$) or tricyanomethane ($[TCN]^-$), and of water and 1-ethyl-3-methylimidazolim tetracyanoborate ([EMIM][TCB]) were studied and characterized by means of experimental water activity data and computational approaches, namely COSMO-RS and MD simulation. It should be noted that [EMIM][TCB] was used due to the unavailability of [BMIM][TCB] from the supplier. Nevertheless, previous studies[8,39] showed that interactions between water and ILs are established mainly through the anion, while the imidazolium cation has a minor contribution.

The set of CN-based ILs used in the present work, will allow us to study the effects of the number of CN groups in the anion, from 1 in $[SCN]^-$ to 4 in $[TCB]^-$, in the interaction of the considered ILs with water molecules. As a reliable property to interpret such interactions, activity coefficients were estimated from water activity measurements for all these binary mixtures, at 298.2 K, which were further evaluated by COSMO-RS. Classical MD simulations were also performed to calculate the number of H-bonds given by coordination numbers, and radial and spatial distribution functions for the different IL-water systems, from which information regarding the local atomic organization is drawn.

Methodology

Experimental Section

Materials

The ILs 1-butyl-3-methylimidazolium thiocyanate, [BMIM][SCN] (mass fraction purity > 98 %), 1-butyl-3-methylimidazolium dicyanamide, [BMIM][DCA] (mass fraction purity > 98 %), 1-butyl-3-methylimidazolium tricyanomethane, [BMIM][TCN] (mass fraction purity > 98 %), were purchased from IoLiTec, while 1-ethyl-3-methylimidazolium tetracyanoborate, [EMIM][TCB] (mass fraction purity > 98 %) was kindly supplied by Merck KGaA Germany. Figure 3.2.1 depicts the chemical structures of the ions composing the studied ILs. The purities were further confirmed by ^{1}H and ^{13}C NMR and found to be in agreement with the purity levels given by the suppliers. In order to reduce the amount of volatile impurities, all samples were dried for at least 48 h under vacuum (10^{-3} Pa) at room temperature, before use. After the drying procedure, the water content of each sample was determined using a Metrohm 831 Karl Fisher coulometer with an associated uncertainty of ±3 μg. The water content was found to be less than 290 ppm for all ILs. The analyte used for the coulometric Karl Fisher titration was Hydranal – Coulomat AG from Riedel-de Haën. In all experiments, water was double distilled, passed by a reverse osmosis system and further treated with a MilliQ plus 185 water purification apparatus.

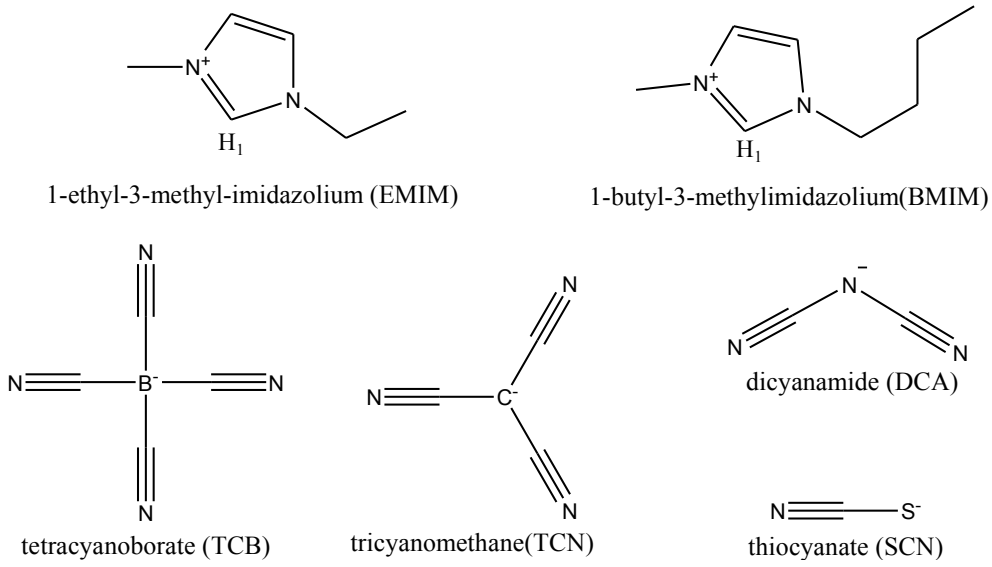

Figure 3.2.1 - Chemical structures of the ions composing the studied ILs.

Water activity measurements

A Novasina hygrometer LabMaster-a_w (Switzerland) was used to measure water activities, a_w. The measuring principle of the instrument is based on resistive-electrolytic method. The accuracy of the instrument is 0.001 a_w, enabling measurements under controlled chamber temperature conditions (±0.15 K), and was previously calibrated with six saturated pure salt standard solutions, with a_w ranging from 0.330 to 0.973, which were included in the instrument. Prior to the measurement, a calibration curve was built using KCl or $CaCl_2$ aqueous solutions at different salt molalities, depending on the water activity range values to be measured. The obtained values were compared to those recommended in the extensive reviews by Archer[40] for KCl, or Rard and Clegg[41] for $CaCl_2$. For each measurement, samples *ca.* 2-3 cm^3 were prepared gravimetrically with uncertainties of ±0.0001 g in the entire range of solubility of ILs. The samples were then charged in the measuring cells and placed in the air-tight equilibrium chamber. The exchange of free water took place until the partial pressure of water vapor reached the equilibrium, which was confirmed following the a_w variation with time. The value of water activity was recorded when it reached a constant value. For solutions with high concentration of IL, times of up to 8 hours were required for constant water activity. At the end, the mole fractions were confirmed by measuring the refractive index (five

measurements were performed for each mixture), using an automated Abbemat 500 Anton Paar refractometer. Those were carried out at the temperature 298.15 K for all samples, at atmospheric pressure. The maximum deviation in temperature is ±0.01 K and the maximum uncertainty in the refractive index measurements is ±0.00002. The water activity coefficients, γ_w, were estimated according to the following equation,

$$\gamma_w = \frac{a_w}{x_w} \tag{3.2.1}$$

where a_w is the water activity and x_w the water mole fraction.

Computational Section

COSMO-RS

The COSMO-RS approach proposed by Klamt and Schuurmann,[42] is a unique method for *a priori* prediction of the phase behavior of pure fluids and their mixtures on the basis of unimolecular quantum chemical calculations. A comprehensive description of the COSMO-RS theory can be found at the original work of Klamt *et al.*[43]. An important advantage of COSMO-RS model is that it can be used to predict the activity coefficient of any component in a mixture without using any experimental information. It uses the molecular structure of the solute/component as single initial input. Thus, it can be used to predict the water activity coefficients in aqueous binary mixtures containing ILs. The reliability of COSMO-RS to predict the activity coefficient of a solute in ILs has been shown by us[18,19] and others.[44,45] Therefore, in this work, COSMO-RS was used to predict water activity coefficients in the binary mixtures with CN-based ILs and to further understand the water-ILs interactions.

The standard procedure on using COSMO-RS to predict activity coefficients consists of two main steps. In the first step, continuum solvation COSMO calculations of electronic density and molecular geometry were performed with the TURBOMOLE 6.5 package[46] at the BP-TZVPD-FINE level,[47] introduced in 2012. It is based on a Turbomole BP-RI-DFT COSMO single point calculation with TZVPD basis set on top of an optimized BP/TZVP/COSMO geometry. The COSMO single point calculation considers the TZVPD basis set, TZVP with diffuse functions, and a novel type of molecular surface cavity construction (fine grid marching tetrahedron cavity, FINE[48]) which creates a COSMO surface whose segments are more

uniform and evenly distributed compared to the standard COSMO cavity. Calculations at the same levels of theory are also performed at the gas phase. In the second step, the estimation of the water activity coefficient data for each binary mixture was performed with the COSMOtherm program using the parameter file BP_TZVPD-FINE_C30_0140 (COSMOlogic GmbH & Co KG, Leverkusen, Germany).[47] In all calculations, the interaction energies of the surface pairs are defined in terms of the screening charge densities σ and σ' of the respective surface segments, with the resulting information being stored in the so-called COSMO files. Subsequently, the chemical potential (μ_s) of a surface segment (σ), the so-called sigma potential (σ - potential) is calculated using the following equation,

$$\mu_s(\sigma) = -\frac{RT}{a_{\text{eff}}} \ln\left[\int p_s(\sigma')\, exp\left\{\frac{a_{\text{eff}}}{RT}\left[\mu_S(\sigma') - E_{\text{misfit}}(\sigma,\sigma') - E_{\text{HB}}(\sigma,\sigma')\right]\right\} d\sigma'\right] \qquad (3.2.2)$$

where a_{eff} represents the effective contact area, $p_s(\sigma)$ stands for the surface screening charge distribution of the whole system, E_{misfit} is the electrostatic misfit energy, E_{HB} is the hydrogen-bonding energy, R is the ideal gas constant and T the absolute temperature. The chemical potential of a compound is available from the integration of the σ-potential over the surface of the molecule, and it is used for the prediction of thermodynamic properties and phase behavior, as it is used on the prediction of the water activity coefficients in systems with ILs using the equation below, [45]

$$\gamma_s^{X_i} = exp\left\{\frac{\mu_S^{X_i} - \mu_{X_i}^{X_i}}{RT}\right\} \qquad (3.2.3)$$

where $\gamma_S^{X_i}$ is the activity coefficient of compound X_i in the solvent S, $\mu_S^{X_i}$ is its chemical potential in the solvent S and $\mu_{X_i}^{X_i}$ is the chemical potential of pure compound X_i. In this work, the ILs were always treated as isolated ions at the quantum chemical level.

Another advantage of using COSMO-RS, is that it can also provide other thermodynamic properties to get further insight toward the interaction of water and ILs. For example, the excess enthalpies can be used to infer on the strength of water-ILs interaction in the binary mixture. The excess enthalpy is defined as the difference between the interaction of IL and water in their mixture and pure state, according to the equation 3.2.4,

$$H^E = H_{i,mix} - H_{i,pure} \quad (3.2.4)$$

The predicted excess enthalpies can be further analyzed according to the contribution of specific interaction of cation, anion and water molecule, according to equations 3.2.5 to 3.2.8,

$$H^E = H^E_{cation} + H^E_{anion} + H^E_{water} \quad (3.2.5)$$

The total excess enthalpy in the COSMO-RS method arises from summing the three specific interactions, namely electrostatic-misfit, H^E_{MF}, hydrogen bonds, H^E_{HB}, and van der Waals forces, H^E_{vdW}. Thereafter, each term of equation 3.2.5 can then be written as following,

$$H^E_{cation} = H^E_{MF,cation} + H^E_{HB,cation} + H^E_{vdW,cation} \quad (3.2.6)$$

$$H^E_{anion} = H^E_{MF,anion} + H^E_{HB,anion} + H^E_{vdW,anion} \quad (3.2.7)$$

$$H^E_{water} = H^E_{MF,water} + H^E_{HB,water} + H^E_{vdW,water} \quad (3.2.8)$$

Therefore, COSMO-RS allows the evaluation of the energetic contributions of all possible specific interactions established by each species and their contributions to the total excess enthalpy, as well as, their mechanisms of interaction.

Molecular dynamics simulations

Molecular dynamics simulations were performed with the GROMACS[49] code, version 4.5.4, for binary aqueous systems, at IL mole fractions of 0.2, 0.4, 0.6 and 0.8, for the following ILs: [BMIM][SCN], [BMIM][DCA], [BMIM][TCN] and [EMIM][TCB]. Further details on the number of molecules in each system are provided in Table B.1 in the Appendix B.

For all the systems, after energy minimization and equilibration runs, production runs of 20 ns within the isothermal-isobaric (NPT) ensemble were performed using a time step of 2 fs. In these simulations, the temperature was maintained constant at 298.15 K using the Nosé-Hoover[50,51] thermostat, and the pressure was kept at 1 bar with the Parrinello-Rahman[52]

barostat. The intermolecular interaction energy between pairs of neighboring atoms was calculated using the Lennard-Jones potential to describe dispersion/repulsion forces and the point-charge Coulomb potential was used for electrostatic forces. Cutoffs of 1.2 and 1.0 nm were set for Lennard-Jones and Coulombic interactions, respectively, and long-range corrections for energy and pressure were also applied. Rigid constraints were enforced on all bonds lengths. Additionally, for each system, simulations within the canonical ensemble (NVT) were also performed for 10 ns, under the same conditions as those considered in the NPT simulations.

The force field parameters for the $[BMIM]^+$ cation were taken from Cadena and Maginn,[53] while those for the $[EMIM]^+$ cation were deduced from the former. The potential parameters for the $[SCN]^-$ anion were those used in our previous work[54] (previous Chapter 3.1), for the $[DCA]^-$ and $[TCN]^-$ anions were considered the OPLS-AA force field[55,56] parameters, while those for the $[TCB]^-$ anion were obtained from the work of Koller *et al.*[57] The atomic charges for the IL cations and anions were recalculated in the present work with the CHelpG scheme[58] using an optimized geometry (minimum energy from several configurations) for each IL ion pair, in the gas phase as previously performed for other systems involving ILs.[54] The calculations were performed at the B3LYP/6-311+G(d) level of theory[59] with the Gaussian 09 code.[60] The total charges on the cations and anions were ±0.804 *e* for [BMIM][SCN], ±0.826 *e* for [BMIM][DCA], ±0.880 *e* for [BMIM][TCN] and ±0.889 *e* for [EMIM][TCB]. The full sets of atomic charges for each IL are compiled in Tables B.2 to B.5 in the Appendix B. Water molecules considered the SPCE model.[61] To validate the combination of the different force fields applied for each cation and anion, densities for each pure IL were estimated, at 298.15 K, and are compared with the experimental values recently published by Neves *et al*.[26] in Table B.6 in the Appendix B. A very satisfactory agreement between experimental and simulated data is observed with relative deviations of 3.2 %, 1.8 %, 1.6 % and 1.2 % in the cases of [BMIM][DCA], [EMIM][TCB], [BMIM][TCN] and [BMIM][SCN], respectively.

In addition, radial and spatial distributions functions, RDFs and SDFs, respectively, as well as coordination numbers, Z, were calculated from the MD trajectories.

Results and Discussion

Water activity and activity coefficients

The experimental water activities together with the respective water activity coefficients, calculated using equation 3.2.1, are given in Table 3.2.1. Figure 3.2.2 presents a comparison of experimental and COSMO-RS water activity coefficients of the ILs. The water activity coefficients of ([BMIM][SCN]+water) and ([BMIM][DCA]+water) binary mixtures present up to x_w = 0.8 values lower than unit, which indicates favorable interactions between [BMIM][SCN] or [BMIM][DCA] and water molecules. On the other hand, unfavorable interactions between [BMIM][TCN] and [EMIM][TCB] with water are observed, being their water activity coefficients higher than unit throughout whole composition. It should be stressed that high and positive values of water activity coefficients in [EMIM][TCB] and [BMIM][TCN] eventually lead to the formation of two phases, as observed experimentally.[62] In the case of [BMIM][TCN] the formation of phases occurs at high water content, x_w=0.80, while for [EMIM][TCB] the phenomenon occurs already at x_w = 0.60. For this reason the experimental data were carefully measured within the region of complete miscibility for these ILs. Accordingly, based on the strength of their interactions with water, the studied cyano-based ILs can be ranked in the order [EMIM][TCB] < [BMIM][TCN] < BMIM][SCN] < [BMIM][DCA].

Table 3.2.1 - Experimental water activities (a_w) and experimental and COSMO-RS water activity coefficients (γ_w) in the binary mixtures at T = 298.2 K.

x_w	a_w	$\gamma_{w,exp}$	$\gamma_{w,COSMO}$	ARD%[a]
[BMIM][SCN] + H_2O				
0.436	0.269	0.617	0.761	23.2
0.541	0.413	0.763	0.812	6.5
0.594	0.492	0.829	0.839	1.1
0.696	0.664	0.954	0.888	6.9
0.812	0.842	1.037	0.931	10.2
0.914	0.948	1.038	0.945	9.0
0.956	0.970	1.015	0.952	6.2
			AAD[b]	9.0
[BMIM][DCA] + H_2O				
0.323	0.151	0.467	0.505	8.0
0.429	0.235	0.548	0.544	0.7

0.526	0.341	0.648	0.586	9.7
0.561	0.381	0.679	0.602	11.3
0.697	0.596	0.856	0.679	20.6
0.800	0.788	0.985	0.754	23.5
0.849	0.869	1.023	0.796	22.2
0.899	0.929	1.034	0.846	18.1
			AAD[b]	14.3
[BMIM][TCN] + H_2O				
0.296	0.357	1.204	1.294	7.5
0.390	0.478	1.227	1.278	4.2
0.493	0.620	1.257	1.254	0.2
0.534	0.662	1.241	1.243	0.2
0.593	0.740	1.248	1.223	2.0
0.720	0.896	1.245	1.165	6.4
0.808	0.970	1.201	1.106	7.9
			AAD[b]	4.1
[EMIM][TCB] + H_2O				
0.350	0.698	1.994	2.158	8.2
0.440	0.799	1.816	2.017	11.1
0.530	0.881	1.662	1.875	12.8
0.620	0.948	1.529	1.725	12.8
			AAD[b]	11.2

[a]Average relative deviation between experimental and COSMO-RS water activity coefficients.

[b]Average absolute deviation between experimental and COSMO-RS water activity coefficients.

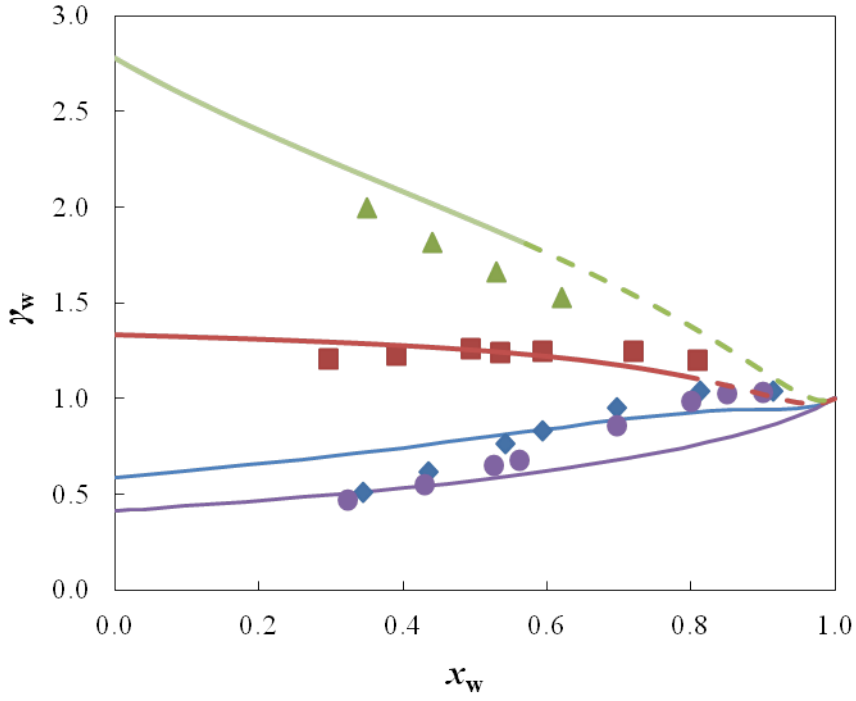

Figure 3.2.2 - Experimental and predicted water activity coefficients, at 298.2 K. Symbols are representing experimental data and full lines the COSMO-RS predictions (●,—) [BMIM][DCA], (◆,—) [BMIM][SCN], (■,—) [BMIM][TCN] and (▲,—) [EMIM][TCB]. The dashed lines for [BMIM][TCN] and [EMIM][TCB] indicate the immiscibility region of these ILs in water.

COSMO-RS Calculations

From the results shown in Figure 3.2.2, it is evident that the COSMO-RS model predicts qualitatively the water activity coefficients of the studied CN-based ILs, with average absolute deviations (AAD) varying between 4.1 % for [BMIM][TCN] and 14.3 % for [BMIM][DCA]. It should be pointed out that the associated BP_TZVPD_FINE_C30_0140.ctd parameter set, used in this work, incorporates the HB2012 hydrogen bonding term and a novel van der Waals dispersion term based on the "D3" method of Grimme *et al.*[63]. These lead to improved thermodynamic property predictions for compound classes. In addition, and since COSMO-RS correctly predicts the experimentally observed trend of CN-based ILs interactions with water, this methodology is going to be used for probing the interactions of ILs and water, in the following discussion.

Figure 3.2.3 (and B.1 in the Appendix B) depicts the σ-profiles and σ–potentials for water and

the four ILs (for each anion and cation) addressed in this study. The σ-profiles are obtained by converting the 3D distribution of the screening charge density into a surface composition function, which can be used to understand the behavior of the molecule in terms of its polarity.

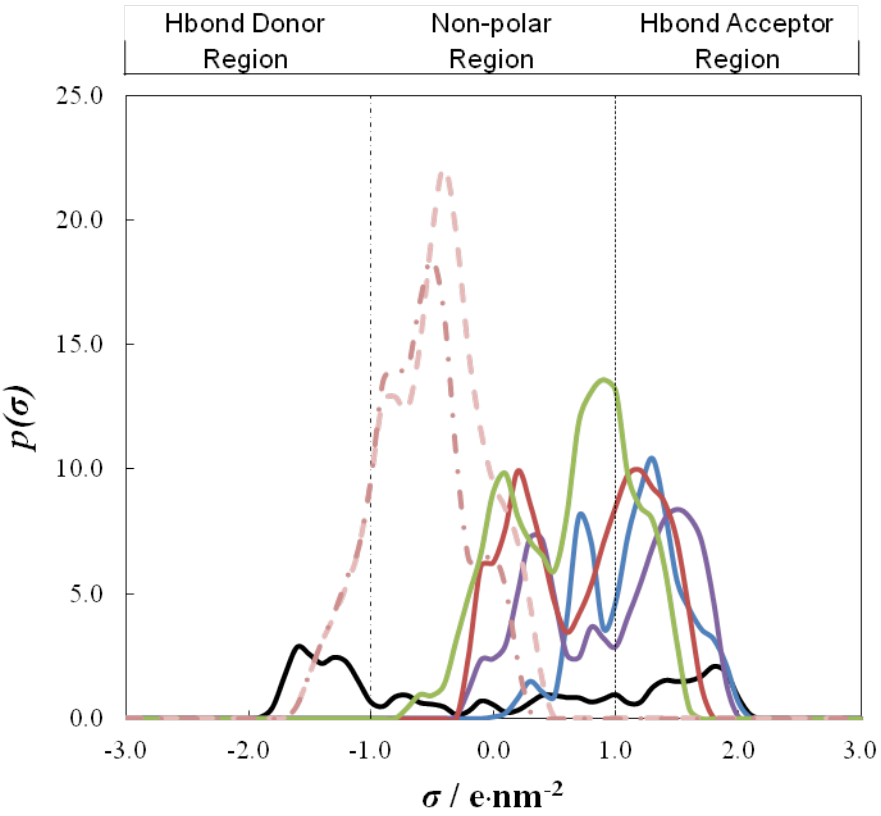

Figure 3.2.3 - Sigma profile for (—) water, (—) $[DCA]^-$, (—) $[SCN]^-$, (—) $[TCN]^-$, (—) $[TCB]^-$, (— —) $[BMIM]^+$ and (— •) $[EMIM]^+$.

The σ–potentials, obtained from equation 3.2.2, describe the affinities of molecules to interact with molecules of the same kind. The two vertical dotted lines in Figure 3.2.3, are the locations of the cut off values for the H-bond donor (σ_{HB} < -1.0 e·nm^{-2}) and acceptor (σ_{HB} > 1.0 e·nm^{-2}) profiles. For instance, the σ-profile of water is very broad, spanning throughout negative, positive and neutral areas from -2.0 to 2.1 e·nm^{-2} because of the expected behavior for water to act as H-bond donor or acceptor. On the negative area, the peak at -1.6 e·nm^{-2} is assigned to the two polar hydrogen atoms of water, indicating the ability of this molecule to act as H-bond donor. On the positive side, broad peaks

centered at 1.8 $e \cdot nm^{-2}$ resulting from the two pairs of electrons belonging to the oxygen atom of the water molecule. This peak designates the ability of water to act also as H-bond acceptor through its oxygen atom. Hence, water can act either as H-bond donor or H-bond acceptor, depending on the behavior of the other molecule in the mixture. Consequently, as displayed by its σ–potential, water presents considerable attraction to both H-bond donors and H-bond acceptors.

Regarding the studied ILs, asymmetries on both σ-profiles and σ–potentials are observed, certainly due to an uneven charge distribution along the ILs' structure. The ILs cations present a shoulder-like peak at -0.9 $e \cdot nm^{-2}$, close to the cut off, attributed to the acidic hydrogen atom in the imidazolium ring that could act as a weak H-bond donor. Meanwhile, the anions present a peak within the positive area indicating their potential as H-bond acceptors. The weak H-bond donor ability of the IL cation is surpassed by the high H-bond acceptor characteristics of the anions, and the studied CN-based ILs as a whole present enhanced interactions with other molecules displaying H-bond donor features, as depicted by their σ–potentials.

It is interesting to observe the shifting of the anion peaks into the positive region. Going from $[SCN]^-$ to $[DCA]^-$, the peak moves to a more positive area, indicating that the latter anion is more electronegative[43]. This shifting is indicative of a stronger ability of $[DCA]^-$ to act as H-bond acceptor when compared to the $[SCN]^-$ anion. Interestingly, further increasing the number of CN-groups into the anion, as in the cases of $[TCN]^-$ and $[TCB]^-$, significantly shifts the peak towards the neutral area, with the latter anion shifting the most. Thus, it indicates that, while increasing the number of CN-groups from thiocyanate to dicyanamide the H-bond acceptor character is increased, a further increase of the number of CN-groups from dicyanamide to tetracyanoborate decreases their ability to act as H-bond acceptor. As a consequence, it is expected that $[DCA]^-$ will have the strongest interaction with water, followed by $[SCN]^-$, $[TCN]^-$, and at last $[TCB]^-$.

Afterwards, the contributions of the electrostatic misfit, hydrogen bonding and van der Waals interactions to the total excess enthalpy of IL and water at equimolar composition, $x_w = 0.5$, estimated through equations 3.2.4 to 3.2.8, are depicted in Figure 3.2.4.

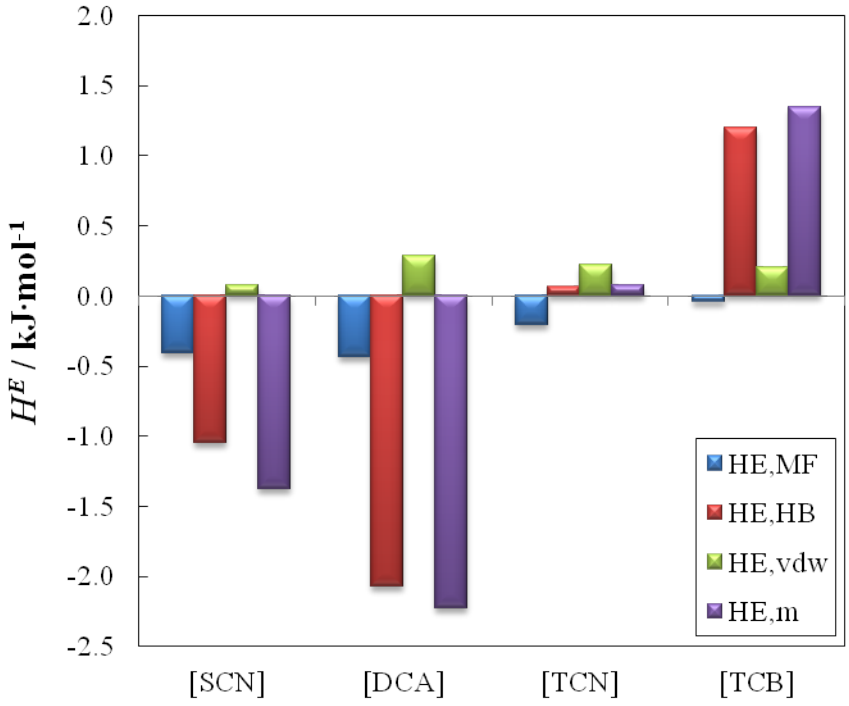

Figure 3.2.4 - Contribution of specific interaction to the total excess enthalpy, at x_w = 0.5 and T = 298.15 K. The contribution of excess enthalpies from electrostatic/misfit is represented by the blue bars, hydrogen bonding through the red bars, van der Waals through the green bars, and total excess enthalpies of the mixtures by the purple bars.

Negative total excess enthalpies are observed for the aqueous binary mixtures of [BMIM][SCN] or [BMIM][DCA], where electrostatic misfit interactions and hydrogen bonding are the main contributions for the exothermic process, while positive total excess enthalpies (endothermic processes) are found for aqueous binary mixtures of [BMIM][TCN] and [EMIM][TCB]. The results demonstrate that the hydrogen bonding between anion and water plays a crucial role and determines the enthalpic nature of the mixtures, albeit the electrostatic misfit has a minor contribution to exothermicity of the mixture, while the van der Waals contribution is always found to be positive. The combination of all these contributions lead to the following behavior with the increase of the number of CN-groups in the anion: from thiocyanate to dicyanamide the total excess enthalpies become more negative while from the latter anion to tetracyanoborate, the sign of the total excess enthalpy is reversed and becomes more positive. In other words, the hydrogen bonding becomes weaker with increasing number of CN-groups in the anion, which is in close agreement with the extended series of

hydrogen bonding basicity taken from the solvatochromic parameter.[64] The solvatochromic parameter β, measures the hydrogen-accepting ability of an ion/compound, and it was measured for several ILs.[26,65–68] In a recent work[64], it was possible to estimate the solvatochromic parameter β for the studied ILs which are, 0.671, 0.762, 0.666 and 0.598 for [BMIM][SCN], [BMIM][DCA], [BMIM][TCN] and [EMIM][TCB], respectively, suggesting that the ability to establish H-bonds increases from [BMIM][SCN] to [BMIM][DCA], and afterwards it decreases with an increase of the CN-groups in the anion.

Molecular dynamics simulations

Radial distribution functions and coordination numbers

Radial distribution function, *g(r)* or RDF, gives the probability of finding a particle at the distance *r*, from another particle (considered as the reference) and will be here used to describe the local structural organization of the mixtures studied in this work. The RDF values provide a quantitative description of enhancement (values above than one) or depletion (values below than one) of densities of atoms, or groups of atoms, around a selected moiety with respect to bulk values. Moreover, the local environment around the reference atom can be accurately represented by the coordination number (Z), which is the average number of atoms of one type surrounding the reference atom within a cut off, r_Z, given by the integral of the RDF.

$$Z(r) = 4\times\pi\times\rho_B\times\int_0^{r_z}\left(r^2 g(r)\right)\cdot dt \tag{3.2.9}$$

The cutoff is usually chosen to be the first local minimum of the corresponding RDF. Figures 3.2.5 and 3.2.6 present the RDFs and Table 3.2.2 compiles the coordination numbers obtained for all systems under study. The analyses of the anion-solvent, cation-solvent, cation-anion and solvent-solvent interactions are based on the RDFs obtained for the N-HW, H1-OW, H1-N and OW-OW pairs, respectively, where N is the nitrogen atom of the cyano group(s) in the anion, H1 is the acidic proton of the cation, and HW and OW stand for proton and oxygen atoms in water.

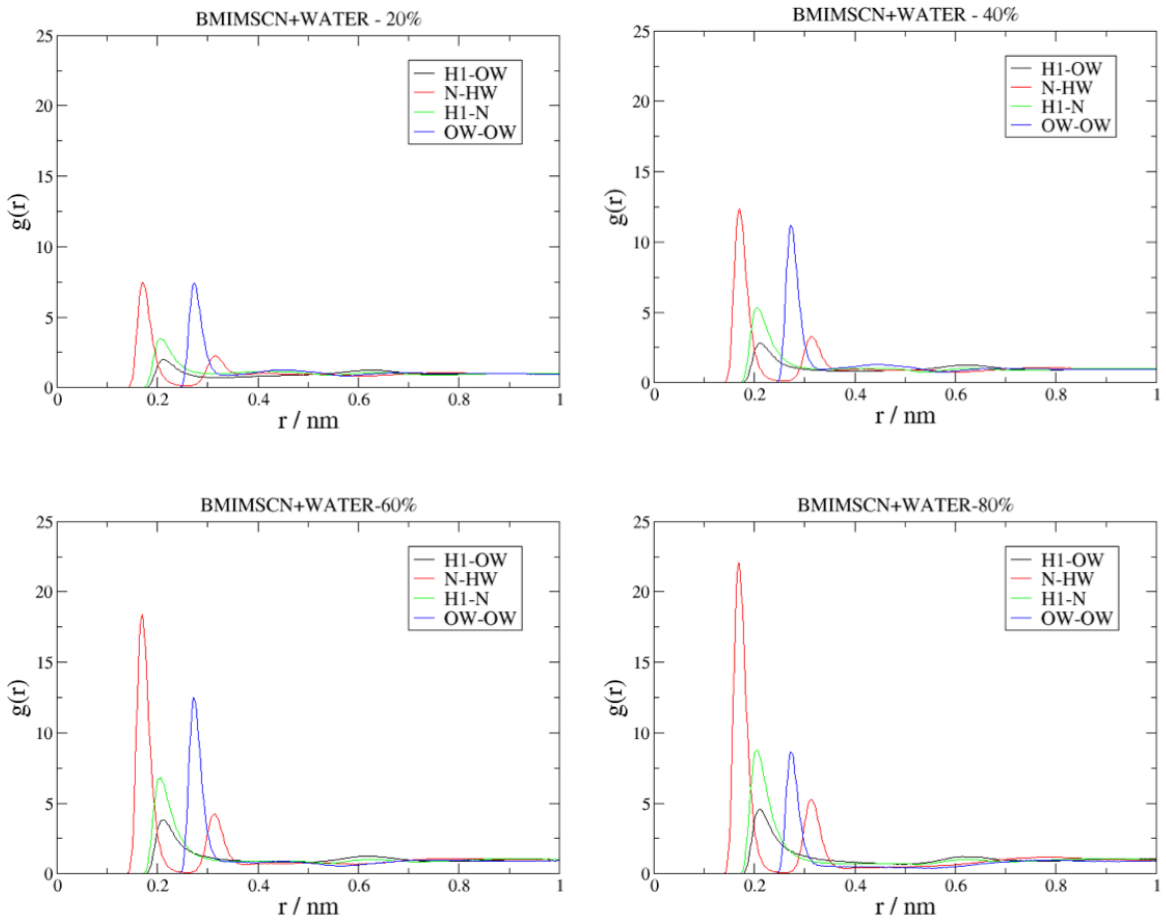

Figure 3.2.5. Radial distributions functions (RDFs) for mixtures of [BMIM][SCN] and water, at different mole fractions of IL and 298.15 K. RDFs for interaction of cation-water (H1-OW, —), anion-water (N-HW, —), cation-anion (H1-N, —) and solvent-solvent (OW-OW, —) are represented in each panel.

Common to all IL systems and similar to what was inferred from the COSMO-RS σ-profiles, the RDFs in Figures 3.2.5 and 3.2.6, and Figures B.2 to B.4 in the Appendix B, show that the primary interaction with water occurs with the anion, through N-HW atoms, while cation-water interactions are observed at the next solvation shell, suggesting that the latter is weaker than the former interaction. Moreover, as expected, interactions established among water molecules also present high values of *g(r)*. The latter interactions seem to be competing with anion-water ones being observed that water-water interactions are predominant in the case of

[EMIM][TCB], for all composition range (see Figure B.4 in Appendix B). In general, all these interactions are enhanced as the content of IL increases in the mixture, which is in agreement with published studies[23] and suggests the formation of water aggregates.

Notice that we performed MD simulations for the systems of water with [BMIM][TCN] and [EMIM][TCB] starting from random configurations and in the time lengths of the simulations phase separation was not observed. For that reason, RDFs and Z values for the system [EMIM][TCB] and water at 20 % of IL's content are also reported.

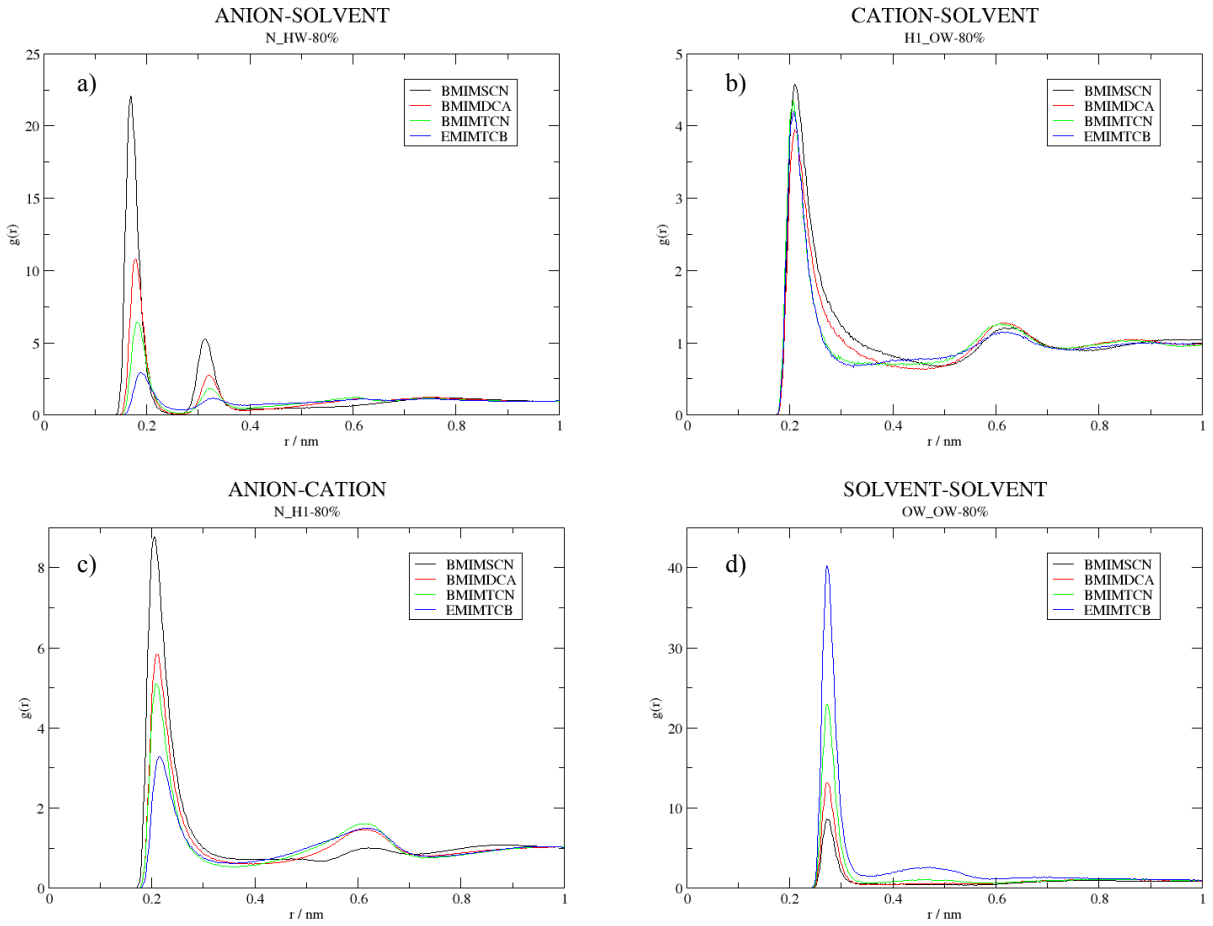

Figure 3.2.6. Radial distributions functions (RDFs) for a) anion-water, b) cation-water, c) cation-anion and d) water-water interactions, at 80IL:20W and 298.15 K. RDFs for [BMIM][SCN] (—), [BMIM][DCA] (—), [BMIM][TCN] (—) and [EMIM][TCB] (—) are represented in each panel.

The RDFs presented, can give us additional information concerning the establishment of hydrogen bonds in a mixture. In concordance with the geometric criteria, in the case of water-water interactions, it is recognized formation of a H-bond when a site-to-site RDF O—O (or O—H) presents a first minimum (r_z) in a distance smaller than 0.35 nm (or 0.26 nm) along with an angle of 30º.[69]

In our systems, the primary interactions are anion-water contacts that are mediated through the nitrogen atoms from the IL's anion with the water's hydrogen atoms. The r_z for all considered systems, for this type of interaction, was found to be 0.26 nm, which is consistent with the establishment of a H-bond. For water-water interactions, 0.35 nm was also found to be the r_z for O—O site-to-site RDFs, confirming the establishment of H-bonds. In Figure 3.2.6.a are shown the RDFs corresponding to anion-water interactions, for all systems addressed, with IL molar percentage of 80 %. The cyano group in the system with the anion $[SCN]^-$ presents higher probability of being surrounded by water than the cyano groups in the other anions, and the RDF presents two well-defined peaks suggesting the presence of two solvation shells. The shapes of the RDFs corresponding to the anion-water interactions are similar but the heights of the peaks decrease from systems having the $[SCN]^-$ anion to $[DCA]^-$ to $[TCN]^-$ and, finally, to $[TCB]^-$. This trend is the opposite of that verified for water-water interactions in the four systems considered, Figure 3.2.6.d, suggesting that segregation of water decreases in the following order $[TCB]^- > [TCN]^- > [DCA]^- > [SCN]^-$. In the case of the cation-solvent interactions, Figure 3.2.6.b, all ILs have similar interactions with water, though the RDF for [BMIM][SCN] is slightly more pronounced than the corresponding interaction in the other studied ILs. Plots similar to those displayed in Figure 3.2.6, for IL mole fractions of 20 %, 40 % and 60 % are provided in the Appendix B (Figures B.5 to B.7) and trends are identical to those described for the 80 % solutions. An exception, however, can be found in the ordering for the cation-solvent interactions, where [BMIM][TCN] presents higher probability of interaction with water. For further analyses, the mixture composed by 80 % of IL and 20 % of water, on molar basis, will be referred as 80IL:20W.

Additional information regarding the interactions involved in the ILs-water solutions can be obtained from the coordination numbers that are reported in Table 3.2.2. These numbers allow to quantify the number of H-bonds that are established between the species, by taking into account not only the heights of the first peaks in the RDFs, but also their widths and the densities of the different systems. Apparent discrepancies with the analyses of the heights of the RDF peaks result from differences in the number of cyano groups in the anions and also

from differences in the density of each composition as a consequence of different contents of each compound.

Table 3.2.2. Coordination number (Z) from the RDF peaks at distance below r_Z nm for anion-solvent, cation-solvent, cation-anion and solvent-solvent interaction, at each considered system and different IL mole fraction.

	[BMIM][SCN]+H_2O								
	anion-solvent		cation-solvent		cation-anion		solvent-solvent		IL-solvent
x_{IL}	r_Z	Z	r_Z	Z	r_Z	Z	r_Z	Z	*Z(total)*
0.2	0.26	2.0	0.40	2.1	0.35	0.5	0.34	2.6	4.1
0.4	0.26	1.4	0.40	1.2	0.35	0.8	0.34	1.7	2.6
0.6	0.26	0.9	0.40	0.7	0.35	1.0	0.34	0.9	1.6
0.8	0.26	0.4	0.40	0.3	0.35	1.1	0.34	0.2	0.7
	[BMIM][DCA]+H_2O								
	anion-solvent		cation-solvent		cation-anion		solvent-solvent		IL-solvent
x_{IL}	r_Z	Z	r_Z	Z	r_Z	Z	r_Z	Z	*Z(total)*
0.2	0.26	3.2	0.40	2.2	0.35	0.8	0.34	2.4	5.4
0.4	0.26	1.9	0.40	1.2	0.35	1.2	0.34	1.3	3.1
0.6	0.26	1.1	0.40	0.6	0.35	1.4	0.34	0.7	1.7
0.8	0.26	0.5	0.40	0.2	0.35	1.5	0.34	0.3	0.7
	[BMIM][TCN]+H_2O								
	anion-solvent		cation-solvent		cation-anion		solvent-solvent		IL-solvent
x_{IL}	r_Z	Z	r_Z	Z	r_Z	Z	r_Z	Z	*Z(total)*
0.2	0.26	3.4	0.40	2.0	0.35	1.0	0.34	2.3	5.4
0.4	0.26	1.9	0.40	1.0	0.35	1.4	0.34	1.4	2.9
0.6	0.26	1.0	0.40	0.5	0.35	1.6	0.34	0.8	1.5
0.8	0.26	0.4	0.40	0.2	0.35	1.7	0.34	0.5	0.6
	[EMIM][TCB]+H_2O								
	anion-solvent		cation-solvent		cation-anion		solvent-solvent		IL-solvent
x_{IL}	r_Z	Z	r_Z	Z	r_Z	Z	r_Z	Z	*Z(total)*
0.2	0.26	3.0	0.40	1.7	0.35	1.4	0.34	2.7	4.7
0.4	0.26	1.6	0.40	0.8	0.35	1.8	0.34	2.0	2.4
0.6	0.26	0.9	0.40	0.4	0.35	1.9	0.34	1.4	1.3
0.8	0.26	0.4	0.40	0.2	0.35	2.1	0.34	0.9	0.6

Results in Table 3.2.2 demonstrate that the largest values concerning the IL-water interactions, *i.e.*, obtained by adding the cation-water and anion-water interactions in all range of

composition, are found for the system with the anion $[DCA]^-$, suggesting more favorable interactions with water, which is in close agreement with the experimental findings from the present study. At 20 % and 40 % of IL, $[DCA]^-$ is followed by (or is nearly equal to) the system with the anion $[TCN]^-$, then by $[TCB]^-$ and finally by $[SCN]^-$. This trend is not obtained, however, for 60 % and 80 % of IL, where it is found that the IL-water coordination numbers for the system with the anion $[DCA]^-$ are still the largest but the ordering of the remaining systems is reversed, *i.e.*, second largest is the system composed by $[SCN]^-$, then $[TCN]^-$ and last $[TCB]^-$. The latter ordering is the same as that obtained for the experimental water activity coefficient data and for the COSMO-RS predictions. The Z values for cation-anion interactions are increasing with the content of IL in the system, contrary to the trends observed for the interactions with water. Regarding water-water interactions, they decrease less dramatically with the content of IL from the system containing the anion $[SCN]^-$, through $[DCA]^-$, $[TCN]^-$ and $[TCB]^-$. As mentioned previously, this trend is accompanied by an increase of cation-anion interactions, suggesting that the systems are gradually losing the propensity to interact with water as the number of CN-groups increase in the IL's anion.

Similar to what was discussed previously, the capacity of these ILs to establish H-bonds can be supported by the solvatochromic parameter β. Moreover, the CHelpG charges calculated at the B3LYP/6-311+G(d) level of theory can also give us some insights regarding the obtained results. Aiming this, and since results have demonstrated that the anions are the mediators of the interactions with water through their nitrogen atoms, atomic charges for all nitrogen atoms in the cyano groups of the anions are reported in Tables B.2 to B.5 (Appendix B). As it can be observed, charges of the nitrogen atoms become less negative in the order $[DCA]^- > [SCN]^- > [TCN]^- > [TCB]^-$ with values of -0.723 *e*, -0.658 *e*, -0.638 *e* and -0.487 *e*. Notice that the ordering of the partial charges in the nitrogen atoms of the cyano group differ slightly from the ordering of the total charge in the anions which becomes less negative in the order $[SCN]^- > [DCA]^- > [TCN]^- > [TCB]^-$.

The differences found in the partial atomic charges of the cyano nitrogen atoms are due to the presence of different central atoms in each anion, *i.e.*, sulfur ($[SCN]^-$), nitrogen ($[DCA]^-$), carbon ($[TCN]^-$) and boron ($[TCB]^-$), which lead to different charge delocalization. Such differences confer different abilities of the anions to establish H-bonds with water molecules with consequences in the properties of the ILs, for instance, in the anomalous behavior of viscosity[30]. Interestingly, the ordering of the partial charges in the nitrogen atoms from the CN-

groups in the anions of the ILs agrees with the ordering of the experimental and predicted water activity coefficients. Nevertheless, it is unquestionable that MD simulations allowed to recognize that an increase of CN-groups on ILs' anion hinders the ability of these CN-based ILs to interact favorably with water, generally on the same order as observed from water activity coefficient data.

Solvent accessible surface areas and spatial distribution functions

Aiming at a tri-dimensional visualization of how each anion interacts with water, *i.e.* the most important interaction type on these systems, the solvent accessible surface areas (*sasa*, the surface area of one molecule that is accessible to a solvent) and the spatial distribution functions (SDFs, a 3D representation of the probability of finding a particle at a certain position) were calculated for solutions 80IL:20W. The *sasa* surfaces were obtained as Connolly surfaces[70] consisting of all points at which a solvent sphere can reach based on the van der Waals radii. Figure B.8 in the Appendix B shows the *sasa* surfaces for each anion under study. The nodes are represented as atoms and the vertices joining the nearest nodes as connect records. Results demonstrate that water connects preferentially to all nitrogen atoms that are sterically available, becoming a specific interaction in the case of $[SCN]^-$.

The SDFs were built and analyzed with the TRAVIS[71] utility considering isosurfaces with values of 6.56 particles·nm^{-3} for the $[BMIM]^+$ and $[EMIM]^+$ cations (red surfaces, Figure B.9 in Appendix B) and of 1.24 particles·nm^{-3} for water (blue surfaces, Figure 3.2.7 and Figure B.9 in Appendix B), around the ILs anions in solutions 80IL:20W. As a common characteristic to all ILs, and in agreement to what was observed above in the analysis of the RDFs, water molecules preferentially interact with the nitrogen atoms of the cyano groups from the anions. Moreover, SDFs for the anion-water interaction clearly show the existence of two solvation shells (Figure 3.2.7). The SDFs for the anion-water and cation-anion interactions (Figure B.9 in Appendix B) suggest a competition between water molecules and cations for the anions since regions concerning the two interaction types are found at similar distances. Furthermore, in the cases of the $[SCN]^-$ and $[DCA]^-$ anions, the SDFs for the cation-anion interactions (Figure B.9) show that the cations not only interact with nitrogen atoms from CN-groups but also with the sulfur atom of $[SCN]^-$ and with the core of $[DCA]^-$. Additionally, the volume of the SDFs for water interacting with the different anions (Figure 3.2.7) decrease with the increase of the hydrophobicity of the anion, suggesting that the interaction is more likely in the

case of the anions with less CN-groups, which is consistent with conclusions arising from all the other analyses developed in this work.

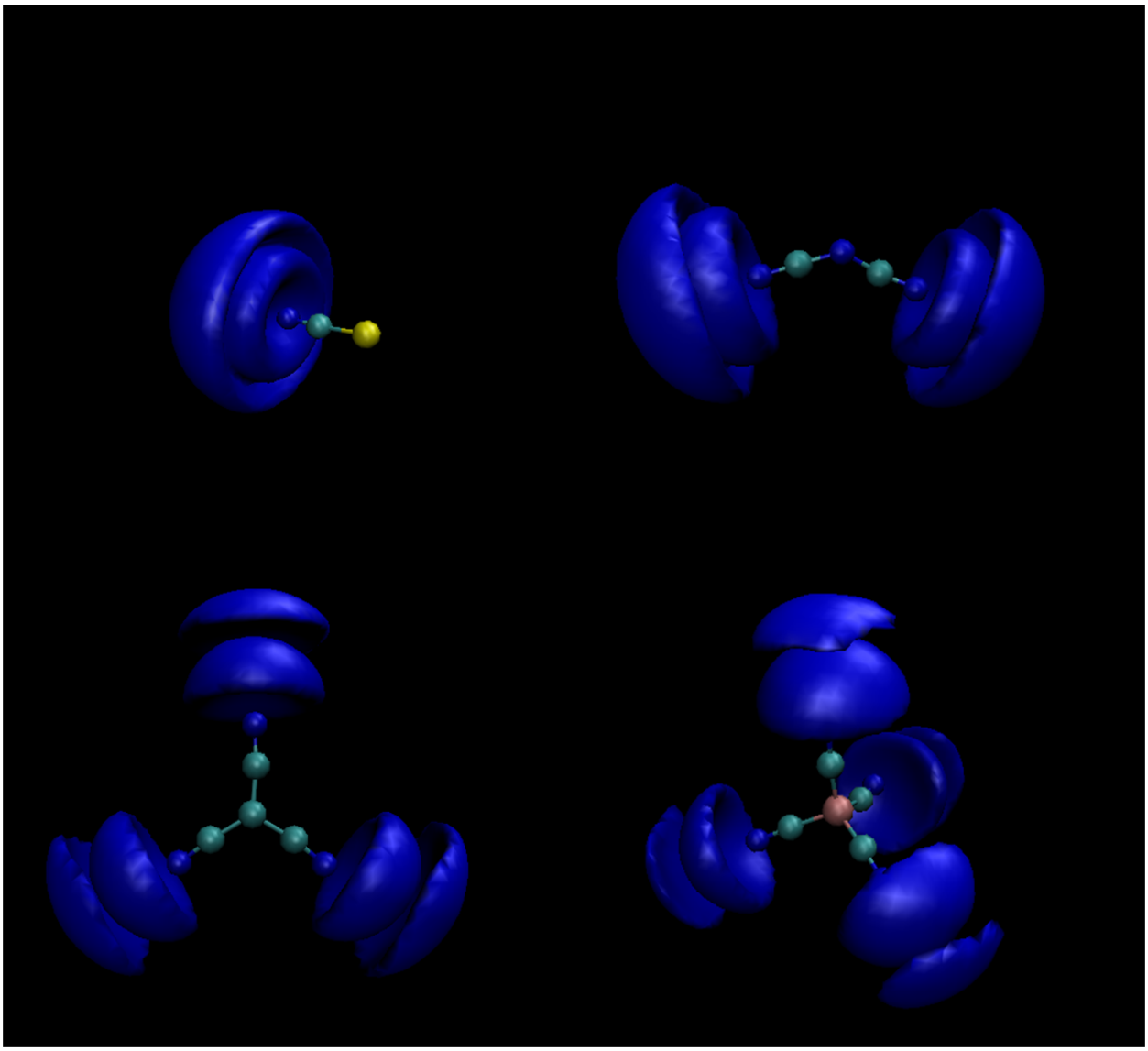

Figure 3.2.7 - Spatial distribution functions (SDF) obtained by TRAVIS[71], for the mixture [BMIM][SCN] (above, left side), [BMIM][DCA] (above, right side), [BMIM][TCN] (down, left side) and [EMIM][TCB] (down, right side) and water, at 80IL:20W. Each anion is the center element, surrounded by oxygen atoms of water (blue surface).

Conclusions

Aiming to study water–ILs interaction, aqueous solutions of [BMIM][SCN], [BMIM][DCA], [BMIM][TCN] and [EMIM][TCB] were studied and characterized by means of experimental and computational techniques.

Experimental water activity and the corresponding water activity coefficients suggest that [BMIM][SCN], [BMIM][DCA] are able to establish favorable interactions with water molecules as given by the negative deviations to ideality. On the contrary, [BMIM][TCN] and [EMIM][TCB] present positive deviations to ideality, indicating non-favorable or weak interactions with water. Moreover, COSMO-RS is shown to be able to quantitatively predict the water activity coefficients, presenting average absolute deviations varying from 4.1 to 14.3 % for the aqueous systems with [BMIM][TCN] and [BMIM][DCA], respectively. According to the sigma profile, generated using COSMO-RS, the electronegativity of the anions plays a crucial role toward their interaction with water molecules. The increasing of the number of CN-groups from $[SCN]^-$ to $[DCA]^-$, slightly increases the electronegativity, improving interactions with water molecules. However, increasing the number of CN-groups from $[DCA]^-$ to $[TCB]^-$ it is observed a decrease of the electronegativity, as well as their ability to act as H-bond acceptors.

Information at the atomic level was retrieved from DFT calculated partial atomic charges, and from the analyses of RDFs, coordination numbers, SDFs and *sasa* surfaces based on the trajectories obtained from MD simulation. They support the trend of IL-water and water-water interactions inferred from the activity coefficients results. According to the partial atomic charges, not only it was possible to infer that the anions establish important interactions with water through the nitrogen atoms of the CN-groups but also that the central atom has a deterministic impact on the charge delocalization of the anion. Due to the latter factor, together with the increasing number of CN-groups, the propensity of interaction with water decreases. Additionally, due to the high ionic interaction between cation and anion, the cations seem to establish some important H-bond contacts with water molecules that should not be neglected, though they seem to be have less effect than those involving the anions. Hence, the propensity for formation of ILs aggregates is expected to be smaller in the case of [BMIM][SCN] and [BMIM][DCA].

In general, the information retrieved from the experimental and computational results shows that the anion governs the interaction between ILs and water. The increase of the number of CN-groups in the ILs' anion from thiocyanate to dicyanamide is accompanied by an increase in the ability of the

anion to establish H-bonds with water, while from dicyanamide to tricyanomethane to tetracyanoborate it is found that the H-bond propensity decreases.

References

(1) Bhattacharjee, A.; Varanda, C.; Freire, M. G.; Matted, S.; Santos, L. M. N. B. F.; Marrucho, I. M.; Coutinho, J. A. P. *J. Chem. Eng. Data*, **2012**, *57*, 3473–3482.

(2) Carvalho, P. J.; Regueira, T.; Santos, L. M. N. B. F.; Fernandez, J.; Coutinho, J. A. P. *J. Chem. Eng. Data*, **2009**, *55*, 645–652.

(3) Almeida, H. F. D.; Lopes-da-Silva, J. A.; Freire, M. G.; Coutinho, J. A. P. *J. Chem. Thermodyn.*, **2013**, *57*, 372–379.

(4) Niazi, A. A.; Rabideau, B. D.; Ismail, A. E. *J. Phys. Chem. B*, **2013**, *117*, 1378–1388.

(5) Kurnia, K. A.; Pinho, S. P.; Coutinho, J. A. P. *Ind. Eng. Chem. Res.*, **2014**, *53*, 12466–12475.

(6) Pereiro, A. B.; Araújo, J. M. M.; Esperança, J. M. S. S.; Marrucho, I. M.; Rebelo, L. P. N. *J. Chem. Thermodyn.*, **2012**, *46*, 2–28.

(7) Zakrzewska, M. E.; Bogel-Lukasik, E.; Bogel-Lukasik, R. *Energy & Fuels*, **2010**, *24*, 737–745.

(8) Cammarata, L.; Kazarian, S. G.; Salter, P. A.; Welton, T. *Phys. Chem. Chem. Phys.*, **2001**, *3*, 5192–5200.

(9) Fumino, K.; Wulf, A.; Ludwig, R. *Angew. Chem. Int. Ed. Engl.*, **2009**, *48*, 3184–3186.

(10) Freire, M. G.; Neves, C. M. S. S.; Silva, A. M. S.; Santos, L. M. N. B. F.; Marrucho, I. M.; Rebelo, L. P. N.; Shah, J. K.; Maginn, E. J.; Coutinho, J. A. P. *J. Phys. Chem. B*, **2010**, *114*, 2004–2014.

(11) Singh, T.; Kumar, A. *J. Phys. Chem. B*, **2007**, *111*, 7843–7851.

(12) Królikowska, M. *Fluid Phase Equilib.*, **2014**, *361*, 273–281.

(13) Królikowska, M.; Karpińska, M.; Zawadzki, M. *J. Phys. Chem. B*, **2012**, *116*, 4292–4299.

(14) Królikowska, M.; Zawadzki, M.; Królikowski, M. *J. Chem. Thermodyn.*, **2014**, *70*, 127–137.

(15) Passos, H.; Khan, I.; Mutelet, F.; Oliveira, M. B.; Carvalho, P. J.; Santos, L. M. N. B. F.; Held, C.; Sadowski, G.; Freire, M. G.; Coutinho, J. A. P. *Ind. Eng. Chem. Res.*, **2014**, 3737–3748.

(16) Domańska, U.; Krolikowski, M.; Paduszynski, K. *J. Chem. Thermodyn.*, **2009**, *41*, 932–938.

(17) Domańska, U.; Marciniak, A.; Królikowska, M.; Arasimowicz, M. *J. Chem. Eng. Data*, **2010**, *55*, 2532–2536.

(18) Khan, I.; Kurnia, K. A.; Mutelet, F.; Pinho, S. P.; Coutinho, J. A. P. *J. Phys. Chem. B*, **2014**, 1848–1860.

(19) Khan, I.; Kurnia, K. A.; Sintra, T. E.; Saraiva, J. A.; Pinho, S. P.; Coutinho, J. A. P. *Fluid Phase Equilib.*, **2014**, *361*, 16–22.

(20) Kelkar, M. S.; Maginn, E. J. *J. Phys. Chem. B*, **2007**, *111*, 4867–4876.

(21) Chevrot, G.; Schurhammer, R.; Wipff, G. *Phys. Chem. Chem. Phys.*, **2006**, *8*, 4166–4174.

(22) Hanke, C. G.; Lynden-Bell, R. M. *J. Phys. Chem. B*, **2003**, *107*, 10873–10878.

(23) Kirchner, B. *Topics in Current Chemistry*; Meijere, V. B. A. De; Kessler, K. N. H. H.; Ley, J. L. S. V; Schreiber, M. O. S.; Vogel, B. M. T. P.; Wong, F. V. H., Eds.; Springer: Germany, 2009.

(24) Bhargava, B. L.; Yasaka, Y.; Klein, M. L. *Chem. Commun.*, **2011**, *47*, 6228–6241.

(25) Zhong, X.; Fan, Z.; Liu, Z.; Cao, D. *J. Phys. Chem. B*, **2012**, *116*, 3249–3263.

(26) Crowhurst, L.; Mawdsley, P. R.; Perez-Arlandis, J. M.; Salter, P. A.; Welton, T. *Phys. Chem. Chem. Phys.*, **2003**, *5*, 2790–2794.

(27) Fumino, K.; Wulf, A.; Ludwig, R. *Phys. Chem. Chem. Phys.*, **2009**, *11*, 8790–8794.

(28) Canongia Lopes, J. N.; Costa Gomes, M. F.; Pádua, A. A. H. *J. Phys. Chem. B*, **2006**, *110*, 16816–16818.

(29) Dommert, F.; Wendler, K.; Berger, R.; Delle Site, L.; Holm, C. *Chemphyschem*, **2012**, *13*, 1625–1637.

(30) Neves, C. M. S. S.; Kurnia, K. A.; Coutinho, J. A. P.; Marrucho, I. M.; Lopes, J. N. C.; Freire, M. G.; Rebelo, L. P. N. *J. Phys. Chem. B*, **2013**, *117*, 10271–10283.

(31) Zhou, D.; Bai, Y.; Zhang, J.; Cai, N.; Su, M.; Wang, Y.; Zhang, M.; Wang, P. *J. Phys. Chem. C*, **2011**, *115*, 816–822.

(32) Marszalek, M.; Fei, Z.; Zhu, D.-R.; Scopelliti, R.; Dyson, P. J.; Zakeeruddin, S. M.; Grätzel, M. *Inorg. Chem.*, **2011**, *50*, 11561–11567.

(33) Heitmann, S.; Krings, J.; Kreis, P.; Lennert, A.; Pitner, W. R.; Górak, A.; Schulte, M. M. *Sep. Purif. Technol.*, **2012**, *97*, 108–114.

(34) Meindersma, G. W.; Hansmeier, A. R.; de Haan, A. B. *Ind. Eng. Chem. Res.*, **2010**, *49*, 7530–7540.

(35) Cláudio, A. F. M.; Freire, M. G.; Freire, C. S. R.; Silvestre, A. J. D.; Coutinho, J. A. P. *Sep. Purif. Technol.*, **2010**, *75*, 39–47.

(36) Swatloski, R. P.; Spear, S. K.; Holbrey, J. D.; Rogers, R. D. *J. Am. Chem. Soc.*, **2002**, *124*, 4974–4975.

(37) Zhao, H.; Baker, G. A.; Song, Z.; Olubajo, O.; Crittle, T.; Peters, D. *Green Chem.*, **2008**, *10*, 696–705.

(38) Conceiçao, L. J. A.; Bogel-Łukasik, E.; Bogel-Łukasik, R. *RSC Adv.*, **2012**, *2*, 1846–1855.

(39) Kurnia, K. A.; Coutinho, J. A. P. *Ind. Eng. Chem. Res.*, **2013**, *52*, 13862–13874.

(40) Archer, D. G. *J. Phys. Chem. Ref. Data*, **1999**, *28*, 1–17.

(41) Rard, J. A.; Clegg, S. L. *J. Chem. Eng. Data*, **1997**, *42*, 819–849.

(42) Klamt, A.; Schuurmann, G. *J. Chem. Soc. Perkin Trans. 2*, **1993**, 799–805.

(43) Klamt, A. *COSMO-RS: From quantum Chemistry to Fluid Phase Thermodynamics and Drug Design*; Elsevier: Amsterdam, 2005.

(44) Reddy, P.; Aslam Siddiqi, M.; Atakan, B.; Diedenhofen, M.; Ramjugernath, D. *J. Chem. Thermodyn.*, **2013**, *58*, 322–329.

(45) Diedenhofen, M.; Eckert, F.; Klamt, A. *J. Chem. Eng. Data*, **2003**, *48*, 475–479.

(46) Furche, F.; Ahlrichs, R.; Hättig, C.; Klopper, W.; Sierka, M.; Weigend, F. *Wiley Interdiscip. Rev. Comput. Mol. Sci.*, **2014**, *4*, 91–100.

(47) Eckert, F.; Klamt, A. COSMOtherm Version C3.0 Release 14.01, 2013.

(48) Klamt, A.; Reinisch, J.; Eckert, F.; Graton, J.; Le Questel, J.-Y. *Phys. Chem. Chem. Phys.*, **2013**, *15*, 7147–7154.

(49) Hess, B.; Kutzner, C.; van der Spoel, D.; Lindahl, E. *J. Chem. Theory Comput.*, **2008**, *4*, 435–447.

(50) Nose, S. *Mol. Phys.*, **1984**, *52*, 255–268.

(51) Hoover, W. G. *Phys. Rev. A*, **1985**, *31*, 1695–1697.

(52) Parrinello, M.; Rahman, A. *J. Appl. Phys.*, **1981**, *52*, 7182–7190.

(53) Cadena, C.; Maginn, E. J. *J. Phys. Chem. B*, **2006**, *110*, 18026–18039.

(54) Batista, M. L. S.; Tomé, L. I. N.; Neves, C. M. S. S.; Rocha, E.; Gomes, J. R. B.; Coutinho, J. A. P. *J. Phys. Chem. B*, **2012**, *116*, 5985–5992.

(55) Jorgensen, W. L.; Maxwell, D. S.; Tirado-Rives, J. *J. Am. Chem. Soc.*, **1996**, *118*, 11225–11236.

(56) Kaminski, G. A.; Friesner, R. A.; Tirado-Rives, J.; Jorgensen, W. L. *J. Phys. Chem. B*, **2001**, *105*, 6474–6487.

(57) Koller, T.; Ramos, J.; Garrido, N. M.; Fröba, A. P.; Economou, I. G. *Mol. Phys.*, **2012**, *110*, 1115–1126.

(58) Breneman, C. M.; Wiberg, K. B. *J. Comput. Chem.*, **1990**, *11*, 361–373.

(59) Becke, A. D. *J. Chem. Phys.*, **1993**, *98*, 5648–5652.

(60) Frisch, M. J. .; Trucks, G. W. .; Schlegel, H. B. .; Scuseria, G. E. .; Robb, M. A. .; Cheeseman, J. R. .; Scalmani, G. .; Barone, V. .; Mennucci, B. .; Petersson, G. A. .; Nakatsuji, H. .; Caricato, M. .; Li, X. .; Hratchian, H. P. .; Izmaylov, A. F. .; Bloino, J. .; Zheng, G. .; Sonnenberg, J. L. .; Hada, M.; Ehara, M. .; Toyota, K. .; Fukuda, R. .; Hasegawa, J. .; Ishida, M. .; Nakajima, T. .; Honda, Y. .; Kitao, O. .; Nakai, H. .; Vreven, T. .; Montgomery, J. A., J. .; Peralta, J. E. .; Ogliaro, F. .; Bearpark, M. .; Heyd, J. J. .; Brothers, E. .; Kudin, K. N. .; Staroverov, V. N. .; Kobayashi, R. .; Normand, J. .; Raghavachari, K. .; Rendell, A. .; Burant, J. C. .; Iyengar, S. S. .; Tomasi, J. .; Cossi, M. .; Rega, N. .; Millam, M. J. .; Klene, M. .; Knox, J. E. .; Cross, J. B. .; Bakken, V. .; Adamo, C. .; Jaramillo, J. .; Gomperts, R. .; Stratmann, R. E. .; Yazyev, O. .; Austin, A. J. .; Cammi, R. .; Pomelli, C. .; Ochterski, J. W. .; Martin, R. L. .; Morokuma, K. .; Zakrzewski, V. G. .; Voth, G. A. .; Salvador, P. .; Dannenberg, J. J. .; Dapprich, S. .; Daniels, A. D. .; Farkas, Ö. .; Foresman, J. B. .; Ortiz, J. V. .; Cioslowski, J. .; Fox, D. J. *Gaussian 09, Revision D.01*; Gaussian, Inc., Wallingford CT, 2009.

(61) Berendsen, H. J. C.; Grigera, J. R.; Straatsma, T. P. *J. Phys. Chem.*, **1987**, *91*, 6269–6271.

(62) Freire, M. G.; Neves, C.; Carvalho, P. J.; Gardas, R. L.; Fernandes, A. M.; Marrucho, I. M.; Santos, L.; Coutinho, J. A. P. *J. Phys. Chem. B*, **2007**, *111*, 13082–13089.

(63) Grimme, S.; Antony, J.; Ehrlich, S.; Krieg, H. *J. Chem. Phys.*, **2010**, *132*, 154104–154123.

(64) Cláudio, A. F.; Swift, L.; Hallett, J.; Welton, T.; Coutinho, J. A. P.; Freire, M. G. *Phys. Chem. Chem. Phys.*, **2014**, *16*, 6593–6601.

(65) Lungwitz, R.; Spange, S. *New J. Chem.*, **2008**, *32*, 392–394.

(66) Lungwitz, R.; Strehmel, V.; Spange, S. *New J. Chem.*, **2010**, *34*, 1135–1140.

(67) Lungwitz, R.; Friedrich, M.; Linert, W.; Spange, S. *New J. Chem.*, **2008**, *32*, 1493–1499.

(68) Ab Rani, M. A.; Brant, A.; Crowhurst, L.; Dolan, A.; Lui, M.; Hassan, N. H.; Hallett, J. P.; Hunt, P. A.; Niedermeyer, H.; Perez-Arlandis, J. M.; Schrems, M.; Welton, T.; Wilding, R. *Phys. Chem. Chem. Phys.*, **2011**, *13*, 16831–16840.

(69) Skarmoutsos, I.; Dellis, D.; Matthews, R. P.; Welton, T.; Hunt, P. A. *J. Phys. Chem. B*, **2012**, *116*, 4921–4933.

(70) Connolly, M. L. *J. Appl. Crystallogr.*, **1983**, *16*, 548–558.

(71) Brehm, M.; Kirchner, B. *J. Chem. Inf. Model.*, **2011**, *51*, 2007–2023.

3.3. Complementary Study of Systems Composed of Ethanol/Water with Cyano-based Ionic Liquids

Adapted from:

Imran Khan*, Marta L. S. Batista*, Pedro J. Carvalho, Luís M. N. B. F. Santos, José R. B. Gomes, João A. P. Coutinho

Vapor-Liquid Equilibria of Imidazolium Ionic Liquid with Cyano containing Anions with Water and Ethanol

Submitted (The Journal of Physical Chemistry)

***Equal contribution**

My direct contribution:
I declare that I have carried out the experimental measurements of density, the molecular dynamics simulations, with the estimation of density, radial and spatial distribution functions, and coordination numbers. I have written the draft of the referenced manuscript, along with Dr. Imran Khan, who was responsible for the VLE data measurement and discussion, with further contributions from Dr. Pedro Carvalho and Prof. Dr. Luís Belchior. For this study I had the supervision of my advisors, Prof. Dr. João A. P. Coutinho and Dr. José R. B. Gomes.

Motivation

In the previous chapter, it was evaluated the mechanism of interaction with water of a specific class of ionic liquids (ILs) bearing cyano groups. It was possible to infer how they perform in a biomass pre-treatment process, where it is required the establishment of hydrogen bonds with glucose, aiming at its acquirement from the lignocellulosic net. Afterwards, glucose is fermented and it will give rise to the product of interest (bioethanol) in aqueous medium. The step that follows is the separation of bioethanol from water, which is made by distillation. However, there is the formation of an azeotrope ethanol-water at ethanol concentrations above 90 %[1], which hinders the separation of the two compounds by simple distillation. In this regard, extractive distillation is the most common method, applied for the separation of azeotropic or close-boiling mixtures. This process is based on the addition of another solvent, the separating agent or entrainer, with high boiling point which alters the relative volatility of the components enabling their separation.[2–4] The search of the best entrainer for ethanol-water azeotropic mixture has been the focus of several works.[1,4,5] The use of ILs in other azeotropic mixtures has also been addressed such as the acetic acid-water[6], aromatic-aliphatic[7,8] or tetrahydrofuran-water[9].

Common to all azeotropic mixtures, ILs have gained importance as entrainers, by recognition of their advantages over common organic compounds.[2–4,10] As mentioned in the first chapter of this thesis, ILs possess good solvation capacity to dissolve a broad variety of compounds, they present a wide liquidus temperature range, extremely low vapor pressures and the ability of fine-tune their properties.[11] These characteristics, together with their easy recovery and reuse, has categorized ILs as feasible candidates to successfully replace common volatile organic compounds in different separation processes.[2–4,9]

The assessment of the applicability of a certain IL to act as entrainer, in different azeotropic systems is usually made through vapor pressure, boiling temperature or through activity coefficient experimental data. Vapor–Liquid Equilibria (VLE) along with activity coefficient data, are means to evaluate the potential of molar excess Gibbs energy (G^E) models, widely used for the description of the non-ideal behavior of the systems. Hence, the possibility of two-phase formation and the type/strength of the interactions established between the IL and water/ethanol can be gauged and a separation process designed.[2,4,12]

Although object of interest during the last decade, only a few studies on VLE with ILs as entrainers for azeotropic separations have been reported.[4] Seiler et al.[9], Jorke et al.[13], Beste et al.[14] and

Lei et al.[15] were among the first to show the use of ILs for separation of azeotropic mixtures. Revelli et al.[16] reported some binary mixtures containing imidazolium-based ILs with light alcohols. In the open literature, there are several imidazolium-based ILs investigated for the extractive distillation of ethanol-water mixtures[17–28]. These studies focused on showing that the ILs may allow breaking the azeotrope, and on validating different procedures to measure VLE data with ILs. Among them, Ge et al.[18] and Orchillés et al.[29] compared and discussed the performance of the anions $[Cl]^-$, $[Ac]^-$, $[DCA]^-$ and $[BF_4]^-$ as they have been found as the most suitable for an effective extractive distillation, according to the effect that they induce in the relative volatility of the system, which is also discussed in detail in the paper of Pereiro *et al.*[4]. The ILs with the anions $[Ac]^-$ and $[DCA]^-$ stand as the best candidates, not only due to their high propensity to interact favorably with water/ethanol, but also due to their lower viscosity (when comparing with the IL with the anion chloride), which enhance the mass transfer efficiency of the extractive distillation[30] or the thermal stability when compared with $[BF_4]^-$ [31]. The strong effect of water upon the viscosity of the ILs may further enhance this aspect and, therefore, it must be taken into account in the design of extraction processes.[32]

The experimental determination of VLE data, aiming at disclosing the ILs activity-structure relationship, is an impractical task if one takes into account the large number of potential ILs that can be prepared by the combination of available cations and anions. To overcome this difficulty, group contribution methods (UNIQUAC[10], UNIFAC[33]), other activity coefficient models (NRTL[10,18,34–36]) or equations of state (for example, The Perturbed-Chain Statistical Association Theory (PC-SAFT)[21]) are commonly applied to correlate experimental data aiming at predicting other systems not previously studied, or predictive models such as COSMO-RS[12,37–40] have been used to scan the ILs in the quest for the best entrainers. Process simulators, such as Aspen Plus, can then be applied for an evaluation of the process and its optimization[2,30].

Additionally, the use of molecular dynamics (MD) simulations has also been reported.[41,42] This computational approach allows the description of real systems at the atomic level, providing an understanding of the molecular interactions that take place.[43] This approach has the advantage of being capable of describing the dynamic behavior of systems, as well as, to predict its thermodynamic and transport properties.[44]

Regarding the large variety of ILs, cyano-based ILs present a set of properties of great interest like low melting points and reduced viscosities[45] and a surprisingly wide hydrogen bond ability presenting themselves either as good solvents for carbohydrates (*e.g.*, when the IL anion is $[DCA]^-$), or as water immiscible (*e.g.*, when the IL anion is $[TCB]^-$). They have been studied for many specific applications, such as their extracting solvent ability for a variety of compounds, *e.g.*, compounds in

biomass (phenolic compounds,[46] carbohydrates[47,48] and sugar alcohols[49]), aromatic-aliphatic compounds[12], and were also shown to successfully extract alcohols from fermentation broth[12,18,50].

In the present chapter, aiming at complementing the study of the binary systems composed of CN-based ILs with water, a systematic study on isobaric VLE binary system of water and ethanol with the same ILs is performed at pressures ranging from 0.05 to 0.1 MPa. The experimental data will be further compared and discussed, inferring the existent interactions (type/strength) and mechanisms, as well as the influence of increasing number of CN-groups in the anion, with those estimated from activity coefficients data, COSMO-RS and MD simulations. The MD simulations address only the systems composed of ethanol and ILs, but the calculated results are compared with those obtained for water-ILs systems and further discussed.

Methodology

Experimental Section

Materials

Four imidazolium-based ILs containing cyano anions were studied, namely 1-butyl-3-methylimidazolium thiocyanate, [BMIM][SCN], 1-butyl-3-methylimidazolium dicyanamide, [BMIM][DCA], 1-butyl-3-methylimidazolium tricyanomethane, [BMIM][TCN] that were acquired from IoLiTec (Germany) and 1-ethyl-3-methylimidazolium tetracyanoborate, [EMIM][TCB], from Merck KGaA Germany, all with mass fraction purities higher than 98 %. To reduce to negligible values the contents of both water and volatile compounds, high vacuum (10^{-5} mbar), stirring, and moderate temperature (303 K) for a period of at least 48 h were applied prior to the measurements. The final IL water content was determined with a Metrohm 831 Karl Fisher coulometer with an associated uncertainty of ±3 μg, using the analyte Hydranal – Coulomat AG from Riedel-de Haën), indicating a water mass fraction lower than 30×10^{-6}. The purities of each ionic liquid were further checked by ^{1}H and ^{13}C NMR. The ethanol used was obtained from Merck with mass fraction purity higher than 99.8 %. Being highly hygroscopic, the ethanol was kept immersed in molecular sieves to assure low water content. Furthermore, between new samples, the ionic liquid was kept under low vacuum (10^{-2} mbar). In all experiments, water was double distilled, passed by a reverse osmosis system and further treated with a MilliQ plus 185 water purification apparatus.

VLE measurement - Apparatus and Procedures

VLE measurements were made with an isobaric microebulliometer at different pressures: 0.05, 0.07, and 0.1 MPa. The apparatus used here and the methodology adopted has been previously described in detail[17]. The equilibrium temperature of the liquid phase was measured, with an uncertainty of 0.2 K, with a fast response glass-sealed Pt100 class 1/10, which was calibrated prior to the measurements by comparison with a NIST-certified Fluke RTD25 standard thermometer, with an uncertainty less than 2×10^{-2} K. The internal pressure of the ebulliometer was kept constant through a vacuum pump Buchi V-700 and a V-850 Buchi pressure monitoring and controller unit. The system pressure was monitored by a MKS, model 728A, Baratron type capacitance manometer, with temperature regulation at 100 ºC to avoid solvent

condensation and with an accuracy of 0.5 %. Only when the equilibrium temperature was constant for a period of at least 30 min, the equilibrium conditions were assumed. The mixture composition was determined through an Anton Paar Abbemat 500 Refractometer, with an uncertainty of 2×10^{-5} nD, using a calibration curve previously established. The adequacy of the apparatus to measure this type of systems was previously confirmed.[15] Additionally, to test the apparatus, measurements of the VLE of pure compounds (ethanol, water, p-xylene, and decane) covering the temperature range of interest for the water+IL and ethanol+IL systems studied in this work were carried out. It was observed an uncertainty in the boiling temperatures of 0.2 K.

Density measurements (Ethanol + IL systems)

In this work, mixtures of [BMIM][SCN], [BMIM][DCA], [BMIM][TCN] and [EMIM][TCB] with ethanol were prepared gravimetrically, with an uncertainty of $\pm10^{-5}$ g, for subsequent measurement of density. In order to guarantee homogenization, mixtures were kept at constant stirring for 24 h, at room temperature in closed vials to minimize moisture absorption.

An automated SVM 3000 Anton Paar rotational Stabinger viscosimeter-densimeter was used to measure density data, at atmospheric pressure and at the temperature of 298.15 K. The viscosimeter-densimeter equipment uses Peltier elements for fast and efficient thermostatization, which has been detailed in Chapter 3.1. The uncertainty in temperature is within ± 0.02 K and the absolute uncertainty for density is ±0.5 kg·m^{-3}. Obtained density data are compiled in Table C.1 at Appendix C.

Computational Section

COSMO-RS

The COSMO-RS is a unique tool for predicting the thermodynamic properties of mixtures on the basis of unimolecular quantum chemical calculations for the individual molecules[51]. COSMO-RS combines the electrostatic advantages and the computational efficiency of the quantum chemical dielectric continuum solvation model COSMO with a statistical thermodynamics approach, based on the results of the quantum chemical calculations.[51,52] The

standard procedure of COSMO-RS calculations consists of two steps: quantum chemical COSMO calculations for all the molecular species involved, and COSMO-RS calculations.[51,52] Following the two-step procedure, COSMO-RS models have been applied and proved to be an excellent tool to evaluate qualitatively the strength of the interactions established by ILs with other compounds (binary or ternary systems), and consequently to predict their VLE[37,40,53,54], activity coefficients[55–58], liquid-liquid equilibria (LLE)[7,8,59], among other properties[60]. Therefore, COSMO-RS is going to be applied to our experimental VLE data, and used to further understand the molecular level interactions as discussed below.

Molecular dynamics simulations

Molecular dynamics simulations were performed with the GROMACS[61] code, version 4.5.4, for the binary mixtures composed of ethanol and [BMIM][SCN], [BMIM][DCA], [BMIM][TCN] and [EMIM][TCB], at IL mole fraction of 0.2, 0.4, 0.6 and 0.8.

For all considered systems, after energy minimization and equilibration runs (10ns) within the canonical ensemble (NVT), followed by a production run of 20 ns, within the isothermal-isobaric (NPT) ensemble. The latter considered a constant temperature of 298.15 K, maintained using the Nosé-Hoover[62,63] thermostat, and a constant pressure kept at 1 bar with the Parrinello-Rahman[64] barostat. The intermolecular interaction energy between pairs of neighboring atoms was calculated using the Lennard-Jones and the point-charge Coulomb potentials for describing dispersion/repulsion and electrostatic forces, respectively. Lennard-Jones and Coulombic interactions were defined setting the cutoffs to 1.2 and 1.0 nm, respectively, and long-range corrections for energy and pressure were also applied. Rigid constraints were enforced on all bonds lengths.

The force field parameters for the $[BMIM]^+$ and $[EMIM]^+$ cations, as well as for the $[SCN]^-$ anion are those discussed in Chapter 3.1 and published in our previous work[65]. The potential parameters for the $[DCA]^-$ and $[TCN]^-$ anions were taken from the OPLS-AA force field[66,67], and the $[TCB]^-$ anion were taken from the work of Koller *et al.*[68]. The atomic charges for the IL cations and anions were recalculated with the CHelpG scheme[69] using a geometry optimized with DFT (minimum energy among different configurations), for each IL ion pair, in the gas phase as performed previously for other systems involving ILs.[44,65] The DFT calculations were performed at the B3LYP/6-311+G(d) level of theory[70] with the Gaussian 09 code.[71] The total charges on the cations and anions were ±0.804 *e* for [BMIM][SCN], ±0.826 *e* for

[BMIM][DCA], ±0.882 *e* for [BMIM][TCN] and ±0.889 *e* for [EMIM][TCB]. The full sets of atomic charges for each IL are compiled in Tables B.2 to B.5 in the Appendix B (related to previous chapter), where the combination of the different force fields applied for each cation and anion. For the ethanol molecules, the force field parameters were taken from the OPLS-AA force field.[66,67]

For validation of the applied force field, density and enthalpy of vaporization were calculated. The latter was obtained according to equation 3.3.1,

$$\Delta H^{vap} = RT - \left(U^{liq} - U^{vap}\right) \quad (3.3.1)$$

where ΔH^{vap} is the enthalpy of vaporization, R is the ideal gas constant, T is the temperature, U^{vap} and U^{liq} are the molar internal energies of the vapor/gas and of the liquid phases, respectively. To reproduce the gas phase, isolated IL ion pairs were considered and simulations were performed at the same temperature of the liquid phase.

In addition, density, radial and spatial distributions functions, and coordination numbers were estimated from the MD trajectories for all mixtures considered.

Results and Discussion

VLE measurements and COSMO-RS predictions

Isobaric VLE data of the binary systems [BMIM][SCN], [BMIM][DCA], [BMIM][TCN] and [EMIM][TCB] with water and ethanol were measured at 0.1, 0.07 and 0.05 MPa, and are reported in Tables 3.3.1 to 3.3.8 and depicted in Figures 3.3.1 and 3.3.2 along with COSMO-RS predictions. The experimental boiling temperature is represented as function of the mole fraction of water/ethanol and compared with the COSMO-RS predictions, in the region of complete miscibility. The COSMO-RS prediction for the binary system [[BMIM][SCN], [BMIM][DCA], [BMIM][TCN] and [EMIM][TCB] with water and ethanol are found to be in close agreement with the experimental boiling points only for water/ethanol mole fractions higher than 0.8. Afterwards, the quality of the predictions degrades with the ILs concentration, for which only a qualitative prediction is achieved, as observed in previous works[55,72].

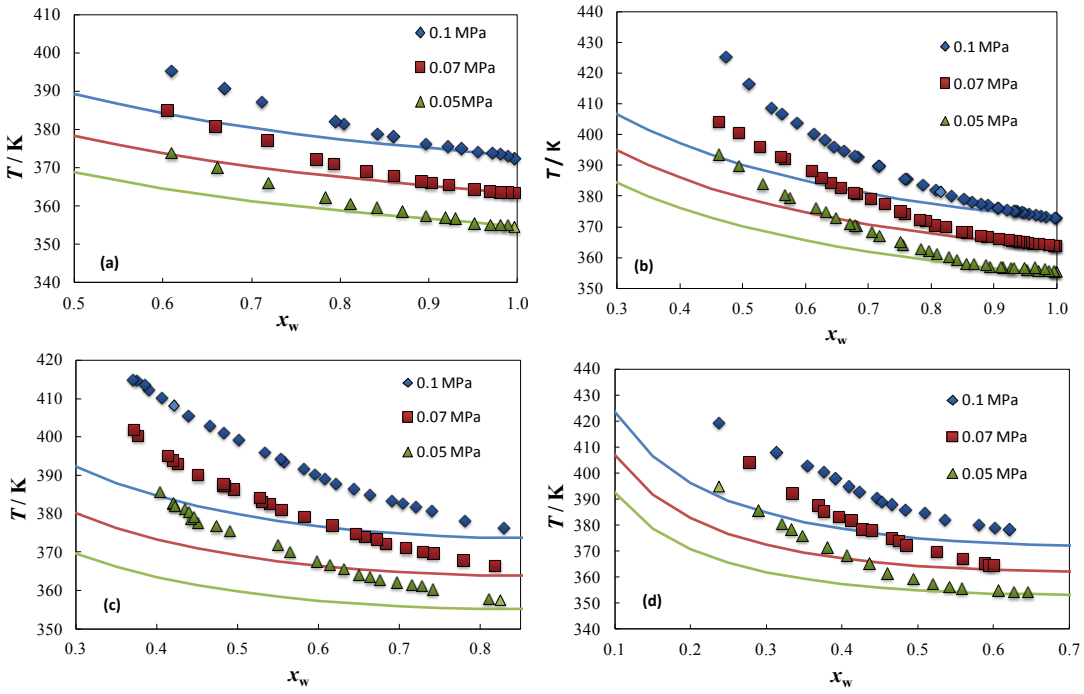

Figure 3.3.1 - Isobaric temperature-composition diagram of (a) [BMIM][SCN]+water, (b) [BMIM][DCA]+water, (c) [BMIM][TCN]+water, (d) [EMIM][TCB]+water. The solid lines represent COSMO-RS predictions.

For the studied systems, and to the best of our knowledge, the VLE data is here reported for the first time. Orchilles et al.[28] reported VLE data for the binary mixture for [BMIM][DCA] with water and ethanol that, in comparison with that of [BMIM][DCA], denotes the well-established weak cation influence on the systems boiling temperatures, within the range of mole fraction investigated, as depicted in Figure C.1 and C.2 at Appendix C. The isobaric VLE data for [BMIM][SCN]+water at 0.01 MPa was previously reported[21] but is included here for comparison with the other CN-based ILs. Figures 3.3.1 and 3.3.2 report the VLE of the studied systems as a function of composition, temperature and pressure. It can be seen that pressure does not have a strong influence on the boiling-point elevation dependency with the concentration, as shown by the parallel behavior of the temperature-composition equilibrium curves at the different pressures (effects on activity coefficients can be observed in Figure C.3).

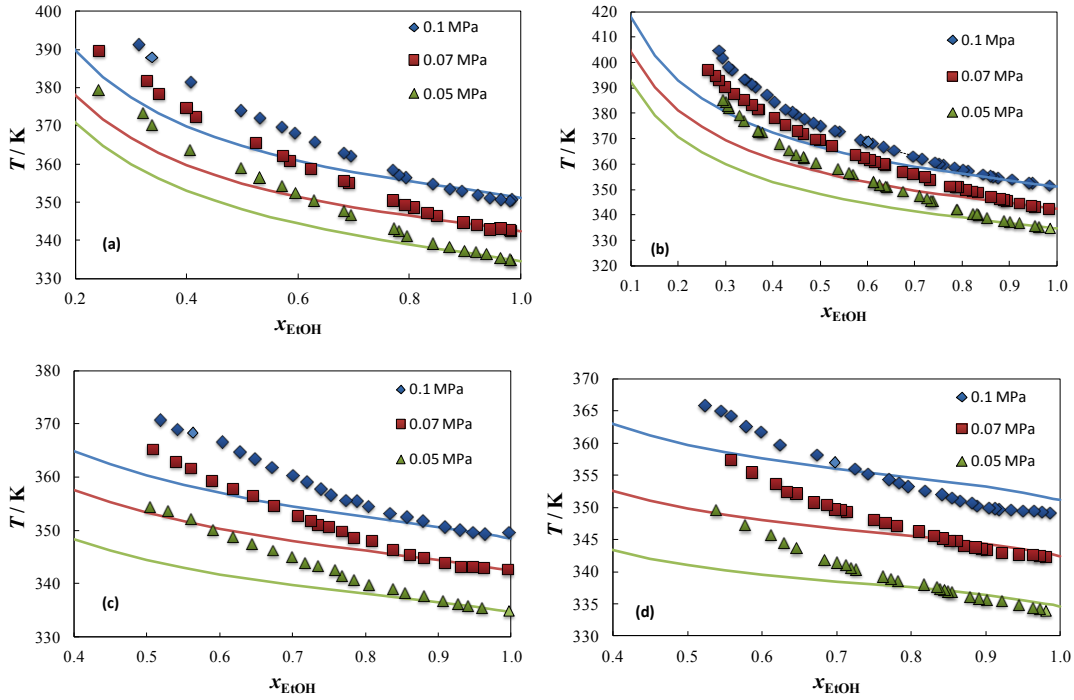

Figure 3.3.2 - Isobaric temperature-composition diagram of (a) [BMIM][SCN]+ethanol, (b) [BMIM][DCA]+ethanol, (c) [BMIM][TCN]+ethanol, (d) [EMIM][TCB]+ethanol. The solid lines represent COSMO-RS prediction.

The measured boiling temperatures decrease with increasing solvent concentration at all pressures investigated, as shown in Figures 3.3.1 and 3.3.2, and the influence of ILs in the boiling temperature of both water and ethanol results in the following trend, [BMIM][DCA] < [BMIM][SCN] < [BMIM][TCN] < [EMIM][TCB], which is identical to the trend of mutual solubility of water and $[BMpyr]^+$ cation-based ILs found and reported by Królikowska *et al.*[73] ($[DCA]^-$ < $[TCN]^-$ < $[TCB]^-$).

Generally, as it is well established, the anion plays a primordial role in the IL interaction with water.[74,75] Regarding the studied ILs, the imidazolium cation was fixed with the aim of studying the anion interactions with water or ethanol. The hydrogen bonding capability of the cyano group with water/ ethanol could be expected to increase with the number of cyano groups in the anion. However, although the expected increased interaction is actually observed from [BMIM][SCN] to [BMIM][DCA], a reversed behavior is observed for the other two compounds displaying further increase in the number of cyano groups. As shown in Chapter 3.2, using COSMO-RS (sigma profile and potential), the anion $[DCA]^-$ is more polar than $[SCN]^-$, which suggests that the former will have higher propensity to establish hydrogen bonds with H-bond donors than $[SCN]^-$. It was found also that

by increasing the number of cyano groups from $[DCA]^-$ to $[TCN]^-$ and to $[TCB]^-$, the ability of these anions to act as H-bond acceptors decrease. As a consequence, it is expected that $[DCA]^-$ presents stronger interactions with water/ethanol than $[SCN]^-$, $[TCN]^-$ and $[TCB]^-$.

Thermodynamic Modeling

The effect of IL on the non-ideality of a solution can be expressed by the activity coefficient of component *i*, γ_i, which can be estimated from the vapor liquid equilibrium data by the equation,

$$\gamma_i = \frac{y_i \emptyset_i p}{x_i \emptyset_i^s p_i^s} \tag{3.3.2}$$

where p and p_i^s are the pressure of the system and the saturation pressure of the pure component *i* at the system temperature, y_i and x_i represent the mole fractions of component *i* in the vapor and liquid phases, respectively, $\emptyset_i$ is the fugacity coefficient of component *i* in the vapor phase, while $\emptyset_i^s$ is the fugacity coefficient of component *i* in its saturated state. The fugacity coefficients $\emptyset_i$ and $\emptyset_i^s$ are close to unity at the pressures used in this study and, since the IL is non-volatile, the vapor phase is only composed of solvent, which leads to y_i equal to unity. Thus, the activity coefficient of solvent in solution can be simplified as,

$$\gamma_i = \frac{p}{x_i p_i^s} \tag{3.3.3}$$

where subscript *S* refers to solvents such as water or ethanol. The pure component saturation pressure p_i^s, of water and ethanol were estimated using correlations obtained from DIPPR's database[76].

The activity coefficient estimated for the studied systems are given in Tables 3.3.1 to 3.3.8 and depicted in Figure C.3 at system pressures of 0.1, 0.07 and 0.05 MPa. The deviations to ideality follow, as expected, the trend: [BMIM][DCA] < [BMIM][SCN] < [BMIM][TCN] < [EMIM][TCB]. For the ethanol containing mixtures the activity coefficient data suggest that the interactions are similar to those present in aqueous systems with the deviation to ideality following the trend [BMIM][DCA] < [BMIM][SCN] < [BMIM][TCN] < [EMIM][TCB], although the differences between [BMIM][DCA]

and [BMIM][SCN], as well as between [BMIM][TCN] and [EMIM][TCB], are not as clear as in aqueous systems where the hydrogen bonding is more intense.

Table 3.3.1. Experimental isobaric VLE data for the system [BMIM][SCN] (1) + water (2) at temperature *T*, liquid mole fraction *x*, and system pressures 0.1, 0.07 and 0.05 MPa.

x_2	*T*/K	γ_2	x_2	*T*/K	γ_2	x_2	*T*/K	γ_2
	0.1 MPa			0.07 MPa			0.05 MPa	
0.9957	372.67	1.0100	0.9954	363.46	0.9944	0.9956	354.69	1.0004
0.9891	373.38	0.9913	0.9889	363.79	0.9886	0.9886	355.14	0.9896
0.9809	373.66	0.9887	0.9808	363.87	0.9909	0.9808	355.19	0.9935
0.9715	373.93	0.9887	0.9680	364.09	0.9957	0.9687	355.25	1.0035
0.9553	374.30	0.9924	0.9505	364.47	0.9995	0.9508	355.70	1.0042
0.9368	375.11	0.9844	0.9220	365.71	0.9822	0.9293	356.85	0.9836
0.9209	375.67	0.9819	0.9027	366.16	0.9865	0.9174	357.11	0.9862
0.8961	376.35	0.9823	0.8910	366.70	0.9796	0.8963	357.61	0.9858
0.8596	378.30	0.9607	0.8601	368.15	0.9633	0.8695	358.75	0.9718
0.8416	378.89	0.9615	0.8295	369.3	0.9576	0.8411	359.68	0.9708
0.8041	381.69	0.9119	0.7925	371.14	0.9375	0.8110	360.61	0.9713
0.7946	382.27	0.9030	0.7727	372.30	0.9223	0.7833	362.25	0.9406
0.7107	387.36	0.8534	0.7173	377.41	0.8296	0.7187	366.03	0.8907
0.6690	390.87	0.8107	0.6581	380.87	0.8027	0.6607	370.29	0.8284
0.6088	395.48	0.7706	0.6046	385.26	0.7540	0.6089	373.87	0.7905

Table 3.3.2. Experimental isobaric VLE data for the system [BMIM][DCA] (1) + water (2) at temperature *T*, liquid mole fraction *x*, and system pressures 0.1, 0.07 and 0.05 MPa.

x_2	*T*/K	γ_2	x_2	*T*/K	γ_2	x_2	*T*/K	γ_2
	0.1 MPa			0.07 MPa			0.05 MPa	
0.9982	373.07	0.9941	0.9993	363.97	0.9689	0.9993	355.39	0.9674
0.9973	373.08	0.9937	0.9993	364.09	0.9631	0.9971	355.63	0.9603
0.9830	373.52	0.9935	0.9957	364.2	0.9640	0.9952	355.71	0.9590
0.9745	373.84	0.9918	0.9878	364.37	0.9654	0.9871	355.87	0.9608
0.9662	374.16	0.9880	0.9716	364.58	0.9738	0.9707	355.97	0.9732
0.9553	374.45	0.9901	0.9627	364.75	0.9765	0.9526	356.14	0.9850
0.9477	374.75	0.9884	0.9540	364.95	0.9767	0.9805	356.31	0.9524
0.9440	374.84	0.9863	0.9473	365.17	0.9783	0.9278	356.69	0.9875
0.9373	375.17	0.9818	0.9433	365.30	0.9763	0.9487	356.78	0.9642
0.9329	375.22	0.9837	0.9400	365.34	0.9796	0.9319	356.83	0.9816
0.9310	375.24	0.9841	0.9349	365.42	0.9793	0.9647	356.91	0.9434
0.9209	375.83	0.9735	0.9288	365.62	0.9798	0.9154	357.08	0.9876
0.9068	376.28	0.9780	0.9236	365.92	0.9742	0.9106	357.24	0.9866
0.9059	376.43	0.9710	0.9077	366.31	0.9757	0.8941	357.30	1.0023

0.8896	377.16	0.9668	0.8897	366.92	0.9746	0.8865	357.92	0.9866
0.8792	377.61	0.9591	0.8798	367.36	0.9696	0.8555	358.04	1.0176
0.8644	378.41	0.9508	0.8579	368.45	0.9552	0.8684	358.26	0.9939
0.8524	379.25	0.9348	0.8494	368.79	0.9527	0.8402	359.46	0.9822
0.8320	380.41	0.9232	0.8233	369.98	0.9412	0.8283	360.39	0.9610
0.8157	381.52	0.9077	0.8053	370.69	0.9377	0.8089	361.29	0.9505
0.8073	382.04	0.9011	0.7916	372.19	0.9038	0.7963	362.39	0.9276
0.7859	383.73	0.8736	0.7813	372.39	0.9092	0.7829	362.87	0.9227
0.7610	385.60	0.8453	0.7579	374.41	0.8722	0.7558	364.39	0.9060
0.7580	385.82	0.8450	0.7510	375.20	0.8560	0.7509	365.22	0.8804
0.7155	389.97	0.7818	0.7252	377.63	0.8142	0.7174	367.28	0.8586
0.7165	389.99	0.7817	0.7035	379.30	0.7923	0.7047	368.53	0.8298
0.6829	392.96	0.7445	0.6806	380.94	0.7743	0.6814	370.26	0.8041
0.6790	393.11	0.7459	0.6766	381.08	0.7764	0.6778	370.75	0.7957
0.6612	394.88	0.7238	0.6560	382.75	0.7556	0.6695	371.28	0.7950
0.6453	396.41	0.7070	0.6412	384.27	0.7347	0.6480	373.12	0.7643
0.6313	398.25	0.6835	0.6246	386.05	0.7110	0.6324	374.91	0.7365
0.6123	400.16	0.6639	0.6100	388.19	0.6787	0.6169	376.41	0.7148
0.5858	403.87	0.6208	0.5662	392.26	0.6414	0.5752	379.34	0.6926
0.5624	406.78	0.5933	0.5614	392.82	0.6355	0.5668	380.54	0.6747
0.5451	408.85	0.5757	0.5272	396.16	0.6092	0.5312	383.99	0.6420
0.5087	416.61	0.4960	0.4943	400.88	0.5622	0.4941	389.87	0.5678
0.4729	425.31	0.4215	0.4620	404.36	0.5418	0.4618	393.60	0.5383

Table 3.3.3. Experimental isobaric VLE data for the system [BMIM][TCN] (1) + water (2) at temperature *T*, liquid mole fraction *x*, and system pressures 0.1, 0.07 and 0.05 MPa.

x_2	*T*/K	γ_2	x_2	*T*/K	γ_2	x_2	*T*/K	γ_2
	0.1 MPa			0.07 MPa			0.05 MPa	
0.8279	376.55	1.0590	0.8175	366.62	1.0709	0.8246	357.52	1.0774
0.7797	378.38	1.0552	0.7780	368.06	1.0669	0.8092	357.93	1.0847
0.7385	380.85	1.0236	0.7406	369.83	1.0506	0.7402	360.37	1.0720
0.7197	381.98	1.0109	0.7283	370.35	1.0497	0.7275	361.25	1.0544
0.7028	382.84	1.0055	0.7076	371.23	1.0451	0.7142	361.56	1.0613
0.6905	383.65	0.9941	0.6829	372.39	1.0387	0.6957	362.29	1.0596
0.6627	385.21	0.9843	0.6720	373.37	1.0206	0.6751	362.99	1.0631
0.6427	386.56	0.9707	0.6564	374.14	1.0167	0.6632	363.63	1.0562
0.6205	387.86	0.9626	0.6453	374.90	1.0053	0.6485	364.41	1.0531
0.6059	389.35	0.9391	0.6163	377.22	0.9719	0.6297	365.69	1.0295
0.5945	390.39	0.9254	0.5817	379.35	0.9552	0.6132	366.80	1.0144
0.5806	391.73	0.9106	0.5525	381.30	0.9422	0.5966	367.81	1.0045
0.5568	393.62	0.8933	0.5389	382.62	0.9239	0.5642	370.30	0.9698
0.5520	394.48	0.8769	0.5295	383.35	0.9174	0.5484	372.14	0.9336
0.5322	396.25	0.8615	0.5256	384.16	0.8996	0.4886	375.77	0.9211
0.5000	399.35	0.8334	0.4944	386.63	0.8812	0.4725	376.89	0.9159

0.4813	401.16	0.8194	0.4838	387.43	0.8772	0.4503	377.76	0.9325
0.4654	402.97	0.8017	0.4808	387.55	0.8792	0.4415	378.81	0.9171
0.4382	405.71	0.7849	0.4815	387.99	0.8654	0.4330	381.49	0.8534
0.4207	408.27	0.7586	0.4496	390.10	0.8655	0.4193	382.68	0.8465
0.4057	410.22	0.7436	0.4252	393.07	0.8324	0.4192	383.07	0.8355
0.3891	412.43	0.7279	0.4179	394.13	0.8190	0.4386	380.66	0.8665
0.3846	413.66	0.7111	0.4125	395.17	0.8031	0.4035	385.82	0.7920
0.3739	414.83	0.7072	0.3756	400.51	0.7482	0.4441	379.50	0.8903
0.3697	415.15	0.7095	0.3702	402.15	0.7224	0.4212	382.15	0.8596

Table 3.3.4. Experimental isobaric VLE data for the system [EMIM][TCB] (1) + water (2) at temperature *T*, liquid mole fraction *x*, and system pressures 0.1, 0.07 and 0.05 MPa.

x_2	*T*/K	γ_2	x_2	*T*/K	γ_2	x_2	*T*/K	γ_2
	0.1 MPa			0.07 MPa			0.05 MPa	
0.2374	419.61	0.9747	0.2774	404.15	0.9095	0.2366	395.15	1.0007
0.3132	408.07	1.0229	0.3337	392.21	1.0916	0.2887	385.60	1.1175
0.3535	402.87	1.0566	0.3678	387.66	1.1467	0.3200	380.38	1.2012
0.3758	400.36	1.0722	0.3758	385.42	1.2083	0.3329	378.36	1.2379
0.3911	397.97	1.1082	0.3958	383.26	1.2329	0.3465	376.16	1.2840
0.4083	395.15	1.1586	0.4116	381.98	1.2378	0.3798	371.55	1.3796
0.4231	392.87	1.2013	0.4266	378.58	1.3414	0.4067	368.55	1.4367
0.4453	390.55	1.2304	0.4396	378.06	1.3254	0.4353	365.29	1.5148
0.4524	389.26	1.2640	0.4649	374.93	1.3979	0.4596	361.55	1.6531
0.4652	388.17	1.2734	0.4747	374.03	1.4133	0.4938	359.46	1.6677
0.4827	386.18	1.3100	0.4847	372.36	1.4691	0.5204	357.29	1.7229
0.5092	384.71	1.3036	0.5244	369.86	1.4863	0.5416	356.46	1.7105
0.5349	382.40	1.3409	0.5585	367.18	1.5397	0.5577	355.63	1.7167
0.5800	380.17	1.3340	0.5882	365.27	1.5697	0.6061	354.87	1.6284
0.6011	379.23	1.3293	0.5948	364.82	1.5788	0.6266	354.47	1.6006
0.6200	378.38	1.3256	0.6008	364.58	1.5770	0.6451	354.18	1.5728

Table 3.3.5. Experimental isobaric VLE data for the system [BMIM][SCN] (1) + ethanol (2) at temperature *T*, liquid mole fraction *x*, and system pressures 0.1, 0.07 and 0.05 MPa.

x_2	*T*/K	γ_2	x_2	*T*/K	γ_2	x_2	*T*/K	γ_2
	0.1 MPa			0.07 MPa			0.05 MPa	
0.9823	350.98	1.0157	0.9810	342.71	1.0057	0.9821	334.98	0.9963
0.9806	350.49	1.0374	0.9795	342.93	0.9966	0.9797	335.22	0.9903
0.9626	350.98	1.0366	0.9629	343.24	1.0007	0.9628	335.60	0.9910
0.9430	351.27	1.0460	0.9433	343.15	1.0254	0.9371	336.66	0.9721
0.9211	352.17	1.0337	0.9192	344.15	1.0095	0.9188	337.14	0.9709
0.8924	353.21	1.0307	0.8966	344.82	1.0067	0.8974	337.43	0.9817
0.8703	353.68	1.0377	0.8495	346.60	0.9878	0.8707	338.37	0.9715

0.8405	355.11	1.0168	0.8321	347.44	0.9747	0.8403	339.41	0.9628
0.7941	356.66	1.0143	0.8072	348.72	0.9543	0.7952	341.42	0.9341
0.7807	357.37	0.9972	0.7901	349.53	0.9453	0.7816	342.53	0.9071
0.7705	358.47	0.9694	0.7700	350.74	0.9230	0.7711	343.40	0.8867
0.6934	362.16	0.9384	0.6902	355.36	0.8602	0.6932	346.71	0.8608
0.6807	363.18	0.9172	0.6814	355.80	0.8567	0.6806	347.91	0.8352
0.6284	365.82	0.9031	0.6232	358.92	0.8324	0.6283	350.64	0.8112
0.5931	368.11	0.8919	0.5844	361.00	0.8216	0.5949	352.53	0.7954
0.5704	369.93	0.8701	0.5717	362.18	0.8042	0.5701	354.33	0.7739
0.5314	372.21	0.8647	0.5231	365.63	0.7755	0.5305	356.71	0.7593
0.4962	374.13	0.8673	0.4162	372.71	0.7605	0.4965	359.18	0.7392
0.4065	381.58	0.8269	0.3987	374.88	0.7373	0.4044	363.75	0.7668
0.3380	388.01	0.8108	0.3499	378.50	0.7445	0.3378	370.45	0.7237
0.3128	391.58	0.7848	0.3269	382.06	0.7095	0.3219	373.45	0.6848
0.2411	401.58	0.7576	0.2430	389.97	0.7438	0.2413	379.45	0.7473

Table 3.3.6. Experimental isobaric VLE data for the system [BMIM][DCA] (1) + ethanol (2) at temperature *T*, liquid mole fraction *x*, and system pressures 0.1, 0.07 and 0.05 MPa.

x_2	*T*/K	γ_2	x_2	*T*/K	γ_2	x_2	*T*/K	γ_2
	0.1 MPa			0.07 MPa			0.05 MPa	
0.9836	351.72	0.9932	0.9844	342.81	0.9980	0.9848	334.88	1.0000
0.9477	352.61	0.9985	0.9537	343.47	1.0008	0.9625	335.67	0.9882
0.9397	352.80	0.9985	0.9459	343.53	1.0065	0.9539	335.81	0.9910
0.9040	353.92	0.9937	0.9213	344.69	0.9850	0.9200	336.87	0.9811
0.8751	354.84	0.9897	0.8929	345.68	0.9744	0.9016	337.36	0.9800
0.8652	355.16	0.9908	0.8888	346.08	0.9644	0.8873	337.97	0.9699
0.8599	355.42	0.9861	0.8787	346.42	0.9621	0.8522	339.10	0.9619
0.8431	356.11	0.9776	0.8615	347.24	0.9491	0.8340	340.31	0.9335
0.8126	357.35	0.9685	0.8322	349.06	0.9131	0.8228	340.70	0.9306
0.8007	357.81	0.9679	0.8211	349.34	0.9151	0.8310	340.56	0.9269
0.7830	358.74	0.9538	0.8064	350.07	0.9051	0.7898	342.26	0.9079
0.7595	359.83	0.9441	0.7900	350.94	0.8926	0.7889	342.38	0.9043
0.7514	360.23	0.9402	0.7862	351.17	0.8888	0.7383	345.65	0.8439
0.7420	360.73	0.9356	0.7737	351.54	0.8901	0.7338	345.69	0.8478
0.7158	362.18	0.9184	0.7304	354.20	0.8500	0.7250	346.73	0.8224
0.6948	363.31	0.9088	0.7195	354.97	0.8376	0.7101	347.79	0.8060
0.6555	365.36	0.8954	0.6953	356.31	0.8247	0.6750	349.31	0.7962
0.6341	366.77	0.8792	0.6737	357.28	0.8190	0.6411	351.19	0.7780
0.6104	368.24	0.8679	0.6374	359.69	0.7920	0.6368	351.49	0.7741
0.6009	368.77	0.8627	0.6334	360.12	0.7831	0.6256	352.15	0.7692
0.5958	368.99	0.8652	0.6159	361.21	0.7746	0.6130	352.91	0.7605
0.5849	369.49	0.8642	0.6043	361.96	0.7669	0.6127	353.10	0.7553
0.5402	372.80	0.8370	0.5926	362.64	0.7628	0.5693	356.02	0.7263
0.5312	373.14	0.8414	0.5748	363.91	0.7510	0.5590	356.71	0.7206
0.4999	375.14	0.8337	0.5233	367.12	0.7351	0.5364	358.02	0.7160

0.4857	376.18	0.8277	0.4978	369.42	0.7126	0.4912	360.51	0.7109
0.4660	377.84	0.8180	0.4897	370.04	0.7078	0.4654	362.56	0.6959
0.4476	379.78	0.7988	0.4640	372.03	0.6982	0.4646	362.82	0.6905
0.4405	380.56	0.7911	0.4519	373.36	0.6851	0.4484	363.99	0.6855
0.4266	381.72	0.7867	0.4263	375.66	0.6717	0.4340	365.43	0.6725
0.4032	384.85	0.7529	0.4026	378.38	0.6497	0.4137	368.09	0.6431
0.3863	387.47	0.7223	0.3709	381.51	0.6347	0.3771	372.43	0.6054
0.3632	390.44	0.7027	0.3691	381.66	0.6365	0.3704	372.80	0.6086
0.3537	391.74	0.6915	0.3568	383.24	0.6258	0.3691	373.39	0.5985
0.3419	393.38	0.6820	0.3372	385.43	0.6176	0.3383	377.27	0.5729
0.3396	393.56	0.6823	0.3188	387.72	0.6078	0.3296	379.34	0.5492
0.3127	397.26	0.6643	0.2990	390.54	0.5923	0.3076	382.19	0.5363
0.3059	398.51	0.6527	0.2858	392.96	0.5772	0.3049	383.14	0.5247
0.2927	401.72	0.6235	0.2777	394.74	0.5631	0.2996	384.79	0.5066
0.2853	404.86	0.5851	0.2617	397.08	0.5574	0.2942	385.45	0.5053

Table 3.3.7. Experimental isobaric VLE data for the system [BMIM][TCN] (1) + ethanol (2) at temperature *T*, liquid mole fraction *x*, and system pressures 0.1, 0.07 and 0.05 MPa.

x_2	*T*/K	γ_2	x_2	*T*/K	γ_2	x_2	*T*/K	γ_2
	0.1 MPa			0.07 MPa			0.05 MPa	
0.9965	349.60	1.0672	0.9961	342.68	0.9888	0.9962	335.05	0.9812
0.9631	349.38	1.1162	0.9618	343.01	1.0100	0.9603	335.35	1.0045
0.9466	349.73	1.1199	0.9475	343.22	1.0164	0.9413	335.80	1.0048
0.9294	350.21	1.1168	0.9303	343.24	1.0343	0.9269	336.21	1.0022
0.9090	350.66	1.1228	0.9087	343.82	1.0337	0.9070	336.65	1.0047
0.8779	351.79	1.1108	0.8812	344.73	1.0266	0.8795	337.65	0.9942
0.8565	352.57	1.1044	0.8604	345.41	1.0224	0.8543	338.29	0.9936
0.8339	353.23	1.1055	0.8378	346.35	1.0119	0.8380	338.98	0.9853
0.8035	354.46	1.0949	0.8080	347.96	0.9802	0.8049	339.82	0.9896
0.7883	355.42	1.0756	0.7839	348.64	0.9830	0.7839	340.80	0.9746
0.7727	355.71	1.0852	0.7681	349.82	0.9570	0.7681	341.62	0.9609
0.7532	356.58	1.0737	0.7493	350.61	0.9508	0.7574	342.49	0.9377
0.7381	357.69	1.0506	0.7355	351.16	0.9478	0.7344	343.33	0.9337
0.7198	359.01	1.0251	0.7248	351.75	0.9396	0.7173	344.06	0.9275
0.7008	360.27	1.0056	0.7062	352.73	0.9281	0.6990	344.91	0.9190
0.6714	361.82	0.9911	0.6749	354.67	0.9007	0.6738	346.32	0.8999
0.6487	363.46	0.9662	0.6449	356.42	0.8854	0.6438	347.50	0.8976
0.6268	364.66	0.9594	0.6177	357.82	0.8741	0.6178	348.86	0.8856
0.6033	366.62	0.9290	0.5889	359.43	0.8631	0.5899	350.12	0.8820
0.5626	368.36	0.9359	0.5593	361.58	0.8379	0.5602	352.10	0.8590
0.5424	369.02	0.9484	0.5390	362.98	0.8260	0.5293	353.64	0.8561
0.5179	370.77	0.9345	0.5071	365.19	0.8104	0.5038	354.42	0.9812

Table 3.3.8. Experimental isobaric VLE data for the system [EMIM][TCB] (1) + ethanol (2) at temperature *T*, liquid mole fraction *x*, and system pressures 0.1, 0.07 and 0.05 MPa.

x_2	*T*/K	γ_2	x_2	*T*/K	γ_2	x_2	*T*/K	γ_2
	0.1 MPa			0.07 MPa			0.05 MPa	
0.9851	349.21	1.0932	0.9804	342.29	1.0241	0.9806	333.95	1.0381
0.9752	349.30	1.1003	0.9720	342.46	1.0256	0.9721	334.23	1.0405
0.9642	349.42	1.1076	0.9632	342.60	1.0289	0.9627	334.41	1.0382
0.9498	349.53	1.1194	0.9439	342.80	1.0413	0.9440	334.93	1.0388
0.9334	349.66	1.1332	0.9218	343.04	1.0556	0.9215	335.53	1.0427
0.9181	349.76	1.1441	0.9010	343.37	1.0652	0.9020	335.57	1.0570
0.9119	349.87	1.1469	0.8939	343.60	1.0635	0.8912	335.87	1.0538
0.9034	349.99	1.1521	0.8863	343.84	1.0620	0.8796	336.21	1.0519
0.8879	350.34	1.1560	0.8704	344.16	1.0671	0.8540	336.81	1.0533
0.8810	350.71	1.1482	0.8616	344.75	1.0520	0.8492	337.05	1.0525
0.8657	351.18	1.1469	0.8519	344.75	1.0640	0.8442	337.27	1.0486
0.8537	351.60	1.1509	0.8418	345.16	1.0604	0.8391	337.42	1.0482
0.8408	352.02	1.1495	0.8310	345.61	1.0544	0.8338	337.63	1.0474
0.8192	352.57	1.1535	0.8108	346.26	1.0554	0.8178	338.06	1.0503
0.7944	353.29	1.1565	0.7805	347.12	1.0572	0.7815	338.57	1.0645
0.7830	353.90	1.1460	0.7658	347.67	1.0553	0.7720	338.94	1.0649
0.7700	354.36	1.1448	0.7498	348.16	1.0552	0.7622	339.34	1.0625
0.7419	355.30	1.1458	0.7136	349.38	1.0559	0.7259	340.47	1.0653
0.7249	356.12	1.1364	0.7059	349.56	1.0583	0.7188	340.67	1.0646
0.6971	356.99	1.1434	0.6975	349.78	1.0601	0.7122	341.06	1.0611
0.6736	358.30	1.1261	0.6878	350.38	1.0513	0.7008	341.47	1.0599
0.6231	359.82	1.1431	0.6693	350.83	1.0627	0.6835	341.86	1.0626
0.5979	361.76	1.1154	0.6458	352.16	1.0393	0.6460	343.71	1.0470
0.5781	362.69	1.1151	0.6330	352.48	1.0500	0.6296	344.60	1.0354
0.5586	364.23	1.0912	0.6188	353.71	1.0239	0.6112	345.71	1.0191
0.5442	365.07	1.0855	0.5872	355.47	1.0097	0.5768	347.27	1.0012
0.5224	366.01	1.0933	0.5586	357.45	0.9843	0.5381	349.64	0.9778

Molecular dynamics simulations

Experimental and computational density of mixture comparison

In addition and for complementing the experimental part of this study, MD simulations were performed for the systems containing the CN-based ILs and ethanol. For the aqueous systems containing the same ILs, MD simulations were performed and discussed above (Chapter 3.2).

The density of a system is usually employed to ascertain the quality of a force field to reproduce such system.[77] As mentioned in the computational detail section, other properties are also used to certify the force fields. Herewith, the experimental densities and enthalpies of

vaporization for pure ILs have been considered and, as can be seen in Table C.2 of Appendix C, the corresponding simulated densities are in very good agreement with the experimental ones, but in the case of the enthalpies the agreement is satisfactory only, very probably due to the lack of accuracy of the experimental results caused by difficulties associated to the experimental determination of this property.[44] Furthermore, and making use of density data measured in this study for mixtures of CN-based ILs and ethanol, a comparison between experimental data and density values obtained from our simulations was also made, as compiled in Table C.1 of Appendix C. The maximum deviation obtained was of 3.14 %, suggesting that the force fields adopted provide a good structural description of the mixtures with ethanol, which is the relevant information from the MD simulations that is used to interpret the experimental findings.

Radial distribution function and coordination numbers

Radial distribution function, *g(r)* or RDF, and coordination numbers (Z) are commonly used in MD simulations to evaluate and describe the atomic local structural organization of mixtures. The first gives the probability of finding a particle at the distance *r*, from another particle (considered as the reference), providing a quantitative description of enhancement or depletion of densities of atoms, or groups of atoms, around a selected moiety with respect to bulk values. The second, the coordination number, is the average number of atoms of one type surrounding the reference atom within a cutoff, r_Z, given by the integral of RDF. The cutoff is usually chosen to be the first local minimum of the corresponding RDF. Figures 3.3.3 and C.4 show all the RDFs for the mixtures considered while the Z numbers calculated for all mixtures and type of interactions are compiled in Table 3.3.9.

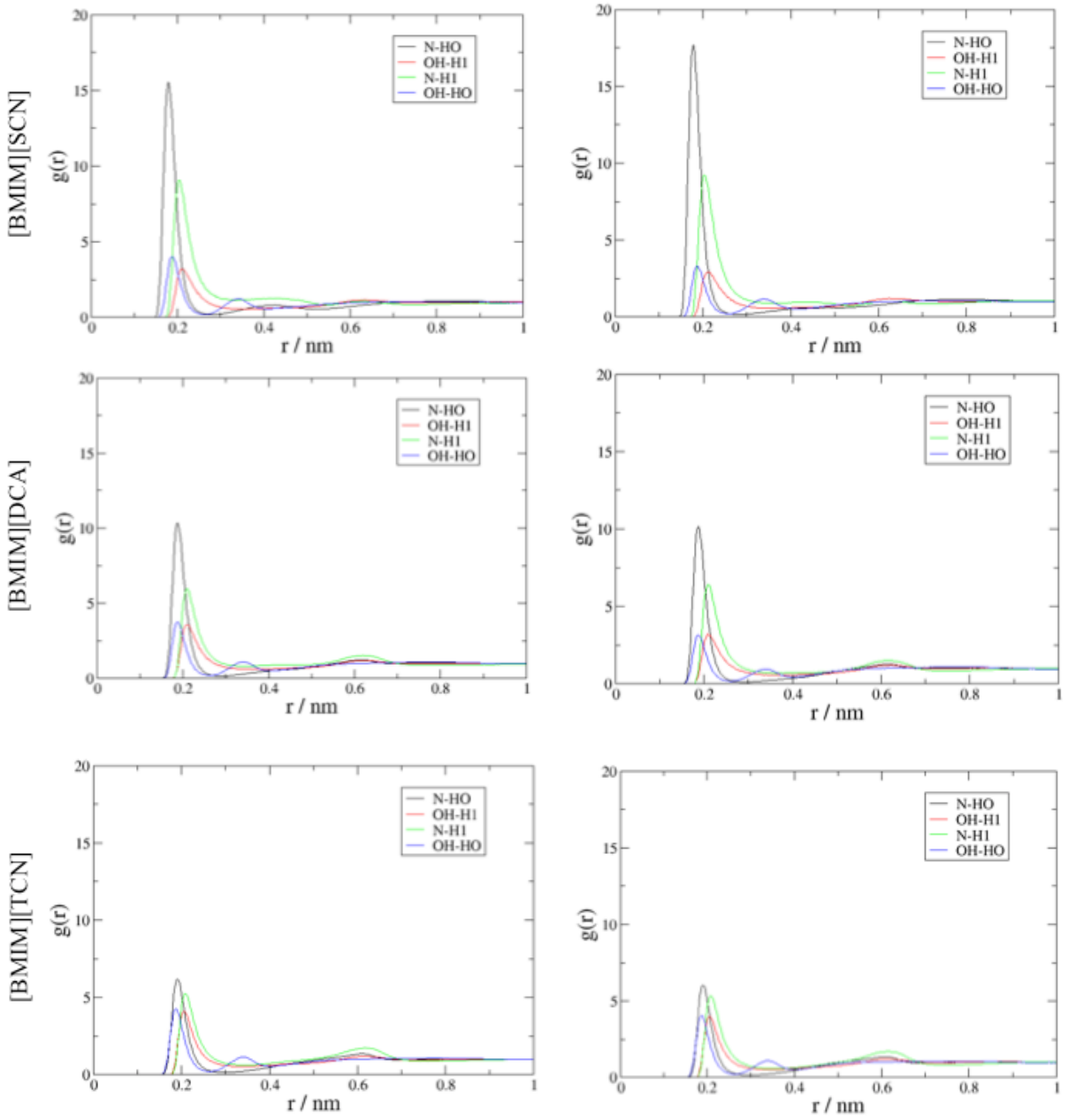
[BMIM][SCN]
[BMIM][DCA]
[BMIM][TCN]
g(r)
r / nm
N-HO
OH-H1
N-H1
OH-HO

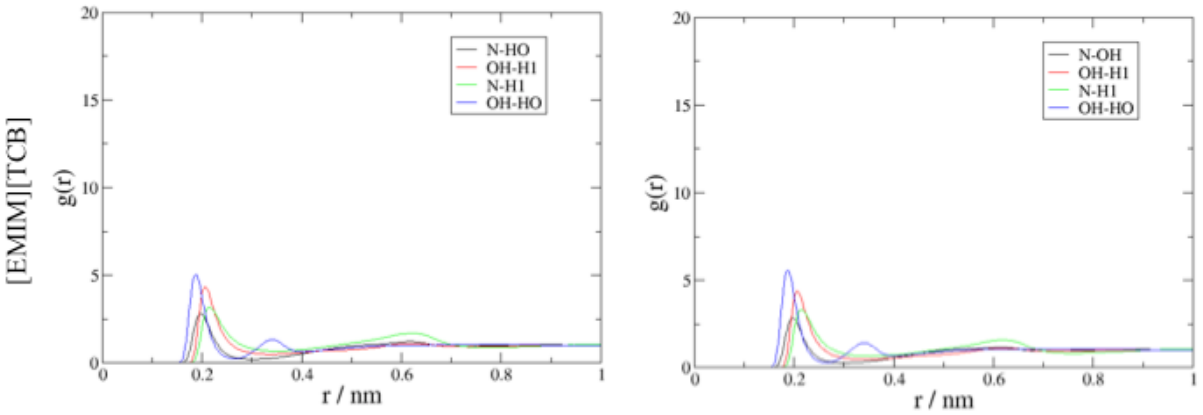

Figure 3.3.3 - Radial distributions functions (RDFs) for a) [BMIM][SCN], b) [BMIM][DCA], c) [BMIM][TCN] and d) [EMIM][TCB], at 0.20 (on the left side) and 0.40 (on the right side) mole fraction of IL and 298.15 K. In each picture is represented all types of interaction, namely RDFs for anion-ethanol (—), cation-ethanol (—), cation-anion (—) and ethanol-ethanol (—) interactions.

The analyses of the anion-solvent, cation-solvent, cation-anion and solvent-solvent interactions were based on the site-to-site RDFs obtained for the N-HO, H1-OH, H1-N and OH-HO pairs, respectively, where N is the nitrogen atom of each anion, H1 is the acidic proton of the cation, HO and OH stands for protons and oxygen atoms in the water molecule, respectively.

The first important feature that can be highlighted is the possibility to verify through the obtained RDFs the mechanism of these interactions, which is the establishment of hydrogen bonds, similar to those occurring in the aqueous systems described in Chapter 3.2. Generally, strong H-bonds are defined when the RDF for a site-to-site Y—H-X interaction, where Y is an oxygen or nitrogen atom and X is an oxygen atom, presents a first minimum (r_z) in a distance smaller than 0.26 nm, while weak H-bonds are defined when the RDF for a site-to-site Y—H-X interaction, where Y is an oxygen or nitrogen atom and X a carbon atom, displays the first minimum in a distance smaller than 0.40 nm.[78] In the systems studied here, the first minimum for anion-solvent and solvent-solvent interactions was found at 0.26 nm while in the case of cation-solvent and cation-anion interactions the first minimum appeared at 0.35 nm. As mentioned previously, this first minimum was used to define the uppermost limit used in the calculation of the coordination numbers reported in Table 3.3.9.

Additionally, Figure 3.3.3 shows that the anion-solvent interaction has a primary role in the interaction occurring between IL and ethanol, which was expected to be common for all CN-based ILs (also observed for aqueous systems), presenting the highest values for the system containing

the anion thiocyanate, followed by $[DCA]^-$, $[TCN]^-$ and finally $[TCB]^-$. Ensuing the anion-solvent interaction and in the same solvation shell, the solvent-solvent interactions occur, being predominant in systems containing the anion $[TCB]^-$. It is worth noting that the RDFs corresponding to the solvent-solvent interactions show a double peak, suggesting the formation of two ethanol solvation shells in all the IL+ethanol systems. In general, the double peak is more pronounced in the system with the anion tetracyanoborate, followed by $[TCN]^- > [SCN]^- > [DCA]^-$. This last trend is also observed for the cation-anion interactions occurring at the second solvation shell. These two latter interactions present the trend that is consistent with the VLE measurements and non-ideality as estimated from the activity coefficients. Simultaneously, at contrary to what has been observed for aqueous systems (Chapter 3.2), the values of *g(r)* corresponding to the interactions established between cation and the solvent suggest that in the case of IL+ethanol systems they are non-negligible.

A more exhaustive comparison between the different systems is possible by the analysis of the coordination numbers, Z, since their values are obtained by taking into account not only the heights of the first peaks in the RDFs, but also their widths and the densities of the different systems. Thus, the values of Z help to clarify the interaction trend within the CN-based ILs and ethanol, providing important additional information concerning the mechanism of interaction between compounds. Table 3.3.9 compiles the calculated coordination numbers for the interactions anion-solvent, cation-solvent, cation-anion, solvent-solvent and finally, IL-solvent. The latter interaction is the sum of the cation-ethanol and anion-ethanol interactions in all range of concentration, enabling to infer general trends of all involved interactions. The first information that can be taken is the dependence of Z with the mole fraction of IL. Results show that, with the exception of cation-anion interactions, with the increase of IL's mole fraction the interaction of type anion-solvent, cation-solvent and solvent-solvent decrease, as shown by a decrease of the respective Z values. Although these results are a consequence of different densities in each system, they suggest that, with the increase of IL's mole fraction, the frequency of cation-anion interactions also increase, hindering the interaction with ethanol.

From the analysis of the Z values obtained for the IL-ethanol interactions, it arises that the highest values are found for the system with the anion $[DCA]^-$, suggesting more favorable interactions with ethanol, which is in close agreement with the activity coefficients reported in the present study (this was also observed for the aqueous systems with the same ILs). Moreover, with the exception of the anion thiocyanate, the propensity to interact with ethanol suggested from the height of the first peak in the RDFs and by the Z values is $[DCA]^- > [TCN]^- > [TCB]^-$. A similar

trend was observed for the aqueous systems, suggesting that an increase of CN-groups in the anion hinders the interaction with polar solvents (water and ethanol), consistent with the non-ideality observed in these systems. Additionally, these results are consistent with the CHelpG atomic charges calculated for the nitrogen atoms in the CN groups (the mediators of the interactions between the anion and water or ethanol) which become less negative in the order $[DCA]^-$ > $[SCN]^-$ > $[TCN]^-$ > $[TCB]^-$, respectively, with values of -0.723 *e*, -0.658 *e*, -0.638 *e* and -0.487 *e*. The differences in the CHelpG charges are directly related with the symmetry of the anion and with the presence of different central atoms in each anion, *i.e.*, sulfur ($[SCN]^-$), nitrogen ($[DCA]^-$), carbon ($[TCN]^-$) and boron ($[TCB]^-$), which lead to different charge delocalization, and hence, different abilities of the anions to establish H-bonds with water or ethanol molecules. Remarkably, the ordering of the partial charges in the nitrogen atoms from the CN-groups in the anions of the ILs agrees with the ordering obtained for VLE and activity coefficient information suggesting a strong relationship between these two parameters.

Table 3.3.9. Coordination numbers (Z) from the RDF peaks at distance below r_Z nm, for anion-ethanol, cation-ethanol, cation-anion and ethanol-ethanol interactions, at each system and different IL mole fraction, addressed in this study.

[BMIM][SCN]+CH_3CH_2OH

	anion-solvent		cation-solvent		cation-anion		solvent-solvent		IL-solvent
x_{IL}	*rz*	Z	r_Z	Z	r_Z	Z	r_Z	Z	*Z(total)*
0.2	0.26	1.44	0.35	1.08	0.35	0.55	0.26	0.46	2.52
0.4	0.26	0.91	0.35	0.57	0.35	0.84	0.26	0.22	1.48
0.6	0.26	0.48	0.35	0.29	0.35	1.04	0.26	0.10	0.77
0.8	0.26	0.20	0.35	0.10	0.35	1.21	0.26	0.03	0.20

[BMIM][DCA]+CH_3CH_2OH

	anion-solvent		cation-solvent		cation-anion		solvent-solvent		IL-solvent
x_{IL}	r_Z	Z	r_Z	Z	r_Z	Z	r_Z	Z	*Z(total)*
0.2	0.26	2.08	0.35	1.04	0.35	0.75	0.26	0.41	3.12
0.4	0.26	1.13	0.35	0.55	0.35	1.17	0.26	0.20	1.68
0.6	0.26	0.58	0.35	0.28	0.35	1.39	0.26	0.09	0.86
0.8	0.26	0.23	0.35	0.11	0.35	1.53	0.26	0.02	0.34

[BMIM][TCN]+CH_3CH_2OH

	anion-solvent		cation-solvent		cation-anion		solvent-solvent		IL-solvent
x_{IL}	r_Z	Z	r_Z	Z	r_Z	Z	r_Z	Z	*Z(total)*
0.2	0.26	1.95	0.35	0.90	0.35	0.87	0.26	0.43	2.85
0.4	0.26	1.08	0.35	0.50	0.35	1.32	0.26	0.23	1.59

0.6	0.26	0.56	0.35	0.25	0.35	1.57	0.26	0.11	0.81
0.8	0.26	0.23	0.35	0.10	0.35	1.72	0.26	0.05	0.33

[EMIM][TCB]+CH_3CH_2OH

	anion-solvent		cation-solvent		cation-anion		solvent-solvent		IL-solvent
x_{IL}	r_Z	Z	r_Z	Z	r_Z	Z	r_Z	Z	*Z(total)*
0.2	0.26	1.54	0.35	0.95	0.35	1.01	0.26	0.53	2.49
0.4	0.26	0.89	0.35	0.53	0.35	1.52	0.26	0.33	1.42
0.6	0.26	0.48	0.35	0.28	0.35	1.82	0.26	0.20	0.77
0.8	0.26	0.21	0.35	0.11	0.35	2.02	0.26	0.09	0.32

Spatial distribution function

For attaining a tri-dimensional (3D) visualization of how each anion interacts with ethanol, the spatial distribution functions (SDFs, a 3D representation of the probability of finding a particle at a certain position) were calculated for all considered mixtures and are depicted, by mole fraction of IL, in Figure 3.3.4. The SDFs were built and analyzed with the TRAVIS (trajectory analyzer and visualizer) computer program[79] considering only the hydrogen atom from the hydroxyl group of ethanol molecules surrounding each anion of the different ILs considered in this study. Isosurfaces for ethanol (iceblue wired surfaces) were obtained with an isovalue of 8 particles·nm^{-3} at 0.2 mole fraction of IL.

Recognizable at all mole fraction of IL, interactions of ethanol with the anions $[SCN]^-$ and $[DCA]^-$ are established preferentially with the nitrogen atoms of the cyanide groups from the anions (excluding the nitrogen atom of the core of $[DCA]^-$ but also with the sulfur atom of $[SCN]^-$).

Nevertheless, the volume of the SDFs for ethanol interacting with the different anions (Figure) decreases with the increase of the number of CN-groups in the anion, suggesting that in the case of the anions with less CN-groups, the interaction is more likely to occur, which is consistent with the analyses made throughout this chapter.

In conclusion, the results from the MD simulations suggest that the increase of the number of CN-groups leads to a decrease of the interactions with ethanol, which is related to the increasing hydrophobicity of the anions. This behavior is similar to that observed for the aqueous systems and supports the non-ideality observed in the VLE and the activity coefficients.

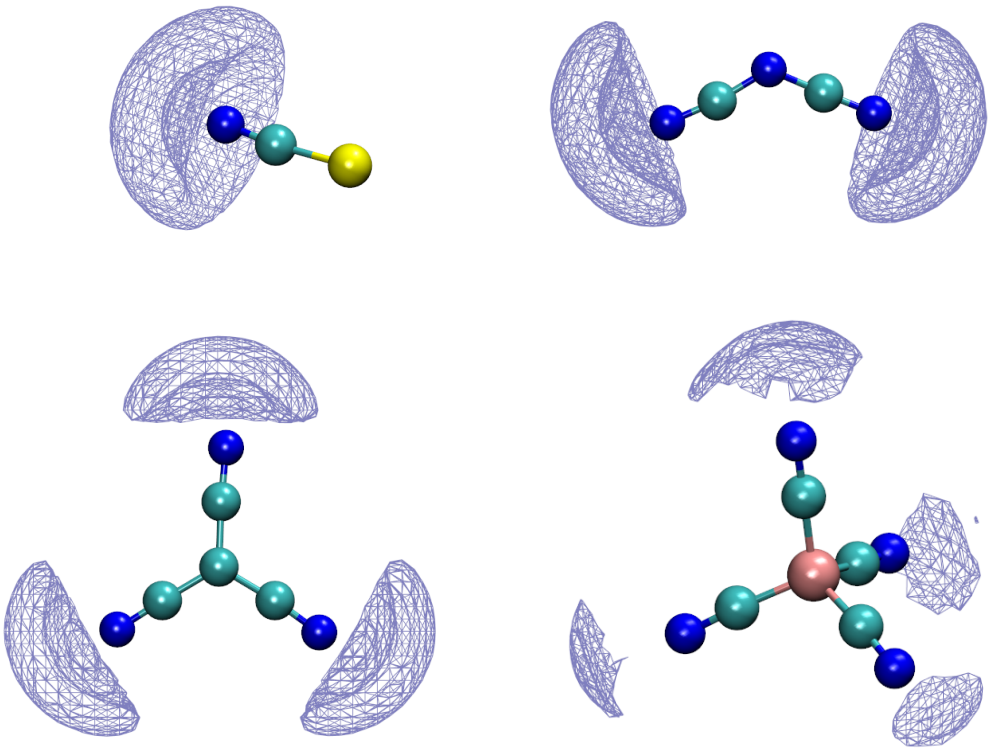

Figure 3.3.4 - Spatial distribution functions (SDFs) for the mixture [BMIM][SCN] (above, left side), [BMIM][DCA] (above, right side), [BMIM][TCN] (down, left side) and [EMIM][TCB] (down, right side) and ethanol, at 0.20 mole fraction of IL. Each anion is the center element, surrounded by hydrogen atoms from the hydroxyl group of ethanol molecules (iceblue wired surface). Color code for spheres is: Cyan is carbon; blue is nitrogen; yellow is sulfur; and pink is boron.

Conclusions

Isobaric VLE data for seven water/ethanol + imidazolium based IL systems containing cyano group at three different pressures were measured and reported in this chapter. Results indicate that the imidazolium-based ILs studied cause boiling-point elevations of different degrees according to the interaction strengths between water/ethanol and the IL. Using the VLE data, activity coefficients were estimated aiming at evaluating the non-ideality of the systems considered in this study. The results obtained suggest that, for both water and ethanol systems, the ability of the anions to interact with the solvent decreases with increasing number of cyano groups, with the system containing the anion $[DCA]^-$ presenting the highest ability to establish favorable interactions.

MD simulations were performed for systems composed of ethanol and four different ILs having the an imidazolium-based cation but different anion. The MD trajectories were used to calculate radial and spatial distribution functions and also coordination numbers, which were used to infer the mechanism of interaction established between ethanol and the ILs. Although presenting slightly different trends, all the calculated properties, along with activity coefficients data, seem to agree and support the experimental findings, where an increase of the number of CN-groups in the ILs' anion leads to a decrease in the propensity to interact with polar solvents with a concomitant increase of the hydrophobicity of the anions.

Finally, from the tested ILs, the IL with the anion $[DCA]^-$ arises as the most appropriate solvent for polar systems having hydrogen bonds.

References

(1) Huang, H. J.; Ramaswamy, S.; Tschirner, U. W.; Ramarao, B. V. *Sep. Purif. Technol.*, **2008**, *62*, 1–21.

(2) Lei, Z.; Dai, C.; Zhu, J.; Chen, B. *AIChE J.*, **2014**, *60*, 3312–3329.

(3) Lei, Z. G.; Li, C. Y.; Chen, B. H. *Sep. Purif. Rev.*, **2003**, *32*, 121–213.

(4) Pereiro, A. B.; Araújo, J. M. M.; Esperança, J. M. S. S.; Marrucho, I. M.; Rebelo, L. P. N. *J. Chem. Thermodyn.*, **2012**, *46*, 2–28.

(5) Vane, L. M. *Biofuels, Bioprod. Biorefining*, **2008**, *2*, 553–588.

(6) Peng, Y.; Fu, J.; Lu, X. *Fluid Phase Equilib.*, **2014**, *363*, 220–227.

(7) Ferreira, A. R.; Freire, M. G.; Ribeiro, J. C.; Lopes, F. M.; Crespo, J. G.; Coutinho, J. A. P. *Ind. Eng. Chem. Res.*, **2011**, *50*, 5279–5294.

(8) Ferreira, A. R.; Freire, M. G.; Ribeiro, J. C.; Lopes, F. M.; Crespo, J. G.; Coutinho, J. A. P. *Ind. Eng. Chem. Res.*, **2012**, *51*, 3483–3507.

(9) Seiler, M.; Jork, C.; Kavarnou, A.; Arlt, W.; Hirsch, R. *AIChE J.*, **2004**, *50*, 2439–2454.

(10) Tsanas, C.; Tzani, A.; Papadopoulos, A.; Detsi, A.; Voutsas, E. *Fluid Phase Equilib.*, **2014**, *379*, 148–156.

(11) Kirchner, B. *Topics in Current Chemistry*; Meijere, V. B. A. De; Kessler, K. N. H. H.; Ley, J. L. S. V; Schreiber, M. O. S.; Vogel, B. M. T. P.; Wong, F. V. H., Eds.; Springer: Germany, 2009.

(12) Gutiérrez, J. P.; Meindersma, G. W.; de Haan, A. B. *Ind. Eng. Chem. Res.*, **2012**, *51*, 11518–11529.

(13) Jork, C.; Seiler, M.; Beste, Y. A.; Arlt, W. *J. Chem. Eng. Data*, **2004**, *49*, 852–857.

(14) Beste, Y.; Eggersmann, M.; Schoenmakers, H. *Chemie Ing. Tech.*, **2005**, *77*, 1800–1808.

(15) Lei, Z.; Arlt, W.; Wasserscheid, P. *Fluid Phase Equilib.*, **2006**, *241*, 290–299.

(16) Revelli, A.-L.; Mutelet, F.; Jaubert, J.-N. *J. Chem. Thermodyn.*, **2010**, *42*, 177–181.

(17) Carvalho, P. J.; Khan, I.; Morais, A.; Granjo, J. F. O.; Oliveira, N. M. C.; Santos, L. M. N. B. F.; Coutinho, J. A. P. *Fluid Phase Equilib.*, **2013**, *354*, 156–165.

(18) Ge, Y.; Zhang, L.; Yuan, X.; Geng, W.; Ji, J. *J. Chem. Thermodyn.*, **2008**, *40*, 1248–1252.

(19) Calvar, N.; Gonzalez, B.; Gomez, E.; Dominguez, A. *J. Chem. Eng. Data*, **2006**, *51*, 2178–2181.

(20) Geng, W.; Zhang, L.; Deng, D.; Ge, Y.; Ji, J. *J. Chem. Eng. Data*, **2010**, *55*, 1679–1683.

(21) Passos, H.; Khan, I.; Mutelet, F.; Oliveira, M. B.; Carvalho, P. J.; Santos, L. M. N. B. F.; Held, C.; Sadowski, G.; Freire, M. G.; Coutinho, J. A. P. *Ind. Eng. Chem. Res.*, **2014**, 3737–3748.

(22) Calvar, N.; González, B.; Gómez, E.; Domínguez, A. *Fluid Phase Equilib.*, **2007**, *259*, 51–56.

(23) Zhang, L.; Ge, Y.; Ji, D.; Ji, J. *J. Chem. Eng. Data*, **2009**, *54*, 2322–2329.

(24) Calvar, N.; González, B.; Gómez, E.; Domínguez, Á. *J. Chem. Eng. Data*, **2008**, *53*, 820–825.

(25) Calvar, N.; González, B.; Gómez, E.; Domínguez, A. *J. Chem. Eng. Data*, **2009**, *54*, 1004–1008.

(26) Calvar, N.; Gomez, E.; Gonzalez, B.; Dominguez, A. *J. Chem. Eng. Data*, **2010**, *55*, 2786–2791.

(27) Orchilles, A. V; Miguel, P. J.; Vercher, E.; Martinez-Andreu, A. *J. Chem. Eng. Data*, **2010**, *55*, 1669–1674.

(28) Orchillés, A. V.; Miguel, P. J.; Llopis, F. J.; Vercher, E.; Martínez-Andreu, A. *J. Chem. Eng. Data*, **2011**, *56*, 4875–4880.

(29) Orchillés, A. V.; Miguel, P. J.; Vercher, E.; Martínez-Andreu, A. *J. Chem. Eng. Data*, **2010**, *55*, 1669–1674.

(30) Quijada-Maldonado, E.; Meindersma, G. W.; de Haan, A. B. *Comput. Chem. Eng.*, **2014**, *71*, 210–219.

(31) Freire, M. G.; Neves, C.; Marrucho, I. M.; Coutinho, J. A. P.; Fernandes, A. M. *J. Phys. Chem. A*, **2010**, *114*, 3744–3749.

(32) Carvalho, P. J.; Regueira, T.; Santos, L. M. N. B. F.; Fernandez, J.; Coutinho, J. A. P. *J. Chem. Eng. Data*, **2009**, *55*, 645–652.

(33) Nebig, S.; Bölts, R.; Gmehling, J. *Fluid Phase Equilib.*, **2007**, *258*, 168–178.

(34) Zhao, J.; Jiang, X.-C.; Li, C.-X.; Wang, Z.-H. *Fluid Phase Equilib.*, **2006**, *247*, 190–198.

(35) Calvar, N.; Gonzalez, B.; Gomez, E.; Dominguez, A. *J. Chem. Eng. Data*, **2008**, *53*, 820–825.

(36) Jiang, X.-C.; Wang, J.-F.; Li, C.-X.; Wang, L.-M.; Wang, Z.-H. *J. Chem. Thermodyn.*, **2007**, *39*, 841–846.

(37) Freire, M. G.; Santos, L. M. N. B. F.; Marrucho, I. M.; Coutinho, J. A. P. *Fluid Phase Equilib.*, **2007**, *255*, 167–178.

(38) Verma, V. K.; Banerjee, T. *J. Chem. Thermodyn.*, **2010**, *42*, 909–919.

(39) Dhanalakshmi, J.; Sai, P. S. T.; Balakrishnan, A. R. *Ind. Eng. Chem. Res.*, **2013**, *52*, 16396–16405.

(40) Freire, M. G.; Ventura, S. P. M.; Santos, L. M. N. B. F.; Marrucho, I. M.; Coutinho, J. A. P. *Fluid Phase Equilib.*, **2008**, *268*, 74–84.

(41) Méndez-Morales, T.; Carrete, J.; Cabeza, O.; Gallego, L. J.; Varela, L. M. *J. Phys. Chem. B*, **2011**, *115*, 11170–11182.

(42) Raabe, G.; Köhler, J. *J. Chem. Phys.*, **2008**, *129*, 144503–144511.

(43) Allen, M. P.; Tildesley, D. J. *Computer Simulation of Liquids*; Oxford University Press, 1987.

(44) Batista, M. L. S.; Coutinho, J. A. P.; Gomes, J. R. B. *Curr. Phys. Chem.*, **2014**, *4*, 151–172.

(45) Neves, C. M. S. S.; Kurnia, K. A.; Coutinho, J. A. P.; Marrucho, I. M.; Lopes, J. N. C.; Freire, M. G.; Rebelo, L. P. N. *J. Phys. Chem. B*, **2013**, *117*, 10271–10283.

(46) Cláudio, A. F. M.; Freire, M. G.; Freire, C. S. R.; Silvestre, A. J. D.; Coutinho, J. A. P. *Sep. Purif. Technol.*, **2010**, *75*, 39–47.

(47) Swatloski, R. P.; Spear, S. K.; Holbrey, J. D.; Rogers, R. D. *J. Am. Chem. Soc.*, **2002**, *124*, 4974–4975.

(48) Zhao, H.; Baker, G. A.; Song, Z.; Olubajo, O.; Crittle, T.; Peters, D. *Green Chem.*, **2008**, *10*, 696–705.

(49) Conceiçao, L. J. A.; Bogel-Łukasik, E.; Bogel-Łukasik, R. *RSC Adv.*, **2012**, *2*, 1846–1855.

(50) Heitmann, S.; Krings, J.; Kreis, P.; Lennert, A.; Pitner, W. R.; Górak, A.; Schulte, M. M. *Sep. Purif. Technol.*, **2012**, *97*, 108–114.

(51) Klamt, A.; Schuurmann, G. *J. Chem. Soc. Perkin Trans. 2*, **1993**, 799–805.

(52) Klamt, A. *COSMO-RS: From quantum Chemistry to Fluid Phase Thermodynamics and Drug Design*; Elsevier: Amsterdam, 2005.

(53) Kato, R.; Gmehling, J. *J. Chem. Thermodyn.*, **2005**, *37*, 603–619.

(54) Döker, M.; Gmehling, J. *Fluid Phase Equilib.*, **2005**, *227*, 255–266.

(55) Khan, I.; Kurnia, K. A.; Mutelet, F.; Pinho, S. P.; Coutinho, J. A. P. *J. Phys. Chem. B*, **2014**, 1848–1860.

(56) Khan, I.; Kurnia, K. A.; Sintra, T. E.; Saraiva, J. A.; Pinho, S. P.; Coutinho, J. A. P. *Fluid Phase Equilib.*, **2014**, *361*, 16–22.

(57) Reddy, P.; Aslam Siddiqi, M.; Atakan, B.; Diedenhofen, M.; Ramjugernath, D. *J. Chem. Thermodyn.*, **2013**, *58*, 322–329.

(58) Diedenhofen, M.; Eckert, F.; Klamt, A. *J. Chem. Eng. Data*, **2003**, *48*, 475–479.

(59) Ferreira, A. R.; Freire, M. G.; Ribeiro, J. C.; Lopes, F. M.; Crespo, J. G.; Coutinho, J. A. P. *Fuel*, **2014**, *128*, 314–329.

(60) Diedenhofen, M.; Klamt, A. *Fluid Phase Equilib.*, **2010**, *294*, 31–38.

(61) Hess, B.; Kutzner, C.; van der Spoel, D.; Lindahl, E. *J. Chem. Theory Comput.*, **2008**, *4*, 435–447.

(62) Nose, S. *Mol. Phys.*, **1984**, *52*, 255–268.

(63) Hoover, W. G. *Phys. Rev. A*, **1985**, *31*, 1695–1697.

(64) Parrinello, M.; Rahman, A. *J. Appl. Phys.*, **1981**, *52*, 7182–7190.

(65) Batista, M. L. S.; Tomé, L. I. N.; Neves, C. M. S. S.; Rocha, E.; Gomes, J. R. B.; Coutinho, J. A. P. *J. Phys. Chem. B*, **2012**, *116*, 5985–5992.

(66) Jorgensen, W. L.; Maxwell, D. S.; Tirado-Rives, J. *J. Am. Chem. Soc.*, **1996**, *118*, 11225–11236.

(67) Kaminski, G. A.; Friesner, R. A.; Tirado-Rives, J.; Jorgensen, W. L. *J. Phys. Chem. B*, **2001**, *105*, 6474–6487.

(68) Koller, T.; Ramos, J.; Garrido, N. M.; Fröba, A. P.; Economou, I. G. *Mol. Phys.*, **2012**, *110*, 1115–1126.

(69) Breneman, C. M.; Wiberg, K. B. *J. Comput. Chem.*, **1990**, *11*, 361–373.

(70) Becke, A. D. *J. Chem. Phys.*, **1993**, *98*, 5648–5652.

(71) Frisch, M. J. .; Trucks, G. W. .; Schlegel, H. B. .; Scuseria, G. E. .; Robb, M. A. .; Cheeseman, J. R. .; Scalmani, G. .; Barone, V. .; Mennucci, B. .; Petersson, G. A. .; Nakatsuji, H. .; Caricato, M. .; Li, X. .; Hratchian, H. P. .; Izmaylov, A. F. .; Bloino, J. .; Zheng, G. .; Sonnenberg, J. L. .; Hada, M.; Ehara, M. .; Toyota, K. .; Fukuda, R. .; Hasegawa, J. .; Ishida, M. .; Nakajima, T. .; Honda, Y. .; Kitao, O. .; Nakai, H. .; Vreven, T. .; Montgomery, J. A., J. .; Peralta, J. E. .; Ogliaro, F. .; Bearpark, M. .; Heyd, J. J. .; Brothers, E. .; Kudin, K. N. .; Staroverov, V. N. .;

Kobayashi, R. .; Normand, J. .; Raghavachari, K. .; Rendell, A. .; Burant, J. C. .; Iyengar, S. S. .; Tomasi, J. .; Cossi, M. .; Rega, N. .; Millam, M. J. .; Klene, M. .; Knox, J. E. .; Cross, J. B. .; Bakken, V. .; Adamo, C. .; Jaramillo, J. .; Gomperts, R. .; Stratmann, R. E. .; Yazyev, O. .; Austin, A. J. .; Cammi, R. .; Pomelli, C. .; Ochterski, J. W. .; Martin, R. L. .; Morokuma, K. .; Zakrzewski, V. G. .; Voth, G. A. .; Salvador, P. .; Dannenberg, J. J. .; Dapprich, S. .; Daniels, A. D. .; Farkas, Ö. .; Foresman, J. B. .; Ortiz, J. V. .; Cioslowski, J. .; Fox, D. J. *Gaussian 09, Revision D.01*; Gaussian, Inc., Wallingford CT, 2009.

(72) Kurnia, K. A.; Coutinho, J. A. P. *Ind. Eng. Chem. Res.*, **2013**, *52*, 13862–13874.

(73) Królikowska, M. *Fluid Phase Equilib.*, **2014**, *361*, 273–281.

(74) Cammarata, L.; Kazarian, S. G.; Salter, P. A.; Welton, T. *Phys. Chem. Chem. Phys.*, **2001**, *3*, 5192–5200.

(75) Cha, S.; Ao, M.; Sung, W.; Moon, B.; Ahlstrom, B.; Johansson, P.; Ouchi, Y.; Kim, D. *Phys. Chem. Chem. Phys.*, **2014**, *16*, 9591–9601.

(76) DIPPR 801 Thermophysical Property Database and DIADEM Predictive Software 2000.

(77) Maginn, E. J. *J. Physics-Condensed Matter*, **2009**, *21*, 373101–373118.

(78) Skarmoutsos, I.; Dellis, D.; Matthews, R. P.; Welton, T.; Hunt, P. A. *J. Phys. Chem. B*, **2012**, *116*, 4921–4933.

(79) Brehm, M.; Kirchner, B. *J. Chem. Inf. Model.*, **2011**, *51*, 2007–2023.

3.4. Evaluation of the latest GROMOS Force Field for the Calculation of Structural, Volumetric and Dynamic Properties of Aqueous Glucose Systems

Adapted from:

Marta L. S. Batista, José R. B. Gomes, João A. P. Coutinho, Edward J. Maginn

Evaluation of the Latest GROMOS Force Field for the Calculation of Structural, Volumetric and Dynamic Properties of Aqueous Glucose Systems

In preparation for publication

My direct contribution:
I declare that I have carried out the molecular dynamics simulations with the estimation of density, viscosity, radial and spatial distribution functions, solvent accessible surface areas and coordination numbers. A significant part of this work was performed during a stay of six months at the University of Notre Dame, IN, USA, under supervision of Prof. Dr. Edward J. Maginn.
For this study I also had the supervision of my advisors, Prof. Dr. João A. P. Coutinho and Dr. José R. B. Gomes.

The previous chapters reported studies regarding the characterization of the interactions between some ionic liquids (ILs) with water and ethanol, aiming at understanding the behavior of systems relevant for the distillation of bioethanol. The following chapters will discuss the interaction between the glucose, relevant in the 2nd generation biofuels as the monomer of cellulose, water and the ionic liquids that could be used in the pre-treatment of biomass. The major issue in the adequate description of glucose in MD simulations is the absence of adequate force fields to describe this compound. In the following chapter a new force field for the description of glucose will be evaluated.

Motivation

As mentioned in Chapter 1, carbohydrates are an important and diverse class of biomolecules, characterized by a vast heterogeneity of compounds differing in their stereochemistry and functionalization. These compounds are essential to many biological functions and are also important in a wide range of industries including food, textile, pulp and paper, biofuels and personal care.[1–3]

One particularly important carbohydrate is *D*-glucose, a hexopyranose with two stereoisomers, namely α-*D*-glucopyranose and β-*D*-glucopyranose, with the latter being the dominant isomer in aqueous solution, in a proportion of 36:64.[4] Glucose is the monomer of cellulose, the most abundant biopolymer, which is being considered as a feedstock for the renewable production of fuels and chemicals.[1–3,5,6] Most biological and industrial processes involving glucose are carried out in aqueous media, so it is important to understand the structural, volumetric and dynamic properties of aqueous glucose solutions. The most common experimental technique used to study the crystalline structure of glucose is X-ray diffraction, while techniques such as NMR and IR are commonly used to characterize aqueous solutions.[1–3] To help in the interpretation of the spectroscopic data, atomistic-level molecular dynamics (MD) simulations have also been performed, providing further understanding of the molecular interactions that take place in these systems.[2] As mentioned and reviewed in Chapter 2, MD simulations can also be used to predict macroscopic thermodynamic and transport properties of liquids.

A key requirement for these simulations is an accurate description of the inter and intramolecular interactions, which are treated using a classical potential energy expression or "force field" (FF).[7] Several FFs have been developed for carbohydrates, including OPLS,[8,9] AMBER,[10,11] CHARMM,[12,13] GLYCAM,[14,15] and GROMOS.[16,17] Within these, some were optimized and validated for hexopyranoses or systems composed of glucose.[18–21] For carbohydrates in aqueous solution, the different FFs have utilized different models for water and have been developed to capture different physical phenomena.[1,2] One of the most difficult features for a FF to capture for aqueous glucose solutions is epimerization or anomerization, *i.e.,* the interconversion between the α-*D*-glucoyranose and β-*D*-glucopyranose (also called mutarotation). This phenomenon and other structural transitions occur due to a complex interplay between the steric, electrostatic, hydrogen bonding and solvation effects present in the system, which is a difficult task for FFs to adequately reproduce and to take into account. Additionally, many of these processes occur over timescales that are long compared to MD simulation times, making their observation difficult without extremely long simulations.[1–3]

One of the key interactions between glucose and water are hydrogen bonds (H-bonds), which occur via the hydroxyl groups of glucose. The establishment of H-bonds is affected by the orientation

of each hydroxyl and hydroxymethyl group in glucose, which in turn is affected by the anomeric effect, 1-3-syn-diaxial repulsions and solvation effects, each of which affects the stability of a given conformer.[22,23] It is thus clear that the study of the orientation of the hydroxyl groups in glucose is fundamental for understanding the interactions between glucose and water. For this reason, the orientation and angles of the hydroxymethyl group (O5-C5-C6-O6, see Figure 3.4.1) and also the free lactol group (C1-O1, Figure 3.4.1) are commonly studied to evaluate if a given solvent is able to favorably interact with glucose.[24]

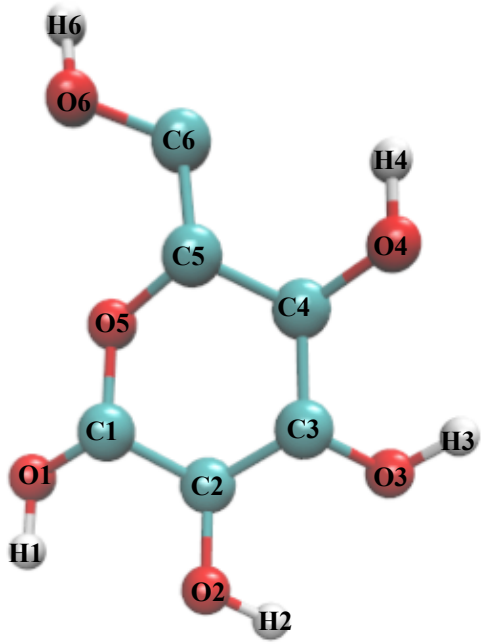

Figure 3.4.1 - Atom labels used in this work for glucose.

The newest version of the GROMOS carbohydrate FF, 56A$_{CARBO}$[3], is adopted in the present chapter to study the mechanisms of glucose and water interactions and the dynamical behavior of this system. This FF is a optimization of the GROMOS 53A6 FF,[25] and fixes a number of shortcomings, including the rotational preferences of the free lactol group and of the hydroxymethyl group. This was done by the introduction of specific Lennard-Jones interaction parameters to account for special intramolecular interactions that are specific for six-membered ring compounds and are responsible for the stability of conformations. The FF was validated by reproducing free energies of ring conformers, anomers, epimers, hydroxymethyl rotamers and glycosidic linkages under dilute aqueous conditions.[3]

While the $56A_{CARBO}$ force field appears to yield good dilute solution properties, we are interested in modeling aqueous glucose solutions at finite concentrations relevant to applications such as fermentation for bioethanol production. Therefore, the main goal of the present study is to test the accuracy of the GROMOS $56A_{CARBO}$ force field at reproducing the volumetric, dynamic and structural properties of aqueous glucose mixtures at finite concentrations. Six mixtures of *β-D*-glucopyranose and water at different concentrations were simulated using the GROMOS $56A_{CARBO}$ FF for *β-D*-glucopyranose and the extended simple point charge (SPC/E) water model[26]. Densities, viscosities, and self-diffusivities were computed and compared with available experimental data. The structure of the solutions was examined by conducting a hydrogen bonding analysis and by computing radial and spatial distribution functions.

Methodology

MD simulations were performed for six systems composed of glucose and water using the GROMACS code version 4.5.5[27]. The systems contained 170 water molecules and 6, 9, 14, 20, 29 or 42 glucose molecules yielding solutions with glucose mole fractions of 0.034, 0.050, 0.076, 0.110, 0.150 and 0.200, respectively. Each box was built with the PACKMOL package[28], with a random distribution of the molecules and imposing a distance of 2.5 Å between molecules to ensure that no atomic overlapping occurs. Water and glucose molecules were described by means of the SPCE model[26] and the GROMOS $56A_{CARBO}$ force field[3], respectively.

Starting configurations were subjected to energy minimization followed by a 20 ns equilibration in the isothermal-isobaric (NPT) ensemble. During this period, the temperature was maintained at 303.15 K via a Nosé-Hoover thermostat[29,30] while the pressure was held at 1 bar with a Parrinello-Rahman barostat.[31] A cutoff of 0.9 nm was applied for nonbonded interactions, and corrections for long-range interactions were taken into account. The time step was 2 fs, and the SHAKE algorithm was employed to constrain all bonds. The same procedure was performed for three independent configurations, and densities were estimated from the average of the three simulations.

Using the densities obtained from the NPT simulations, a configuration of the system at the average density for each considered mixture was taken and simulations were then run in the canonical (NVT) ensemble. The system was equilibrated by running an annealing schedule for 15 ns from 298.15 to 500.15 K and then finally to 313.15 K. Production runs were then carried out for an additional 65 ns time interval at 313.15 K. A time step of 1 fs was used, with energies recorded every 10 fs. Once again, the SHAKE algorithm was employed to constrain all bonds, a cutoff of 0.9 nm was applied for non-bonded interactions, and corrections for long-range interactions were taken into account. Additionally, three independent NVT simulations of 20 ns duration were performed in order to estimate uncertainties. For these simulations, a time step of 2 fs was used. The independent trajectories were generated by assigning different initial velocity distributions to a given equilibrated configuration. All other conditions were the same as in the previous NVT runs.

Results and Discussion

Conformational Analysis

As previously mentioned, the study of the different angle conformations of specific groups can help to infer the types of interactions that glucose is able to establish. The orientation of the hydroxymethyl group is impacted by the conformation of the dihedral angle (O5-C5-C6-O6, see Figure 3.4.1).[1,3] There are three known conformations for this dihedral angle: gauche-gauche (*gg*), where the angle is nominally -60º; trans-gauche (*tg*), with an angle of 180º; and gauche-trans (*gt*), with an angle of 60º (see Figure 3.4.2). This analysis was previously applied to a system composed of cellulose and water.[32] It is well known that in the case of the crystalline structure of cellulose the *tg* conformation is predominant, while in aqueous solution the *gg* conformation becomes far more populated, followed by *gt* and *tg*.[33,34] For this reason, the conformation *tg* is associated with a crystalline-like state of glucose and the conformation *gg* is associated with an amorphous state of glucose in water. In the presence of other solvents, for example ionic liquids, the *gt* conformation is the most populated state.[32,35]

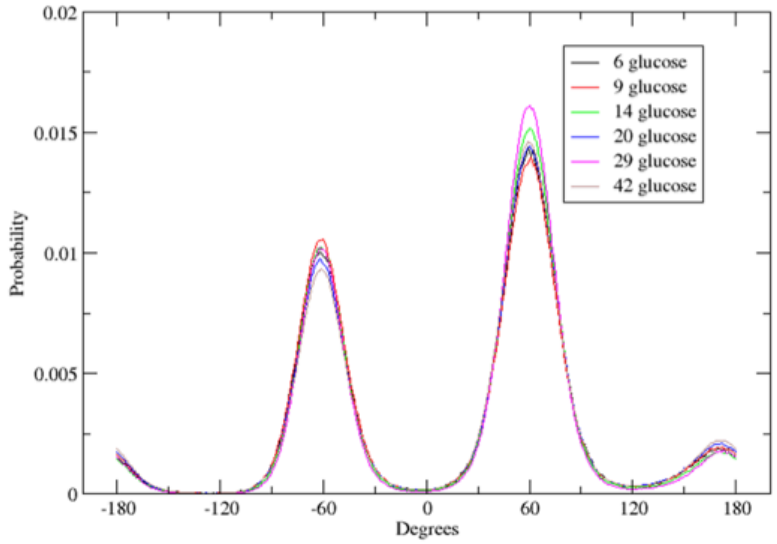

Figure 3.4.2 - Probability distribution of the hydroxymethyl group angle in glucose as a function of concentration.

The computed distribution of the hydroxymethyl group as a function of glucose concentration is shown in Figure 3.4.2. The results show that the predominant conformations are *gg* and *gt*,

indicative of an amorphous structure for glucose when interacting with water. These results are similar for all six mixtures examined.

Density

Values of the densities for each mixture were used to evaluate the ability of the $56A_{CARBO}$ force field for reproducing systems composed of glucose and water by comparison with experimental densities taken from Comesaña *et al.*.[36] As can be seen in Figure 3.4.3, experimental and calculated densities become larger with the increase of the glucose mole fraction in the mixtures. The calculated densities overestimate the experimental ones in the entire glucose mole fraction range considered in this study. Good agreement is found for the solution with the smallest glucose mole fraction, but the difference reaches a maximum of 6.93 % for 0.2 mole fraction (Table 3.4.1).

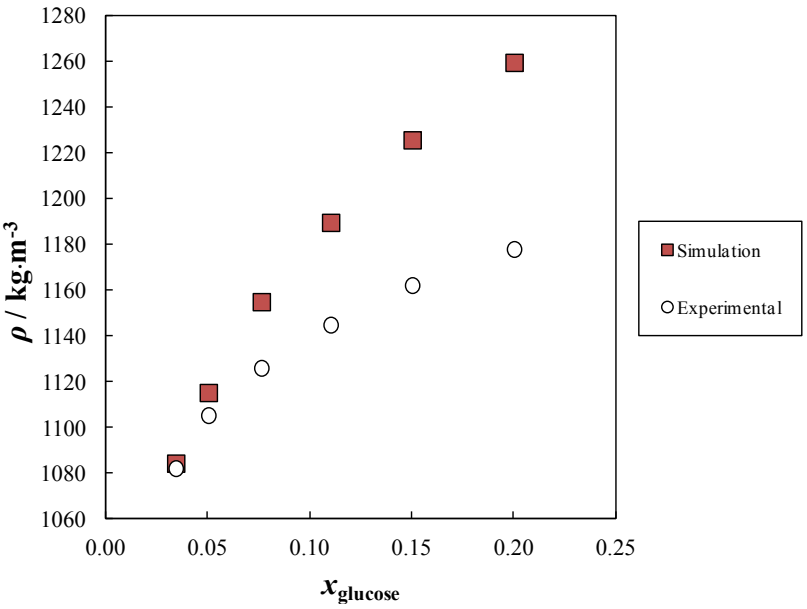

Figure 3.4.3 - Comparison of experimental[36] and simulation density values at 303.15 K.

In order to understand if the consistent overestimation of the densities of the glucose aqueous solutions was due to deficiencies in the SPC/E or the $56A_{CARBO}$ force fields, two new sets of MD simulations were performed using: i) $56A_{CARBO}$ force field for glucose and TIP3P model[37] for water, and ii) OPLS[9] force field for glucose and SPC/E for water. Both water models are known to do a reasonable job modelling pure water properties. Glucose mole fractions were

0.034, 0.076 and 0.200 for case i) and 0.034 and 0.050 for case ii). Results are compared in Table D.1 of Appendix D with those obtained with SPC/E and $56A_{CARBO}$ models for water and glucose, respectively. The computed and experimental densities are similar in both cases at low glucose concentrations. At higher glucose concentrations, densities are overestimated by both the OPLS and $56A_{CARBO}$ models, being the overestimation more pronounced when the former force field is considered. This suggests that the water model is not the origin of the discrepancies between the experimental and calculated densities, but that instead the problem lies in the glucose models (and the way they interact with water). These results highlight the limitations of currently available force fields for the description of glucose at finite concentrations. Despite the problems in matching experimental solution densities, other properties were computed to assess the overall performance of the glucose model.

Table 3.4.1 - Experimental[36] and computational densities (ρ) for different glucose+water mixtures at 303.15 K. Values in parentheses denote the uncertainties (the standard deviation) estimated with the calculated results. AAD represents the absolute deviations of the simulated data from the experimental values.

$x_{glucose}$	ρ_{exp} / kg·m^{-3}	ρ_{sim} / kg·m^{-3}	AAD[a)] %
0.034	1081.8	1084.0(±0.1)	0.20
0.050	1105.0	1114.9(±0.1)	0.89
0.076	1125.7	1154.6(±0.1)	2.57
0.110	1144.6	1189.3(±0.4)	3.91
0.150	1161.9	1225.4(±0.2)	5.47
0.200	1177.7	1259.4(±0.5)	6.93

[a)] AAD = ABS((ρ_{exp} - ρ_{sim})/ ρ_{exp})*100

Viscosity

Shear viscosity is an important transport property that can be determined from MD simulations via the following Green-Kubo relation,

$$\eta = \frac{V}{k_B T} \int_0^\infty \langle P_{\alpha\beta}(t_0 + t) \cdot P_{\alpha\beta}(t_0) \rangle dt \tag{3.4.1}$$

where the brackets indicate an ensemble average, V is the volume of the system, T is the temperature and k_B is the Boltzmann constant. Inside the brackets, $P_{\alpha\beta}$ is the off-diagonal

components of the pressure tensor. To achieve good statistics, very long simulations are required. Numerical integration of equation 3.4.1 can lead to large errors, especially due to noise at long times. Following the work of Rey-Castro and Vega[38], the numerical integral obtained via equation 3.4.1 was fit to a double exponential of the following form,

$$\eta(t) = A\alpha\tau_1\left(1 - e^{-t/\tau_1}\right) + A(1-\alpha)\tau_2\left(1 - e^{-t/\tau_2}\right) \tag{3.4.2}$$

where A and α are empirical fitting parameters, $0 < \alpha < 1$, and τ_1, τ_2 are characteristic decay times that differ by an order of magnitude. These parameters were obtained from a least-squares fit of equation 3.4.1 to the simulation results. The shear viscosity was estimated from equation 3.4.2 by taking the limit as t goes to infinity. The uncertainty $\Delta\eta$ was estimated via the following relation

$$\Delta\eta = \sqrt{\frac{2A[\alpha\tau_1 + (1-\alpha)\tau_2]}{t_{max}}} \tag{3.4.3}$$

where t_{max} is the maximum decay time considered in the calculation of the autocorrelation function. The values of the fitting parameters used in equation 3.4.2 are compiled at Table D.2 of Appendix D, as a function of glucose mole fraction. Typical values of t_{max} ranged from 80 ns to 120 ns, depending on the viscosity of the solution. Viscosity results at a temperature of 313.15 K are depicted in Figure 3.4.4 along with experimental data taken from Comesaña *et al.*[36]. Figure 3.4.4 shows that simulated viscosities are significantly higher than the experimental data above a glucose mole fraction of 0.11. At lower glucose concentrations, agreement with experimental data is good, with a maximum deviation around 10 % (see Table 3.4.2). This result is consistent with the density data, since overestimation of density should lead to slower dynamics and higher viscosities.

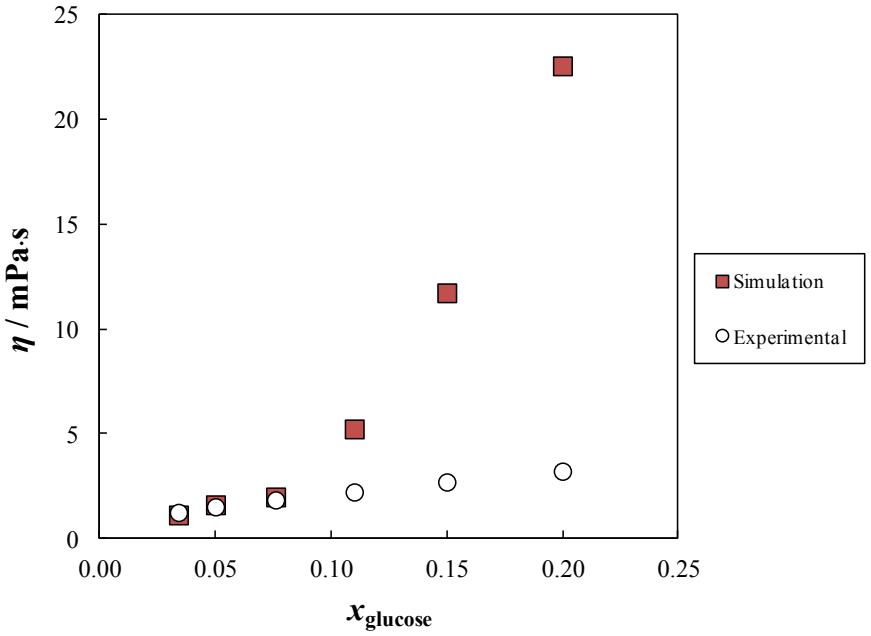

Figure 3.4.4. Comparison of experimental[36] and simulation viscosity values at 313.15 K.

As with the densities, a comparison was made between the viscosities obtained using the $56A_{CARBO}$ force field and the OPLS glucose force field. In both cases, water was modeled with the SPC/E force field at glucose mole fractions of 0.036 and 0.05. The results are reported in Table D.3 at Appendix D and show that the OPLS force field also significantly overestimates the viscosity, especially at higher glucose concentrations.

Table 3.4.2 - Experimental[36] and calculated viscosities (η) at 313.15 K. Values in parentheses denote uncertainties estimated accordingly to equation 3.4.3. AAD represents the absolute deviations of the simulated data from the experimental values.

$x_{glucose}$	η_{exp} / mPa.s	η_{sim} / mPa.s	AAD[a)] %
0.034	1.205	1.085 (±0.134)	9.97
0.050	1.475	1.571 (±0.198)	6.50
0.076	1.804	1.945 (±0.441)	7.83
0.110	2.182	5.195 (±0.360)	138.09
0.150	2.660	11.697 (±0.541)	339.75
0.200	3.175	22.541 (±0.751)	609.94

a) AAD = ABS((ρ_{exp} - ρ_{sim})/ ρ_{exp})*100

Self-diffusion coefficients

As mentioned at the chapter 2.1.5, self-diffusion is another important transport property from the application point of view since it is related with mass transfer. Self-diffusion coefficients of water and glucose were computed via the following Einstein relation,

$$D_i = \frac{1}{6}\lim_{t\to\infty}\frac{d}{dt}\langle\left|\overrightarrow{r_i(t)} - \overrightarrow{r_i(0)}\right|^2\rangle \quad (3.4.4)$$

where the term in brackets is the mean squared displacement. The slope of the mean square displacement gives the value of D_i. In this work, slopes were determined over time intervals of 7500 to 10000 ps for glucose and 7500 and 12500 ps for water. The results are given in Table 3.4.3. As expected, water has a larger self-diffusion coefficient than glucose, and water mobility decreases with increasing glucose concentration. We are unaware of any experimental diffusivity data for the concentrations studied here, but the simulation values are of the same magnitude as those measured experimentally by Ribeiro *et al.*[39] under different concentrations.

Table 3.4.3 - Computed self-diffusion coefficients at 313.15 K. Values in parentheses denote uncertainty (the standard deviation) associated with the calculated data.

$x_{glucose}$	D_{water} / (1E^{-5} cm^2/s)	$D_{glucose}$ / (1E^{-5} cm^2/s)
0.034	6.151(±0.263)	1.200(±0.735)
0.050	5.044(±0.141)	0.792(±0.485)
0.076	3.816(±0.288)	0.756(±0.217)
0.110	3.205(±0.181)	0.508(±0.221)
0.150	2.629(±0.126)	0.459(±0.094)
0.200	1.461(±0.105)	0.203(±0.071)

Radial distributions functions and coordination numbers

To probe the underlying structure of the solutions, radial distribution functions (*g(r)* or RDF) were computed for various sites on glucose and water. Specifically, RDFs between glucose atoms O1, O2, O3, O4, O5 and O6 were computed with water oxygen atoms (OW). In addition, water-water (OW - OW) and glucose-glucose (O1 with HO3, HO4 and HO6) RDFs where computed. Coordination numbers (Z) for these pairs were obtained by integrating the

RDFs out to a radial cutoff r_Z. This cutoff distance was chosen to be the first local minimum of the corresponding RDF.

As mentioned previously, the mechanism of interaction between glucose and water is mediated through hydrogen bonds. RDFs can provide information concerning the establishment of H-bonds in a mixture. According to geometric criteria, in the case of water-water interactions, a H-bond can be considered to exist when a site-to-site RDF O—O has a first minimum at a distance less than 0.35 nm (or an O—H distance is less than 0.26 nm).[40] These values were used for r_Z to determine H-bonding interactions between glucose-water, glucose-glucose and water-water. Results are shown in Figure 3.4.5 and also in Figures D.1 and D.2 of Appendix D.

It is possible to observe in Figure 3.4.5 that with increasing glucose content, the heights of the peaks related with the water oxygen atoms surrounding the oxygen atoms of glucose increase. The peaks also become sharper, suggesting that the number of water molecules surrounding glucose is reduced and only a few strongly bound water molecules remain in the vicinity of glucose. This analysis is supported by the values of the coordination numbers, as discussed below. From the RDF heights it can be understood that three types of atoms in glucose have an affinity towards water. Atoms O6 and O1 have the highest affinity for water, followed by atoms O2, O3 and O4. Atom O5 presents the lowest affinity for water and from the RDF profile showing *g(r)* values lower than one it is suggested that O5 is not establishing direct contacts with water molecules. This is presumably due to a steric hindrance effect. The results for atoms O6 and O1 agree with those reported in previous studies[22,23] where it was shown that these hydroxyl groups can interact with water as hydrogen bond acceptors. For water-water interactions, Figure D.1 shows that the first water-water RDF peak becomes sharper as the concentration of glucose increases in the mixture. As is the case with the first peak in the water-glucose RDF, this is due to the fact that at high glucose concentrations water has only a few strongly associated neighboring water molecules.

Not surprisingly, glucose-glucose interactions increase with increasing concentrations of glucose. This can be seen in Figure D.2, which shows various site-site RDFs for glucose-glucose interactions. The first peak occurs around 0.18 nm and is weak, with values of *g(r)* below one at the lowest glucose concentration. As glucose concentration increases, this first peak approaches a value of 1.5. For all mixtures considered, the O1 atom of glucose interacts preferentially with HO6, which can be understood from a balance of steric effects.

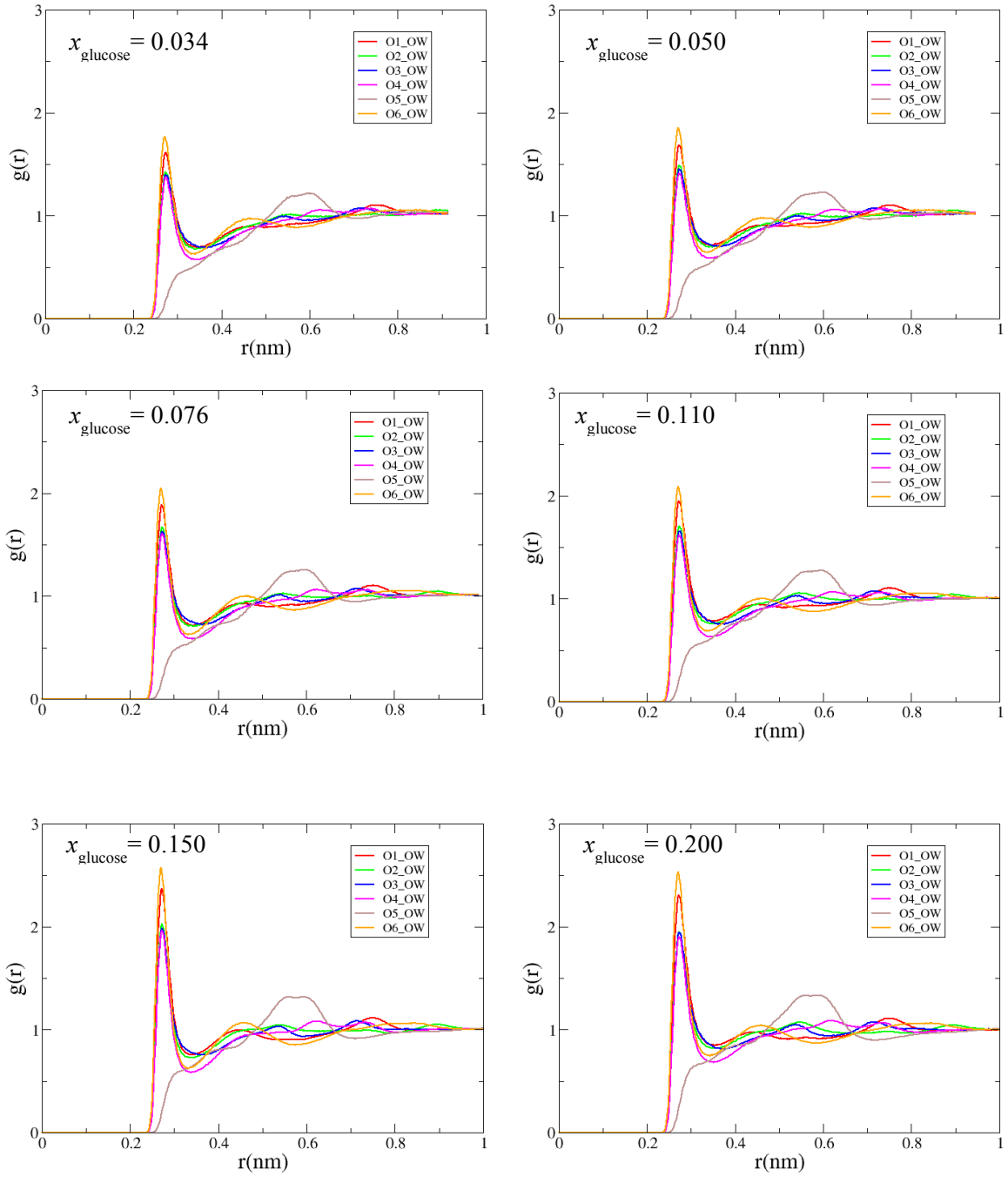

Figure 3.4.5 - Radial distributions functions (RDFs) for glucose-water interactions, at six different glucose mole fraction and a temperature of 313.15 K. RDFs for interaction between O1-OW(—), O2-OW(—), O3-OW(—), O4-OW (—), O5-OW (—) and O6-OW (—) are represented in each panel.

The results for the coordination numbers are compiled in Table 3.4.4, as well as in Tables D.3 and D.4 of Appendix D. Confirming the observations made from the RDFs, there is a consistent decrease of the Z values for interactions between oxygen atoms in glucose and water oxygen atoms (OW) with increasing glucose concentration. Additionally, the Z values for O1-OW and O6-OW interactions are larger than those corresponding to the remaining glucose oxygen atoms. The Z values calculated for the water-water and glucose-glucose interactions, Tables D.4 and D.5, show a decrease in the former case and a slight increase in the latter case with increasing glucose concentration.

Table 3.4.4 - Coordination number (Z) from the RDF peaks for glucose-water interactions, at each mixture considered.

$x_{glucose}$	reference atoms		Z
	glucose	water	
0.034	O1	OW	2.54
	O2		2.33
	O3		2.38
	O4		2.13
	O5		-
	O6		2.57
0.050	O1	OW	2.42
	O2		2.21
	O3		2.23
	O4		2.01
	O5		-
	O6		2.42
0.076	O1	OW	2.21
	O2		2.03
	O3		2.07
	O4		1.85
	O5		-
	O6		2.19
0.110	O1	OW	2.06
	O2		1.86
	O3		1.87
	O4		1.69
	O5		-
	O6		2.01

0.150	O1	OW	1.82
	O2		1.62
	O3		1.66
	O4		1.48
	O5		-
	O6		1.78
0.200	O1	OW	1.57
	O2		1.40
	O3		1.43
	O4		1.29
	O5		-
	O6		1.57

The results suggest that at low glucose content, glucose is interacting predominantly with water, and water with itself. As the number of glucose molecules increase in the system, glucose begins to self-associate. This self-association is likely overestimated in the simulations, which is why the density and transport properties do not agree with experiment at higher glucose concentrations. Improvements in the glucose force field will need to be made to modulate the degree of glucose self-association. Some strategies will be outlined below.

Spatial Distribution Functions

Figure 3.4.6 shows three-dimensional spatial distribution functions (SDFs) for water around glucose. These plots were generated using the TRAVIS package[41]. Consistent with the RDFs and Z values, the SDFs show that at low glucose concentrations, each glucose molecule is essentially surrounded by water. As the glucose concentration increases, other glucose molecules displace water, such that the glucose molecules are not completely solvated by water.

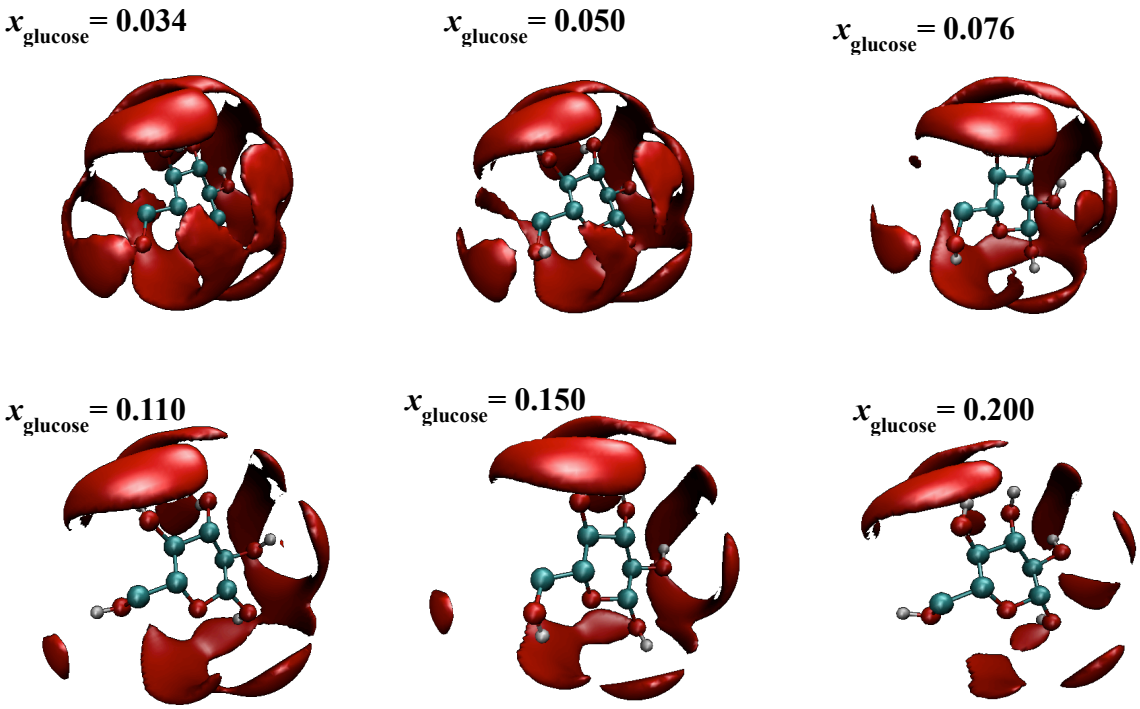

Figure 3.4.6 - Spatial distribution functions (SDFs) as a function of glucose concentration. A glucose molecule is the central element, surrounded by oxygen atoms of water (red surfaces with isovalues of 52 particle·nm^{-3}). Color code for spheres: Cyan is carbon; red is oxygen; and white is hydrogen.

Hydrogen bonds

The definition of a hydrogen bond can be based on different criteria but, due to its simplicity, a geometric criterion is usually chosen, based on the distance of between hydrogen and an acceptor (H—A) and the angle of H-O—A. The former is defined and chosen from the intermolecular site-to-site radial distribution functions and the latter can be defined as 30º for intermolecular H-bonds and 60º for intramolecular H-bonds.[22] The definition for H-bonds established with water is that the distance of H-O is smaller than 0.26 nm (or the distance of O-O is smaller than 0.35 nm), and the angle H-O—O is smaller than 30º.[42,43] These criteria are also adopted here.

Figure 3.4.7 depicts the number of hydrogen bonds established between glucose and water per glucose molecule basis (red series) and between water molecules per water molecule basis (blue series). Numerical values are given in Table D.6 of Appendix D. As expected, and in agreement with previous results, the number of H-bonds established between glucose and

water decreases with increasing glucose concentration, as does the number of water-water H-bonds.

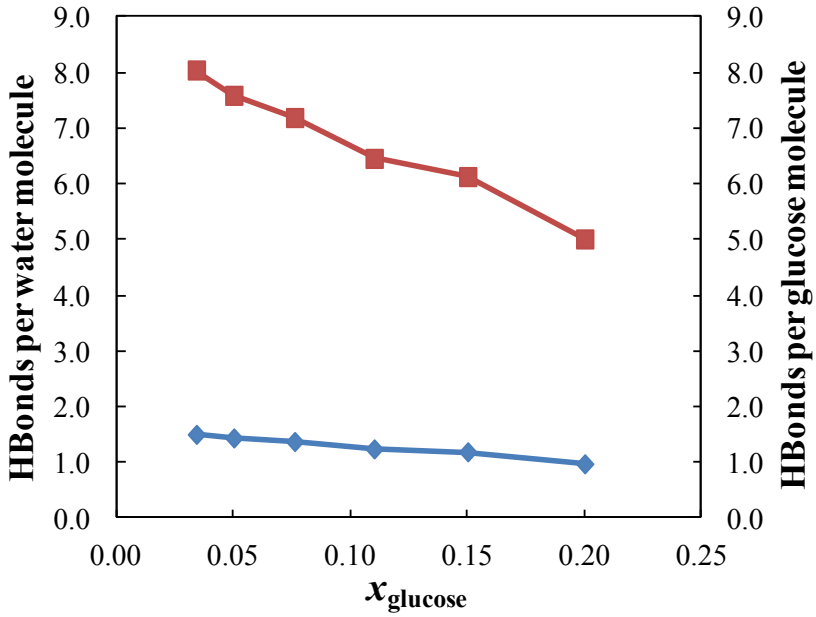

Figure 3.4.7 - The number of hydrogen bonds between glucose and water molecules (red, right axis) and water with water molecules (blue, left axis) as function of glucose concentration, at 313.15 K.

Strategy to refine the glucose force field for mixtures with water

Several works are found in the literature aiming at the improvement of force fields to reproduce properties of different systems, such as viscosity and diffusivity.[44–47] These improvements are based on the usage of different strategies to estimate atomic partial charges (*e.g.*, CHelpG[48], Blöchl[49], NPA[50,51]), or on the consideration of polarizable force fields with the introduction, for example, of Drude oscillators[52] (for ionic liquids, see Chapter 2). The consideration of different approaches (*e.g.* CHelpG, NPA) for calculating the atomic charges leads to different sets of values. The magnitude of the charges is found to have direct influence in the properties calculated for a specific system.[44,53,54] Thus, rescaling atomic charges arises as a simple way to improve the description of a system under study and to obtain properties that are in satisfactory agreement with the experimental ones (e.g. transport properties of systems composed of ionic liquids[53,55–57]).

Hence, recognizing the lack of ability of the GROMOS carbohydrate FF, $56A_{CARBO}{}^{3}$, to reproduce experimental values of density and viscosity at glucose mole fractions above ~0.1, it was applied the factor of 0.8 to the atomic charges of glucose, which was chosen after some tests with different scaling factors for the system with the highest glucose concentration. Simulations using the rescaled charges, without changing the other simulation parameters, were repeated for systems with glucose mole fractions of 0.034, 0.050, 0.076, 0.110, 0.150 and 0.200. New density and viscosity values are depicted in Figures 3.4.8 and 3.4.9 while Tables D.7 and D.8 contain their numerical values. The experimental values (straight line series), and previous predicted values (with no rescaling charges, dotted-line series) are also included in these figures. The obtained results present now a maximum deviation of 1.6 % for the density (against 7 % in the simulations with original glucose atomic charges), and of 35 % for the viscosity (against ~600 % in the simulations with original glucose atomic charges). The improvement in these properties is notorious, especially for the systems with glucose mole fraction above 0.1. For systems with glucose mole fraction below 0.1, predicted new values are underestimating experimental values (either for density and viscosity), presenting higher deviations than previously obtained, suggesting that in this concentration range intermediate values between original and rescaled charges would provide a better description of the systems.

On the whole, results suggest that the rescaling charges methodology yields density and viscosity values in very good agreement with the experimental ones. A significant decrease in the deviations to the experimental data is found for both properties but it is much more pronounced in the case of viscosity (Tables D.7 and D.8). However, this improvement was only attained where the GROMOS $56A_{CARBO}$ FF fails to predict density and viscosity values (*i.e.*, at glucose mole fractions above 0.1). For continuous improvement, the use of polarizable force fields, such as that recently proposed by Patel *et al.*[52], may constitute an alternative solution.

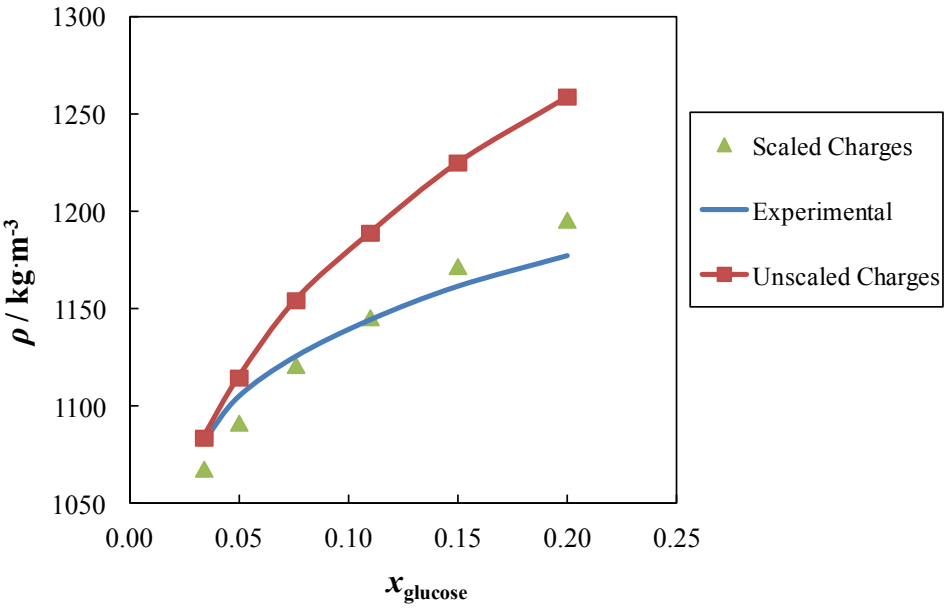

Figure 3.4.8. Comparison of experimental[36] (line series) and simulation density values estimated with scaled charges (dot series) and with the original charges (dotted-line series) at 313.15 K.

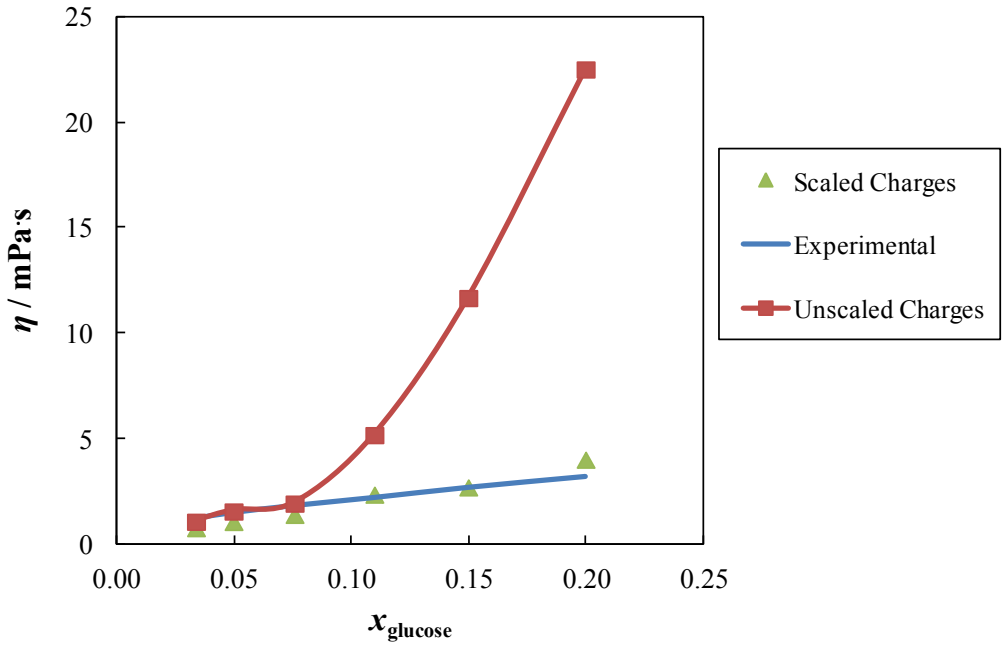

Figure 3.4.9. Comparison of experimental[36] (line series) and simulation viscosity values estimated with scaled charges (dotted series) and with the original charges (dotted-line series) at 313.15 K.

Conclusions

A molecular dynamics simulation study was carried out to determine the properties of aqueous solutions of D-glucose as a function of glucose concentration. The newest version of the GROMOS force field, the $56A_{CARBO}$, was selected to model glucose, and the SPC/E model was used for water. The glucose force field has been well tested under infinite dilution aqueous conditions, but has not been evaluated so far for its ability to model properties under finite glucose concentrations. In the present work, densities, viscosities, and self-diffusivities were computed and compared to available experimental data. The structure of each solution was characterized via hydrogen bond analysis, radial and spatial distributions functions, and coordination numbers.

The computed densities and viscosities showed reasonable agreement with experiment below a glucose mole fraction of 0.15, but deviations became significant at higher concentrations. Specifically, computed densities were over 5 % too large at high concentrations, while viscosities were overestimated by more than 100 %. At the lowest concentrations studied (where the properties are dominated by water-water interactions), the densities and viscosities agreed well with experimental data. A small number of tests were run with an alternative glucose force field (OPLS) and a different water model (TIP3P). The OPLS force field performed slightly worse than the $56A_{CARBO}$ force field at reproducing experimental densities and viscosities. Still, it should be noted that the force fields tested despite providing a poor quantitative description of these properties at high concentrations, they impart qualitative correct trends with concentration increase. Self-diffusivities were also computed with the $56A_{CARBO}$ force field, and while there are no experimental data under the conditions of the simulations, it is expected that the simulated self-diffusivities are also low, given the trend with viscosity.

By examining hydrogen bond formation, coordination numbers, and spatial / radial distribution functions, it was determined that the glucose molecules tend to self-associate at finite concentrations. In essence, water does not fully hydrate the glucose molecules at higher concentrations, which leads to the overestimation of density and viscosity. The results suggest that improved glucose force fields could be developed if modifications are made that attenuate these self-interactions between glucose molecules and that promote better water solvation.

Preliminary studies using a modified version of the $56A_{CARBO}$ force field, obtained by scaling the atomic charges of glucose by a factor of 0.8, leads to significant improvements in the values of the calculated densities and viscosities at glucose mole fractions in the range of 0.034 to 0.200, without decreasing too much the quality of the results at diluted mole fractions.

References

(1) Fadda, E.; Woods, R. J. *Drug Discov. Today*, **2010**, *15*, 596–609.

(2) Foley, B. L.; Tessier, M. B.; Woods, R. J. *Wiley Interdiscip. Rev. Comput. Mol. Sci.*, **2012**, *2*, 652–697.

(3) Hansen, H. S.; Hünenberger, P. H. *J. Comput. Chem.*, **2011**, *32*, 998–1032.

(4) Mason, P. E.; Neilson, G. W.; Enderby, J. E.; Saboungi, M.-L.; Brady, J. W. *J. Phys. Chem. B*, **2005**, *109*, 13104–13111.

(5) Mayes, H. B.; Tian, J.; Nolte, M. W.; Shanks, B. H.; Beckham, G. T.; Gnanakaran, S.; Broadbelt, L. J. *J. Phys. Chem. B*, **2014**, *118*, 1990–2000.

(6) Matthews, J. F.; Beckham, G. T.; Bergenstråhle-Wohlert, M.; Brady, J. W.; Himmel, M. E.; Crowley, M. F. *J. Chem. Theory Comput.*, **2012**, *8*, 735–748.

(7) Gubbins, K. E.; Moore, J. D. *Ind. Eng. Chem. Res.*, **2010**, *49*, 3026–3046.

(8) Kony, D.; Damm, W.; Stoll, S.; van Gunsteren, W. F. *J. Comput. Chem.*, **2002**, *23*, 1416–1429.

(9) Damm, W.; Frontera, A.; Tirado-Rives, J.; Jorgensen, W. L. *J. Comput. Chem.*, **1997**, *18*, 1955–1970.

(10) Glennon, T. M.; Zheng, Y.-J.; Le Grand, S. M.; Shutzberg, B. A.; Merz, K. M. *J. Comput. Chem.*, **1994**, *15*, 1019–1040.

(11) Momany, F. A.; Willett, J. L. *Carbohydr. Res.*, **2000**, *326*, 194–209.

(12) Ha, S. N.; Giammona, A.; Field, M.; Brady, J. W. *Carbohydr. Res.*, **1988**, *180*, 207–221.

(13) Guvench, O.; Hatcher, E. R.; Venable, R. M.; Pastor, R. W.; Mackerell, A. D. *J. Chem. Theory Comput.*, **2009**, *5*, 2353–2370.

(14) Woods, R. J.; Dwek, R. A.; Edge, C. J.; Fraser-Reid, B. *J. Phys. Chem.*, **1995**, *99*, 3832–3846.

(15) Kirschner, K. N.; Yongye, A. B.; Tschampel, S. M.; González-Outeiriño, J.; Daniels, C. R.; Foley, B. L.; Woods, R. J. *J. Comput. Chem.*, **2008**, *29*, 622–655.

(16) Koehler, J. E. H.; Saenger, W.; Gunsteren, W. F. *Eur. Biophys. J.*, **1987**, *15*, 197–210.

(17) Lins, R. D.; Hünenberger, P. H. *J. Comput. Chem.*, **2005**, *26*, 1400–1412.

(18) Lelong, G.; Howells, W. S.; Brady, J. W.; Talón, C.; Price, D. L.; Saboungi, M.-L. *J. Phys. Chem. B*, **2009**, *113*, 13079–13085.

(19) Ziemys, A.; Ferrari, M.; Cavasotto, C. N. *J. Nanosci. Nanotechnol.*, **2009**, *9*, 6349–6359.

(20) Biarnés, X.; Ardèvol, A.; Planas, A.; Rovira, C. *Biocatal. Biotransformation*, **2010**, *28*, 33–40.

(21) Zhang, J.; Zheng, Q.; Zhang, H. *Chem. Phys. Lett.*, **2010**, *484*, 338–343.

(22) Chen, C.; Li, W. Z.; Song, Y. C.; Weng, L. D.; Zhang, N. *Comput. Theor. Chem.*, **2012**, *984*, 85–92.

(23) Suzuki, T. *Phys. Chem. Chem. Phys.*, **2008**, *10*, 96–105.

(24) Chen, T.; Chidambaram, M.; Lin, Z. P.; Smit, B.; Bell, A. T. *J. Phys. Chem. B*, **2010**, *114*, 5790–5794.

(25) Oostenbrink, C.; Villa, A.; Mark, A. E.; van Gunsteren, W. F. *J. Comput. Chem.*, **2004**, *25*, 1656–1676.

(26) Berendsen, H. J. C.; Grigera, J. R.; Straatsma, T. P. *J. Phys. Chem.*, **1987**, *91*, 6269–6271.

(27) Hess, B.; Kutzner, C.; van der Spoel, D.; Lindahl, E. *J. Chem. Theory Comput.*, **2008**, *4*, 435–447.

(28) Martínez, L.; Andrade, R.; Birgin, E. G.; Martínez, J. M. *J. Comput. Chem.*, **2009**, *30*, 2157–2164.

(29) Hoover, W. G. *Phys. Rev. A*, **1985**, *31*, 1695–1697.

(30) Nose, S. *Mol. Phys.*, **1984**, *52*, 255–268.

(31) Parrinello, M.; Rahman, A. *J. Appl. Phys.*, **1981**, *52*, 7182–7190.

(32) Liu, H.; Sale, K. L.; Holmes, B. M.; Simmons, B. A.; Singh, S. *J. Phys. Chem. B*, **2010**, *114*, 4293–4301.

(33) Nishiyama, Y.; Langan, P.; Chanzy, H. *J. Am. Chem. Soc.*, **2002**, *124*, 9074–9082.

(34) Nishiyama, Y.; Sugiyama, J.; Chanzy, H.; Langan, P. *J. Am. Chem. Soc.*, **2003**, *125*, 14300–14306.

(35) Liu, H.; Cheng, G.; Kent, M.; Stavila, V.; Simmons, B. A.; Sale, K. L.; Singh, S. *J. Phys. Chem. B*, **2012**, *116*, 8131–8138.

(36) Comesaña, J. F.; Otero, J. J.; García, E.; Correa, A. *J. Chem. Eng. Data*, **2003**, *48*, 362–366.

(37) Jorgensen, W. L.; Chandrasekhar, J.; Madura, J. D.; Impey, R. W.; Klein, M. L. *J. Chem. Phys.*, **1983**, *79*, 926–935.

(38) Rey-Castro, C.; Vega, L. F. *J. Phys. Chem. B*, **2006**, *110*, 14426–14435.

(39) Ribeiro, A. C. F.; Ortona, O.; Simões, S. M. N.; Santos, C. I. A. V.; Prazeres, P. M. R. A.; Valente, A. J. M.; Lobo, V. M. M.; Burrows, H. D. *J. Chem. Eng. Data*, **2006**, *51*, 1836–1840.

(40) Skarmoutsos, I.; Dellis, D.; Matthews, R. P.; Welton, T.; Hunt, P. A. *J. Phys. Chem. B*, **2012**, *116*, 4921–4933.

(41) Brehm, M.; Kirchner, B. *J. Chem. Inf. Model.*, **2011**, *51*, 2007–2023.

(42) Luzar, A.; Chandler, D. *Nature*, **1996**, *379*, 55–57.

(43) Haughney, M.; Ferrario, M.; McDonald, I. R. *Mol. Phys.*, **1986**, *58*, 849–853.

(44) Youngs, T. G. A.; Hardacre, C. *Chem phys chem*, **2008**, *9*, 1548–1558.

(45) Dommert, F.; Wendler, K.; Berger, R.; Delle Site, L.; Holm, C. *Chemphyschem*, **2012**, *13*, 1625–1637.

(46) Schröder, C. *Phys. Chem. Chem. Phys.*, **2012**, *14*, 3089–3102.

(47) Kirchner, B. *Topics in Current Chemistry*; Meijere, V. B. A. De; Kessler, K. N. H. H.; Ley, J. L. S. V; Schreiber, M. O. S.; Vogel, B. M. T. P.; Wong, F. V. H., Eds.; Springer: Germany, 2009.

(48) Breneman, C. M.; Wiberg, K. B. *J. Comput. Chem.*, **1990**, *11*, 361–373.

(49) Blöchl, P. E. *J. Chem. Phys.*, **1995**, *103*, 7422–7428.

(50) Reed, A. E.; Curtiss, L. A.; Weinhold, F. *Chem. Rev.*, **1988**, *88*, 899–926.

(51) Reed, A. E.; Weinstock, R. B.; Weinhold, F. *J. Chem. Phys.*, **1985**, *83*, 735.

(52) Patel, D. S.; He, X.; MacKerell, A. D. *J. Phys. Chem. B*, **2015**, *119*, 637–652.

(53) Ghatee, M. H.; Zolghadr, A. R.; Moosavi, F.; Ansari, Y. *J. Chem. Phys.*, **2012**, *136*, 124706–124720.

(54) Zhang, Y.; Maginn, E. J. *J. Phys. Chem. B*, **2012**, *116*, 10036–10048.

(55) Bhargava, B. L.; Balasubramanian, S. *J. Chem. Phys.*, **2007**, *127*, 114510–114516.

(56) Chaban, V. *Phys. Chem. Chem. Phys.*, **2011**, *13*, 16055–16062.

(57) Dommert, F.; Schmidt, J.; Krekeler, C.; Zhao, Y. Y.; Berger, R.; Delle Site, L.; Holm, C. *J. Mol. Liq.*, **2010**, *152*, 2–8.

3.5. Ionic Liquids Assessment as Glucose Solvents

Adapted from:

Marta L. S. Batista, Helena Passos, Bruno J. M. Henriques, Mara G. Freire, Edward J. Maginn, João A. P. Coutinho, José R. B. Gomes

Why do ionic liquids are better glucose solvents than water?

<u>In preparation for publication</u>

My direct contribution:

I declare that I have carried out the molecular dynamics simulations used to estimate the density, viscosity, radial and spatial distribution functions, coordination numbers and hydrogen bonds. Part of these calculations was performed in the facilities of University of Notre Dame, IN, USA, under supervision of Prof. Dr. Edward Maginn. In this study, Helena Passos and Bruno Henriques carried out the experimental measurements (density, viscosity and solubility measurements).

To this study, I had the supervision of my advisors, Prof. Dr. João A. P. Coutinho and Dr. José R. B. Gomes, and further contributions from Dr. Mara Freire.

Motivation

The carbohydrate *D*-glucose, a hexopyranose with two stereoisomers (*α-D*-glucopyranose and *β-D*-glucopyranose), is the monomer of cellulose, the most abundant biopolymer found in wood.[1] *D*-glucose is an essential compound to many biological functions and for different chemical industries, highlighting its role as a renewable feedstock in the production of biofuel.[2–4] In fact, one of the main goals of biorefineries is to recover cellulose from wood, and further proceed to its hydrolysis in order to obtain glucose, which upon fermentation will produce bioethanol.[5–8] Several alternatives for the recovery of cellulose from wood were discussed already in Chapter 1.4 and, therefore, only some important remarks are provided below. It is known that common solvents, such as water, are not able to dissolve cellulose, which has lead to the use of different solvents. Nevertheless, the tested solvents (carbon disulfide, LiCl-based solvents[9], dimethylsulfoxide (DMSO)/paraformaldehyde[10] and also N-methylmorpholine-N-oxide (NNMO)[11]) are either volatile, toxic, expensive or difficult to recover.[12]

Among the alternatives to be used as solvents, ionic liquids have been proposed and extensively studied. For instance, in the past decade, it has been reported the use of ILs as solvent for the pre-treatment and dissolution of wood and cellulose.[4,12,13] However, for an effective dissolution, it is required to choose a proper ionic liquid, with specific properties. A good solvent should have low melting point, reduced viscosity, should be non-toxic or corrosive and easy to recover, storable and stable, and should not decompose the lignocellulosic constituents. If these properties are achieved, the use of ILs will allow an effective dissolution and promote a "greener" and sustainable process of biofuel production.[4,12]

Among the huge number of possible combinations between cations and anions that can compose an IL, the task of finding those that fulfill the previous requirements is a very difficult one to be performed merely through experimental means. Nevertheless, in studies published by Pinkert et al.[13], Mäki-Arvela et al.[12] several experimental works applying different ILs to dissolve cellulose, lignin and wood are referenced. Complementing the previous studies, Holm and Lassi[4] published their perspective on the application and performance of different ILs as cellulose solvents. The authors showed that the dissolution proceed by the establishment of hydrogen bonds, similar to those existent between glucose molecules that are responsible for the crystalline structure of cellulose. Accordingly, the authors state that small cations, with functionalized groups, and anions with a high ability to establish hydrogen bonds are the best ions to interact with cellulose.

In respect to the identification of the best anions, the hydrogen bond basicity parameter, β, can be applied.[12,14,15] This parameter allows the identification of the anions with higher ability to establish hydrogen bonds with glucose, as a consequence of their polarity. Therefore, chloride, acetate, formate and phosphate anions arise as anions that can promote effectively the dissolution of cellulose. However, the adequate combination between cations and anions is the key for a successful pre-treatment of lignocellulosic biomass and/or cellulose dissolution[16,17].

Moreover, aiming at a broader screening of the best solvent for cellulose (and lignin), Casas et al.[18] simulated the solubility of a cellulose oligomer in 750 different ILs by using the COSMO-RS approach, according to a specific methodology, which allowed the evaluation of the type/strength of interaction through the estimation of activity coefficients and, in a separate study[19] also with excess enthalpies. Common to the experimental studies, the 1-ethyl-3-methylimidazolium acetate (or chloride) were shown to be excellent candidates to act as cellulose solvents. Before Casas and co-workers, Kahlen et al.[20] have also used COSMO-RS to estimate the solubility of cellulose (represented by cellotriose) in 2000 ILs, and have proposed new ILs for cellulose dissolution.

Although it is well known that is through the establishment of hydrogen bonds that ILs and cellulose interact, the H-bond mechanisms for different ILs with cellulose are still not well known.[16] With the purpose of disclosing the existent interactions, computational approaches have been applied.[21–24] Among the various computational approaches (Chapter 2), molecular dynamics simulations present advantages, being able to estimate macroscopic thermophysical properties including transport ones, such as viscosity and diffusivity.[25] Furthermore, most of the available force fields developed to reproduce proteins or carbohydrates, including OPLS,[26,27] AMBER,[28,29] CHARMM,[30,31] GLYCAM,[32,33] and GROMOS[34,35] have received improvements in the past few years. The main difficulties of the force fields in the reproduction of systems composed of carbohydrates are related to the high heterogeneity of compounds, which differ in their stereochemistry and functionalization.[2,36] The heterogeneity of compounds can be observed when glucose is placed in an aqueous medium. Here, different conformations can co-exist due an interconversion of both glucose conformers, caused by a complex interplay between the steric, electrostatic, hydrogen bonding and solvation effects present in the system. These phenomena are barely taken into account by FFs, hindering their quality to adequately reproduce these systems. Additionally, the structural transitions occur over timescales that are too long when compared to practical MD simulation times, making their observation difficult without performing extremely long simulations.[2,36,37]

A recent publication by Gupta and Jiang[38] reviews computational MD works devoted to the study of the cellulose dissolution in ILs (mainly composed of imidazolium-based cations and

chloride/acetate anions). In those studies, different representations/models of cellulose were used, such as, glucose derivatives, cellobiose, oligomers, microfibrils or Iβ crystalline structure, and finally, glucose molecules. Through these MD simulations, it was evaluated the solubility of cellulose in ILs according to the solubility parameters[39,40], structural and energetic[41–43] properties, including the study of the effect of different ILs' cations and anions, and their impact in the establishment of hydrogen bonds.

The collected studies were able to provide some insights regarding the interactions conducing to the cellulose dissolution. It was observed that the anion of the IL establishes the primary and stronger interaction with cellulose, by disrupting the hydrogen bonds of cellulose (*i.e.*, those established between glucose monomers[38]), while a secondary role was proposed for the cation which establishes only weak van der Walls interactions[41] or H-bonds, through the acidic proton of the imidazolium cation[23] with cellulose. Nevertheless, the cation was also suggested as having an indispensable role in the initial breakup of H-bonds, when, strongly connected with the anion, is also able to break cellulose chains that are apart and at short distance.[38,44]

Other studies addressed the addition of water to the system of IL+glucose, the former also seen as an impurity.[13] The introduction of water will reduce the interactions initially formed by the anion and glucose, which will be replaced by glucose-glucose and water-anion interactions, according to the higher affinity of the anion with water. This phenomenon can be used to achieve the cellulose regeneration, with the precipitation of cellulose/glucose using water as anti-solvent.[45–47] Not only water but also other compounds such as acetone and ethanol were evaluated as anti-solvents.[46,48,49] Water presents the highest ability as anti-solvent, followed by ethanol and acetone, according to a decrease of the propensity to interact with the selected IL's anion. The regenerated cellulose is of type II, i.e, amorphous cellulose, as suggested by the torsion angles of the hydroxymethyl group of glucose.[40,50]

Additionally, some other studies were published aiming at disclosing the differences in the ability to dissolve cellulose/glucose between the common solvents (water and methanol/ethanol) and ILs.[41,51] Both from the estimation of interaction energies[41] and potential mean forces[42,43], ILs were found to present the best capacities as cellulose solvents. This ability has been explained by a reduction of solvent entropy (when in process of cellulose dissolution) that is lower in the case of ILs and favorable to dissolution, which is also supported by the favorable values obtained when estimating the interaction energies.

The present chapter is dedicated to understand the differences in the interactions between glucose and water and between glucose and some ILs aiming at the understanding of the enhanced ability of some ILs to dissolve carbohydrates.

The molecule of glucose will be here used as a model species dispersed in water or in ILs composed of the cation 1-ethyl-3-methylimidazolium with the anions thiocyanate, dicyanamide, tricyanomethane, tetracyanoborate and acetate.

This chapter is divided into four sections. The first section reports the experimental solubility of D-glucose in water and the four CN-based ILs previously mentioned plus, for alkyl chain length effect evaluation, 1-butyl-3-methylimidazolium thiocyanate/dicyanamide. Afterwards, MD simulations are performed with three distinct objectives. Firstly, it is addressed the comparison between systems composed of glucose and water with others composed of ILs with the anion thiocyanate and dicyanamide. Then, after evaluating the propensity of ILs with the anion thiocyanate and dicyanamide, it is evaluated the impact of ILs' anion bearing different number of cyano groups (from 1 to 4) in glucose dissolution. Structural information at the atomic level gathered from the interaction of the four CN-based ILs with a single glucose molecule is then transposed to the microscopic level. Ultimately, the interactions occurring between glucose and the thiocyanate and dicyanamide based ILs will also be compared with those determined for another IL that is being considered as a good candidate to dissolve cellulose, *i.e.*, the 1-ethyl-3-methylimidazolium acetate, as an attempt to understand the differences among the interactions established between the ILs and glucose.

Methodology

Experimental Section

Materials

The monosaccharide evaluated in this study was D-(+)-glucose (purity of > 99 wt%) acquired from Scharlau. Regarding the ILs used, 1-ethyl-3-methylimidazolium thiocyanate, [EMIM][SCN] (mass fraction purity > 98 %), 1-ethyl-3-methylimidazolium dicyanamide, [EMIM][DCA] (mass fraction purity > 99.5 %), 1-butyl-3-methylimidazolium thiocyanate, [BMIM][SCN] (mass fraction purity > 98 %), 1-butyl-3-methylimidazolium dicyanamide, [BMIM][DCA] (mass fraction purity > 98 %), were purchased from IoLiTec, while 1-ethyl-3-methylimidazolium tricyanomethane, [EMIM][TCN] (mass fraction purity > 98 %), 1-ethyl-3-methylimidazolium tetracyanoborate, [EMIM][TCB] (mass fraction purity > 98 %) were supplied by Merck KGaA Germany. The purities were further confirmed by ^{1}H and ^{13}C NMR

and found to be in agreement with the purity levels given by the suppliers. In order to reduce the amount of volatile impurities, all ILs and D-(+)-glucose samples were dried for at least 48 h under vacuum (10^{-3} Pa) at room temperature, before use. After the drying procedure, the water content of each sample was determined using a Metrohm 831 Karl Fisher coulometer with an associated uncertainty of ±3 μg. The water content was found to be < 0.091 wt% for all samples. The analyte used for the coulometric Karl Fisher titration was Hydranal – Coulomat AG from Riedel-de Haën.

Solubility measurements

Prior to measurements, it was recognized that all ILs have complete miscibility with water, with the exception of 1-ethyl-3-methylimidazolium tetracyanoborate, [EMIM][TCB], as mentioned in Chapter 3.2. For this reason, two procedures were applied to measure the solubility of glucose in these ILs, according to the nature of the IL (hydrophilic or hydrophobic).

The first methodology is applied to the hydrophilic ILs (having a complete miscibility with water). To vials containing *ca.* 3 cm^3 of each IL, it was added an amount of glucose in excess. The mixtures were left under constant stirring for at least 72 h, at the temperature of interest, in order to achieve the equilibrium. The temperature was kept constant using a thermostatized bath, Jubalo F12, maintaining temperature with an uncertainty of ±0.01 K. After the equilibration, and aiming at the separation of the phases, the samples were centrifuged during 20 minutes, at 4500 rpm, in an Eppendorf 5804 centrifuge. Afterwards, the vial was placed again in the thermostatized bath, around 30 minutes. Then, approximately 1 g (gravimetrically weighted with the uncertainty of ±0.0001 g) of the IL rich phase was taken, and diluted in distilled water in a volumetric ratio previously defined. The quantification of the content of glucose in this sample was determined through the DNS (3,5-dinitrosalycilic acid) method.[52] This method is based on a reduction-oxidation reaction when adding the DNS to a carbohydrate solution. Here, the sugar (the carbonyl groups) will be oxidized and the DNS will be reduced to 3-amino-5-nitrisalicylate acid. After this reaction, the reducing sugars are easily determined using UV spectroscopy at a wavelength of 540 nm. Accordingly, to a 1 cm^3 of the aqueous solution with an IL previously prepared, it was added 1 cm^3 of a standard DNS solution. This mixture was placed in the thermostatized bath, at a temperature of 373 K, for 10 minutes. The following step consisted in placing the samples for a few minutes into ice, and

again diluted in 10 cm^3 of distilled water. The quantification of glucose was made using a UV-Vis spectrophotometer, the Shimadzu UV-1700 Pharma-Spec, at the wavelength of 540 nm.
The second method, applied to [EMIM][TCB] (the hydrophobic IL), is similar to that previously described. After the equilibration step and the centrifugation of all the samples, approximately 1 g of the IL rich phase was weighted and registered. To this solution it was added 3 cm^3 of dichloromethane, an anti-solvent, promoting the precipitation of glucose. The following step was the filtration of the previous solution and further washing with dichloromethane to ensure the removal of IL's traces. Here, the quantification of sugar was determined by weight, with an uncertainty of ±0.0001 g. All solubility measurements were carried at least three times.

Density and viscosity measurements

The density and viscosity of systems composed of glucose and [EMIM][SCN]/[EMIM][DCA] were experimentally measured for direct comparison with values from MD simulations in order to check if the latter were able to reproduce real systems composed of glucose and ILs.
For these measurements, amounts of D-(+)-glucose were dried in an oven at 378 K and the ILs were also dried for at least 48 h under vacuum (10^{-3} Pa), at room temperature. The water content of each IL and glucose, after the drying step, was determined by Karl Fischer titration using a Metrohm 831 Karl Fischer coulometer. The average water content of [EMIM][DCA], [EMIM][SCN] and glucose were 0.17, 0.11 and 1.14 %, respectively.
Glucose and ILs mixtures were then prepared at the following mole fractions: 0.004, 0.034, 0.060 and 0.100. Using an automated SVM 300 Anton Paar rotational Stabinger viscometer-densimeter, density and viscosity measurements were performed, at the temperature range of (308.15 to 333.15) K, with an uncertainty of ±0.02 K, and at atmospheric pressure (≈ 0.1 MPa). The absolute uncertainty in density is $\pm 5\times10^{-4}$ $g\cdot cm^3$ and the relative uncertainty in dynamic viscosity is ±0.35 %. Further details on the equipment have been addressed in Chapter 3.1.

Computational Section

Molecular dynamics simulations

MD simulations were performed for systems composed of glucose and water and different ILs using the version 4.5.5 of the GROMACS code[53]. For this study, the chosen ILs were [EMIM][SCN], [EMIM][DCA], [EMIM][TCN], [EMIM][TCB] and 1-ethyl-3-methylimidazolium acetate ([EMIM][Ac]). Regarding the systems composed of glucose and water, [EMIM][SCN], [EMIM][DCA] and [EMIM][Ac], simulations were performed for systems containing 170 water/ILs molecules and 6, 11 or 20 glucose molecules yielding solutions with glucose mole fractions of 0.034, 0.060 and 0.100, respectively. Each box was built with the PACKMOL package[54], with a random distribution of the molecules and imposing a distance of 2.5 Å between the molecules to ensure that no atomic overlapping occurs. Additionally, simulations were also performed for systems composed by 250 molecules of each of the CN-based ILs and a single glucose molecule, which correspond to 0.004 glucose mole fractions.

Water and glucose molecules were described by means of the SPCE model[55] and the OPLS[27] force field (an all-atom approach), respectively. The force field parameters for the $[EMIM]^+$ cation and the anions $[SCN]^-$, $[DCA]^-$, $[TCN]^-$ and $[TCB]^-$ were described in detail in previous chapters (namely, Chapters 3.1 and 3.2). For the anion $[Ac]^-$, the force field parameters were based on the OPLS-AA force field[56] as used by Chandran et al.[57]. The atomic charges for the IL cation and anions were recalculated in the present work with the CHelpG scheme[58], using an optimized DFT geometry (minimum energy from several configurations) for each IL ion pair, in the gas phase as performed previously for other systems involving ILs (Chapters 3.1 and 3.2). The DFT calculations were performed at the B3LYP/6-311+G(d,p) level of theory[59] with the Gaussian 09 code.[60] The total charges on the cations and anions were ±0.775 *e* for [EMIM][SCN], ±0.824 *e* for [EMIM][DCA], ±0.858 *e* for [EMIM][TCN], ±0.887 *e* for [EMIM][TCB], and ±0.887 *e* for [EMIM][Ac]. The full sets of atomic charges for each IL are compiled in Tables E.1 to E.5 of the Appendix E. To validate the applied force fields for each system considered, densities for each pure IL were estimated, at 298.15 K, and are compared with the experimental values recently published by Neves *et al*.[26] in Table E.6 of the Appendix E. A satisfactory agreement between experimental and simulated data is observed with relative deviations of 4.1 %, 4.0 %, 3.9 %, 2.2 % and 2.1 % in the cases of [EMIM][SCN], [EMIM][Ac], [EMIM][DCA], [EMIM][TCB] and [EMIM][TCN], respectively. Note that,

slight differences in the atomic charges when compared with those used in previous studies result from the consideration of a different level of theory during the estimation of the charges according to the CHelpG scheme. Enthalpies at T = 313.15 K corresponding to the interactions between the glucose monomer and water, and between the glucose monomer and the anions (species X in equation 3.5.1) thiocyanate, dicyanamide and acetate, were computed at the B3LYP/6-311+G(d,p) level of theory as:

$$\Delta H_{int} = H_{glucose-X} - H_{glucose} - H_X \quad (3.5.1)$$

In the calculation of the enthalpies, a scale factor of 0.9887[61] was used to correct the frequencies. These enthalpies include also the corrections for the zero-point vibration energy (ZPVE) and for the basis set superposition error (BSSE, obtained with the Counterpoise method[62]).

For all mixtures considered, starting configurations were subjected to energy minimization followed by a 20 ns equilibration in the isothermal-isobaric (NPT) ensemble. During this period, the temperature was maintained at 313.15 K via a Nosé-Hoover thermostat[63,64] while the pressure was held at 1 bar with a Parrinello-Rahman barostat.[65] A cutoff of 0.9 nm was applied for non-bonded interactions for the aqueous system and for systems composed of ILs cutoffs of 1.2 and 1.0 nm were set for Lennard-Jones and Coulombic interactions. Corrections for long-range interactions were also taken into account. The time step was 2 fs, and all bonds were constrained. The same procedure was performed for three independent configurations, and densities were estimated from the average of the three simulations.

Using the densities obtained from the NPT simulations, a configuration of the system at the average density for each considered mixture was taken and simulations were then run in the canonical (NVT) ensemble. The system was equilibrated by running an annealing schedule for 15 ns from 298.15 to 500.15 K and then finally to 313.15 K. Production runs were then carried out for additional 65 ns (minimum time length) at 313.15 K. A time step of 1 fs was used, with energies recorded every 10 fs. Once again, a cutoff of 0.9 nm was applied for non-bonded interactions for the aqueous systems, while for those composed of ILs, cutoffs of 1.2 and 1.0 nm were set for Lennard-Jones and Coulombic interactions, respectively. Corrections for long-range interactions were also taken into account.

Results and Discussion

Solubility measurements

Figure 3.5.1 depicts the results obtained from the experimental measurement of the solubility of glucose in the ILs composed of the cation 1-ethyl-3-methylimidazolium and 1-butyl-3-methylimidazolium with the anions thiocyanate, dicyanamide, and in the ILs 1-ethyl-3-methylimidazolium tricyanomethane and 1-ethyl-3-methylimidazolium tetracyanoborate. Additionally, by applying the DNS method, an extra measurement was performed to attain the solubility of glucose in water, which is also represented in Figure 3.5.1. The corresponding values are compiled in Table E.7 (Appendix E).

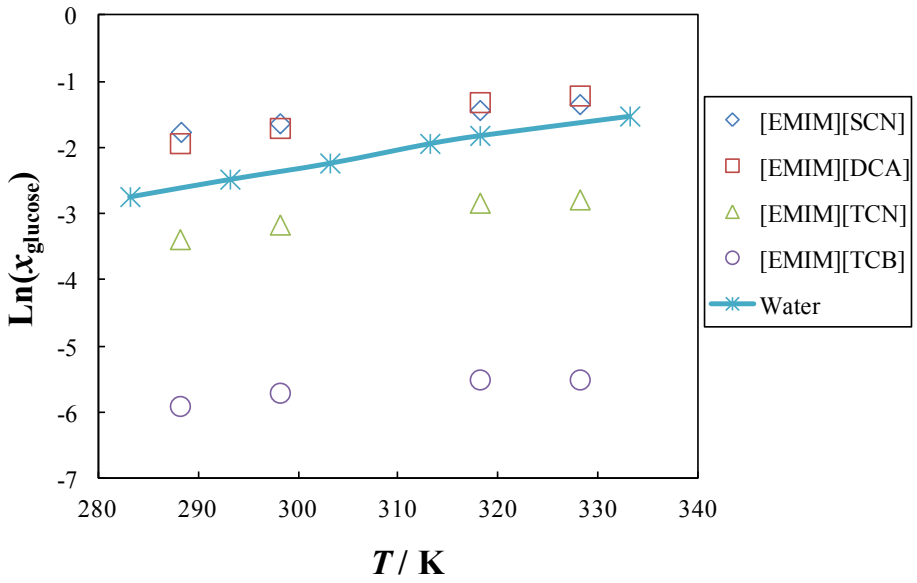

Figure 3.5.1 – The solubility of glucose in water, [EMIM][SCN], [EMIM][DCA], [EMIM][TCN] and [EMIM][TCB], in a temperature range of (283.15 – 333.15) K.

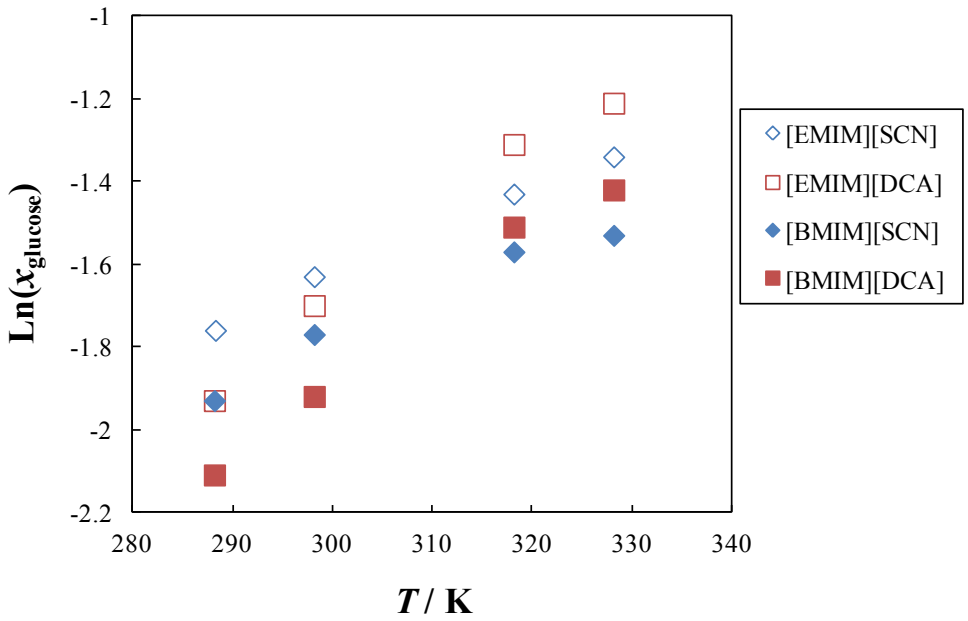

Figure 3.5.2 – Effect of different alkyl chain length of IL's cation on glucose solubility, in a temperature range of (283.15 – 333.15) K.

From the results depicted in Figure 3.5.1, it is possible to recognize that some of the chosen ILs have higher dissolution power than water, namely, [EMIM][SCN] and [EMIM][DCA]. However, the other CN-based ILs, with higher number of cyano groups in the ILs' anion, have a lower capacity to dissolve glucose. Additionally, it is worth noticing the minor differences in the values of the solubility of glucose in [EMIM][SCN] and [EMIM][DCA]. At low temperatures, the [EMIM][SCN] seems to present a higher ability to dissolve glucose, but with the increase of temperature, [EMIM][DCA] becomes the most efficient (Figure 3.5.1). Moreover, for thiocyanate and dicyanamide based ILs, it was evaluated the effect of changing the alkyl chain length of the IL's cation (Figure 3.5.2). The observations above are shared by the latter ILs but, as it can be understood from Figure 3.5.2, systems composed by cations with shorter alkyl chains show higher capacity to dissolve glucose, being this difference more noticeable with the increase of temperature. The latter observations and the good solubility capacity of thiocyanate and dicyanamide based ILs were already discussed elsewhere[3,4,66]. It is important to highlight that these solubility results are able to demonstrate that the anion has more influence in the dissolution of the sugar than the cation, as visible by the significant differences on the solubility of glucose on the various ILs (Figures 3.5.1 and 3.5.2). For this reason, the following sections will report the molecular dynamics simulation results for systems composed of

glucose and ILs with the cation 1-ethyl-3-methylimidazolium and with four CN-based anions, with the aim of understanding their capacity to dissolve glucose.

Molecular dynamics simulations

Why do ionic liquids are better glucose solvents than water?

Calculated density and viscosity

Values of density and viscosity calculated from MD simulations, and their comparison with experimental values measured in this study are presented in Figures 3.5.3 and 3.5.4 for the binary systems composed of glucose and [EMIM][SCN] and [EMIM][DCA], with the corresponding numerical values provided in Tables E.8 and E.9 of the Appendix E. The results show that, in general, our simulations slightly underestimate densities and viscosities. Deviations from experimental values are larger in the case of binary systems composed of [EMIM][SCN], but differences can be considered acceptable[67] and similar to what was obtained in a study performed by Jahn et al.[68]. However, for the systems containing [EMIM][DCA], a very good agreement with experimental densities and viscosities was attained. It is worth to note that, as mentioned in detail in Chapter 2, the viscosity of ILs is one of the most difficult properties to be reproduced through MD simulations. Viscosities were calculated here according to the Green-Kubo relation and to the methodology applied by Rey-Castro and Vega[69] (Chapter 3.4), and a satisfactory agreement with the experimental values was attained (numerical values of the fitting parameters employed can be found in Table E.10). These results suggest that the chosen force fields are acceptable for reproducing the binary systems composed of glucose and differences can be related to the set of atomic charges used in the simulations. In fact, some differences were already observed for the density values of the pure compounds (Tables E.1 and E.2, Appendix E).

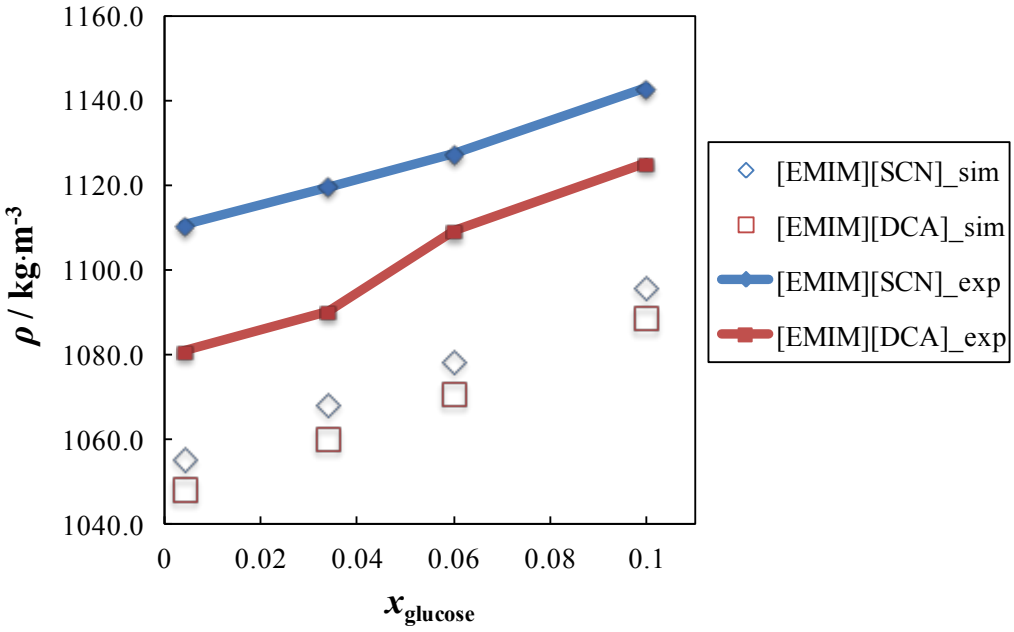

Figure 3.5.3 – Comparison of experimental and computed density, for systems composed of glucose and [EMIM][SCN] and [EMIM][DCA], at 313.15 K.

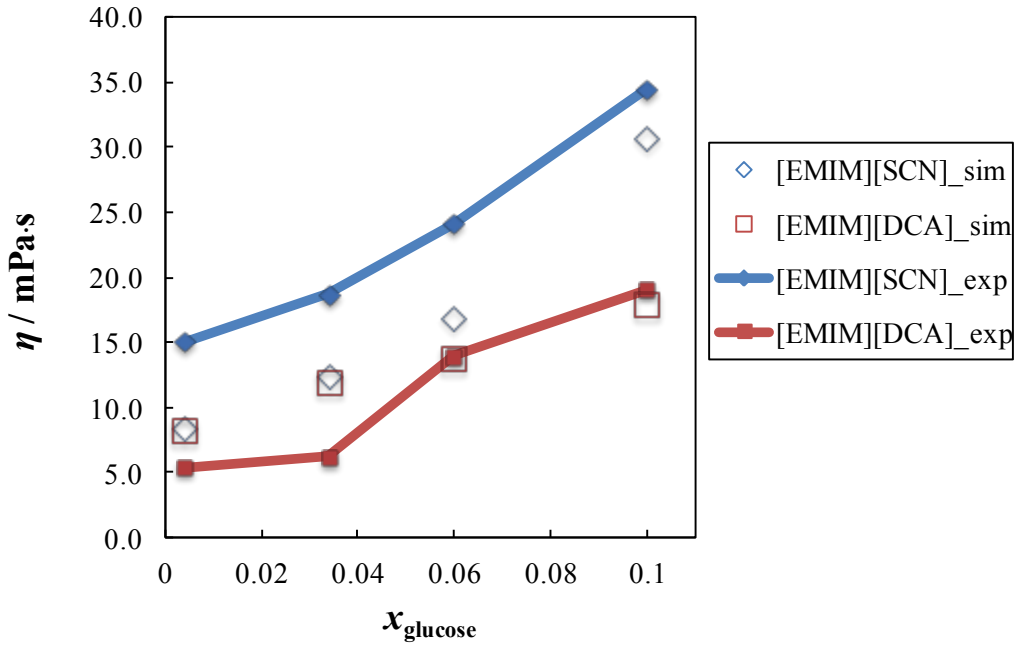

Figure 3.5.4 – Comparison of experimental and computed viscosity, for systems composed of glucose and [EMIM][SCN] and [EMIM][DCA], at 313.15 K.

Values of density and viscosity obtained for systems composed of water and glucose were already mentioned and discussed in Chapter 3.4 (namely, Tables D.1 and D.3, Appendix D). For those, although producing overestimated values, a good agreement with experimental densities and viscosities is also found when considering mole fraction of glucose above 0.1.

Radial distribution functions and coordination numbers

To disclose the underlying interactions, the structural arrangement was evaluated by computing radial distribution functions (*g(r)* or RDF) for various sites on glucose and water/ILs.

Specifically for this study, interactions established through the cation and the anion of ILs and water were addressed by computing RDFs for the atoms H_1 (acidic proton of imidazolium ring), N (of cyano groups) and H_w, O_w, respectively, with oxygen and hydrogen atoms of all hydroxyl groups of glucose (see Figures 3.5.5, 3.5.6 and E.1). Coordination numbers (Z) for these pairs were also computed by integrating the RDFs using a radial cutoff r_Z. This cutoff distance was chosen to be the first local minimum of the corresponding RDF, as performed in previous chapters.

As mentioned, the interactions established by glucose are made through their hydroxyl groups, by means of hydrogen bonds. Fortunately, RDFs have the capability of providing information regarding the establishment of H-bonds. Strong H-bonds are recognizable by the presence of a RDF for a site-to-site Y—H-X interaction, where Y is an oxygen or nitrogen atom and X an oxygen atom, with a first minimum (r_z) at a distance smaller than 0.26 nm, whereas weak H-bonds show a RDF for a site-to-site Y—H-X interaction, where Y is an oxygen or nitrogen atom and X a carbon atom, with the first minimum at a distance smaller than 0.40 nm[70]. A clear observation in Figures 3.5.6 and E.1 is the appearance of the first minimum of the site-to-site interactions in the anion-glucose and water-glucose RDFs at a distance smaller or equal to 0.26 nm (strong H-bonds). For cation-glucose interactions (Figure E.1), RDFs present a minimum at a distance equal to 0.32 nm, *i.e.*, suggesting weaker H-bonds.

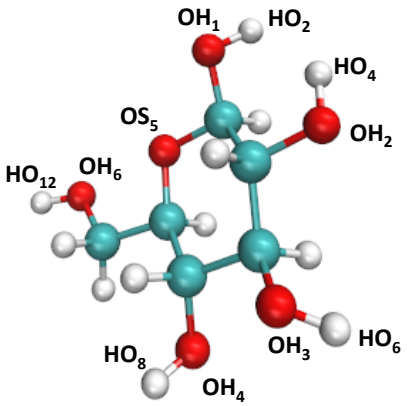

Figure 3.5.5 – Atom labels used in this study for glucose.

It is possible to perceive in Figure 3.5.6 that the profiles calculated for the anion-glucose and water-glucose (O_w-$H_{glucose}$) interactions are similar for the various ILs, while water presents a specific interaction profile. The latter is characterized by a presence of a double peak, suggesting the existence of interactions at two solvation shells. However, both peaks present small values of *g(r)*, in particular the second peak, suggesting a low probability to occur. Overall, in the entire range of composition, the IL containing the anion $[SCN]^-$ shows a higher probability of interacting with glucose molecules given by the highest values of *g(r)*, followed by the anion $[DCA]^-$ and water (note that the scale used in the graphical representation of the RDFs is different for each system). Nevertheless, the proton atom HO_2 of glucose (Figure 3.5.5) presents itself as the mediator of those interactions since, for all solvents, it shows a higher probability to interact than the other hydrogen atoms of glucose's hydroxyl groups.

The analysis of the RDFs corresponding to the cation-glucose (H_1-$O_{glucose}$) and water-glucose (H_W-$O_{glucose}$) interactions in Figure E.1, shows once more that the ILs present a higher probability to interact with glucose. Here, and for all solvents, the mediator is the oxygen atom OH_3 (Figure 3.5.5). Although the cation evaluated in this section is the same for the two ILs studied, the cation in [EMIM][DCA] presents higher values of *g(r)*, followed by the cation of [EMIM][SCN] and water. The latter solvent, by presenting the lowest values of *g(r)* acting either as a H-bond acceptor or donor, supports the experimental findings, *i.e.*, the selected ILs have higher ability to dissolve glucose than water.

Concerning the interactions established by glucose and water, another information could be extracted. In Chapter 3.4, the oxygen atom OS_5 of glucose was found to not establish interactions with water molecules, due to a steric hindrance (the neighbor atoms had the

highest propensity to interact with water). Herewith, despite the molecule of glucose is described with another force field (an all-atom approach), the same behavior is observed. However, in the systems with ILs, interactions with OS_5 seem to occur, suggesting that the preferential orientation of OS_5 neighboring groups in the glucose molecule are different systems with water and with ILs.

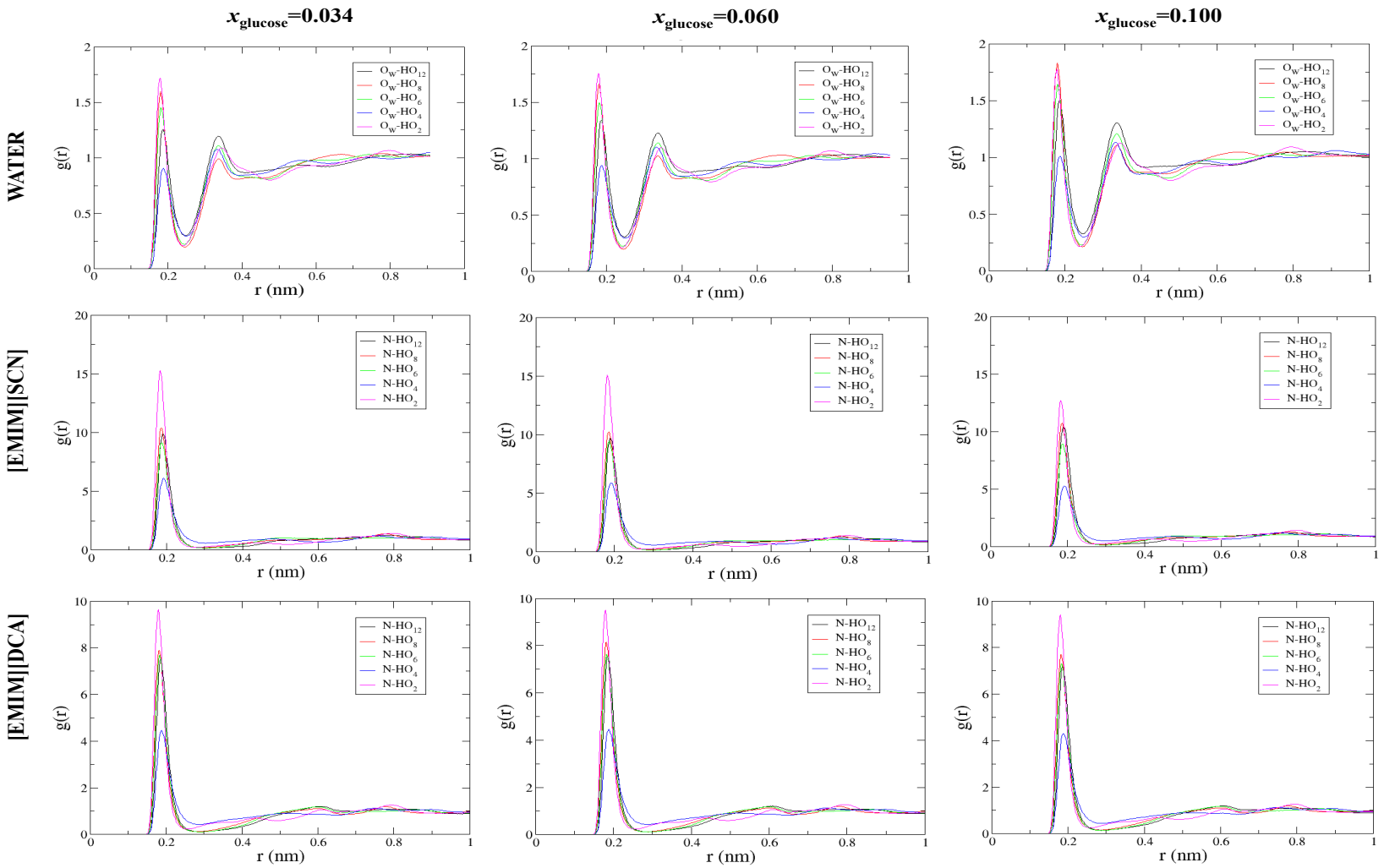

Figure 3.5.6 - Radial distributions functions (RDFs) for glucose-water (above row), glucose-[EMIM][SCN] (middle row) and glucose-[EMIM][DCA] (bottom row) interactions, at three different glucose mole fraction and a temperature of 313.15 K. DFs for interaction between O_W/N-HO_{12}(—), O_W/N-HO_8(—), O_W/N-HO_6(—), O_W/N-HO_4(—), O_W/N-HO_2 (—) are represented in this figure.

Table 3.5.1 – Coordination numbers (Z) from the RDFs peaks for glucose-water (O_W-$HO_{glucose}$) and anion-glucose, at each mixture considered.

WATER

$x_{glucose}$=0.034				$x_{glucose}$=0.060				$x_{glucose}$=0.100			
Water	Glucose	Z	r_Z	Water	Glucose	Z	r_Z	Water	Glucose	Z	r_Z
	HO_{12}	0.82	0.25		HO_{12}	0.75	0.25		HO_{12}	0.67	0.25
	HO_8	0.83	0.25		HO_8	0.75	0.25		HO_8	0.66	0.25
O_W	HO_6	0.81	0.25	**O_W**	HO_6	0.72	0.25	**O_W**	HO_6	0.62	0.25
	HO_4	0.68	0.25		HO_4	0.61	0.25		HO_4	0.52	0.25
	HO_2	0.86	0.25		HO_2	0.75	0.25		HO_2	0.62	0.25

[EMIM][SCN]

$x_{glucose}$=0.034				$x_{glucose}$=0.060				$x_{glucose}$=0.100			
Anion	Glucose	Z	r_Z	Anion	Glucose	Z	r_Z	Anion	Glucose	Z	r_Z
	HO_{12}	0.71	0.26		HO_{12}	0.67	0.26		HO_{12}	0.69	0.26
	HO_8	0.70	0.26		HO_8	0.66	0.26		HO_8	0.67	0.26
N	HO_6	0.64	0.26	**N**	HO_6	0.63	0.26	**N**	HO_6	0.58	0.26
	HO_4	0.57	0.26		HO_4	0.53	0.26		HO_4	0.46	0.26
	HO_2	0.88	0.26		HO_2	0.83	0.26		HO_2	0.68	0.26

[EMIM][DCA]

$x_{glucose}$=0.034				$x_{glucose}$=0.060				$x_{glucose}$=0.100			
Anion	Glucose	Z	r_Z	Anion	Glucose	Z	r_Z	Anion	Glucose	Z	r_Z
	HO_{12}	0.92	0.26		HO_{12}	0.91	0.26		HO_{12}	0.87	0.26
	HO_8	0.89	0.26		HO_8	0.90	0.26		HO_8	0.86	0.26
N	HO_6	0.90	0.26	**N**	HO_6	0.88	0.26	**N**	HO_6	0.81	0.26
	HO_4	0.74	0.26		HO_4	0.73	0.26		HO_4	0.71	0.26
	HO_2	0.98	0.26		HO_2	0.95	0.26		HO_2	0.94	0.26

To complement the analysis from RDFs, coordination numbers (Z) were calculated and values are compiled in Tables 3.5.1 and E.11. It is worth mentioning that coordination numbers are the quantification of the peaks of RDFs, giving an estimate (in this study computed from site-to-site RDFs) of how many atoms are at the vicinity of the atom of reference. The calculation

takes into account the heights and widths of the peaks of RDFs and also the density of the system, thus providing a numerical meaning to RDFs.

Table 3.5.1 presents the Z values for anion-glucose and water-glucose (O_w-$H_{glucose}$) interactions. From this table it is possible to verify that with the increase of glucose content in the system the values of Z decrease for all solvents; however this decrease is more evident for water-glucose interactions. Supporting the findings extracted from RDFs, the hydrogen atom HO_2 is that presenting the highest Z values, and although common to all systems, interactions with the anion $[DCA]^-$ have more probability to occur, followed by the anion $[SCN]^-$ and then water. When comparing the anion $[SCN]^-$ and water, higher values of Z are determined for interactions between water and the remaining hydrogen atoms of glucose's hydroxyl groups.

Regarding the interactions cation-glucose and water acting as a H-bond donor (Table E.11), a decrease of Z values is seen with the increase of glucose concentration. The oxygen atom OH_3, is the atom presenting higher Z values, supporting the information taken from RDFs. From the quantification of RDFs for water-glucose interactions (H_W-$O_{glucose}$) significant higher values of Z are obtained, suggesting that water predominantly interacts with glucose as a H-bond donor, rather than what was observed at RDFs.

Additionally, the coordination numbers for water-water (O_W-H_W) and cation-anion (H_1-N) interactions were also computed (Table E.10). The obtained results present, as expected, a decrease of interaction with the content of glucose in the system.

Spatial distribution functions

Figure 3.5.7 shows spatial distribution functions (SDFs) obtained with the TRAVIS[71] package for glucose surrounded by water, the cation $[EMIM]^+$, and by the anion $[SCN]^-$ and $[DCA]^-$.

The SDFs were obtained with the a fixed radius of solvation with value 1.8 nm but different isovalues were used for the atoms in the water molecules (36 particle nm^{-3}) and in the cations and anions of the ILs (7 particle nm^{-3}). Atoms of water are represented by red surfaces, atoms from the ILs' anions and cations by blue and mauve surfaces, respectively. Consistent with the RDFs and Z values, the SDFs show a decrease of solvent molecules surrounding glucose with the content of glucose. This effect is more pronounced in aqueous systems than in systems composed by ILs, where the difference is practically undetectable.

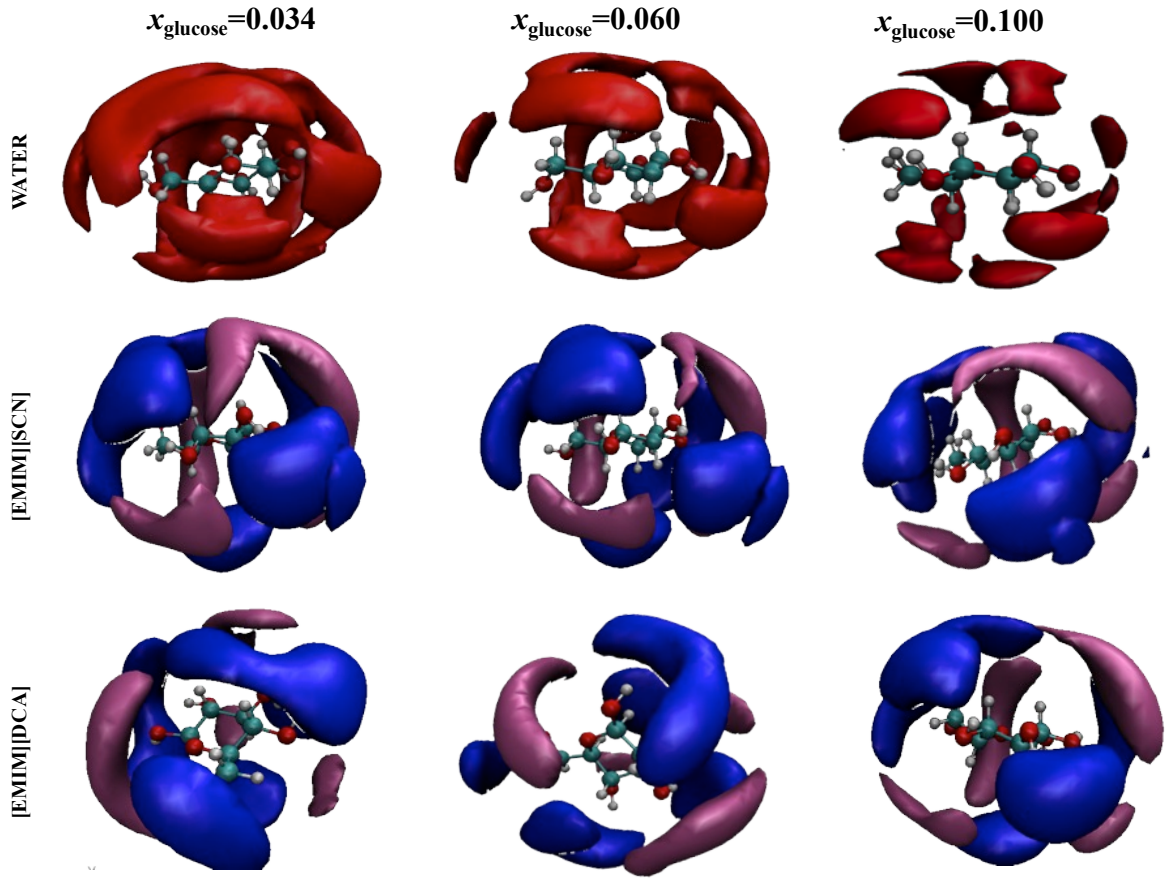

Figure 3.5.7 - Spatial distributions functions (SDFs) for glucose-water and glucose-anion/cation interactions, at three different glucose mole fraction and a temperature of 313.15 K. The central molecule is glucose, surrounded by water molecules (red surfaces), cations of IL (mauve surfaces) and anions of IL (blue surface). Isovalues for atoms in water and ILs are 36 and 7 particle·nm^{-3}, respectively.

Hydrogen Bonds

Table 3.5.2 compiles the number of hydrogen bonds per glucose molecule established between glucose and water, [EMIM][SCN] and [EMIM][DCA], at two different concentrations. These H-bonds were calculated using the g_hbond tool in the GROMACS code. All possible H-bond donors and acceptors in the systems were considered. The geometric criteria were 0.26 nm for the H-O distance (0.35 nm for the O-O distance), and 30º for the angle H-O—O. The comparison of the number of H-bonds established by water, [EMIM][SCN] or [EMIM][DCA] solvents with glucose shows that the highest number of H-bonds occurs in the latter solvent at both concentrations analyzed. Curiously, at the lowest concentration, water has the ability to

establish more hydrogen bonds with glucose than [EMIN][SCN], but this ordering is reversed when $x_{glucose}$ is equal to 0.100.

Table 3.5.2 – Number of hydrogen bonds established between glucose and water, [EMIM][SCN], [EMIM][DCA] and [EMIM][Ac], at two different glucose concentrations, at 313.15 K.

	H-bond per glucose			
$x_{glucose}$	Water	[EMIM][SCN]	[EMIM][DCA]	[EMIM][Ac]
0.034	3.6	3.3	4.2	4.8
0.100	2.8	3.0	4.0	4.8

To understand the experimental observations where [EMIM][SCN] and [EMIM][DCA] show better ability than water to dissolve glucose, further computer simulations were performed with the Gaussian 09 code[60] for estimating the strength of the H-bond interactions between the three solvents and glucose. These calculations were performed with the B3LYP/6-311+G(d,p) approach and considered structural models in vacuum consisting of a single glucose molecule interacting with a single water molecule, and glucose interacting separately with the anions $[SCN]^-$ or $[DCA]^-$ (similar calculations were made for the anion acetate, also included in Table 3.5.3, but results are going to be discussed and compared with the CN-based anions in a later section). From the RDFs it is clear that the most relevant solvent-glucose interactions occur with the atoms HO_2 and OH_1 (Figure 3.5.5). The interaction enthalpies calculated for the most stable configurations obtained by full optimization of the atomic positions of water, $[SCN]^-$, and $[DCA]^-$ in the vicinity of these bonds are compiled in Table 3.5.3.

Table 3.5.3 – Enthalpies calculated with the B3LYP/6-311+G(d,p) approach and at T = 313.15 K for glucose interactions with water, thiocyanate, dicyanamide and acetate.

	Interaction Enthalpy ($kJ \cdot mol^{-1}$)
Glucose-water	-25.1
Glucose-SCN	-111.2
Glucose-DCA	-94.7
Glucose-Ac	-153.9

The calculated enthalpies are -25.1, -111.2 and -94.7 $kJ \cdot mol^{-1}$ for interactions between glucose and water, $[SCN]^-$, and $[DCA]^-$, respectively. Thus, despite the complexity of the molecular systems was significantly reduced, the data in Table 3.5.3 suggest that the glucose molecules establish more favorable interactions with the ILs than with water. These findings support the experimental observations and the results from the MD simulations.

Evaluation of the CN-based ionic liquids' ability to dissolve glucose

The data above suggest that when fixing the cation, the $[DCA]^-$ anion presents better capacity to dissolve glucose than when the anion is $[SCN]^-$. Since the interactions with glucose involve the cyano moieties of these two anions, it would be interesting to understand what would be the effect of increasing the number of cyano groups in the strength of the interactions with glucose, and, indirectly, in the solubility of glucose. Experimental findings demonstrated that on going from anions with two to four cyano groups, the solubility of glucose in the corresponding ILs is reduced. These results are somewhat intriguing and to shed light upon it MD simulations were carried out, and RDFs and SDFs were computed aiming at further understanding the interactions between these cyano containing anions and glucose.

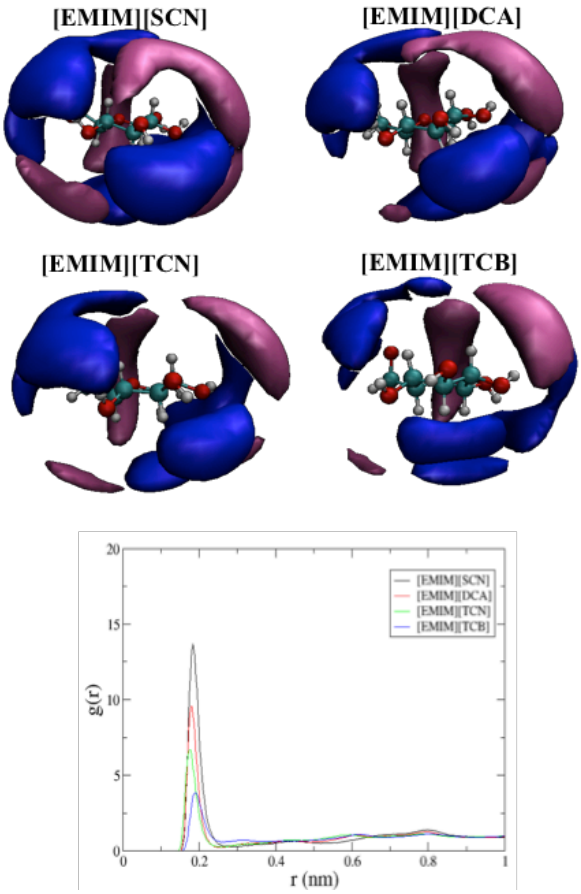

Figure 3.5.8 - Radial distributions functions (RDFs) and spatial distribution functions (SDFs) for glucose-anion interactions for the anions of CN-based ILs, at infinite dilution and a temperature of 313.15 K. Black, red, green and blue lines are used for RDFs corresponding to the interactions between [EMIM][SCN], [EMIM][DCA], [EMIM][TCN] and [EMIM][TCB] and glucose, while mauve and blue surfaces are used for SDFs concerning the glucose interactions with the cations and the anions, respectively.

Figure 3.5.8 depicts SDFs and RDFs concerning the interactions between four different ILs and glucose. The results obtained are in good agreement with the solubility measurements when, in general, an increase of the number of CN-groups in the anion decreases their ability to establish H-bonds. These differences were addressed previously in Chapters 3.2 and 3.3. The capacity of these CN-based ILs to interact successfully with glucose is highly correlated with their capacity to establish H-bonds as previously discussed. Interestingly, the strength of the interactions between the cyano groups from the anions and the hydroxyl groups from glucose seems to be correlated with the value of the atomic charges in the nitrogen atoms of the cyano

group in the each anions, which become less negative in the order of $[DCA]^-$ > $[SCN]^-$ > $[TCN]^-$ > $[TCB]^-$. The numeric values of the charges are -0.721 *e*, -0.666 *e*, -0.641 *e* and -0.486 *e*, respectively. The different charges in the cyano groups together with the different group symmetries of the anions induces different charge delocalization, and thus different polarities. The [EMIM][DCA], being the most polar IL among the CN-based ILs considered in this study, is that presenting the highest propensity to establish H-bonds with glucose, *i.e.*, it arises has the best solvent to dissolve glucose.

Performance of [EMIM][SCN] and [EMIM][DCA] vs [EMIM][Ac]: comparison to one of the best glucose solvents

This final section is dedicated to the comparison of one of the best ILs known to dissolve cellulose, and thus glucose, namely 1-ethyl-3-methylimidazolium acetate[12,18,70], [EMIM][Ac], with [EMIM][SCN] and [EMIM][DCA]. In the literature, it can be found solubility values of 39.41, 18.59 and 10.6 wt% for [BMIM][Ac][71], [BMIM][DCA][71] and [BMIM][SCN][72], respectively, at approximately ≈ 40 ºC. Since the cation is the same in these three ILs, the values of the solubilities suggest that the anion acetate has a very important propensity to interact with glucose, expectedly much higher than those found for the CN-based anions analysed above. Thus, it seems natural to compare directly the data reported above for the CN-based anions with the results from additional MD simulations concerning the structural arrangement of acetate around glucose molecules (e.g. RDFs, SDFs, and coordination numbers) and the results from B3LYP calculations regarding the strength of the hydrogen bonds established.

The computed RDFs and SDFs for three different glucose concentrations are found in Figure 3.5.9. The height of the peaks in the RDFs calculated for glucose interactions with [EMIM][SCN] are higher than those obtained for [EMIM][DCA], while those concerning the interactions with the [EMIM][Ac] stand between the two calculated for the two former ILs. At the lowest glucose concentration, the height of the RDF peak for [EMIM][Ac] is more similar to that of [EMIM][DCA] while upon the increase in the glucose concentration the RDF peak for [EMIM][Ac] becomes closer to that calculated for [EMIM][SCN]. Importantly, despite the differences are small, the maximum of the peak for the [EMIM][Ac] solvent occurs at smaller

r_Z values than those for [EMIM][DCA] and [EMIM][SCN]. This suggests that the interactions between glucose and the former solvent are more important than those with the CN-based ILs. The calculated SDFs for glucose-acetate interactions (Figure 3.5.9) seem to confirm the latter hypothesis. In fact, from comparison of the SDFs in Figures 3.5.7 (for [EMIM][DCA] and [EMIM][SCN]) and 3.5.9 ([EMIM][Ac]) it is found that the anion $[Ac]^-$ is also surrounding the hydroxyl groups of glucose, but the surfaces are denser than those for the cyano-based ILs, which suggests that the interactions are more specific and more localized. The coordination numbers reported in Table E.11 are in favor of these conclusions, *i.e.*, their values are larger when the solvent is [EMIM][Ac] than when the solvent is [EMIM][DCA] or [EMIM][SCN]. It is worth mentioning that an increase of the content of glucose in the system, has the same effect on the interactions as for $[SCN]^-$ and $[DCA]^-$, being almost undetectable.

The number of H-bonds established between glucose and the acetate anion and their energies of interaction in the gas phase are reported in Tables 3.5.2 and 3.5.3, respectively. As it can be seen, their values are larger than those calculated for the other solvents studied here, which are supporting the idea that the ability to dissolve glucose is correlated with the number and strength of the hydrogen bonds established with the glucose molecules. This ability can also be sustained by the polarity of the solvent, which can be given by the β solvatochromic parameter. The latter measures the hydrogen-accepting ability of an ion/compound and is considered a good indicator for determining glucose solvents. The β solvatochromic parameter for [EMIM][Ac] has a value of 0.85,[73] which is significantly higher than the values 0.762[15] and 0.671[15] reported for the anions dicyanamide and thiocyanate, respectively. This demonstrates the polar character of the anion acetate, and then its propensity to establish H-bonds with glucose/cellulose.

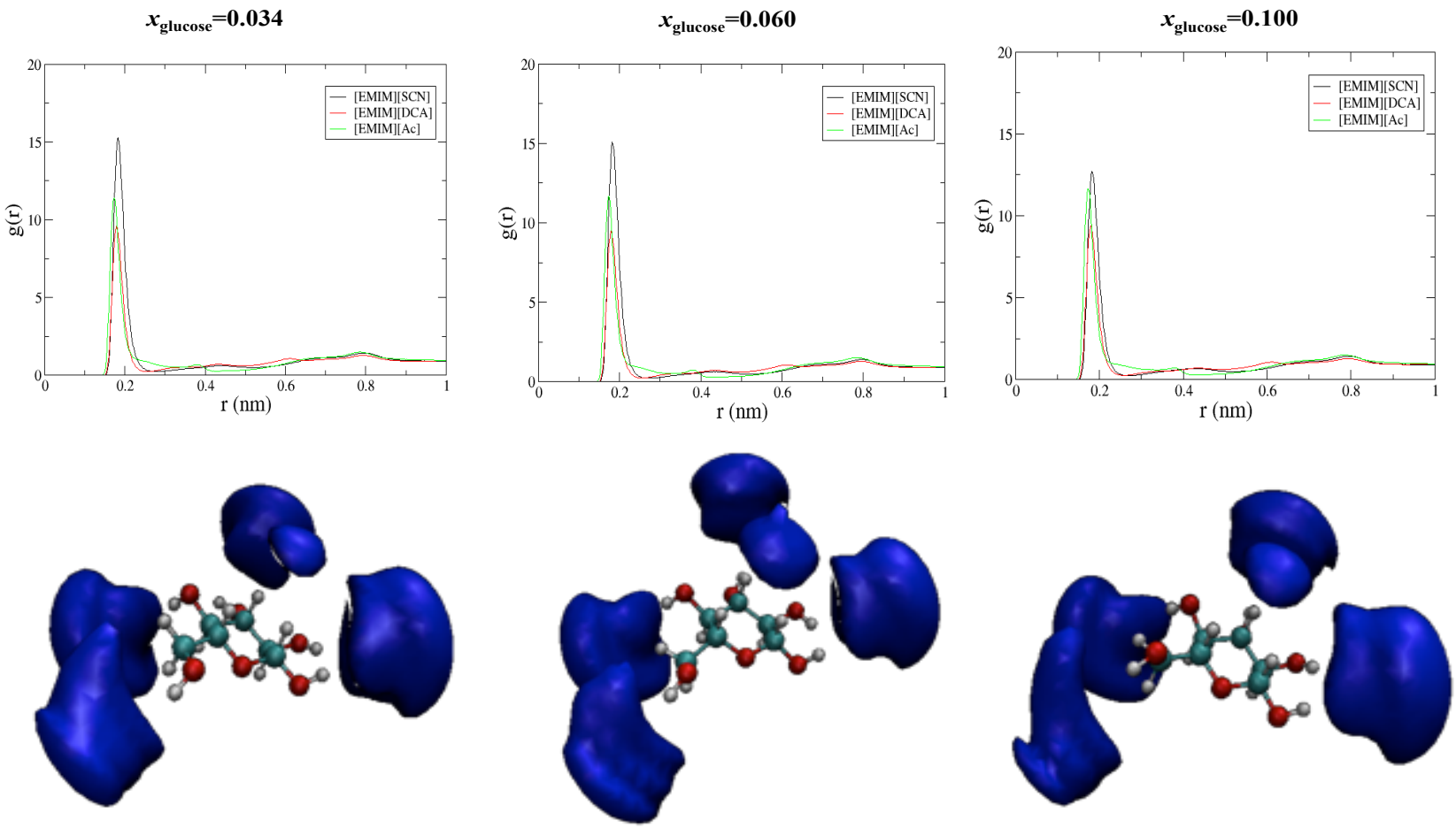

Figure 3.5.9 - Radial distributions functions (RDFs) and Spatial distribution functions for glucose-anion interactions for the anions of CN-based ILs and [EMIM][Ac], at different glucose concentrations and a temperature of 313.15 K. RDFs for interaction between [EMIM][SCN](—), [EMIM][DCA](—), and [EMIM][Ac](—) with glucose are represented in this figure. Additionally, at SDFs, the blue surfaces represent the acetate anion surrounding a glucose molecule.

Conclusions

In this study, the solubility of glucose in water and in different ILs was evaluated by means of experimental and computational techniques. The chosen ILs were composed by the 1-ethyl-3-methylimidazolium cation and the thiocyanate, dicyanamide, tricyanomethane and tetracyanoborate anions, often referred as the CN-based ILs. Additionally, for a more complete characterization of these systems, other ILs were also studied, namely 1-butyl-3-methylimidazolium thiocyanate, 1-butyl-3-methylimidazolium dicyanamide and 1-ethyl-3-methylimidazolium acetate.

The experimental measurements of glucose allowed to recognize that [EMIM][SCN] and [EMIM][DCA] have higher dissolution power than water. However, the two other CN-based ILs, presenting three and four of cyano groups in the ILs' anion, have lower capacity to dissolve glucose. Moreover, as expected, the solubility results showed that the anion has more influence in the dissolution of the sugar than the cation.

Information retrieved from computational results supports the experimental findings. On the whole, it was possible to observe and conclude that the interactions between glucose and ILs are mediated by the anion with the establishment of H-bonds. The propensity of the IL's anion to interact with glucose is, however, determined by its polarity that, on its turn, influences the strength/ability of those interactions. Therefore, the [EMIM][DCA] is the CN-based IL with the highest ability to dissolve glucose, followed by [EMIM][SCN]. The CN-based ILs with three and four cyano groups in its anion are less polar compounds, hindering their ability to establish H-bonds. However, when evaluating the ability of the CN-based ILs, water and [EMIM][Ac] (the latter being considered one of the best solvents for glucose dissolution) to establish H-bonds, it is recognized that water is establishing less H-bonds with glucose, followed by [EMIM][SCN], [EMIM][DCA] and, finally, [EMIM][Ac]. From the interaction enthalpies calculated in the gas phase with the hybrid B3LYP approach, it was possible to support that glucose is establishing more favorable interactions with the ILs rather than water. Additionally, it was observed that the [EMIM][Ac] not only is the IL establishing the most favorable H-bonds (as well as in number) with glucose, but that its interactions with glucose seems to be more specific and local than in the case of the other ILs.

Finally, the trends gathered from the different properties computed in this work are well correlated with the capacities of the different solvents to dissolve glucose.

References

(1) Sjöström, E. Wood Chemistry: Fundamentals and Applications, Second Edition, 1993.

(2) Foley, B. L.; Tessier, M. B.; Woods, R. J. *Wiley Interdiscip. Rev. Comput. Mol. Sci.*, **2012**, *2*, 652–697.

(3) Zakrzewska, M. E.; Bogel-Lukasik, E.; Bogel-Lukasik, R. *Energy & Fuels*, **2010**, *24*, 737–745.

(4) Holm, J.; Lassi, U. *Ionic Liquids: Applications and Perspectives*; Kokorin, A., Ed.; InTech, 2011.

(5) Demirbas, A. *Energy Sources*, **2005**, *27*, 327–337.

(6) Alvira, P.; Tomás-Pejó, E.; Ballesteros, M.; Negro, M. J. *Bioresour. Technol.*, **2010**, *101*, 4851–4861.

(7) Da Costa Lopes, A. M.; João, K. G.; Rubik, D. F.; Bogel-Łukasik, E.; Duarte, L. C.; Andreaus, J.; Bogel-Łukasik, R. *Bioresour. Technol.*, **2013**, *142*, 198–208.

(8) Magalhães da Silva, S. P.; da Costa Lopes, A. M.; Roseiro, L. B.; Bogel-Łukasik, R. *RSC Adv.*, **2013**, *3*, 16040–16050.

(9) Tamai, N.; Tatsumi, D.; Matsumoto, T. *Biomacromolecules*, **2004**, *5*, 422–432.

(10) Masson, J. F.; Manley, R. S. *Macromolecules*, **1991**, *24*, 6670–6679.

(11) Heinze, T.; Liebert, T. *Prog. Polym. Sci.*, **2001**, *26*, 1689–1762.

(12) Mäki-Arvela, P.; Anugwom, I.; Virtanen, P.; Sjoholm, R.; Mikkola, J. P. *Ind. Crops Prod.*, **2010**, *32*, 175–201.

(13) Pinkert, A.; Marsh, K. N.; Pang, S.; Staiger, M. P. *Chem. Rev.*, **2009**, *109*, 6712–6728.

(14) Anderson, J. L.; Ding, J.; Welton, T.; Armstrong, D. W. *J. Am. Chem. Soc.*, **2002**, *124*, 14247–14254.

(15) Cláudio, A. F.; Swift, L.; Hallett, J.; Welton, T.; Coutinho, J. A. P.; Freire, M. G. *Phys. Chem. Chem. Phys.*, **2014**, *16*, 6593–6601.

(16) Medronho, B.; Lindman, B. *Curr. Opin. Colloid Interface Sci.*, **2014**, *19*, 32–40.

(17) Lu, B.; Xu, A.; Wang, J. *Green Chem.*, **2014**, *16*, 1326–1335.

(18) Casas, A.; Omar, S.; Palomar, J.; Oliet, M.; Alonso, M. V.; Rodriguez, F. *RSC Adv.*, **2013**, *3*, 3453–3460.

(19) Casas, A.; Palomar, J.; Alonso, M. V.; Oliet, M.; Omar, S.; Rodriguez, F. *Ind. Crops Prod.*, **2012**, *37*, 155–163.

(20) Kahlen, J.; Masuch, K.; Leonhard, K. *Green Chem.*, **2010**, *12*, 2172–2181.

(21) Novoselov, N. P.; Sashina, E. S.; Petrenko, V. E.; Zaborsky, M. *Fibre Chem.*, **2007**, *39*, 153–158.

(22) Xu, H.; Pan, W.; Wang, R.; Zhang, D.; Liu, C. *J. Comput. Aided. Mol. Des.*, **2012**, *26*, 329–337.

(23) Youngs, T. G. A.; Hardacre, C.; Holbrey, J. D. *J. Phys. Chem. B*, **2007**, *111*, 13765–13774.

(24) Lopez, C. A.; Rzepiela, A. J.; de Vries, A. H.; Dijkhuizen, L.; Huenenberger, P. H.; Marrink, S. J. *J. Chem. Theory Comput.*, **2009**, *5*, 3195–3210.

(25) Haile, J. M. Molecular Dynamics Simulation: Elementary Methods, 1992.

(26) Kony, D.; Damm, W.; Stoll, S.; van Gunsteren, W. F. *J. Comput. Chem.*, **2002**, *23*, 1416–1429.

(27) Damm, W.; Frontera, A.; Tirado-Rives, J.; Jorgensen, W. L. *J. Comput. Chem.*, **1997**, *18*, 1955–1970.

(28) Glennon, T. M.; Zheng, Y.-J.; Le Grand, S. M.; Shutzberg, B. A.; Merz, K. M. *J. Comput. Chem.*, **1994**, *15*, 1019–1040.

(29) Momany, F. A.; Willett, J. L. *Carbohydr. Res.*, **2000**, *326*, 194–209.

(30) Ha, S. N.; Giammona, A.; Field, M.; Brady, J. W. *Carbohydr. Res.*, **1988**, *180*, 207–221.

(31) Guvench, O.; Hatcher, E. R.; Venable, R. M.; Pastor, R. W.; Mackerell, A. D. *J. Chem. Theory Comput.*, **2009**, *5*, 2353–2370.

(32) Woods, R. J.; Dwek, R. A.; Edge, C. J.; Fraser-Reid, B. *J. Phys. Chem.*, **1995**, *99*, 3832–3846.

(33) Kirschner, K. N.; Yongye, A. B.; Tschampel, S. M.; González-Outeiriño, J.; Daniels, C. R.; Foley, B. L.; Woods, R. J. *J. Comput. Chem.*, **2008**, *29*, 622–655.

(34) Koehler, J. E. H.; Saenger, W.; Gunsteren, W. F. *Eur. Biophys. J.*, **1987**, *15*, 197–210.

(35) Lins, R. D.; Hünenberger, P. H. *J. Comput. Chem.*, **2005**, *26*, 1400–1412.

(36) Fadda, E.; Woods, R. J. *Drug Discov. Today*, **2010**, *15*, 596–609.

(37) Hansen, H. S.; Hünenberger, P. H. *J. Comput. Chem.*, **2011**, *32*, 998–1032.

(38) Gupta, K. M.; Jiang, J. *Chem. Eng. Sci.*, **2015**, *121*, 180–189.

(39) Derecskei, B.; Derecskei-Kovacs, A. *Mol. Simul.*, **2006**, *32*, 109–115.

(40) Hauru, L. K. J.; Hummel, M.; King, A. W. T.; Kilpeläinen, I.; Sixta, H. *Biomacromolecules*, **2012**, *13*, 2896–2905.

(41) Liu, H.; Sale, K. L.; Holmes, B. M.; Simmons, B. A.; Singh, S. *J. Phys. Chem. B*, **2010**, *114*, 4293–4301.

(42) Cho, H. M.; Gross, A. S.; Chu, J.-W. *J. Am. Chem. Soc.*, **2011**, *133*, 14033–14041.

(43) Gross, A. S.; Bell, A. T.; Chu, J.-W. *J. Phys. Chem. B*, **2011**, *115*, 13433–13440.

(44) Rabideau, B. D.; Agarwal, A.; Ismail, A. E. *J. Phys. Chem. B*, **2013**, *117*, 3469–3479.

(45) Ding, Z.-D.; Chi, Z.; Gu, W.-X.; Gu, S.-M.; Liu, J.-H.; Wang, H.-J. *Carbohydr. Polym.*, **2012**, *89*, 7–16.

(46) Liu, H.; Sale, K. L.; Simmons, B. A.; Singh, S. *J. Phys. Chem. B*, **2011**, *115*, 10251–10258.

(47) Swatloski, R. P.; Spear, S. K.; Holbrey, J. D.; Rogers, R. D. *J. Am. Chem. Soc.*, **2002**, *124*, 4974–4975.

(48) Gupta, K. M.; Hu, Z.; Jiang, J. *RSC Adv.*, **2013**, *3*, 4425–4433.

(49) Gupta, K. M.; Hu, Z.; Jiang, J. *RSC Adv.*, **2013**, *3*, 12794–12801.

(50) Liu, H.; Cheng, G.; Kent, M.; Stavila, V.; Simmons, B. A.; Sale, K. L.; Singh, S. *J. Phys. Chem. B*, **2012**, *116*, 8131–8138.

(51) Payal, R. S.; Bharath, R.; Periyasamy, G.; Balasubramanian, S. *J. Phys. Chem. B*, **2012**, *116*, 833–840.

(52) Miller, G. L. *Anal. Chem.*, **1959**, *31*, 426–428.

(53) Hess, B.; Kutzner, C.; van der Spoel, D.; Lindahl, E. *J. Chem. Theory Comput.*, **2008**, *4*, 435–447.

(54) Martínez, L.; Andrade, R.; Birgin, E. G.; Martínez, J. M. *J. Comput. Chem.*, **2009**, *30*, 2157–2164.

(55) Berendsen, H. J. C.; Grigera, J. R.; Straatsma, T. P. *J. Phys. Chem.*, **1987**, *91*, 6269–6271.

(56) Jorgensen, W. L.; Maxwell, D. S.; Tirado-Rives, J. *J. Am. Chem. Soc.*, **1996**, *118*, 11225–11236.

(57) Chandran, A.; Prakash, K.; Senapati, S. *Chem. Phys.*, **2010**, *374*, 46–54.

(58) Breneman, C. M.; Wiberg, K. B. *J. Comput. Chem.*, **1990**, *11*, 361–373.

(59) Becke, A. D. *J. Chem. Phys.*, **1993**, *98*, 5648–5652.

(60) Frisch, M. J. .; Trucks, G. W. .; Schlegel, H. B. .; Scuseria, G. E. .; Robb, M. A. .; Cheeseman, J. R. .; Scalmani, G. .; Barone, V. .; Mennucci, B. .; Petersson, G. A. .; Nakatsuji, H. .; Caricato, M. .; Li, X. .; Hratchian, H. P. .; Izmaylov, A. F. .; Bloino, J. .; Zheng, G. .; Sonnenberg, J. L. .; Hada, M.; Ehara, M. .; Toyota, K. .; Fukuda, R. .; Hasegawa, J. .; Ishida, M. .; Nakajima, T. .; Honda, Y. .; Kitao, O. .; Nakai, H. .; Vreven, T. .; Montgomery, J. A., J. .; Peralta, J. E. .; Ogliaro, F. .; Bearpark, M. .; Heyd, J. J. .; Brothers, E. .; Kudin, K. N. .; Staroverov, V. N. .; Kobayashi, R. .; Normand, J. .; Raghavachari, K. .; Rendell, A. .; Burant, J. C. .; Iyengar, S. S. .; Tomasi, J. .; Cossi, M. .; Rega, N. .; Millam, M. J. .; Klene, M. .; Knox, J. E. .; Cross, J. B. .; Bakken, V. .; Adamo, C. .; Jaramillo, J. .; Gomperts, R. .; Stratmann, R. E. .; Yazyev, O. .; Austin, A. J. .; Cammi, R. .; Pomelli, C. .; Ochterski, J. W. .; Martin, R. L. .; Morokuma, K. .; Zakrzewski, V. G. .; Voth, G. A. .; Salvador, P. .; Dannenberg, J. J. .; Dapprich, S. .; Daniels, A. D. .; Farkas, Ö. .; Foresman, J. B. .; Ortiz, J. V. .; Cioslowski, J. .; Fox, D. J. *Gaussian 09, Revision D.01*; Gaussian, Inc., Wallingford CT, 2009.

(61) Merrick, J. P.; Moran, D.; Radom, L. *J. Phys. Chem. A*, **2007**, *111*, 11683–11700.

(62) Boys, S. F.; Bernardi, F. *Mol. Phys.*, **1970**, *19*, 553–566.

(63) Hoover, W. G. *Phys. Rev. A*, **1985**, *31*, 1695–1697.

(64) Nose, S. *Mol. Phys.*, **1984**, *52*, 255–268.

(65) Parrinello, M.; Rahman, A. *J. Appl. Phys.*, **1981**, *52*, 7182–7190.

(66) Liu, Q.; Janssen, M. H. A.; van Rantwijk, F.; Sheldon, R. A. *Green Chem.*, **2005**, *7*, 39–42.

(67) Maginn, E. J. *Acc. Chem. Res.*, **2007**, *40*, 1200–1207.

(68) Jahn, D. A.; Akinkunmi, F. O.; Giovambattista, N. *J. Phys. Chem. B*, **2014**, *118*, 11284–11294.

(69) Rey-Castro, C.; Vega, L. F. *J. Phys. Chem. B*, **2006**, *110*, 14426–14435.

(70) Skarmoutsos, I.; Dellis, D.; Matthews, R. P.; Welton, T.; Hunt, P. A. *J. Phys. Chem. B*, **2012**, *116*, 4921–4933.

(71) Brehm, M.; Kirchner, B. *J. Chem. Inf. Model.*, **2011**, *51*, 2007–2023.

(72) Freire, M. G.; Teles, A. R. R.; Rocha, M. A. A.; Schröder, B.; Neves, C. M. S. S.; Carvalho, P. J.; Evtuguin, D. V.; Santos, L. M. N. B. F.; Coutinho, J. A. P. *J. Chem. Eng. Data*, **2011**, *56*, 4813–4822.

(73) Rosatella, A. A.; Branco, L. C.; Afonso, C. A. M. *Green Chem.*, **2009**, *11*, 1406–1413.

(74) Conceiçao, L. J. A.; Bogel-Łukasik, E.; Bogel-Łukasik, R. *RSC Adv.*, **2012**, *2*, 1846–1855.

(75) Lungwitz, R.; Strehmel, V.; Spange, S. *New J. Chem.*, **2010**, *34*, 1135–1140.

4. Conclusions and Future Work

The emerging stringent environmental worldwide regulations impelled the development of several processes aiming at the improvement of fuels with the reduction of sulfur compounds, as well as, the development of new, "greener" alternatives, such as the production of biofuels.

In this matter, a new class of solvents, the ionic liquids, have gained a special importance due to their unique properties that enable and encourage their use on different areas as extracting solvents, such as in the case of desulfurization processes and at biochemical processes of conversion of lignocellulosic compounds to biofuels (more specifically on the pre-treatment of lignocellulosic materials).

Being composed of bulky and poorly coordinated organic cations and inorganic/organic anions, the number of possible combinations is very large and the characterization of these fascinating systems by experimental laboratorial work only is an impossible task. Computational approaches have been used for complementing experimental studies and to obtain new data. Within the different types of computational approaches that can be used to study systems composed by pure ionic liquids or by mixtures of ionic liquids and other compounds (briefly described in Chapter 2), classical MD simulations anchored on force fields developed with the aid of *ab initio* approaches have been shown to be appropriate for calculating several properties of ionic liquids (Chapter 2). From a concise review of the application of MD simulations in the prediction of ILs' properties it was found that is unquestionable the importance of the usage of MD as a reliable complement to experimental procedures, achieving good reproduction of densities, melting points and structural atomic organization. However, viscosities and diffusion coefficients are over and underestimated, respectively, requiring longer times of simulation. Though a lot of improvements have to be made, MD simulations can provide important information regarding mechanisms occurring at the atomic level, helping to disclose phenomena that usually are difficult to be explained.

Aiming at evaluating the performance of ILs as extracting solvents, different studies were carried out by experimental and computational means. To evaluate the capacity of ILs, systems composed of ILs and thiophene/benzene, ILs and water/ethanol, and glucose with ILs and water were chosen. The goal was to identify the mechanisms of interactions established by ILs, for further application in desulfurization processes and pre-treatment of lignocellulosic biomass (enabling the evaluation/design of the most suitable IL). Results revealed that, as expected, interactions with sulfur compounds are promoted through π-π interaction, originally from the aromatic character of ILs. These interactions can, however, produce different phase behaviors (LCST or UCST), depending on the individual characteristics of each IL and their interaction mechanism (Chapter 3.1). Having in mind that viscosity is one of the main drawbacks for the use of ILs at an industrial field, CN-based ILs were

studied. Characterized by low melting points and viscosities, these ILs are interesting for industrial purposes, *e.g*. as solvents for the production of biofuels. By studying ILs with one to four CN groups at the IL's anion, namely, thiocyanate, dicyanamide, tricyanomethane and tetracyanoborate anions, it was possible to show that their capacity to establish hydrogen bonds with polar solvents (water or ethanol) is not enhanced with the increase of CN groups in the anion but, instead, such capacity is strongly determined by the polarity of the anion (Chapter 3.2 and 3.3).

Regarding interactions established by glucose, the chosen system was primarily glucose with water, to infer on their mechanism of interaction and to evaluate their dynamic behavior. The ability of the new force field GROMOS $56A_{CARBO}$ for glucose molecules was evaluated to model properties of aqueous solutions of glucose. Obtained results are quite good for diluted solutions but as the concentration increases the glucose molecules tend to self-associate leading to the overestimation of properties. However, modifying the original force field by scaling the atomic charges of glucose by a factor of 0.8, leads to significant improvements in the values of the calculated densities and viscosities at glucose mole fractions in the range of 0.034 to 0.200, without decreasing too much the quality of the results at diluted mole fractions. Nonetheless, after a comparison of these results with those obtained with another force field, it was clear that improvements on the actual force fields, as well as the development from scratch of new force fields, able to successfully describe concentrated carbohydrate systems are necessary (Chapter 3.4).

As mentioned and detailed at Chapter 1.4.1, ILs can be applied to pre-treat and dissolve wood, cellulose and its simple sugars. Accordingly, Chapter 3.5 was devoted to the study of the performance of CN-based ILs to dissolve glucose either employing experimental and computational techniques. Moreover, this study evaluated and compared the CN-based ILs with an organic solvent, water, and one of the best cellulose solvents, the 1-ethyl-3-methylimidazolium acetate. The results obtained, agree with the conclusions extracted from previous chapters. The polarity of ILs is determinant in their ability to establish H-bonds and then, to interact successfully with glucose. Although computational results underestimated the values of some thermophysical properties determined experimentally for CN-based ILs, the conclusions arising from the computational work and from the experimental measurements are the same. The [EMIM][DCA] is the best glucose solvent among CN-based ILs, establishing stronger H-bonds with glucose than water.

For future work, aiming at the continued improvement of the processes of biofuels production and the implementation of ionic liquids in this field, it is suggested the utilization of this kind of computational approaches for the screening of other neat ionic liquids, or of a mixture of ionic liquids, with characteristics desired for biofuel production, namely high chemical and thermal stability, low

vapor pressure and melting point, and reduced viscosity. The screening would be improved with the use of a polarizable force field, which definitely affects (and improves) the prediction of properties by means of molecular dynamics simulations. Moreover, it has been reported that the use of a co-solvent in a mixture of IL and cellulose/glucose enables the dissolution of the carbohydrate. This co-solvent can be a common organic solvent, or even another ionic liquid. This could be considered an open issue of research, with characteristics to be investigated by computational approaches.

5. Appendixes

Appendix A

Tables

Table A.1 - CHelpG charges for [BMIM][SCN]. Atom labeling corresponds to Figure 3.1.1.

[BMIM][SCN]	atomic charge / *e*
H(7)	0.0478
H(8)	0.0044
H(4)	0.0693
H(12)	-0.0424
C(7)	-0.0529
C(9)	0.0234
H(1)	0.1743
H(5)	0.0452
N(1)	0.0931
C(2)	0.0809
H(14)	0.0168
H(3)	0.1461
C(8)	0.3325
C(5)	-0.2096
C(10)	-0.1093
N(2)	0.0775
C(6)	0.0068
H(9)	-0.0830
C(4)	-0.1369
H(2)	0.2044
H(10)	-0.0899
H(4)	0.0790
H(13)	0.0272
H(15)	0.0255
H(6)	0.0608
N	-0.6514
C	0.3836
S	-0.5234

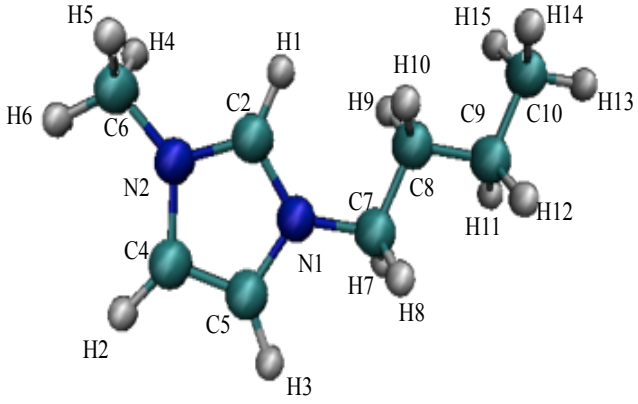

Table A.2 - CHelpG charges for [BMIM][NTf_2]. Atom labeling corresponds to Figure 3.1.1.

[BMIM][NTf_2]	atomic charge/ *e*
H(7)	0.0830
H(8)	0.0640
H(4)	-0.0250
H(12)	-0.0450
C(7)	-0.0940
C(9)	0.2180
H(1)	0.0760
H(5)	0.1480
N(1)	0.1310
C(2)	0.0890
H(14)	0.0470
H(3)	0.2160
C(8)	0.2090
C(5)	-0.2240
C(10)	-0.2640
N(2)	0.0870
C(6)	-0.1280
H(9)	-0.0170
C(4)	-0.1380
H(2)	0.1840
H(10)	-0.0360
H(4)	0.0890
H(13)	0.0640
H(15)	0.0700
H(6)	0.0930
O(1)	-0.5170
F(1)	-0.1960
F(2)	-0.2200
O(4)	-0.5170
C(1)	0.5550
O(3)	-0.5170
S(1)	0.9530
S(2)	0.9530
O(2)	-0.5170
N(1)	-0.5870
F(3)	-0.1630
F(4)	-0.1960

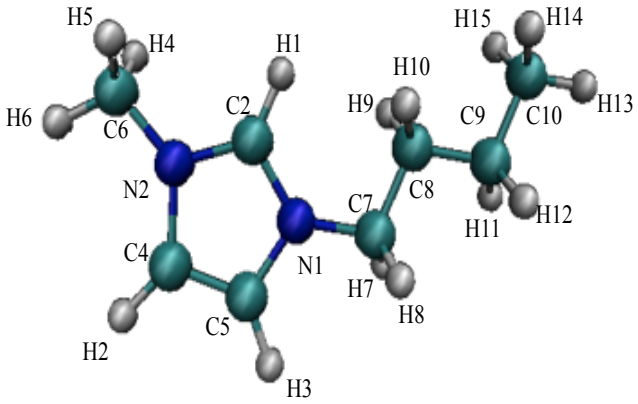

C(2)	0.5550	
F(5)	-0.2200	
F(6)	-0.1630	

Table A.3 - CHelpG charges for thiophene. Atom labeling as in Figure 3.1.1.

Thiophene	atomic charge / *e*
CS	-0.0700
HCS	0.0930
CC	-0.2050
HCC	0.1680
S	0.0280

Table A.4 - Lennard-Jones parameters for the cation $[BMIM]^+$.

$[BMIM]^+$	σ / Å	ε / $kJ \cdot mol^{-1}$
C(ring)	0.3207	0.2093
N(ring)	0.3296	0.8374
H(1)	0.2616	0.0327
H(2 and 3)	0.1604	0.1926
C(chain)	0.4054	0.0837
H(chain)	0.2352	0.0921
C(terminal)	0.3875	0.2303

Table A.5 - Lennard-Jones parameters for the anion $[NTf_2]^-$.

$[NTf_2]^-$	σ / Å	ε / $kJ \cdot mol^{-1}$
S	0.3550	1.0460
O	0.2960	0.8786
N	0.3250	0.7113
C	0.3500	0.2761
F	0.2950	0.2218

Table A.6 - Lennard-Jones parameters for the anion $[SCN]^-$.

$[SCN]^-$	σ / Å	ε / kJ·mol^{-1}
N	0.2976	0.8767
C	0.3361	0.4058
S	0.3308	1.9056

Table A.7 - Lennard-Jones parameters for thiophene.

thiophene	σ / Å	ε / kJ·mol^{-1}
S	0.3550	1.0460
CC	0.3550	0.3200
CS	0.3750	0.3400
H	0.2420	0.1255

Table A.8 – Experimental LLE in the ([BMIM][NTf_2]+thiophene) binary system

T / K	x_{IL}
272.2	0.511
288.0	0.500
290.6	0.496
300.3	0.490
303.4	0.487
336.5	0.471

Table A.9 - Excess molar volumes obtained for the different systems of ILs and thiophene/benzene, at different temperatures.

[BMIM][SCN] + Thiophene				
	T / K			
x_{IL}	298.15	308.15	318.15	328.15
	V^E / cm^3·mol^{-1}			
1.000	0.000	0.000	0.000	0.000
0.897	-0.691	-0.691	-0.732	-0.782
0.857	-0.920	-0.920	-0.968	-1.044
0.754	-1.260	-1.260	-1.348	-1.443
0.390	-1.998	-1.998	-2.192	-2.449
0.299	-2.184	-2.184	-2.404	-2.651
0.000	0.000	0.000	0.000	0.000

[BMIM][NTf$_2$] + Thiophene

	T / K			
x_{IL}	298.15	308.15	318.15	328.15
	V^E / cm^3·mol^{-1}			
1.000	0.000	0.000	0.000	0.000
0.911	-0.333	-0.340	-0.367	-0.382
0.724	-0.631	-0.655	-0.716	-0.783
0.664	-0.842	-0.886	-0.949	-1.041
0.439	-3.653	-3.773	-3.923	-4.097
0.230	-5.015	-5.185	-5.363	-5.597
0.000	0.000	0.000	0.000	0.000

[BMIM][SCN] + Benzene

	T / K			
x_{IL}	298.15	308.15	318.15	328.15
	V^E / cm^3·mol^{-1}			
1.0000	0.000	0.000	0.000	0.000
0.7666	-0.927	-1.023	-1.120	-1.220
0.7420	-1.021	-1.116	-1.212	-1.329
0.6081	-1.578	-1.720	-1.860	-2.035
0.4906	-1.814	-1.955	-2.142	-2.352
0.0000	0.000	0.000	0.000	0.000

[BMIM][CF$_3$SO$_3$] + Benzene

	T / K			
x_{IL}	298.15	308.15	318.15	328.15
	V^E / cm^3·mol^{-1}			
1.000	0.000	0.000	0.000	0.000
0.878	-0.553	-0.572	-0.615	-0.659
0.696	-1.415	-1.499	-1.601	-1.706
0.647	-1.345	-1.432	-1.554	-1.665
0.427	-2.380	-2.512	-2.688	-2.859
0.000	0.000	0.000	0.000	0.000

[EMIM][NTf$_2$] + Benzene

	T / K			
x_{IL}	298.15	308.15	318.15	328.15
	V^E / cm^3·mol^{-1}			
1.000	0.000	0.000	0.000	0.000
0.865	-0.543	-0.581	-0.613	-0.678
0.661	-1.338	-1.431	-1.548	-1.667

0.529	-1.822	-1.921	-2.026	-2.105
0.508	-1.990	-2.120	-2.273	-2.440
0.000	0.000	0.000	0.000	0.000

Table A.10 – Viscosity deviations obtained for the different systems of ILs and thiophene/benzene, at different temperatures.

[BMIM][SCN] + Thiophene

	T / K			
x_{IL}	298.15	308.15	318.15	328.15
	Δln(*η*)			
1.000	0.000	0.000	0.000	0.000
0.897	0.267	0.256	0.246	0.238
0.857	0.349	0.333	0.321	0.312
0.754	0.517	0.496	0.479	0.466
0.390	1.269	1.210	1.161	1.126
0.299	1.380	1.315	1.263	1.228
0.000	0.000	0.000	0.000	0.000

[BMIM][NTf_2] + Thiophene

	T / K			
x_{IL}	298.15	308.15	318.15	328.15
	Δln(*η*)			
1.000	0.000	0.000	0.000	0.000
0.911	0.203	0.193	0.185	0.178
0.724	0.549	0.522	0.500	0.484
0.664	0.674	0.640	0.612	0.592
0.439	1.197	1.139	1.093	1.060
0.230	1.346	1.275	1.217	1.177
0.000	0.000	0.000	0.000	0.000

[BMIM][SCN] + Benzene

	T / K			
x_{IL}	298.15	308.15	318.15	328.15
	Δln(*η*)			
1.0000	0.000	0.000	0.000	0.000
0.7666	0.752	0.736	0.725	0.776
0.7420	0.680	0.659	0.641	0.683
0.6081	0.482	0.466	0.452	0.479
0.4906	0.440	0.425	0.413	0.437
0.0000	0.000	0.000	0.000	0.000

[BMIM][CF_3SO_3] + Benzene				
	T / K			
x_{IL}	298.15	308.15	318.15	328.15
	Δln(*η*)			
1.000	0.000	0.000	0.000	0.000
0.878	0.914	0.884	0.858	0.914
0.696	0.836	0.805	0.779	0.816
0.647	0.772	0.735	0.704	0.729
0.533	0.655	0.625	0.599	0.621
0.427	0.296	0.281	0.269	0.276
0.000	0.000	0.000	0.000	0.000
[EMIM][NTf_2] + Benzene				
	T / K			
x_{IL}	298.15	308.15	318.15	328.15
	Δln(*η*)			
1.000	0.000	0.000	0.000	0.000
0.865	0.812	0.784	0.784	0.757
0.661	0.820	0.785	0.785	0.756
0.529	0.610	0.590	0.590	0.569
0.508	0.268	0.262	0.262	0.256
0.000	0.000	0.000	0.000	0.000

Table A.11 - ^{1}H NMR chemical shift deviations for the protons of [BMIM][SCN], estimated trough the difference between [BMIM][SCN] with thiophene (for different compositions) and pure [BMIM][SCN].

atom identification	x_{IL}	Δ*δ* / ppm	atom identification	x_{IL}	Δ*δ* / ppm
	0.17	-0.4225		0.17	-0.5644
	0.22	-0.4407		0.22	-0.6135
H(2)	0.30	-0.3880	H(5)	0.30	-0.4972
	0.39	-0.3181		0.39	-0.3852
	0.63	-0.1511		0.63	-0.1681
	0.17	-0.4572		0.17	-0.5155
	0.22	-0.4918		0.22	-0.5566
H(7)	0.30	-0.4114	H(6)	0.30	-0.4622
	0.39	-0.3273		0.39	-0.3630
	0.63	-0.1533		0.63	-0.1645
H(4)	0.17	-0.5882	H(8)	0.17	-0.3451

	0.22	--		0.22	-0.3711
	0.30	--		0.30	-0.3103
	0.39	-0.4047		0.39	-0.2476
	0.63	-0.1750		0.63	-0.1187
	0.17	-0.2328		0.17	-0.1552
	0.22	-0.2491		0.22	-0.1127
H(9)	0.30	-0.2110	H(10)	0.30	-0.0887
	0.39	-0.1700		0.39	-0.0710
	0.63	-0.0836		0.63	-0.0229

Table A.12 - ^{1}H NMR chemical shift deviations for the protons of thiophene, estimated trough the difference between [BMIM][SCN] with thiophene (for different compositions) and pure [BMIM][SCN].

atom identification	x_{IL}	$\Delta\delta$ / ppm
	0.17	0.3760
	0.22	0.3319
H(C-S)	0.30	0.4236
	0.39	0.4930
	0.63	0.6036
	0.17	0.1870
	0.22	0.1618
H(C-C)	0.30	0.2136
	0.39	0.2563
	0.63	0.3291

Table A.13 - ^{1}H NMR chemical shift deviations for the protons of [BMIM][NTf_2], estimated trough the difference between [BMIM][NTf_2] with thiophene (for different compositions) and pure [BMIM][NTf_2].

atom identification	x_{IL}	$\Delta\delta$ / ppm	atom identification	x_{IL}	$\Delta\delta$ / ppm
	0.22	-0.5826		0.22	-0.5785
H(2)	0.26	-0.7045	H(5)	0.26	-0.7083
	0.39	-0.4678		0.39	-0.4566
	0.63	-0.2101		0.63	-0.2003
H(4)	0.22	-0.5854	H(7)	0.22	-0.4528

	0.26	-0.7213		0.26	-0.5537
	0.39	-0.4635		0.39	-0.3585
	0.63	-0.2030		0.63	-0.1591
H(6)	0.22	-0.4734	H(8)	0.22	-0.3460
	0.26	-0.5910		0.26	-0.4269
	0.39	-0.3683		0.39	-0.2731
	0.63	-0.1582		0.63	-0.1208
H(9)	0.22	-0.2395	H(10)	0.22	-0.1444
	0.26	-0.2983		0.26	-0.1275
	0.39	-0.1870		0.39	-0.0705
	0.63	-0.0829		0.63	-0.0059

Table A.14 - ^{1}H NMR chemical shift deviations for the protons of thiophene, estimated through the difference between [BMIM][NTf_2] with thiophene (for different compositions) and pure [BMIM][NTf_2].

atom identification	x_{IL}	$\Delta\delta$ / ppm
H(C-S)	0.22	-0.0189
	0.26	-0.0854
	0.39	0.0274
	0.63	0.1100
H(C-C)	0.22	0.1877
	0.26	0.1428
	0.39	0.1720
	0.63	0.2822

Table A.15 - ^{13}C NMR chemical shift deviations for the protons of [BMIM][SCN], estimated trough the difference between [BMIM][SCN] with thiophene (for different compositions) and pure [BMIM][SCN].

atom identification	x_{IL}	$\Delta\delta$ / ppm	atom identification	x_{IL}	$\Delta\delta$ / ppm
C(2)	0.17	-0.9170	C(4)	0.17	-0.3450
	0.22	-0.9620		0.22	-0.3690
	0.30	-0.8370		0.30	-0.3130
	0.39	-0.6820		0.39	-0.2520
	0.63	-0.3220		0.63	-0.1210
C(11)	0.17	0.4620	C(5)	0.17	-0.3200
	0.22	0.5020		0.22	-0.3520
	0.30	0.4010		0.30	-0.2790

	0.39	0.3230		0.39	-0.2140
	0.63	0.1600		0.63	-0.0940
	0.17	-0.2470		0.17	-0.6540
	0.22	-0.2670		0.22	-0.7030
C(7)	0.30	-0.2220	C(6)	0.30	-0.5880
	0.39	-0.1750		0.39	-0.4680
	0.63	-0.0800		0.63	-0.2200
	0.17	-0.2230		0.17	-0.1080
	0.22	-0.2410		0.22	-0.1160
C(8)	0.30	-0.1990	C(9)	0.30	-0.0980
	0.39	-0.1570		0.39	-0.0760
	0.63	-0.0730		0.63	-0.0340
	0.17	--			
	0.22	-0.0080			
C(10)	0.30	0.0080			
	0.39	0.0170			
	0.63	0.0170			

Table A.16 - ^{13}C NMR chemical shift deviations for the protons of thiophene, estimated trough the difference between [BMIM][SCN] with thiophene (for different compositions) and pure [BMIM][SCN].

atom identification	x_{IL}	$\Delta\delta$ / ppm
	0.17	0.3300
	0.22	0.3290
C(C-S)	0.30	0.3650
	0.39	0.4110
	0.63	0.4700
	0.17	0.5900
	0.22	0.5160
C(C-C)	0.30	0.6770
	0.39	0.7910
	0.63	0.9670

Table A.17 - ^{13}C NMR chemical shift deviations for the protons of [BMIM][NTf_2], estimated trough the difference between [BMIM][NTf_2] with thiophene (for different compositions) and pure [BMIM][NTf_2].

atom identification	x_{IL}	$\Delta\delta$ / ppm	atom identification	x_{IL}	$\Delta\delta$ / ppm

C(2)	0.22	-0.8720	C(5)	0.22	-0.3280
	0.26	-1.0360		0.26	-0.4120
	0.39	-0.7100		0.39	-0.2560
	0.63	-0.3240		0.63	-0.1070
C(4)	0.22	-0.2880	$C(NTf_2)$	0.22	0.2030
	0.26	-0.3540		0.26	0.2815
	0.39	-0.2300		0.39	0.1620
	0.63	-0.0990		0.63	0.1635
C(6)	0.22	-0.2880	C(7)	0.22	-0.1780
	0.26	-0.3580		0.26	-0.2200
	0.39	-0.2250		0.39	-0.1380
	0.63	-0.0950		0.63	-0.0590
C(8)	0.22	-0.1500	C(9)	0.22	0.0500
	0.26	-0.1830		0.26	0.0640
	0.39	-0.1180		0.39	0.0430
	0.63	-0.0500		0.63	0.0230
C(10)	0.22	0.3160			
	0.26	0.3860			
	0.39	0.2580			
	0.63	0.1210			

Table A.18 - ^{13}C NMR chemical shift deviations for the protons of thiophene, estimated trough the difference between [BMIM][NTf_2] with thiophene (for different compositions) and pure [BMIM][NTf_2].

atom identification	x_{IL}	$\Delta\delta$ / ppm
C(C-S)	0.22	0.2210
	0.26	0.2030
	0.39	0.2270
	0.63	0.2180
C(C-C)	0.22	0.1440
	0.26	0.1050
	0.39	0.1670
	0.63	0.1820

Table A.19 - Position and intensities of the RDF peak maxima corresponding to the interactions of sulfur atom from thiophene with selected carbons atoms from the cation of [BMIM][SCN], represented at Figure 3.1.11.a.

S(TP)_X([BMIM][SCN])	*r* / nm	*g(r)*	*r* / nm	*g(r)*
	1st solvation shell		others solvation shells	
S_C10	0.3953	1.7353		
S_C2			0.5939	1.1331
S_C4	0.3782	1.1471		
S_C5	0.3819	1.2626		
S_C6	0.3880	1.2731		
S_C9			0.4995	1.3957

Table A.20 - Position and intensities of the RDF peak maxima corresponding to the interactions of sulfur atom from thiophene with selected carbons atoms from the cation of [BMIM][NTf_2], represented at Figure 3.1.12.a.

S(TP)_X([BMIM][NTf_2])	*r* / nm	*g(r)*	*r* / nm	*g(r)*
	1st solvation shell		others solvation shells	
S_C10	0.3880	1.7108		
S_C2	0.3782	0.8214	0.5841	1.2206
S_C4	0.3831	1.3571		
S_C5	0.3831	1.3571		
S_C6	0.3966	1.6548		
S_C9			0.5007	1.3186

Table A.21 - Position and intensities of the RDF peak maxima corresponding to the interactions of sulfur atom from $[SCN]^-$ with thiophene, represented at Figure 3.1.11.b.

S(SCN)_TP	*r* / nm	*g(r)*	*r* / nm	*g(r)*
	1st solvation shell		others solvation shells	
S_CC	0.3868	1.0776	0.4848	1.1085
S_CS	0.3733	1.2626		
S_S	0.3999	0.8424	0.5118	1.1120

Table A.22 - Position and intensities of the RDF peak maxima corresponding to the interactions of carbon atom, C(1), from $[NTf_2]^-$ with thiophene, represented at Figure 3.1.12.b.

C(NTf_2)_TP	*r* / nm	*g(r)*	*r* / nm	*g(r)*
	1st solvation shell		others solvation shells	
C_CC	0.4493	1.2525	0.5681	1.2311
C_CS	0.4419	1.2311	0.5706	1.2171
C_S	0.4284	1.1821	0.5816	1.1366

Table A.23 - Position and intensities of the RDF peak maxima corresponding to the interactions of CC atom from thiophene with selected carbons atoms from the cation of [BMIM][SCN], represented at Figure A.5.a.

	r / nm	*g(r)*	*r* / nm	*g(r)*
CC(TP)_X([BMIM][SCN])	1st solvation shell		others solvation shells	
CC_C10	0.4100	1.5987		
CC_C2			0.6037	1.1436
CC_C4	0.3904	1.0910		
CC_C5	0.3966	1.1786		
CC_C6	0.4027	1.1891		
CC_C9			0.5130	1.4552

Table A.24 - Position and intensities of the RDF peak maxima corresponding to the interactions of CS atom from thiophene with selected carbons atoms from the cation of [BMIM][SCN], represented at Figure A.5.b.

	r / nm	*g(r)*	*r* / nm	*g(r)*
CS(TP)_X([BMIM][SCN])	1st solvation shell		others solvation shells	
CS_C10	0.4100	1.4937	0.5142	1.4482
CS_C2			0.6074	1.1261
CS_C4	0.3966	1.0315		
CS_C5	0.4027	1.1191		
CS_C6	0.4027	1.1191		
CS_C9	0.5154	1.4587		

Table A.25 - Position and intensities of the RDF peak maxima corresponding to the interactions of CC atom from thiophene with selected carbons atoms from the cation of [BMIM][NTf_2], represented at Figure A.6.a.

	r / nm	*g(r)*	*r* / nm	*g(r)*
CC(TP)_X([BMIM][NTf_2])	1st solvation shell		others solvation shells	
CC_C10	0.4125	1.5567	0.5081	1.4307
CC_C2	0.4137	0.8074	0.5951	1.2066
CC_C4	0.3941	1.2521		
CC_C5	0.4002	1.0840		
CC_C6	0.4015	1.3501		
CC_C9			0.5203	1.4097

Table A.26 - Position and intensities of the RDF peak maxima corresponding to the interactions of CS atom from thiophene with selected carbons atoms from the cation of [BMIM][NTf_2], represented at Figure A.6.b.

	r / nm	*g(r)*	*r* / nm	*g(r)*
CS(TP)_X([BMIM][NTf_2])	1st solvation shell		others solvation shells	
CS_C10	0.4076	1.4622	0.5154	1.4447
CS_C2	0.4174	0.8249	0.5926	1.1821
CS_C4	0.3953	1.2031		
CS_C5	0.3966	1.0770		
CS_C6	0.4113	1.2101	0.5069	1.1541
CS_C9			0.5020	1.3852

Table A.27 - Position and intensities of the RDF peak maxima corresponding to the interactions of carbon atom from $[SCN]^-$ with thiophene, represented at Figure A.7.a.

	r / nm	*g(r)*	*r* / nm	*g(r)*
C(SCN)_TP	1st solvation shell		others solvation shells	
C_CC	0.3941	0.7549	0.5044	1.0070
C_CS	0.3819	0.8494	0.5167	0.8634
C_S			0.5252	1.0350

Table A.28 - Position and intensities of the RDF peak maxima corresponding to the interactions of nitrogen atom from $[SCN]^-$ with thiophene, represented at Figure A.7.b.

	r / nm	*g(r)*	*r* / nm	*g(r)*
N(SCN)_TP	1st solvation shell		others solvation shells	
N_CC	0.3794	0.6464	0.4701	0.8214
N_CS	0.3598	0.7479		
N_S	0.4971	0.8634	0.6135	0.9300

Table A.29 - Position and intensities of the RDF peak maxima corresponding to the interactions of S(1) atom from $[NTf_2]^-$ with thiophene, represented at Figure A.8.a.

	r / nm	*g(r)*	*r* / nm	*g(r)*
$S(NTf_2)$_TP	1st solvation shell		others solvation shells	
S_CC			0.5755	1.2871

S_CS	0.4664	0.9440	0.5841	1.1856
S_S			0.5767	1.2451

Table A.30 - Position and intensities of the RDF peak maxima corresponding to the interactions of N(1) atom from $[NTf_2]^-$ with thiophene, represented at Figure A.8.b.

	r / nm	*g(r)*
$N(NTf_2)$_TP	1st solvation shell	
N_CC	0.6012	1.4307
N_CS	0.5890	1.3782
N_S	0.6037	1.4027

Table A.31 - Position and intensities of the RDF peak maxima corresponding to the interactions of F(1) atom from $[NTf_2]^-$ with thiophene, represented at Figure A.8.c.

	r / nm	*g(r)*	*r* / nm	*g(r)*
$F(NTf_2)$_TP	1st solvation shell		others solvation shells	
F_CC	0.3598	0.9650	0.4640	1.0280
F_CS	0.3561	0.9335	0.5363	1.0875
F_S	0.3426	0.9685	0.5056	1.0455

Table A.32 - Position and intensities of the RDF peak maxima corresponding to the interactions of O(1) atom from $[NTf_2]^-$ with thiophene, represented at Figure A.8.d.

	r / nm	*g(r)*	*r* / nm	*g(r)*
$O(NTf_2)$_TP	1st solvation shell		others solvation shells	
O_CC	0.3525	0.8634	0.5890	1.1156
O_CS	0.3635	0.7759	0.4689	0.8740
O_S	0.3635	0.6814	0.4995	0.8985

Figures

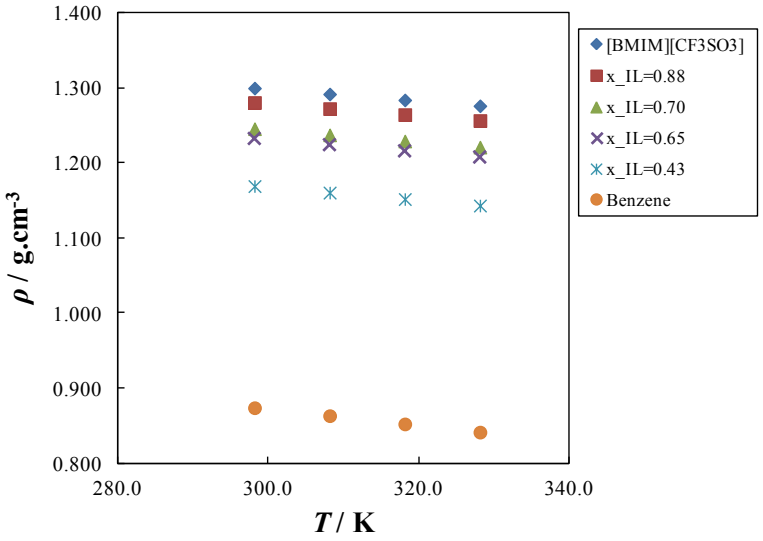

Figure A.1 – Density as a function of temperature, for different mole fraction of [BMIM][CF_3SO_3] in binary mixtures with benzene.

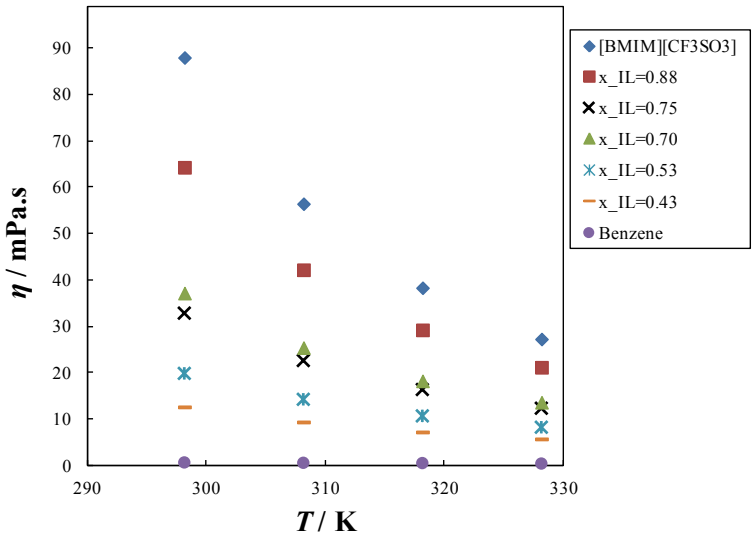

Figure A.2 – Viscosity as a function of temperature, for different mole fraction of [BMIM][CF_3SO_3] in the binary mixture with benzene.

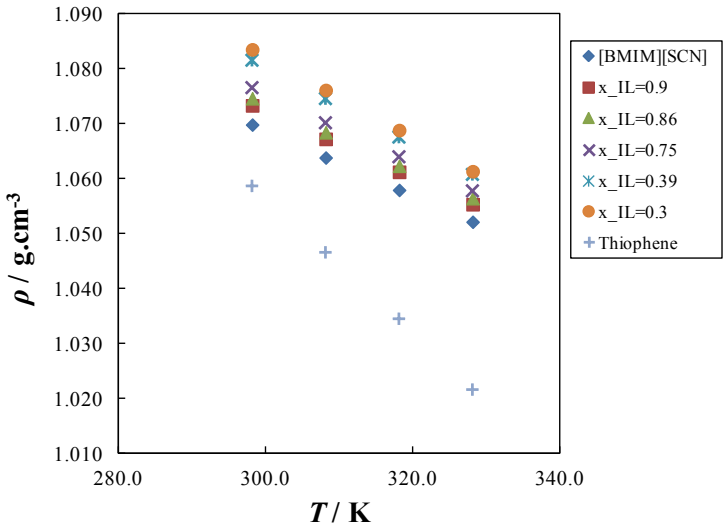

Figure A.3 - Density as a function of temperature, for different mole fraction of [BMIM][SCN] in binary mixtures with thiophene.

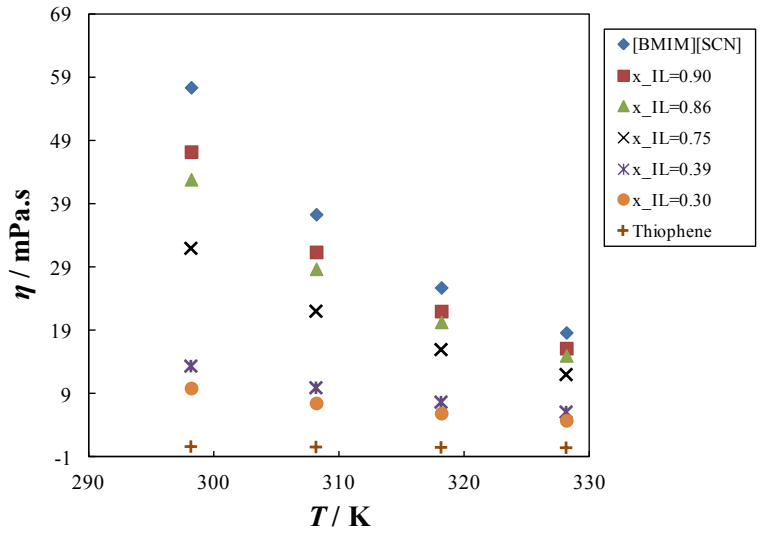

Figure A.4 - Viscosity as a function of temperature, for different mole fraction of [BMIM][SCN] in binary mixtures with thiophene.

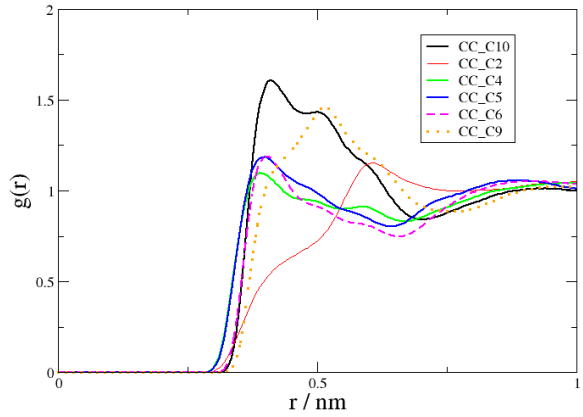

a)

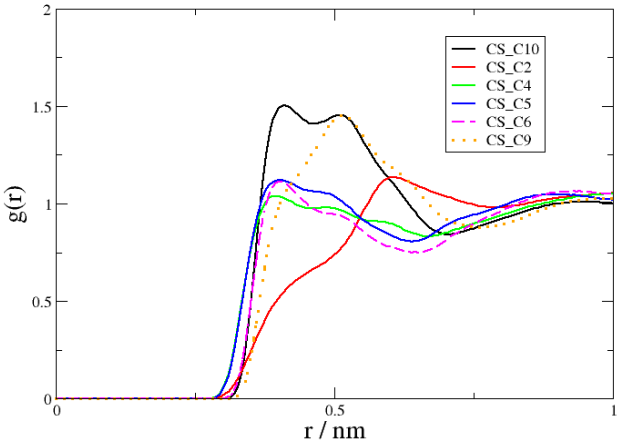

b)

Figure A.5 - Radial distribution functions of the cation $[BMIM]^+$ around atoms of thiophene, a) the CC atom and b) the CS atom, in the system [BMIM][SCN] with thiophene.

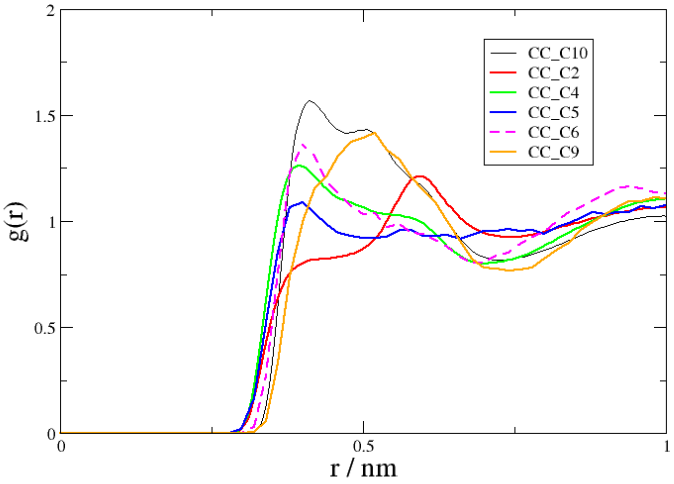

a)

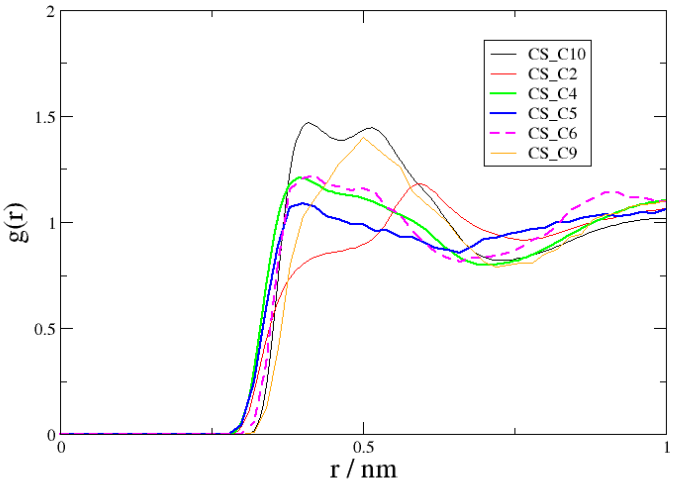

b)

Figure A.6 - Radial distribution functions of the cation $[BMIM]^+$ around atoms of thiophene, a) the CC atom and b) the CS atom, in the system $[BMIM][NTf_2]$ with thiophene.

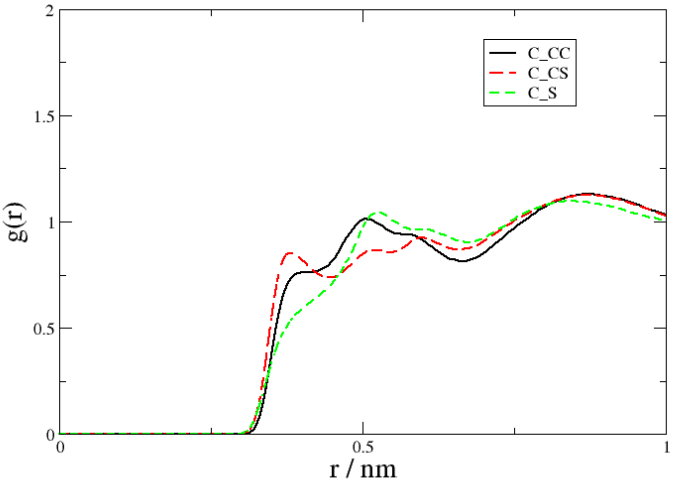

a)

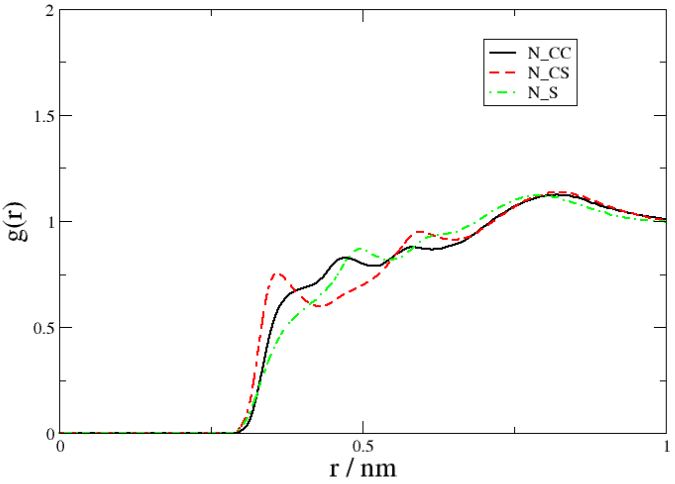

b)

Figure A.7 - Radial distribution functions of thiophene around atoms of the anion $[SCN]^-$, a) the C atom; b) the N atom, in the system [BMIM][SCN] with thiophene.

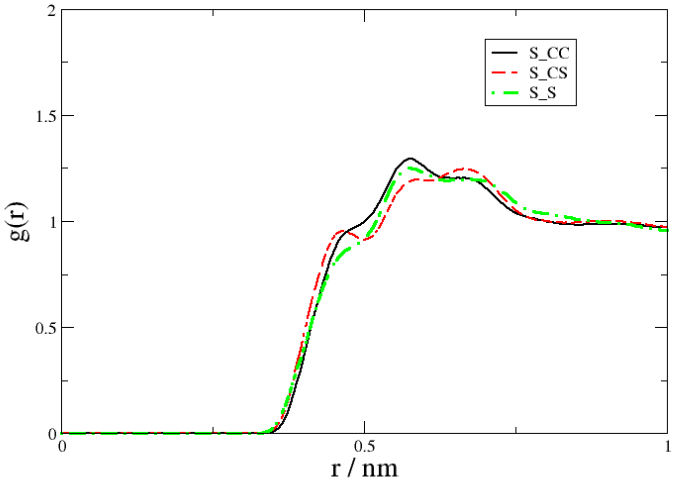

a)

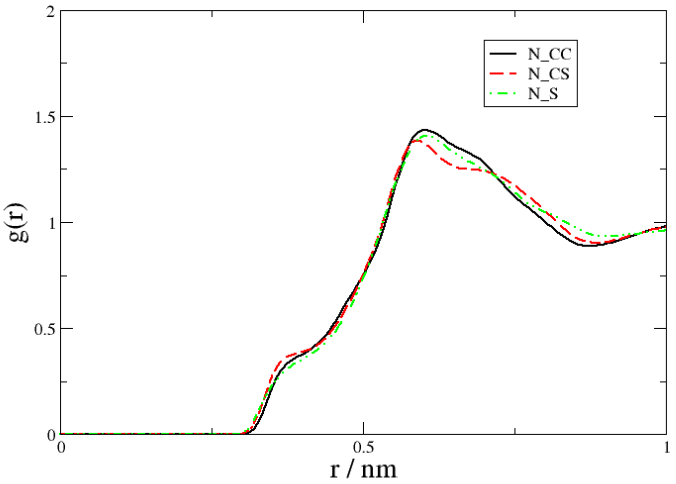

b)

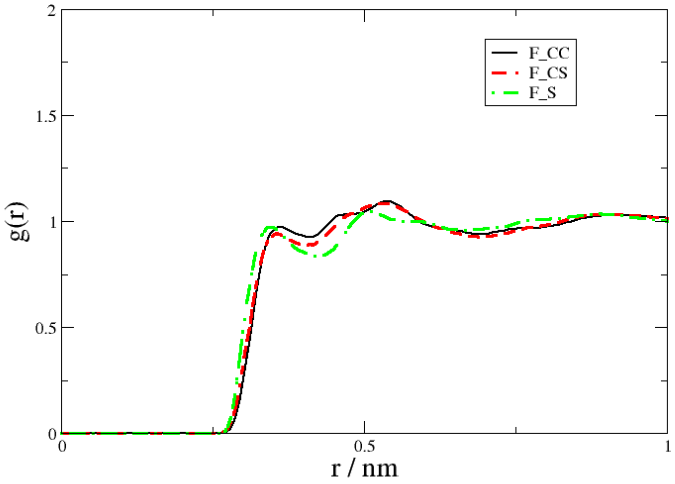

c)

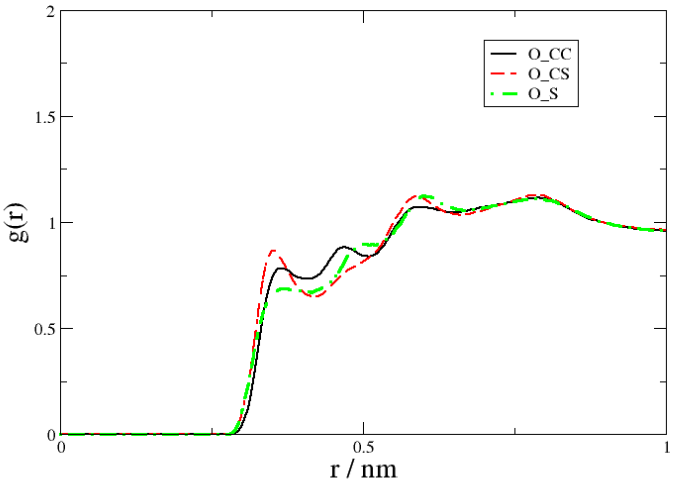

d)

Figure A.8 - Radial distribution functions of thiophene around atoms of the anion $[NTf_2]^-$, a) the S1 atom; b) the N1 atom; c) the F1 atom and d) the O1 atom, in the system [BMIM][NTf_2] with thiophene.

Appendix B

Tables

Table B.1 - Number of water molecules and IL pairs in each simulation box.

system	number of molecules	
x_{IL}	water	IL
0.2	160	40
0.4	120	80
0.6	40	60
0.8	20	80

Table B.2 - Atomic charges for [BMIM][SCN].

[BMIM][SCN]	
atom	**charge / *e***
H1	0.17
H2	0.21
H3	0.15
H4	0.06
H5	0.06
H6	0.06
H7	0.03
H8	0.03
H9	-0.09
H10	-0.09
H11	0.02
H12	0.02
H13	0.02
H14	0.02
H15	0.02
N1	0.09
N3	0.08
C2	0.08
C4	-0.14
C5	-0.21
C6	0.01
C7	-0.05
C8	0.33

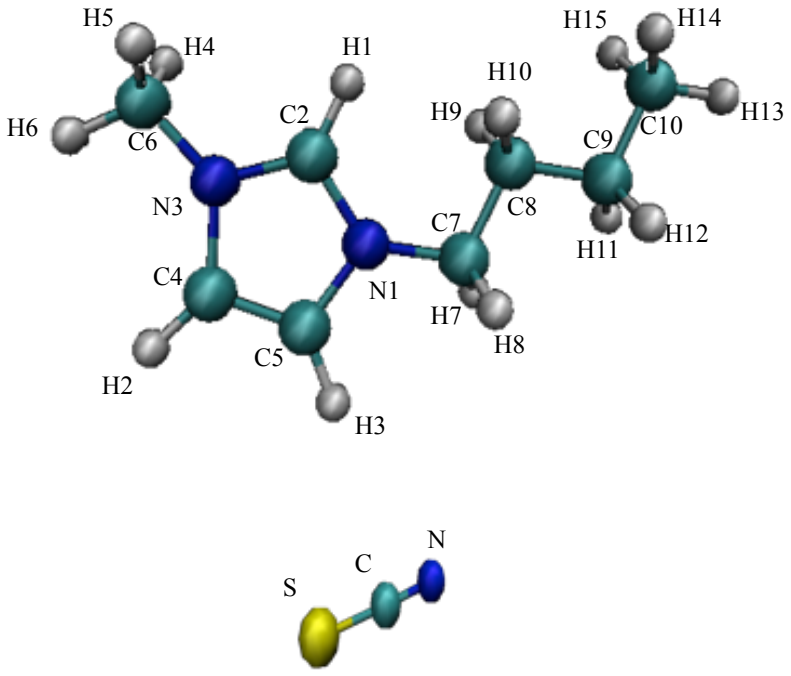

C9	0.02
C10	-0.11
N	-0.658
C	0.384
S	-0.530

Table B.3 - Atomic charges for [BMIM][DCA].

[BMIM][DCA]	
atom	**charge / *e***
H1	0.176
H2	0.188
H3	0.202
H4	0.097
H5	0.097
H6	0.097
H7	0.069
H8	0.069
H9	-0.039
H10	-0.039
H11	-0.048
H12	-0.048
H13	0.052
H14	0.052
H15	0.052
N1	0.135
N3	0.089
C2	-0.005
C4	-0.131
C5	-0.192
C6	-0.102
C7	-0.072
C8	0.109
C9	0.267
C10	-0.249
N_1	**-0.694**
C	**0.657**
N_2	**-0.723**

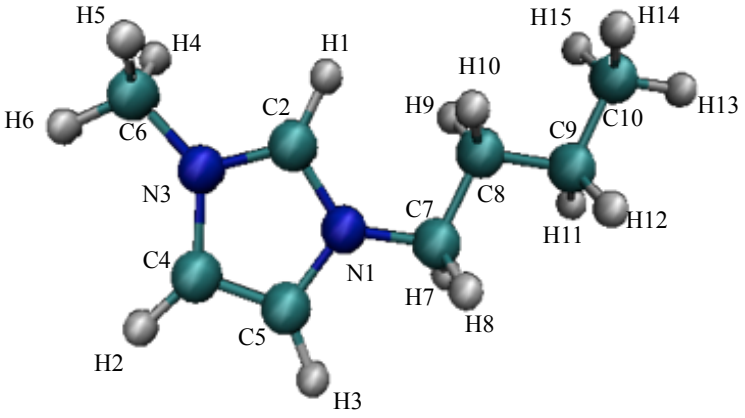

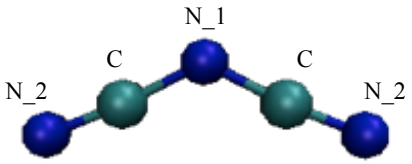

Table B.4 - Atomic charges for [BMIM][TCN].

[BMIM][TCN]	
atom	**charge / *e***
H1	0.228
H2	0.196
H3	0.229
H4	0.117
H5	0.117
H6	0.117
H7	0.142
H8	0.142
H9	-0.016
H10	-0.016
H11	-0.061
H12	-0.061
H13	0.048
H14	0.048
H15	0.048
N1	0.281
N3	0.139
C2	-0.139
C4	-0.135
C5	-0.233
C6	-0.174
C7	-0.251
C8	0.024
C9	0.326
C10	-0.236
C	**-0.624**
C_1	**0.552**
N_1	**-0.638**

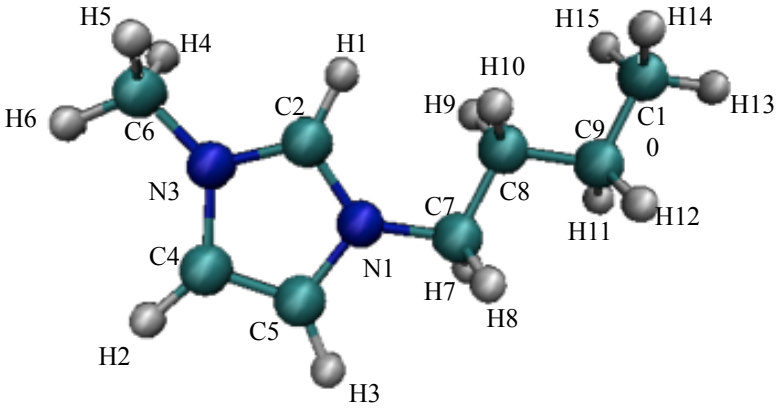

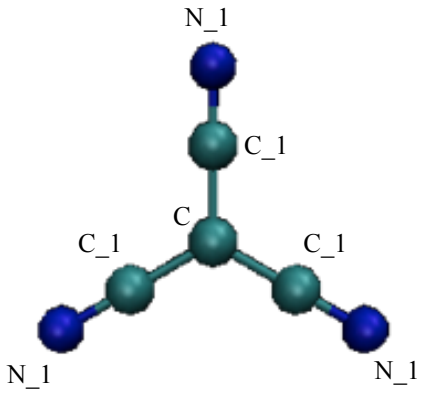

Table B.5 - Atomic charges for [EMIM][TCB].

[EMIM][TCB]	
atom	**charge / *e***
H1	0.213
H2	0.190
H3	0.207
H4	0.096
H5	0.096
H6	0.096
H7	0.052
H8	0.052
H9	0.060
H10	0.060
H11	0.060
N1	0.129
N3	0.114
C2	-0.098
C4	-0.127
C5	-0.163
C6	-0.099
C7	0.152
C8	-0.201
B	**0.143**
C	**0.229**
N	**-0.487**

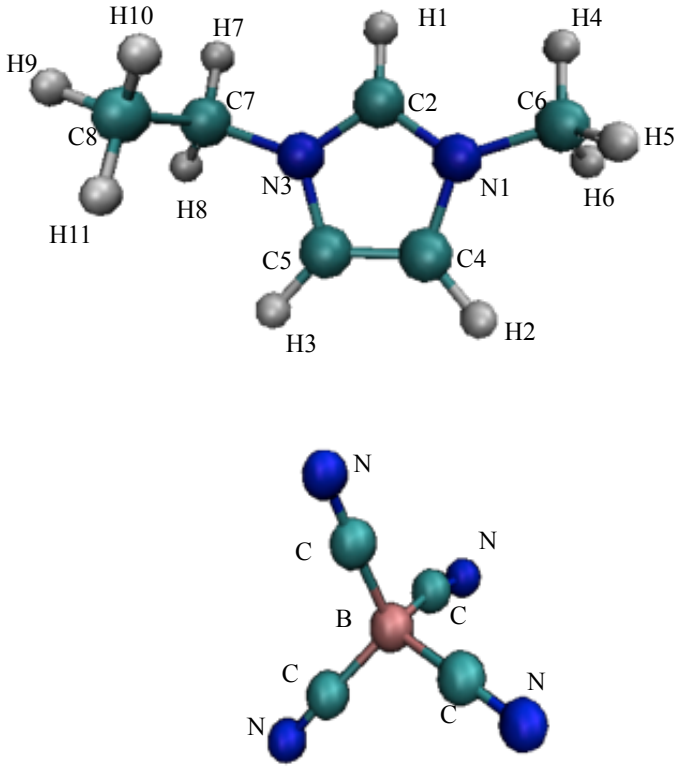

Table B.6 - Experimental and computational density values for each pure IL addressed in this study, at 298.15 K. Values in parentheses denote the relative deviations of simulated values from experimental ones.

IL	ρ_{exp} [a] / kg·m^{-3}	ρ_{sim} / kg·m^{-3}
[BMIM][SCN]	1069.5	1082.0 (1.2 %)
[BMIM][DCA]	1060.3	1026.5 (3.2 %)
[BMIM][TCN]	1047.5	1030.6 (1.6 %)
[EMIM][TCB]	1036.1	1054.8 (1.8 %)

[a] Taken from C. M. S. S. Neves, K. A. Kurnia, J. A. P. Coutinho, I. M. Marrucho, J. N. C. Lopes, M. G. Freire, and L. P. N. Rebelo, *J. Phys. Chem. B*, 2013, **117**, 10271–10283.

Figures

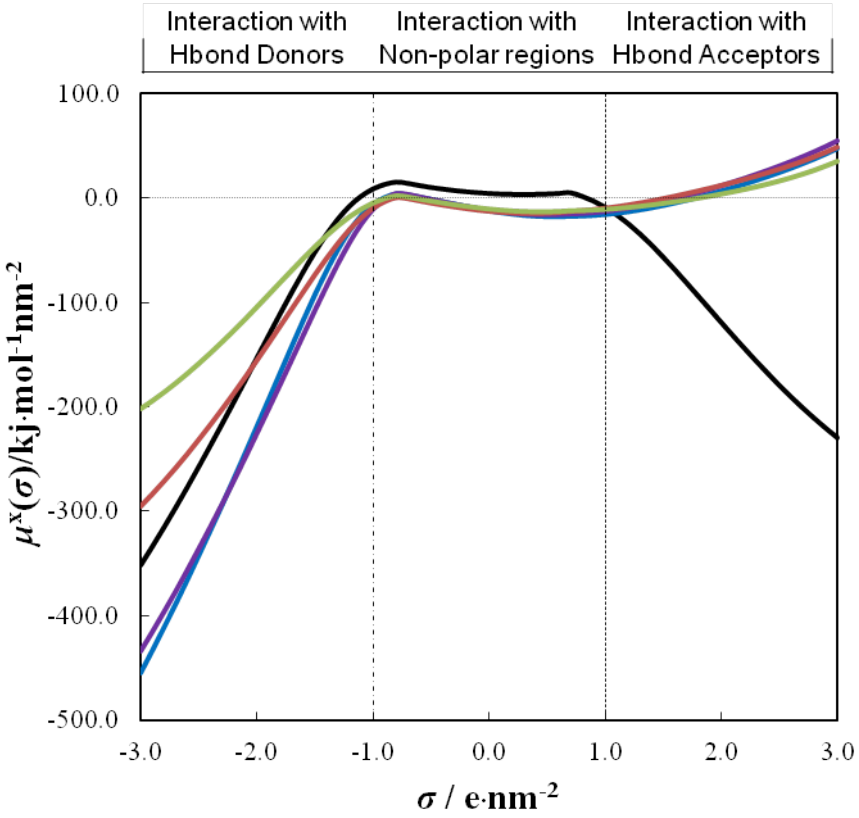

Figure B.1 - Sigma potential for (—) water, (—) [BMIM][DCA], (—)[BMIM][SCN], (—)[BMIM][TCN] and (—) [BMIM][TCB].

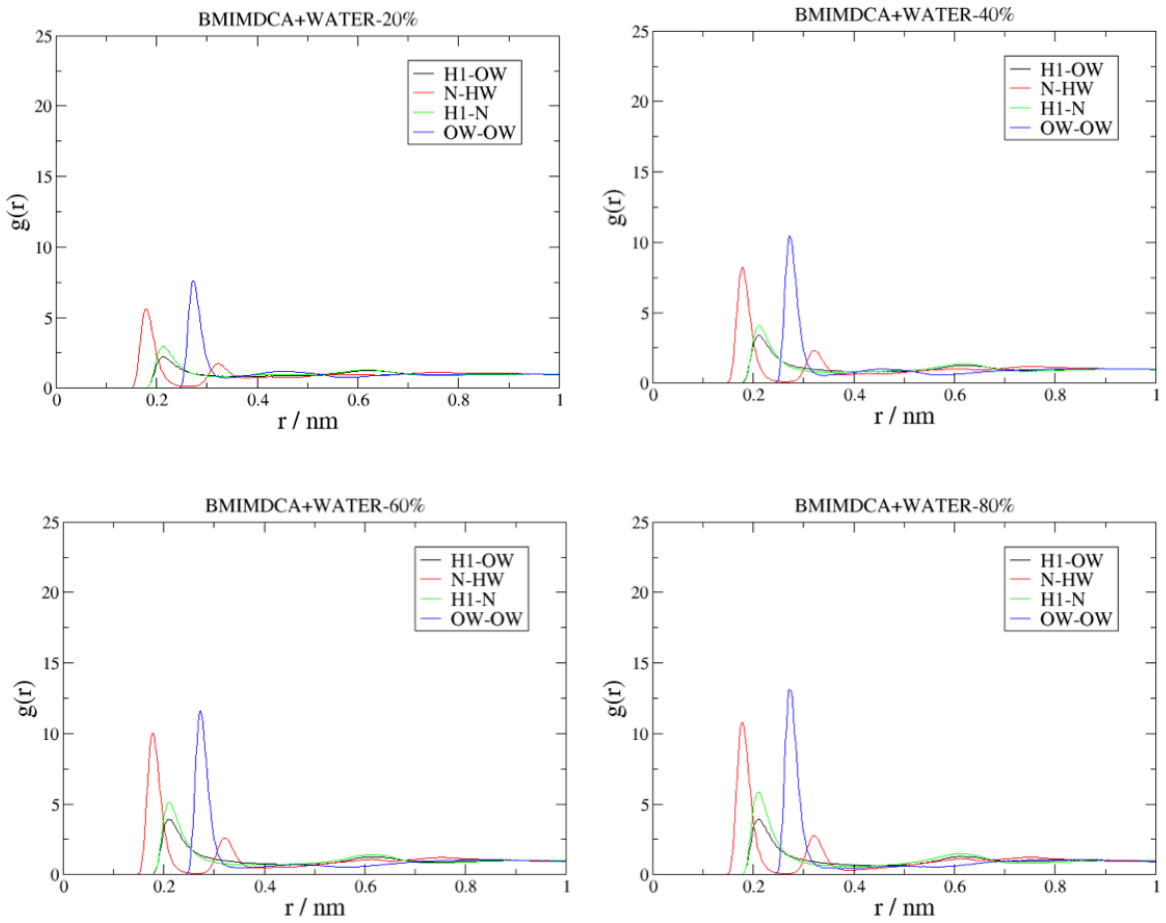

Figure B.2 - Radial distributions functions (RDFs) regarding the mixture [BMIM][DCA] and water, for different mole fractions of IL, at 298.15 K. RDFs for interaction of cation-water (H1-OW, ▬), anion-water (N-HW, ▬), cation-anion (H1-N, ▬) and solvent-solvent (OW-OW, ▬) are represented in each picture.

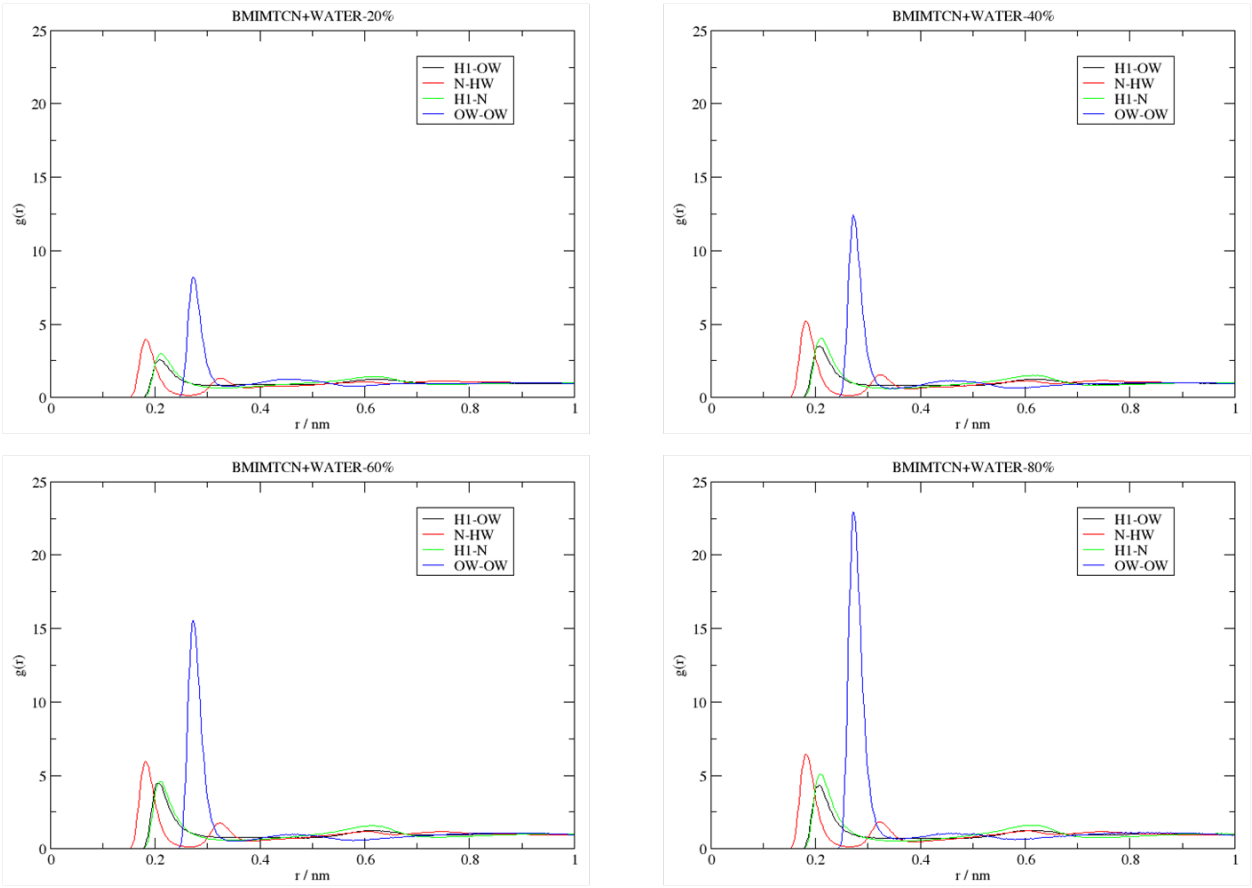

Figure B.3 - Radial distributions functions (RDFs) regarding the mixture [BMIM][TCN] and water, for different mole fractions of IL , at 298.15 K. RDFs for interaction of cation-water (H1-OW, ▬), anion-water (N-HW, ▬), cation-anion (H1-N, ▬) and solvent-solvent (OW-OW, ▬) are represented in each picture.

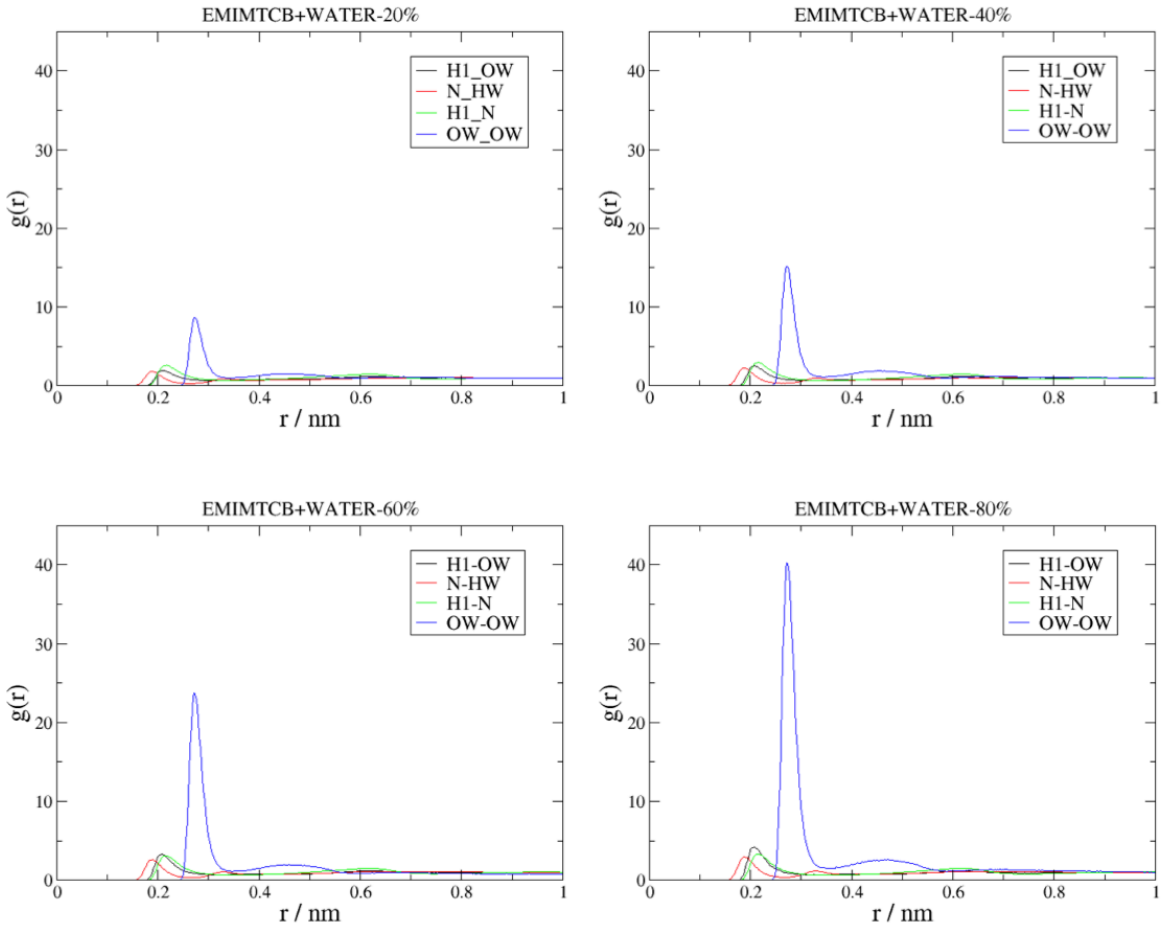

Figure B.4 - Radial distributions functions (RDFs) regarding the mixture [EMIM][TCB] and water, for different mole fractions of IL, at 298.15 K. RDFs for interaction of cation-water (H1-OW, ▬), anion-water (N-HW, ▬), cation-anion (H1-N, ▬) and solvent-solvent (OW-OW, ▬) are represented in each picture.

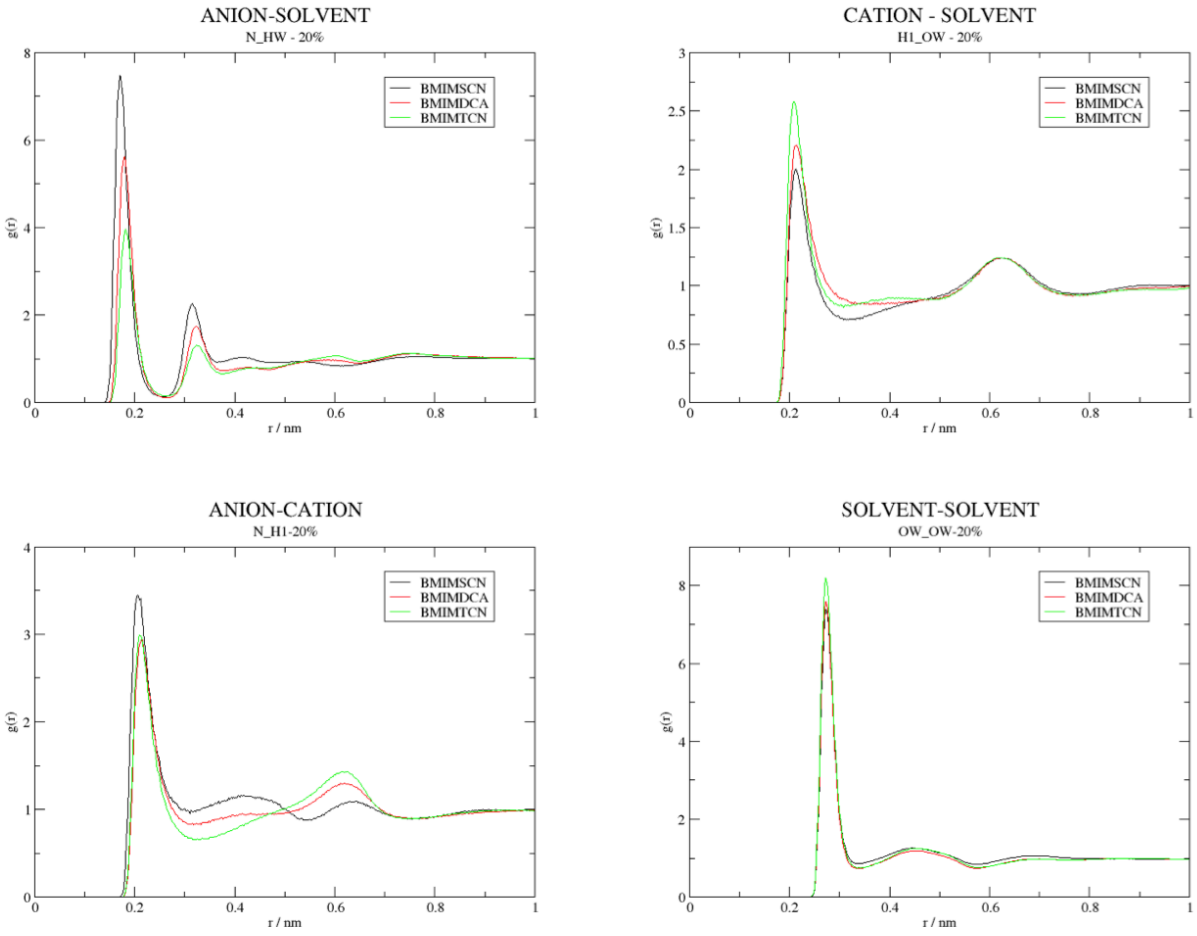

Figure B.5 - RDFs for anion-water (above, left side), cation-water (above, right side), cation-anion (down, left side) and water-water interactions (down, right side), at 0.20 IL mole fraction and at the temperature of 298.15 K. RDFs for [BMIM][SCN] (—), [BMIM][DCA] (—) and [BMIM][TCN] (—) are represented in each picture.

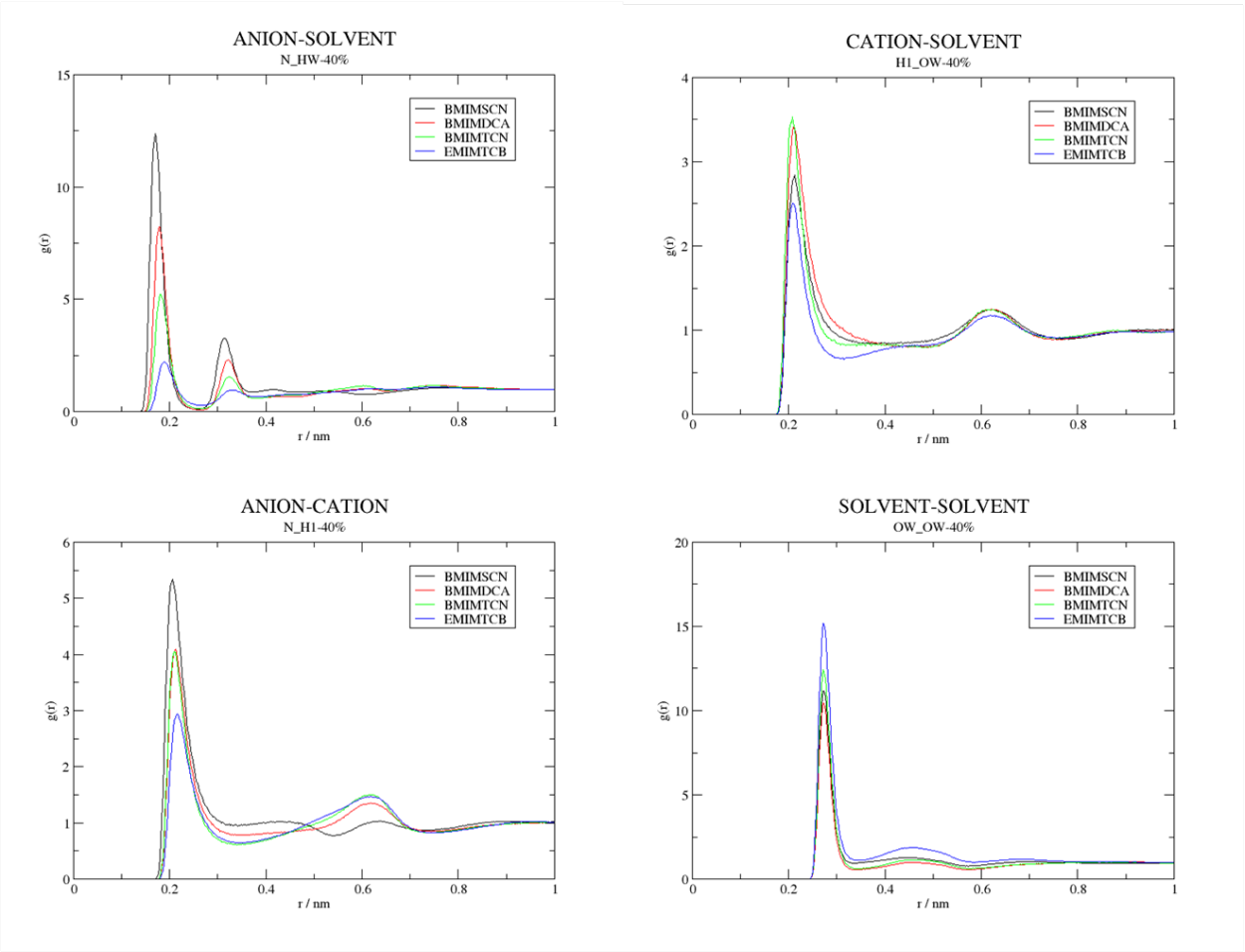

Figure B.6 - RDFs for anion-water (above, left side), cation-water (above, right side), cation-anion (down, left side) and water-water interactions (down, right side), at 0.40 IL mole fraction and at the temperature of 298.15 K. RDFs for [BMIM][SCN] (—), [BMIM][DCA] (—), [BMIM][TCN] (—) and [EMIM][TCB] (—) are represented in each picture.

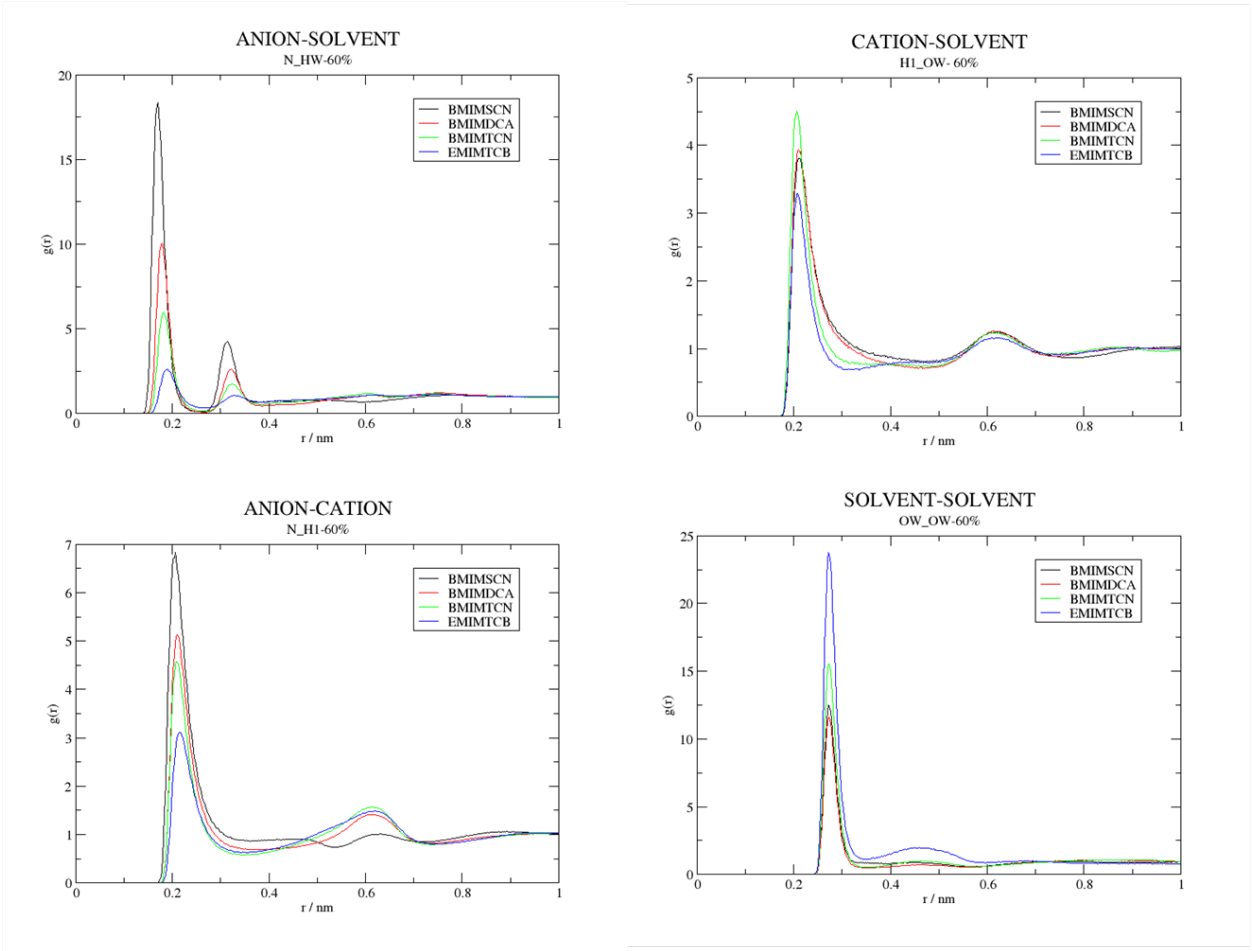

Figure B.7 - RDFs for anion-water (above, left side), cation-water (above, right side), cation-anion (down, left side) and water-water interactions (down, right side), at 0.60 IL mole fraction and at the temperature of 298.15 K. RDFs for [BMIM][SCN] (—), [BMIM][DCA] (—), [BMIM][TCN] (—) and [EMIM][TCB] (—) are represented in each picture.

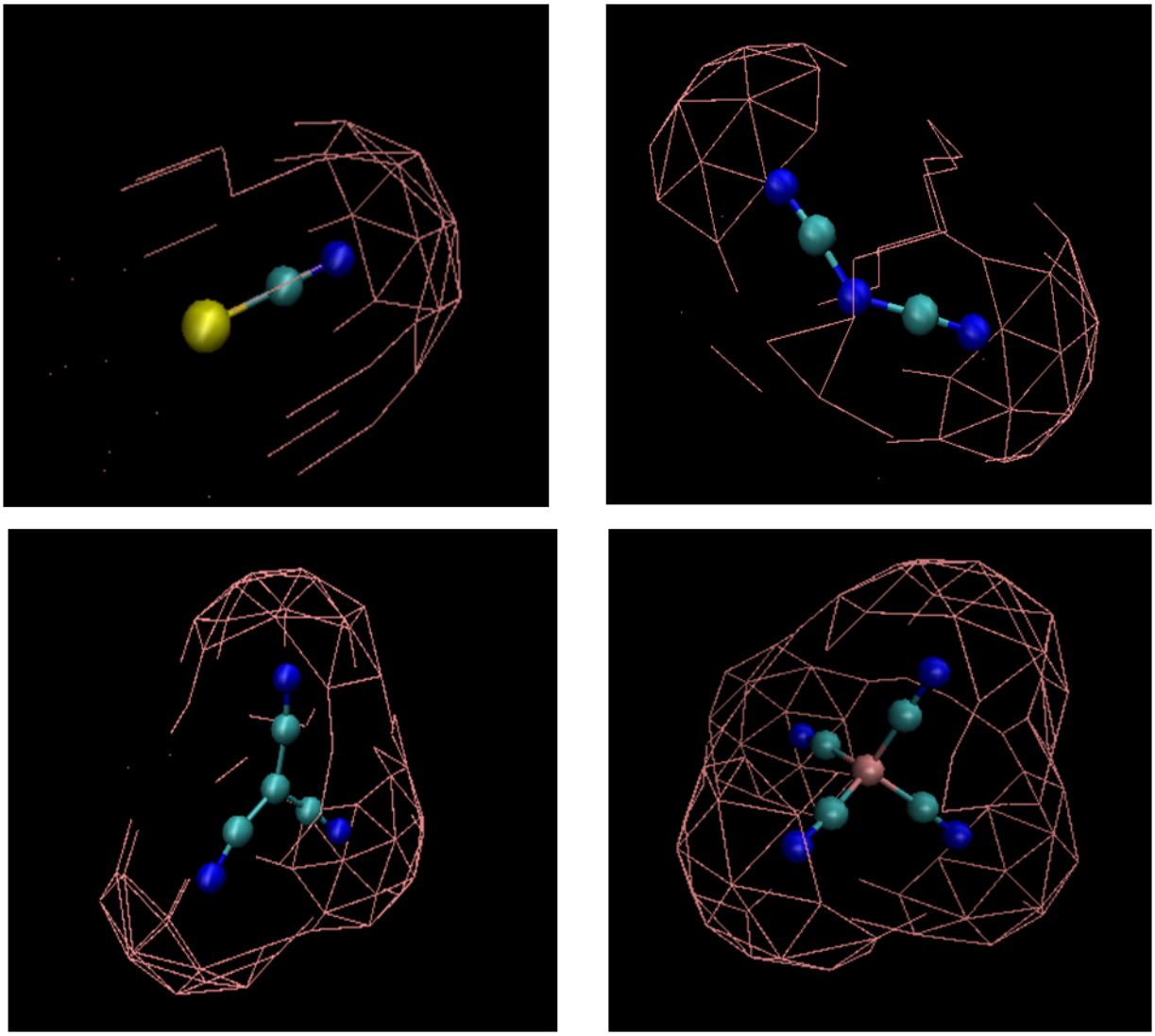

Figure B.8 - Solvent accessible surface area for each IL's anion under study, at 80IL:20W.

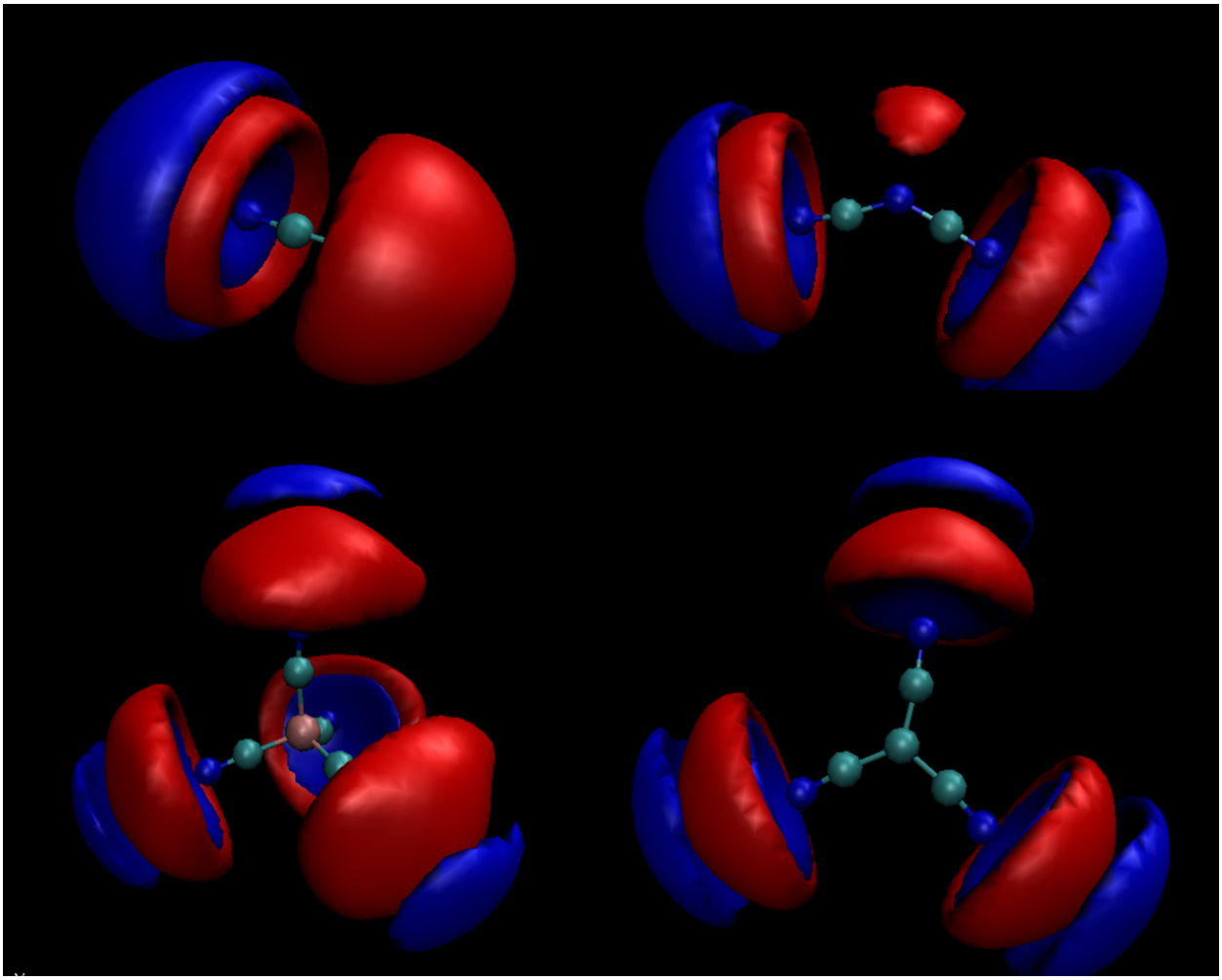

Figure B.9 - SDF for the mixtures [BMIM][SCN] (above, left side), [BMIM][DCA] (above, right side), [EMIM][TCB] (down, left side) and [BMIM][TCN] (down, right side) and water, at 80IL:20W. Each anion is the centre element, surrounded by oxygen atoms of water (blue surface) and the H1 proton of the cation $[BMIM]^+$ or $[EMIM]^+$.

Appendix C

Figures

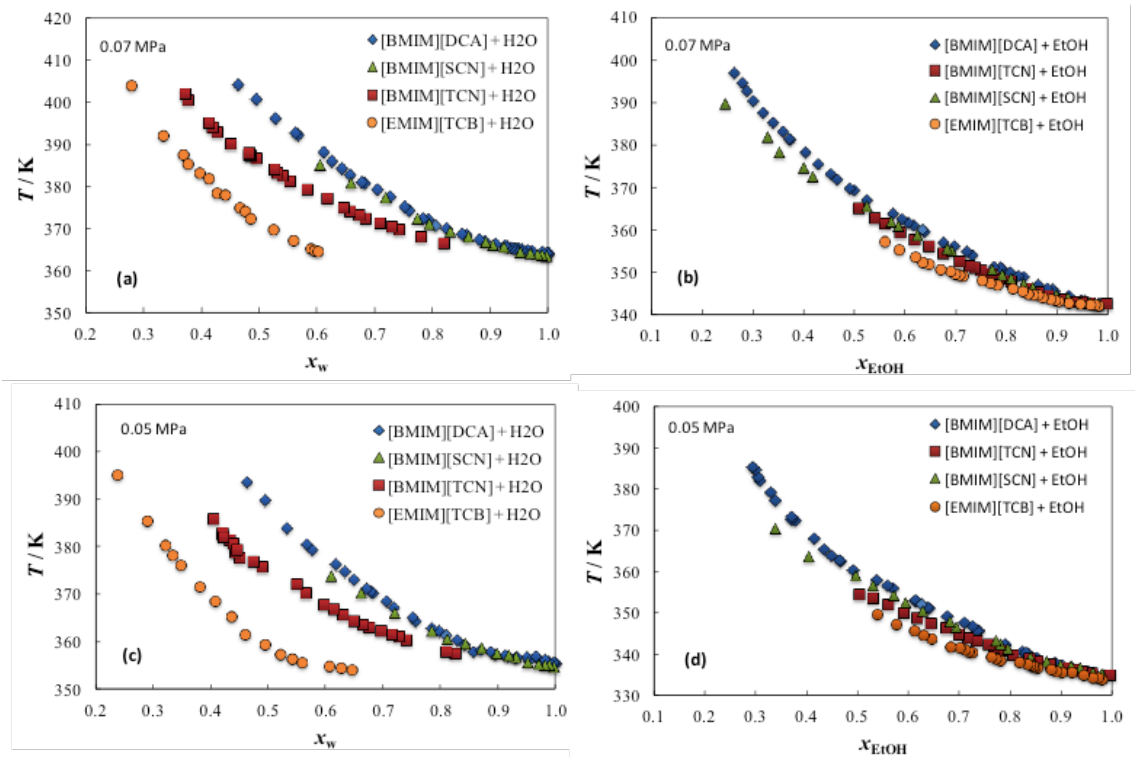

Figure C.1 - Isobaric temperature-composition diagram of [BMIM][SCN] (green triangle), [BMIM][DCA] (blue diamond), [BMIM][TCN] (red square) and [BMIM][TCB] (orange circle); (a) & (c) water; (b) & (d) ethanol at 0.07 and 0.05 MPa respectively.

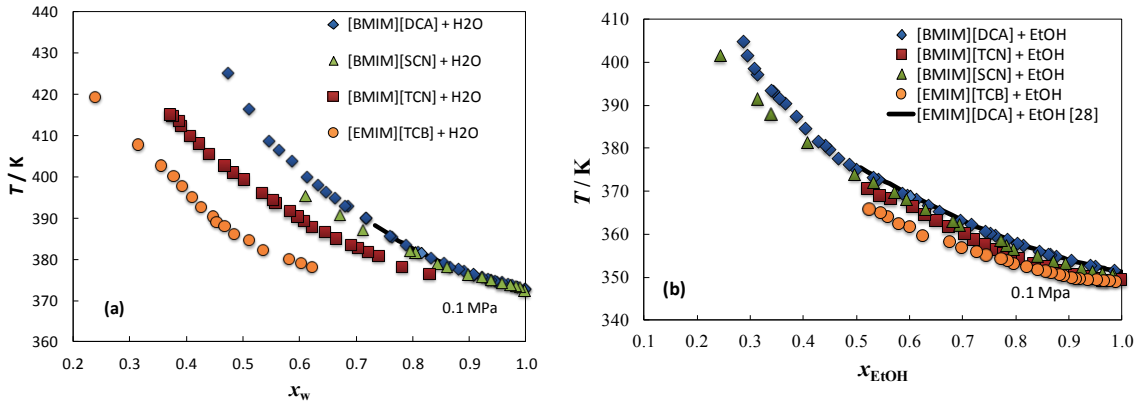

Figure C.2 - Isobaric temperature-composition diagram of [BMIM][SCN] (green triangle), [BMIM][DCA] (blue diamond), [BMIM][TCN] (red square) and [EMIM][TCN] (orange circle) + (a) water; (b) ethanol at 0.1 MPa. The solid lines represents the Orchilles et al.[28] data for [EMIM][DCA].

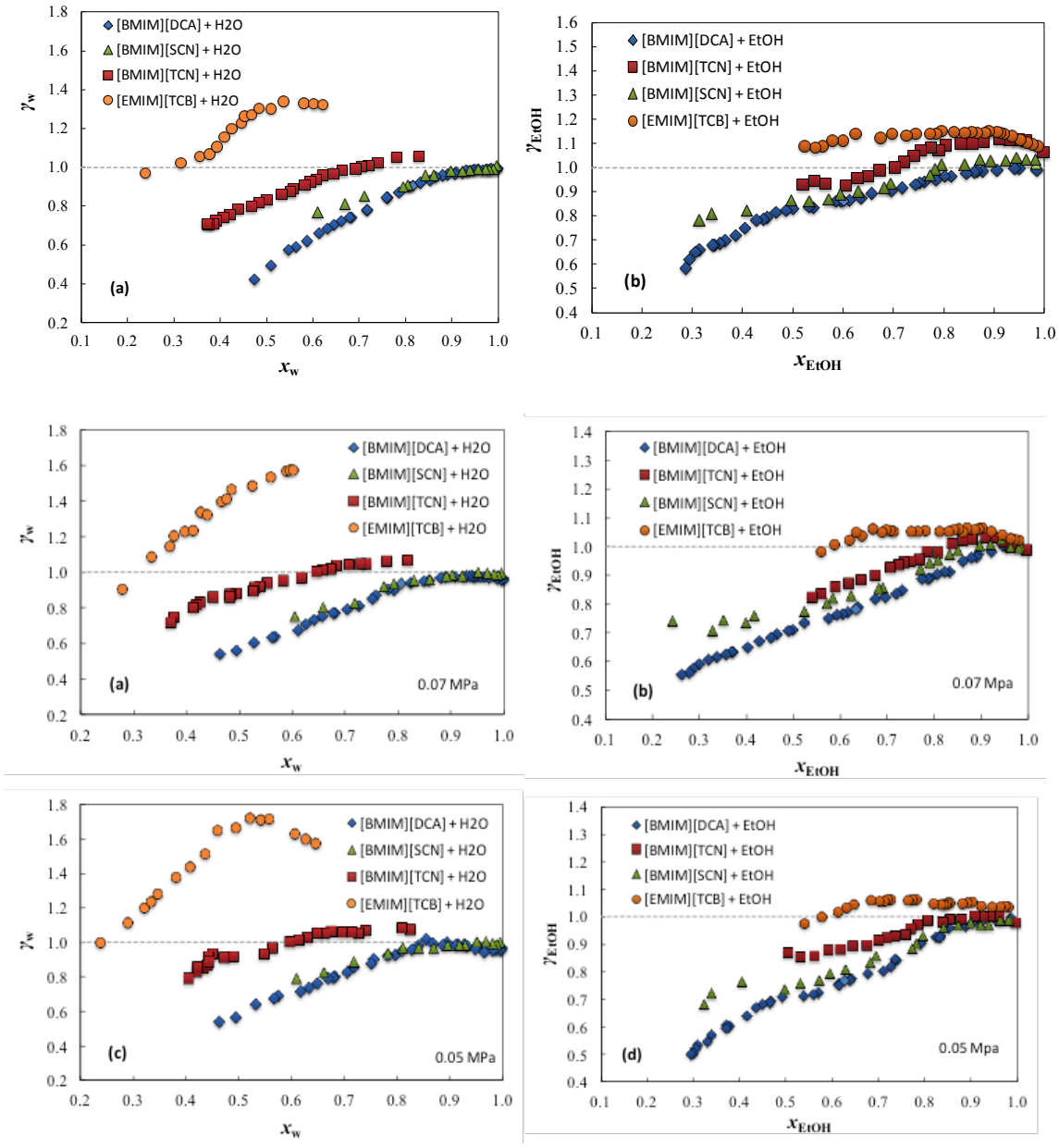

Figure C.3 - Activity coefficients of [BMIM][SCN] (green triangle), [BMIM][DCA] (blue diamond), [BMIM][TCN] (red square) and [EMIM][TCB] (orange circle) as function of (a) & (c) water, (b) & (d) ethanol mole fractions, at 0.1 (first row), 0.07 (middle row) and 0.05 (last row) MPa.

[BMIM][SCN]

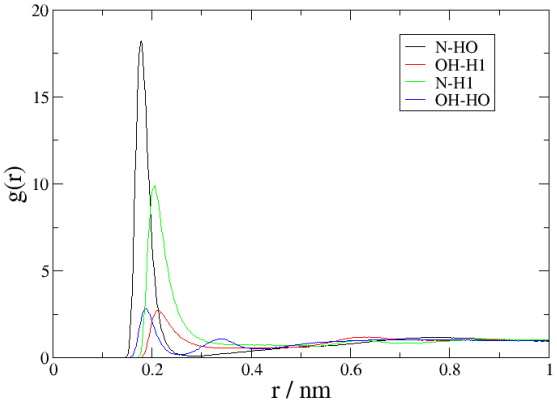

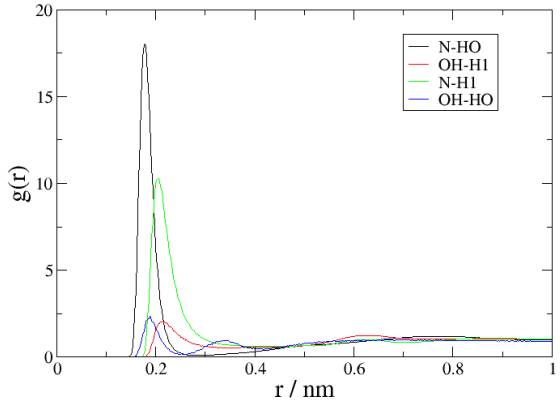

[BMIM][DCA]

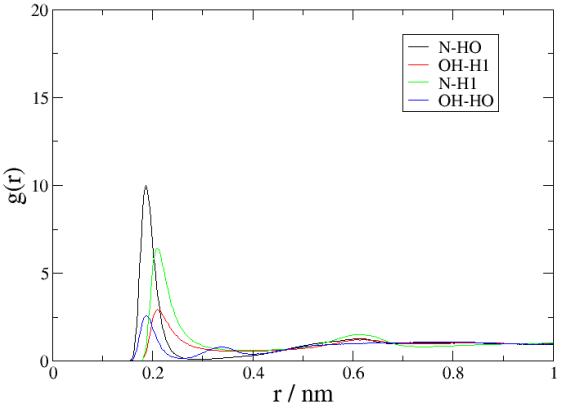

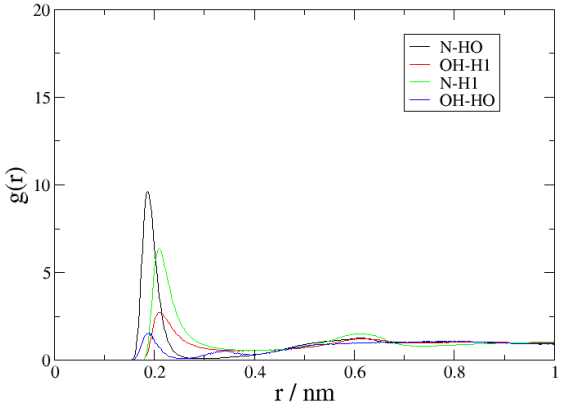

[BMIM][TCN]

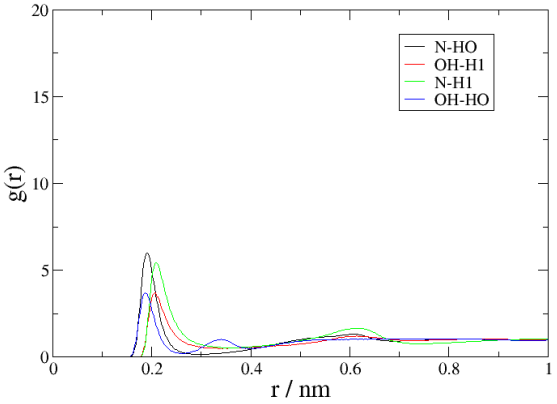

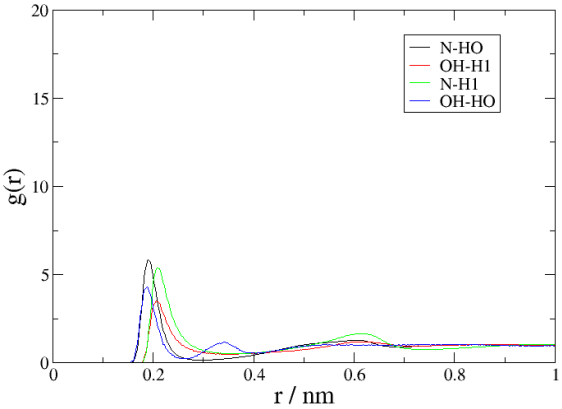

[EMIM][TCB]

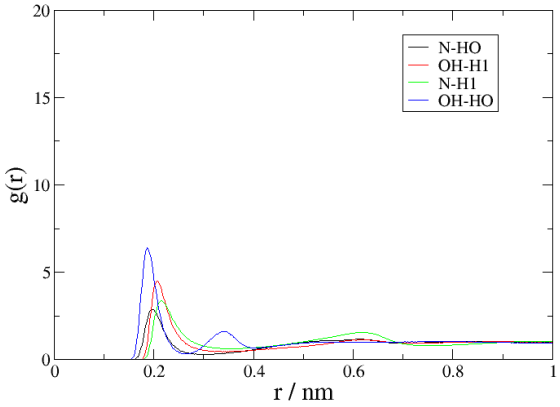

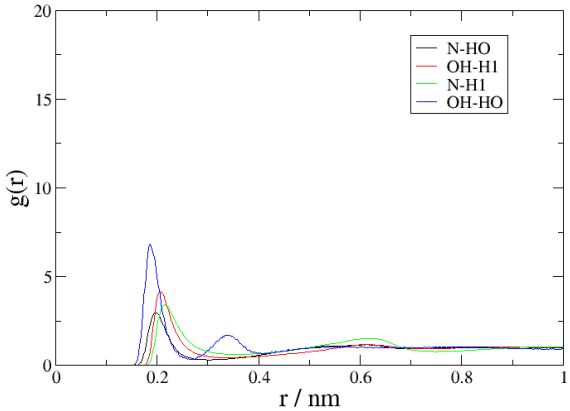

Figure C.4 - Radial distributions functions (RDFs) for a) [BMIM][SCN], b) [BMIM][DCA], c) [BMIM][TCN] and d) [EMIM][TCB], at 0.60 (on the left side) and 0.80 (on the right side) mole fraction of IL and 298.15 K. In each picture is represented all types of interaction, namely RDFs for anion-ethanol (—), cation-ethanol (—), cation-anion (—) and ethanol-ethanol (—) interactions.

Tables

Table C.1 – Comparison between experimental and simulated density values, obtained for different mole fractions of CN-based ILs, at 298.15 K.

[BMIM][SCN] + Ethanol

experimental		***simulation***		
x_{IL}	ρ_{exp} / (g·cm^{-3})	x_{IL}	ρ_{sim} / (g·cm^{-3})	AAD
0.20	0.925	0.2	0.931	0.66
0.40	0.991	0.4	1.001	1.01
0.59	1.026	0.6	1.042	1.53
0.80	1.053	0.8	1.068	1.44

[BMIM][DCA] + Ethanol

experimental		***simulation***		
x_{IL}	ρ_{exp} / (g·cm^{-3})	x_{IL}	ρ_{sim} / (g·cm^{-3})	AAD
0.19	0.917	0.20	0.914	0.31
0.40	0.983	0.40	0.967	1.63
0.63	1.023	0.60	0.998	2.46
0.83	1.045	0.80	1.017	2.75

[BMIM][TCN] + Ethanol

experimental		***simulation***		
x_{IL}	ρ_{exp} / (g·cm^{-3})	x_{IL}	ρ_{sim} / (g·cm^{-3})	AAD
0.26	0.944	0.20	0.914	3.14
0.47	0.992	0.40	0.967	2.55
0.65	1.017	0.60	0.998	1.92
0.83	1.035	0.80	1.017	1.75

[EMIM][TCB] + Ethanol

experimental		***simulation***		
x_{IL}	ρ_{exp} / (g·cm^{-3})	x_{IL}	ρ_{sim} / (g·cm^{-3})	AAD
0.20	0.914	0.20	0.922	0.88
0.40	0.969	0.40	0.984	1.57
0.60	1.001	0.60	1.020	1.98
0.80	1.022	0.80	1.044	2.23

Table C.2 – Comparison between experimental and simulated density and enthalpies of vaporization values, obtained for different CN-based ILs, at 298.15 K.

IL	ρ_{exp} [a] / kg·m^{-3}	ρ_{sim} / kg·m^{-3}	ΔH^{vap}_{sim} / kJ·mol^{-1}	ΔH^{vap}_{exp} / kJ·mol^{-1}
[BMIM][SCN]	1069.5	1082.0	123.0	114.5 - 148 [b]
[BMIM][DCA]	1060.3	1026.5	125.3	157.2 [c]
[BMIM][TCN]	1047.5	1030.6	140.4	155.6 [d]
[EMIM][TCB]	1036.1	1054.8	133.4	137.5 [e]

[a] Taken from C. M. S. S. Neves et al., *J. Phys. Chem. B*, 2013, 117, 10271–10283.

[b] Taken from A. Marciniak et al., *Int. J. Mol. Sci*., 2010, 11, 1973-1990.

[c] Taken from V. N. Emel'yanenko et al., *J. Am. Chem. Soc.*, 2007, 129, 3930-3937.

[d] Taken from S. P. Verevkin et al., *Angew. Chem.*, 2008, 120, 5149–5152.

[e] Taken from K. Fumino et al., *Chem.Phys,Chem*, 2010, 11, 1623-1626.

Appendix D

Tables

Table D.1 - Computed density as a function of glucose concentration estimated using TIP3P water model, and with OPLS FF for some selected glucose mole fractions, at 303.15 K. Values in parentheses denote uncertainty related to the computational estimation.

$x_{glucose}$	ρ_{exp} [a] / kg·m^{-3}	ρ_{TIP3P} [b] / kg·m^{-3}	AAD %
0.034	1081.8	1071.5	0.95
0.076	1125.7	1144.9	1.71
0.200	1177.7	1252.7	6.36
$x_{glucose}$	ρ_{exp} [a] / kg·m^{-3}	ρ_{OPLS} [c] / kg·m^{-3}	AAD %
0.034	1081.8	1110.2(±0.2)	2.62
0.050	1105.0	1151.4(±0.4)	4.20

a) Comesaña et al., *J. Chem. Eng. Data*, 2003, 362-366
b) Jorgensen et al., *J. Chem. Phys.*, 1983, *79*, 926–935
c) Damm et al., *J. Comput. Chem.*, 1997, *18*, 1955–1970

Table D.2 – Fitting parameters and decay times obtained using equation 3.4.2 of the Chapter 3.4.

$x_{glucose}$	A	α	τ_1	τ_2
0.034	1540.42	2.39E-03	3.73E-02	6.17E-04
0.050	1240.70	2.11E-03	8.83E-02	1.08E-03
0.076	986.376	4.42E-02	9.38E-03	1.63E-03
0.110	1249.15	4.47E-02	3.83E-02	2.56E-03
0.150	1245.33	8.42E-02	5.25E-02	5.43E-03
0.200	1649.77	1.75E-01	5.67E-02	4.53E-03

Table D.3 - Experimental and computational viscosity values estimated using OPLS FF for some selected glucose mole fractions, at 313.15 K. Values in parentheses denote uncertainty related to the computational estimation.

$x_{glucose}$	η_{exp} [a] / mPa·s	η_{OPLS} [b] / mPa·s	AAD %
0.034	1.205	1.308(±0.181)	8.55
0.050	1.475	1.980(±0.230)	34.24

a) Comesaña et al., *J. Chem. Eng. Data*, 2003, 362-366
b) Damm et al., *J. Comput. Chem.*, 1997, *18*, 1955–1970

Table D.4 - Coordination number (Z) from the RDF peaks for water-water interactions, at each mixture considered.

$x_{glucose}$	reference_atom	atom2	Z
0.034	**OW**	**OW**	4.78
0.050			4.51
0.076			4.19
0.110			3.88
0.150			3.36
0.200			2.99

Table D.5 - Coordination number (Z) from the RDF peaks for glucose-glucose interactions, at each mixture considered.

$x_{glucose}$	reference_atom	atom2	**Z**
0.034	O1	HO3	0.02
		HO6	0.02
		HO4	0.02
0.050	O1	HO3	0.02
		HO6	0.03
		HO4	0.03
0.076	O1	HO3	0.04
		HO6	0.05
		HO4	0.04
0.110	O1	HO3	0.05
		HO6	0.05
		HO4	0.05
0.150	O1	HO3	0.07
		HO6	0.07
		HO4	0.07
0.200	O1	HO3	0.09
		HO6	0.09
		HO4	0.08

Table D.6 – Values for the hydrogen bonds established between glucose and water molecules and for water with water molecules.

$x_{glucose}$	H-Bonds water-water (per water basis)	H-Bonds glucose-water (per glucose basis)
0.034	1.49	8.04
0.050	1.43	7.58
0.076	1.36	7.19
0.110	1.23	6.45
0.150	1.18	6.12
0.200	0.96	5.00

Table D.7 – Experimental and computational densities (ρ) for different glucose+water mixtures at 303.15 K. Values in parentheses denote the uncertainties (the standard deviation) estimated with the calculated results applying the scaling factor 0.8 to atomic charges. AAD represents the absolute deviations of the simulated data from the experimental values.

$x_{glucose}$	ρ_{exp} [a)] / kg·m^{-3}	ρ_{sim} / kg·m^{-3}	AAD %
0.034	1081.8	1068.1	1.27
0.050	1105.0	1091.7	1.20
0.076	1125.7	1121.4	0.39
0.110	1144.6	1145.9	0.11
0.150	1161.9	1172.2	0.89
0.200	1177.7	1196.1	1.56

a) Comesaña et al., *J. Chem. Eng. Data*, 2003, 362-366

Table D.8 – Experimental and calculated viscosities (η) by applying the scaling factor 0.8 to atomic charges, at 313.15 K. Values in parentheses denote uncertainties estimated accordingly to equation 3.4.3. AAD represents the absolute deviations of the simulated data from the experimental values.

$x_{glucose}$	η_{exp} [a)] / mPa·s	η_{sim} / mPa·s	AAD %
0.034	1.205	0.781	35.20
0.050	1.475	1.075	27.11
0.076	1.804	1.412	21.71
0.110	2.182	2.371	8.68
0.150	2.660	2.716	2.09
0.200	3.175	4.030	26.93

a) Comesaña et al., *J. Chem. Eng. Data*, 2003, 362-366

Figures

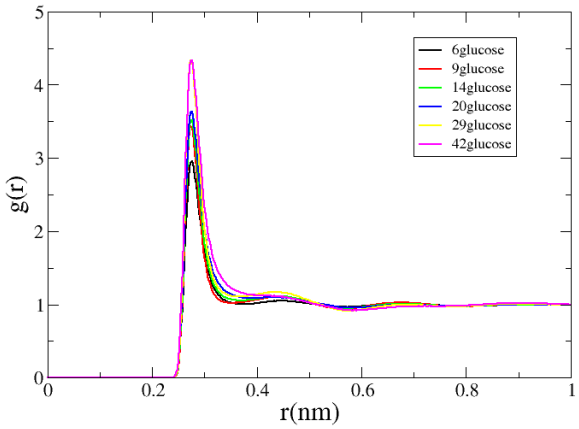

Figure D.1 - Radial distributions functions (RDFs) for water-water interactions, at six different glucose mole fractions and temperature of 313.15 K. RDFs for the systems composed of 6 glucose molecules (—), 9 glucose molecules (—), 14 glucose molecules (—), 20 glucose molecules (—), 29 glucose molecules (—) and 42 glucose molecules (—) are represented in this figure.

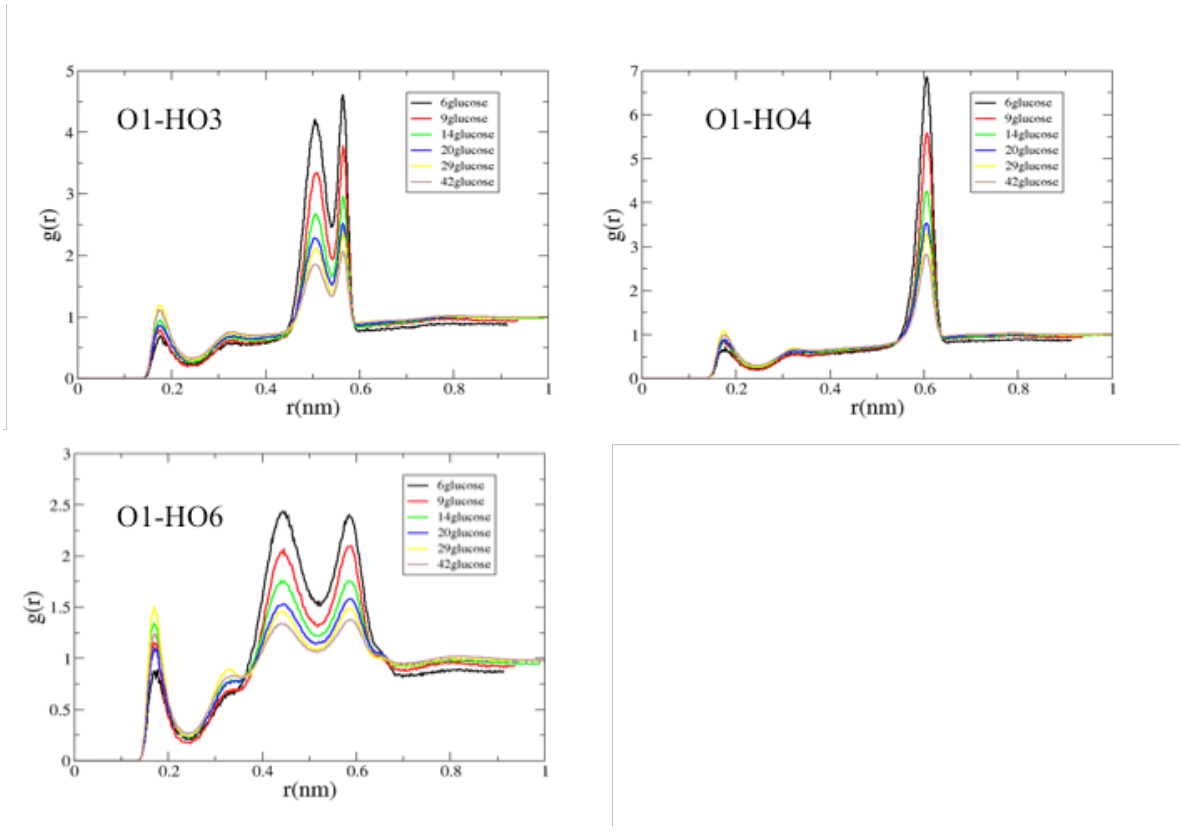

Figure D.2 - Radial distributions functions (RDFs) for glucose-glucose interactions, at six different glucose mole fractions and temperature of 313.15 K. RDFs for systems composed of 6 glucose molecules (—), 9 glucose molecules (—), 14 glucose molecules (—), 20 glucose molecules (—), 29 glucose molecules (—) and 42 glucose molecules (—). RDFs for O1-HO3, O1-HO4 and O1-HO6 interactions are represented in this figure.

Appendix E

Table E.1 - Atomic charges for [EMIM][SCN].

[EMIM][SCN]	
atom	**charge / *e***
C4	-0.17967
N1	0.09864
C2	0.08288
N3	-0.05516
C5	-0.12135
C6	-0.04704
C7	0.25101
H2	0.17728
H3	0.18593
H1	0.14445
H6	0.07377
H8	-0.00559
H7	-0.00559
H5	0.07377
H4	0.07377
C8	0.04155
H10	-0.00445
H11	-0.00445
H9	-0.00445
S	-0.53746
C	0.42796
N	-0.6658

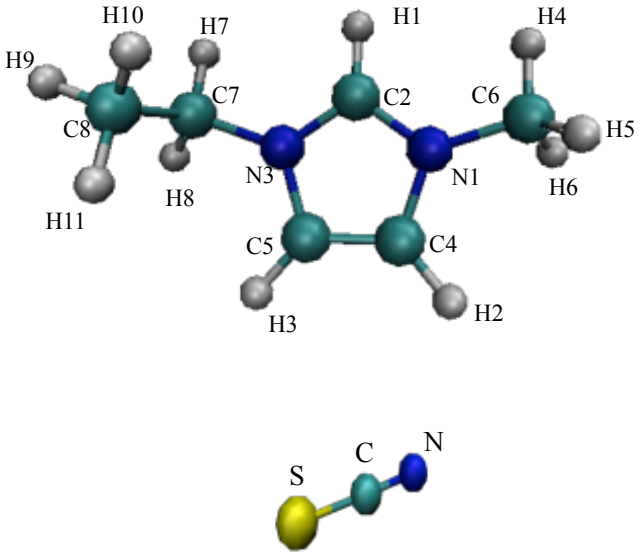

Table E.2 - Atomic charges for [EMIM][DCA].

[EMIM][DCA]	
atom	**charge / *e***
C4	-0.13321
N1	0.08405
C2	0.04292
N3	-0.00529
C5	-0.14042
C6	-0.09034
C7	0.23065
H2	0.18286
H3	0.18509
H1	0.15955
H6	0.09453
H8	0.01502
H7	0.01502
H5	0.09453
H4	0.09453
C8	-0.10889
H10	0.03440
H11	0.03440
H9	0.03440
N_1	-0.68818
C_1	0.65334
N_2	-0.72115

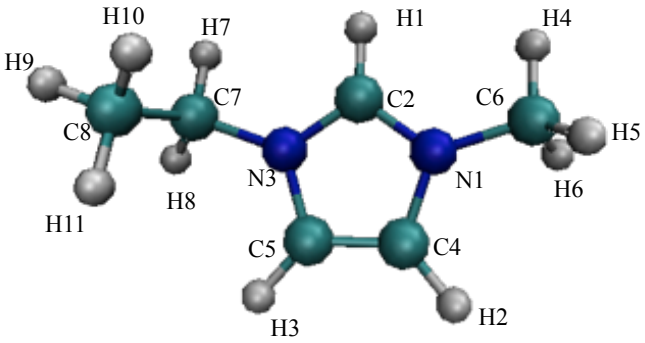

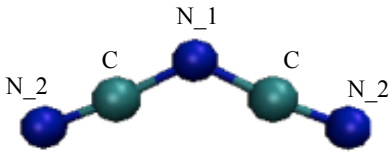

Table E.3 - Atomic charges for [EMIM][TCN].

[EMIM][TCN]	
atom	**charge / *e***
C4	-0.15202
N1	0.16614
C2	-0.08743
N3	0.06418
C5	-0.14453
C6	-0.1517
C7	0.08452
H2	0.18617
H3	0.19177
H1	0.21125
H6	0.11338
H8	0.04461
H7	0.04461
H5	0.11338
H4	0.11338
C8	-0.03404
H10	0.03131
H11	0.03131
H9	0.03131
C_3	-0.69743
C_1	0.58754
N_1	-0.64093

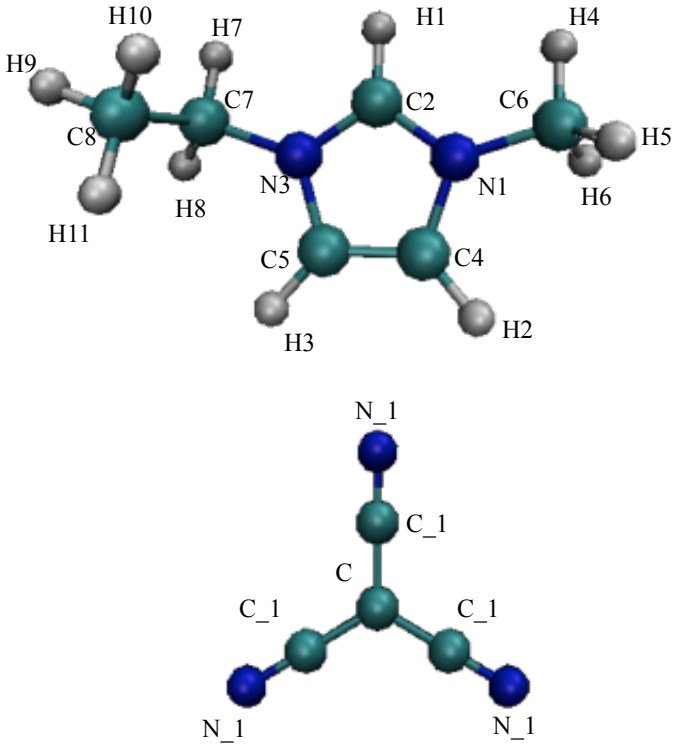

Table E.4 - Atomic charges for [EMIM][TCB].

[EMIM][TCB]	
atom	**charge / *e***
C4	-0.11805
N1	0.10915
C2	-0.09005
N3	0.12574
C5	-0.16698
C6	-0.05765
C7	0.11606
H2	0.18534
H3	0.20587
H1	0.20803
H6	0.08597
H8	0.06102
H7	0.06102
H5	0.08597
H4	0.08597
C8	-0.18562
H10	0.05837
H11	0.05837
H9	0.05837
B	**0.14410**
C	**0.22857**
N	**-0.48632**

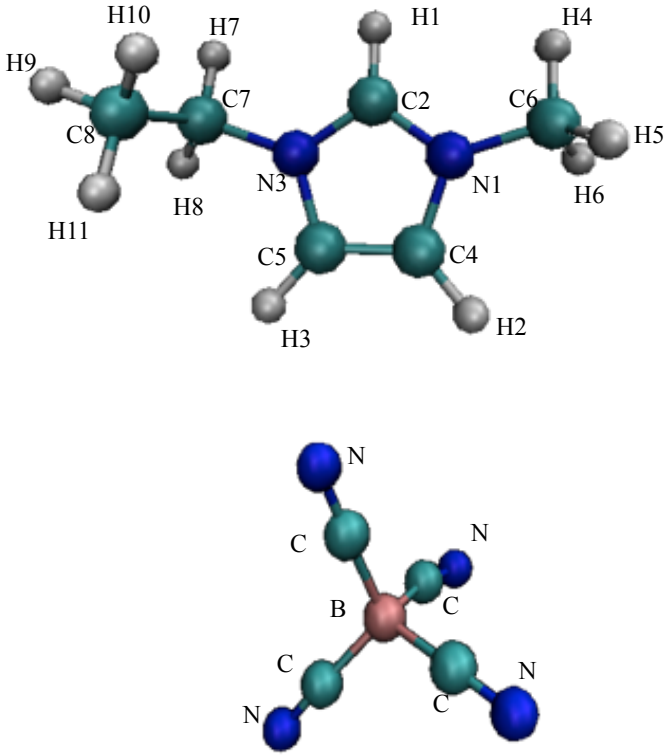

Table E.5 - Atomic charges for [EMIM][Ac].

[EMIM][Ac]	
atom	**charge / *e***
C4	-0.14278
N1	0.14751
C2	-0.02435
N3	0.05208
C5	-0.20946
C6	-0.1634
C7	0.16798
H2	0.16331
H3	0.19426
H1	0.23379
H6	0.11395
H8	0.02647
H7	0.02647
H5	0.11395
H4	0.11395
C8	-0.04468
H10	0.02175
H11	0.02175
H9	0.02175
CO	0.95231
O1	-0.82463
O2	-0.82463
CC	-0.30958
HC1	0.05741
HC2	0.05741
HC3	0.05741

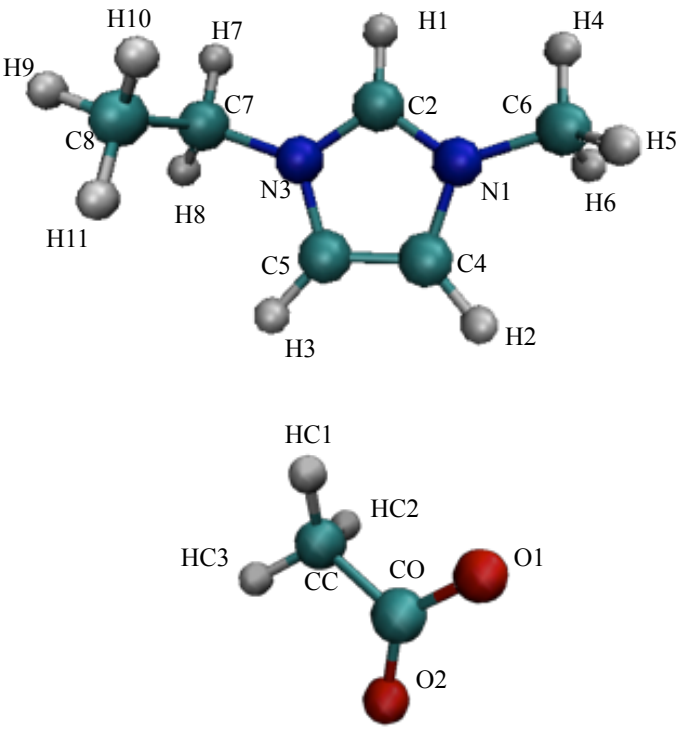

Table E.6 – Experimental and computational density values for each pure IL addressed in this study, at 298.15 K. Values in parentheses denote the relative deviations of simulated values from experimental values, respectively.

IL	ρ_{exp} / **kg·m^{-3}**	ρ_{sim} / **kg·m^{-3}**
[EMIM][SCN]	1117.0[a]	1071.040 (4.1%)
[EMIM][DCA]	1104.0[a]	1061.093 (3.9%)
[EMIM][TCN]	1081.9[a]	1058.913 (2.1%)
[EMIM][TCB]	1036.1[a]	1059.560 (2.2%)
[EMIM][Ac]	1099.3[b]	1055.0 (4.0%)

[a] Taken from C. M. S. S. Neves et at., *J. Phys. Chem. B*, 2013, **117**, 10271–10283.

[b] Taken from M.G. Freire et al., *J. Chem. Eng. Data*, 2011, 56, 4813-4822.

Table E.7 – Experimental values for glucose solubility in different ILs and water, in a temperature range of (283.15 – 333.15) K.

[EMIM][SCN]			
T / K	$(1/T)$ / K^{-1}	x_{glu}	$\ln(x_{glu})$
288.25	0.00347	0.1720	-1.76
298.15	0.00335	0.1950	-1.63
318.15	0.00314	0.2390	-1.43
328.15	0.00305	0.2620	-1.34
[EMIM][DCA]			
T / K	$(1/T)$ / K^{-1}	x_{glu}	$\ln(x_{glu})$
288.15	0.00347	0.1450	-1.93
298.15	0.00335	0.1830	-1.70
318.15	0.00314	0.2700	-1.31
328.15	0.00305	0.2980	-1.21
[EMIM][TCN]			
T / K	$(1/T)$ / K^{-1}	x_{glu}	$\ln(x_{glu})$
288.15	0.00347	0.0340	-3.38
298.15	0.00335	0.0430	-3.16
318.15	0.00314	0.0590	-2.83
328.15	0.00305	0.0620	-2.78
[EMIM][TCB]			
T / K	$(1/T)$ / K^{-1}	x_{glu}	$\ln(x_{glu})$
288.15	0.00347	0.0029	-5.90
298.15	0.00335	0.0034	-5.70
318.15	0.00314	0.0042	-5.50
328.15	0.00305	0.0042	-5.50
Water			
T / K	$(1/T)$ / K^{-1}	x_{glu}	$\ln(x_{glu})$
283.15	0.00353	0.0648	-2.74
293.15	0.00341	0.0843	-2.47
303.15	0.00330	0.1075	-2.23
313.15	0.00319	0.1446	-1.93
318.15	0.00314	0.1631	-1.81
333.15	0.00300	0.2188	-1.52
[BMIM][SCN]			
T / K	$(1/T)$ / K^{-1}	x_{glu}	$\ln(x_{glu})$
288.15	0.00347	0.1450	-1.93
298.15	0.00335	0.1700	-1.77

318.15	0.00314	0.2090	-1.57
328.15	0.00305	0.216	-1.53

[BMIM][DCA]

T / K	$(1/T)$ / K^{-1}	x_{glu}	$\ln(x_{glu})$
288.15	0.00347	0.1220	-2.11
298.15	0.00335	0.1470	-1.92
318.15	0.00314	0.2200	-1.51
328.15	0.00305	0.2410	-1.42

Table E.8 – Experimental and computational values of density for the mixtures composed of glucose and ionic liquids, at 313.15 K. Values in parentheses denote uncertainty related to the computational estimation.

[EMIM][SCN]+Glucose

$x_{glucose}$	ρ_{exp} / kg·m^{-3}	ρ_{sim} / kg·m^{-3}	AAD%
0.004	1110.6	1055.7 (±0.1)	4.56
0.034	1119.7	1068.6 (±0.1)	4.30
0.06	1127.3	1078.8 (±0.8)	4.14
0.1	1143.1	1095.8 (±0.4)	4.94

[EMIM][DCA]+Glucose

$x_{glucose}$	ρ_{exp} / kg·m^{-3}	ρ_{sim} / kg·m^{-3}	AAD%
0.004	1081.0	1048.4 (±0.5)	2.75
0.034	1090.3	1060.3 (±0.4)	3.44
0.06	1109.4	1071.2 (±0.3)	3.21
0.1	1125.2	1089.0 (±0.2)	3.02

Table E.9 – Experimental and computational values of viscosity for the mixtures composed of glucose and ionic liquids, at 313.15 K. Values in parentheses denote uncertainty related to the experimental measurements and computational estimation.

[EMIM][SCN]+Glucose

$x_{glucose}$	η_{exp} / mPa·s	η_{sim} / mPa·s	AAD%
0.004	15.065	8.377 (±0.455)	33.57
0.034	18.667	12.400 (±0.650)	30.08
0.06	24.132	16.874 (±0.876)	11.08
0.1	34.482	30.662 (±0.458)	44.40

[EMIM][DCA]+Glucose

$x_{glucose}$	η_{exp} / mPa·s	η_{sim} / mPa·s	AAD%
0.004	5.396	8.291 (±0.549)	92.42
0.034	6.232	11.990 (±0.586)	1.49

0.06	13.964	13.755 (±0.547)	5.94
0.1	19.107	17.973 (±0.462)	53.65

Table E.10 – Fitting parameters and decay times obtained using equation 3.4.2 of the Chapter 3.4.

[EMIM][SCN]+Glucose

$x_{glucose}$	A	α	τ_1	τ_2
0.004	170.46	1.26E-01	7.82E-02	4.50E-02
0.034	519.63	1.58E-01	1.00E-01	9.49E-03
0.06	433.69	1.27E-01	1.82E-01	1.82E-02
0.1	440.34	1.64E-01	2.87E-01	2.73E-02

[EMIM][DCA]+Glucose

$x_{glucose}$	A	α	τ_1	τ_2
0.004	439.44	1.15E-01	9.25E-02	9.97E-03
0.034	279.01	2.88E-02	4.68E-01	3.06E-02
0.06	585.59	1.68E-01	1.00E-01	7.99E-03
0.1	610.15	2.01E-01	1.07E-01	9.83E-03

Table E.11 – Coordination numbers (Z) for the systems composed of glucose with water and [EMIM][SCN], [EMIM][DCA] and [EMIM][Ac].

WATER

$x_{glucose}$=0.034				$x_{glucose}$=0.060				$x_{glucose}$=0.100			
Water	Water	Z	r_Z	Water	Water	Z	r_Z	Water	Water	Z	r_Z
O_W	H_W	1.75	0.25	**O_W**	H_W	1.63	0.25	**O_W**	H_W	1.48	0.25
Water	Glucose	Z	r_Z	Water	Glucose	Z	r_Z	Water	Glucose	Z	r_Z
H_W	OS_5			**H_W**	OS_5			**H_W**	OS_5		
	OH_1	1.13	0.25		OH_1	0.99	0.25		OH_1	0.85	0.25
	OH_2	1.16			OH_2	1.06			OH_2	0.90	
	OH_3	1.19			OH_3	1.09			OH_3	0.95	
	OH_4	1.02			OH_4	0.93			OH_4	0.83	
	OH_6	1.35			OH_6	1.22			OH_6	1.06	

[EMIM][SCN]

$x_{glucose}$=0.034				$x_{glucose}$=0.060				$x_{glucose}$=0.100			
Anion	Cation	Z	r_Z	Anion	Cation	Z	r_Z	Anion	Cation	Z	r_Z
N	H_1	1.22	0.4	**N**	H_1	1.18	0.4	**N**	H_1	1.13	0.4

Cation	Glucose	Z	r_Z	Cation	Glucose	Z	r_Z	Cation	Glucose	Z	r_Z
	OS_5	0.49	0.32		OS_5	0.46	0.32		OS_5	0.44	0.32
	OH_1		0.32		OH_1		0.32		OH_1		0.32
H_1	OH_2	0.48	0.32	**H_1**	OH_2	0.50	0.32	**H_1**	OH_2	0.44	0.32
	OH_3	0.62	0.32		OH_3	0.59	0.32		OH_3	0.55	0.32
	OH_4	0.38	0.32		OH_4	0.35	0.32		OH_4	0.33	0.32
	OH_6	0.53	0.32		OH_6	0.51	0.32		OH_6	0.49	0.32

[EMIM][DCA]

$x_{glucose}$=0.034				$x_{glucose}$=0.060				$x_{glucose}$=0.100			
Anion	Cation	Z	r_Z	Anion	Cation	Z	r_Z	Anion	Cation	Z	r_Z
N	H_1	1.95	0.4	**N**	H_1	1.89	0.4	**N**	H_1	1.83	0.4
Cation	Glucose	Z	r_Z	Cation	Glucose	Z	r_Z	Cation	Glucose	Z	r_Z
	OS_5	0.48	0.32		OS_5	0.50	0.32		OS_5	0.46	0.32
	OH_1		0.32		OH_1		0.32		OH_1		0.32
H_1	OH_2	0.54	0.32	**H_1**	OH_2	0.52	0.32	**H_1**	OH_2	0.50	0.32
	OH_3	0.65	0.32		OH_3	0.61	0.32		OH_3	0.56	0.32
	OH_4	0.35	0.32		OH_4	0.36	0.32		OH_4	0.31	0.32
	OH_6	0.51	0.32		OH_6	0.51	0.32		OH_6	0.49	0.32

[EMIM][Ac]

$x_{glucose}$=0.034				$x_{glucose}$=0.060				$x_{glucose}$=0.100			
Anion	Cation	Z	r_Z	Anion	Cation	Z	r_Z	Anion	Cation	Z	r_Z
O_1	H_1	2.38	0.4	**O_1**	H_1	2.35	0.4	**O_1**	H_1	2.28	0.4
Cation	Glucose	Z	r_Z	Cation	Glucose	Z	r_Z	Cation	Glucose	Z	r_Z
	OS_5	0.25	0.32		OS_5	0.20	0.32		OS_5	0.23	0.32
	OH_1		0.32		OH_1		0.32		OH_1		0.32
H_1	OH_2	0.46	0.32	**H_1**	OH_2	0.50	0.32	**H_1**	OH_2	0.45	0.32
	OH_3	0.63	0.32		OH_3	0.68	0.32		OH_3	0.61	0.32
	OH_4	0.34	0.32		OH_4	0.41	0.32		OH_4	0.34	0.32
	OH_6	0.36	0.32		OH_6	0.35	0.32		OH_6	0.35	0.32
Anion	Glucose	Z	r_Z	Anion	Glucose	Z	r_Z	Anion	Glucose	Z	r_Z
	HO_{12}	1.87	0.26		HO_{12}	1.97	0.26		HO_{12}	1.89	0.26
O_1	HO_8	2.15	0.26	**O_1**	HO_8	2.17	0.26	**O_1**	HO_8	2.06	0.26
	HO_6	1.87	0.26		HO_6	1.85	0.26		HO_6	1.90	0.26
	HO_4	1.93	0.26		HO_4	1.95	0.26		HO_4	1.85	0.26

HO_2	2.47	0.26	HO_2	2.45	0.26	HO_2	2.38	0.26

Figures

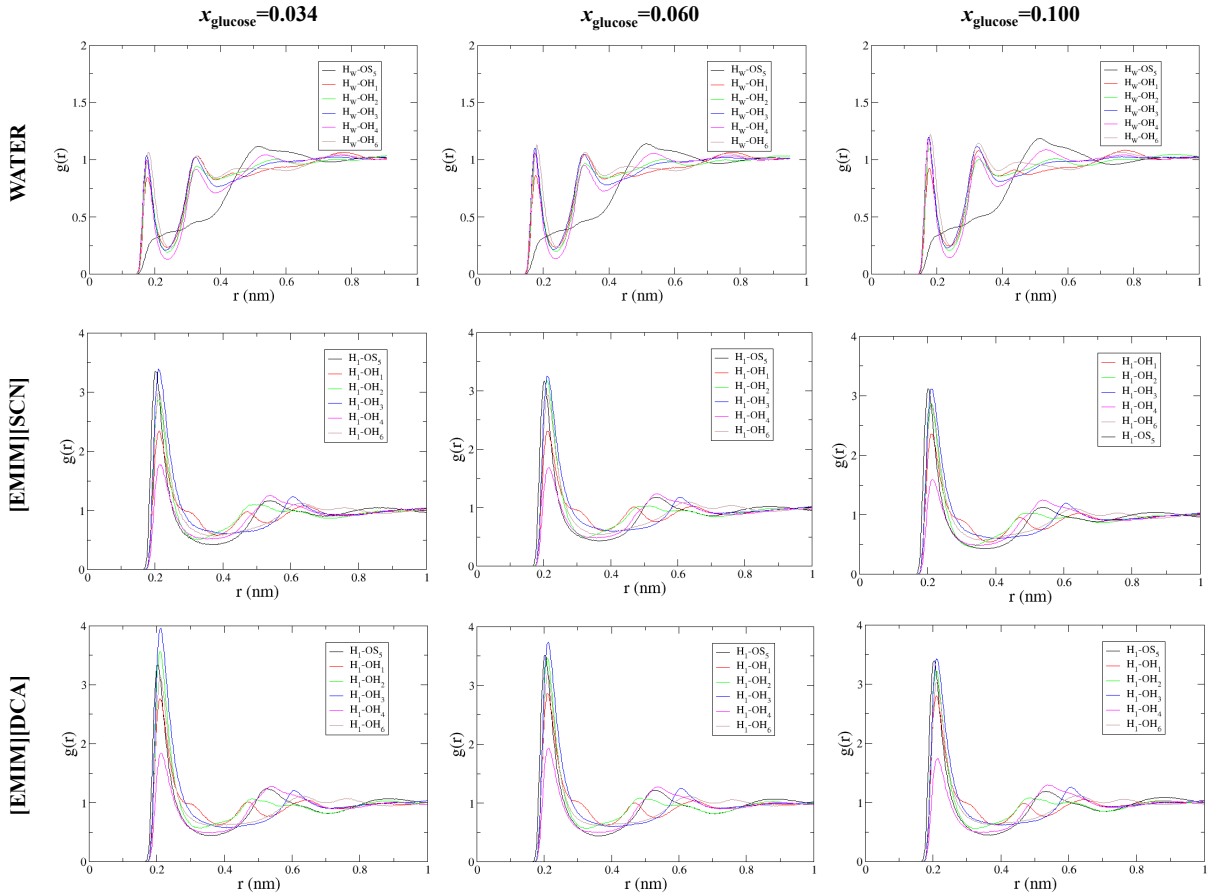

Figure E.1 – Radial distributions functions (RDFs) for glucose-water (above row), glucose-[EMIM][SCN] (middle row) and glucose-[EMIM][DCA] (bottom row) interactions at three different glucose mole fraction and a temperature of 313.15 K. RDFs for interaction between H_W/H_1-OS_5(—), H_W/H_1-OH_1(—), H_W/H_1-OH_2(—), H_W/H_1-OH_3(—), H_W/H_1-OH_4(—),H_W/H_1-OH_4(—) are represented in this figure.